Thermomechanical Response of Shape Memory Alloy Hybrid Composites

Travis L. Turner
Langley Research Center, Hampton, Virginia

January 2001

The NASA STI Program Office . . . in Profile

Since its founding, NASA has been dedicated to the advancement of aeronautics and space science. The NASA Scientific and Technical Information (STI) Program Office plays a key part in helping NASA maintain this important role.

The NASA STI Program Office is operated by Langley Research Center, the lead center for NASA's scientific and technical information. The NASA STI Program Office provides access to the NASA STI Database, the largest collection of aeronautical and space science STI in the world. The Program Office is also NASA's institutional mechanism for disseminating the results of its research and development activities. These results are published by NASA in the NASA STI Report Series, which includes the following report types:

- TECHNICAL PUBLICATION. Reports of completed research or a major significant phase of research that present the results of NASA programs and include extensive data or theoretical analysis. Includes compilations of significant scientific and technical data and information deemed to be of continuing reference value. NASA counterpart of peer-reviewed formal professional papers, but having less stringent limitations on manuscript length and extent of graphic presentations.

- TECHNICAL MEMORANDUM. Scientific and technical findings that are preliminary or of specialized interest, e.g., quick release reports, working papers, and bibliographies that contain minimal annotation. Does not contain extensive analysis.

- CONTRACTOR REPORT. Scientific and technical findings by NASA-sponsored contractors and grantees.

- CONFERENCE PUBLICATION. Collected papers from scientific and technical conferences, symposia, seminars, or other meetings sponsored or co-sponsored by NASA.

- SPECIAL PUBLICATION. Scientific, technical, or historical information from NASA programs, projects, and missions, often concerned with subjects having substantial public interest.

- TECHNICAL TRANSLATION. English-language translations of foreign scientific and technical material pertinent to NASA's mission.

Specialized services that complement the STI Program Office's diverse offerings include creating custom thesauri, building customized databases, organizing and publishing research results . . . even providing videos.

For more information about the NASA STI Program Office, see the following:

- Access the NASA STI Program Home Page at *http://www.sti.nasa.gov*

- Email your question via the Internet to help@sti.nasa.gov

- Fax your question to the NASA STI Help Desk at (301) 621-0134

- Telephone the NASA STI Help Desk at (301) 621-0390

- Write to:
  NASA STI Help Desk
  NASA Center for AeroSpace Information
  7121 Standard Drive
  Hanover, MD 21076-1320

NASA/TM-2001-210656

Thermomechanical Response of Shape Memory Alloy Hybrid Composites

Travis L. Turner
Langley Research Center, Hampton, Virginia

January 2001

Acknowledgments

Preface

This research results presented herein constitute a dissertation prepared by Travis L. Turner under the direction of Professor Mahendra P. Singh of the Virginia Polytechnic Institute and State Univeristy, Department of Engineering Science and Mechanics.

Contents

List of Figures

List of Tables

Summary

This study examines the use of embedded shape memory alloy (SMA) actuators for adaptive control of the themomechanical response of composite structures. Control of static and dynamic responses are demonstrated including thermal buckling, thermal post-buckling, vibration, sonic fatigue, and acoustic transmission. A thermomechanical model is presented for analyzing such shape memory alloy hybrid composite (SMAHC) structures exposed to thermal and mechanical loads. Also presented are (1) fabrication procedures for SMAHC specimens, (2) characterization of the constituent materials for model quantification, (3) development of the test apparatus for conducting static and dynamic experiments on specimens with and without SMA, (4) discussion of the experimental results, and (5) validation of the analytical and numerical tools developed in the study.

The constitutive model developed to describe the mechanics of a SMAHC lamina captures the material nonlinearity with temperature of the SMA and matrix material if necessary. It is in a form that is amenable to commercial finite element (FE) code implementation. The model is valid for constrained, restrained, or free recovery configurations with appropriate measurements of fundamental engineering properties. This constitutive model is used along with classical lamination theory and the FE method to formulate the equations of motion for panel-type structures subjected to steady-state thermal and dynamic mechanical loads. Mechanical loads that are considered include acoustic pressure, inertial (base acceleration), and concentrated forces. Four solution types are developed from the governing equations including thermal buckling, thermal post-buckling, dynamic response, and acoustic transmission/radiation. These solution procedures are compared with closed-form and/or other known solutions to benchmark the numerical tools developed in this study.

Practical solutions for overcoming fabrication issues and obtaining repeatable specimens are demonstrated. Results from characterization of the SMA constituent are highlighted with regard to their impact on thermomechanical modeling. Results from static and dynamic tests on a SMAHC beam specimen are presented, which demonstrate the enormous control authority of the SMA actuators. Excellent agreement is achieved between the predicted and measured responses including thermal buckling, thermal post-buckling, and dynamic response due to inertial loading.

The validated model and thermomechanical analysis tools are used to demonstrate a variety of static and dynamic response behaviors associated with SMAHC structures. Topics of discussion include the fundamental mechanics of SMAHC structures, control of static (thermal buckling and post-buckling) and dynamic responses (vibration, sonic fatigue, and acoustic transmission), and SMAHC design considerations for these applications. The dynamic response performance of a SMAHC panel specimen is compared to conventional response abatement approaches. SMAHCs are shown to have significant advantages for vibration, sonic fatigue, and noise control.

Chapter 1
Introduction

1.1 Background and Motivation

The effects of noise and vibration transmission and propagation proliferate throughout our everyday experiences. These effects range from annoyance or interference with other activities to mechanical failures, loss of hearing, and even loss of life. Attempts to attenuate or otherwise remedy noise and vibration problems date back as far as our acknowledgment of them. Methods of noise/vibration reduction typically involve increases in one or more of three things; mass, stiffness, or damping. Conventional noise/vibration abatement attempts typically consist of post-design treatments to reduce the noise/vibration at the source or reduce the perception of the noise/vibration. Examples of conventional treatments include sound-absorbing blanket or foam, lead-vinyl or viscoelastic damping layers, viscoelastic vibration isolators, tuned vibration absorbers, etc. These add-on treatments can be adequate for some applications where weight is not an issue and system parameters do not vary widely. However, there are other applications where weight-efficiency and adaptability are all-important. One class of such applications arises in the area of high-performance aerospace structures.

Excitation levels for many aerospace vehicle structures are high due to engine noise and turbulent boundary layer fluctuating pressures. The ever-increasing need for weight-efficient structures in these applications leads to significant sonic fatigue and interior noise issues. Conventional aerospace structures typically employ passive treatments such as structural stiffening, constrained-layer damping, and acoustic absorption materials to reduce the structural response and interior acoustic levels. These treatments typically suffer from substantial weight penalty and are often limited to relatively low temperatures and/or high frequencies. Smart materials may enable new structural design paradigms for high-performance, durable structures.

A significant amount of research in the last several years has greatly advanced the field of control of flexible structures through the use of smart materials. The field of smart structures involves a broad range of technologies that enable the realization of structural systems that are able to sense and to control their own behavior, such that the range of operational performance may be extended over conventional structures. Smart structures have the ability to change stiffness, shape, natural frequency, damping, and other mechanical characteristics in response to changes in temperature, electric field, or magnetic field. The most common smart materials are piezoelectric materials, shape memory alloys, magnetostrictive materials, electrorheological fluids and magnetorheological fluids. All of these adaptive materials have great potential in a variety of applications. Shape memory alloys (SMAs) appear to have significant advantages for

high-performance aerospace vehicles in the areas of structural response control, structural shape control, and damping enhancement.

Shape memory alloys have been investigated for a variety of applications since their discovery. Early potential for applications in self-erecting structures, thermally actuated devices, and energy-conversion systems was identified by Buehler and Wang [1]. Other potential applications including damping or energy absorbing devices, thermally actuated couplings and fasteners, and biomedical devices were briefly described by Wayman and Shimizu [2]. Later, Wayman [3] and Otsuka and Shimizu [4] gave more detailed descriptions of specific devices such as pipe couplings, thermostats, a robot hand, and various biomedical systems. Other researchers have reported progress on similar applications, but an entire new field of applications was created when Rogers and Robertshaw [5] introduced the idea of embedding SMA actuators in a composite laminate. A structure of this type has been termed a shape memory alloy hybrid composite (SMAHC).

Numerous researchers have investigated the use of SMA actuators, either external to a structure or embedded within the structure, for static and dynamic structural control. Studies have considered SMA actuators, external to the structure, for active vibration control [6, 7, 8] and shape control [9, 10] of cantilevered beams. Other studies have proposed SMA actuators for vibration control of space structures [11] and presented analytical formulations to demonstrate the vibration/structural acoustic control of SMAHC panels [12, 13]. Active vibration control of flexible linkage mechanisms using SMAHCs has been investigated by Venkatesh et al. [14]. Studies of thermal post-buckling [15] and random dynamic response [16] suppression of SMAHC panels were presented using a thermoelastic finite element (FE) formulation. A different approach was offered by Ro and Baz [17, 18, 19], where thermal, static, and dynamic analyses were developed for the case of SMA actuators passing through sleeves in composite plates. Birman [20] investigated optimal distributions of SMA actuators in sleeves to improve the buckling performance of sandwich panels under mechanical loading. Theses have also been devoted to studying the dynamic response tuning capability of Nitinol actuators [21] and predicting the structural acoustic behavior of SMAHC panels [22].

Shape memory alloys are a class of materials that exhibit a diffusionless martensitic transformation when cooled from the higher-temperature austenitic state. The interaction of temperature and applied stress in driving the martensitic and reverse transformations can be used to exploit phenomena such as the *shape memory effect* (SME) [23] and *pseudo-elasticity*. The SME can be described in simple terms in the following manner. A SMA can be easily deformed in the low temperature martensitic condition and can be returned to its original configuration by heating through the reverse transformation temperature range. This type of SME is termed *free recovery*. Conversely, in a constrained recovery configuration, the SMA element is prevented from recovering the initial strain and a large tensile stress (*recovery stress*) is induced. A situation in which the actuator performs work (deforms under load) is called *restrained recovery*. Extensive work has been done to characterize these materials, both qualitatively through theoretical models [24, 25, 26, 27] and quantitatively for particular alloy compositions [28, 29, 30]. Compilations of papers have also been published [31, 32, 33, 34], which give a good overview of the characteristics of SMAs and their applications. Birman [35] gave a comprehensive review of work

done in the areas of alloy characterization, constitutive modeling, and applications. Some detail on thermomechanical characteristics of SMAs will be given in Chapters 2 and 3.

Although there are several alloy systems that exhibit the shape memory effect, Nitinol has the most engineering significance. The name for this family of alloys was derived from Nickel, Titanium, and Naval Ordnance Laboratory and was patented by Buehler and Wiley [23]. The SME for this family of alloys is limited to nearly equiatomic compositions, i.e., Nickel content from 53 to 57 percent by weight. Nitinol is considered to be the shape memory alloy with the most potential for engineering applications because of its ductility at low temperature, high degree of shape-recovery capability, large pseudoelastic hysteresis, corrosion and fatigue resistance, biomedical compatibility, and relatively high electrical resistance.

The literature referred to in this introduction is by no means comprehensive, but should serve as a guide to work that has been done and the state of the art in this area. Other references to specific works in the literature appear at relevant places throughout the remainder of this document. The scope and objectives of the present work, including a description of the contributions made to the state of the art, are given in the next section.

1.2 Scope and Objectives

A Nitinol alloy was chosen for this study because it is the most readily available alloy and because of the favorable shape memory and electrical resistance characteristics. The relatively high electrical resistance is beneficial for experimental situations involving activation of the actuators by resistive heating. Because of the ability of SMA actuators to induce large tensile forces and recover large strains, they are particularly attractive for applications involving adaptive structural stiffening (constrained recovery) and shape control (restrained recovery). The environment associated with many aerospace applications includes inherently elevated temperatures and broadband surface pressure excitation. Embedded SMA elements are particularly suited to such applications because they generate global structural stiffening and obviate control electronics and auxiliary power. It is for these reasons that the present work will focus on SMAHC panel-type structures with embedded actuators operating in a constrained recovery mode for adaptive structural stiffening.

The purpose of the present work is to develop and experimentally validate an analytical tool that captures the material nonlinearity of SMAs and complex thermomechanical behavior of SMAHC laminates. Constitutive theories for SMAHC structures could be developed from the previously mentioned models for SMA thermomechanical behavior [24, 25, 26, 27], as was done by Boyd and Lagoudas [36] and Birman [37]. However, these models are difficult to use in practice. An alternative approach is to employ a constitutive model which makes use of experimental measurements of fundamental engineering properties. Two such models are developed as part of the present work. Differences between the two models and reasons for development of the refined model are discussed in Chapter 2. The model is used in mechanics-of-materials approach to develop the constitutive relations for SMAHC material systems. The model captures the material nonlinearity of the SMA, as well as that for the matrix material when appropriate, and is shown to be quite general in that it can be used to model constrained, restrained, or free recovery behavior.

The complex nature of SMAHC structures and the goal of experimental validation dictate the use of the FE method to facilitate accurate thermomechanical analysis. Because no commercial FE codes have the capability of modeling the constitutive behavior of SMAHC laminates, a research FE code was developed as part of this work. However, it is a goal of this work to cast the constitutive model and thermomechanical FE formulation such that it can be readily implemented in a commercial FE code.

The experimental configurations that will be considered for demonstration of adaptive structural stiffening by thermal activation of embedded SMA actuators involve immovable in-plane boundary conditions. This condition leads to a potential for structural instability due to thermal buckling and demands that the FE analysis be capable of predicting static, thermal buckling and post-buckling behavior in addition to analysis of the response due to practical dynamic excitation types. To this end, the constitutive relations are used in conjunction with von Kármán strain-displacement relations to allow for the generality of large, out-of-plane deflection due to thermal post-buckling.

A brief description of the work performed in this study and contributions made have been given in this section. The manner in which the detailed discussions of various topics are organized in this document is given in the following section.

1.3 Research Organization

Some detail of the general thermomechanical behavior of SMAs is given in Chapter 2 with an emphasis on phenomena observed in the mechanical testing performed in this work. That is followed by development of a constitutive model to describe the behavior of SMA actuators embedded in a composite matrix. The constitutive model is used with the von Kármán strain-displacement relations and classical lamination theory to develop the resultant force and moment relations for a SMAHC laminate. The particular material system used in this study is described in Chapter 3. An overview of the processes involved in fabricating SMA hybrid composite specimens is followed by results from thermomechanical property testing of the constituent materials.

Chapter 4 begins with a description of the rectangular plate element used in the finite element formulation. This is followed by development of the equations governing the thermomechanical response of a SMAHC laminate to steady-state thermal and dynamic mechanical loads. The governing equations are separated into static and dynamic components by assuming small (geometrically linear) dynamic motion about a potentially large (geometrically nonlinear) thermally deflected shape.

Description of the solution procedures begins in Chapter 5 with the static response. Equations governing static stability and large static deflection are first developed and then used to present thermal buckling and thermal post-buckling solution procedures. A overview flowchart is shown in each case. The solution procedures are then validated against a series of known solutions. The chapter is concluded with experimental validation of the model for the case of a SMAHC beam clamped at both ends and heated uniformly by DC electrical current.

Continuous and discrete frequency domain solutions are shown in Chapter 6 for predicting the dynamic response. The dynamic response solution procedure is validated against known

solutions and experimental measurements for isotropic and conventional composite beam specimens excited by random inertial loading. The analysis is then validated with experimental measurements of the dynamic response performance of a SMAHC beam specimen subjected to steady-state thermal and dynamic inertial loads. Chapter 6 concludes with correlation of predicted and measured dynamic responses of a clamped aluminum panel subjected to random acoustic pressure, which introduces the topic of acoustic radiation in preparation for Chapter 7.

Continuous and discrete frequency domain solutions are shown in Chapter 7 for predicting the acoustic radiation from a known panel response. The acoustic radiation solution procedure is validated against a classical analysis method. Chapter 7 is concluded with comparisons against experimental measurement from a fully clamped aluminum panel subjected to spatially uniform, temporally random acoustic pressure.

A variety of application and demonstrations are discussed in Chapter 8 which show the complex thermomechanical behavior of SMAHC structures and the effectiveness of embedded SMA actuators in attenuating dynamic response as compared to conventional response abatement approaches. Finally, a detailed summary and concluding remarks are given in Chapter 9.

Chapter 2
Background on SMAs and Constitutive Modeling

A general discussion of the thermomechanical behavior of SMAs begins this chapter. This discussion will serve as an overview and motivation of the SMAHC constitutive modeling section. Material property data for the material system used in this study will be presented in the next chapter, which will be used to quantify the constitutive model for the specific materials used. The constitutive model will be used in Chapter 4 to develop a finite element formulation for the thermomechanical response of SMAHC structures.

2.1 Background on Shape Memory Alloys

A very brief introduction to SMAs and the SME was given in Chapter 1. An overview of some essential characteristics of SMAs will given in this section to facilitate understanding of results and discussions to be presented later in this document.

The thermoelastic martensitic and reverse transformations are shown schematically in Figure 2.1 in terms of the martensitic fraction versus temperature. At high temperature, a shape memory alloy exists in a usually cubic phase called austenite. Martensite is the low-temperature phase and has a lesser symmetry. The reference temperatures indicated in Figure 2.1 mark the start and finish temperatures for the forward transformation to martensite and the reverse transformation to austenite, respectively. The thermoelastic martensitic transformation occurs when the alloy in the austenitic parent phase is cooled through the transformation temperature range $M_s \rightarrow M_f$, producing martensite. The reverse transformation occurs when the alloy is heated through the reverse transformation temperature range $A_s \rightarrow A_f$ and the material structure returns to that of austenite. It is known that a shape memory alloy specimen shows no macroscopic deformation during the martensitic transformation, described by Wayman and Duerig in [32] for example. Because the martensite is of a lower-order symmetry than the parent phase, the crystalline structure change in the forward transformation produces several martensite variants that are self-accommodating (called *twinning*) so that no macroscopic deformation results. However, the crystalline change to austenite is unique. When a stress is applied to the twinned martensite, the variant in the sense of the stress grows at the expense of other variants (called *detwinning*). Thus, inducing the crystallographically unique reverse transformation causes a strain recovery, and the material reverts to its original configuration. This sequence is the basis of the SME and is shown schematically in Figure 2.2.

In Nitinol for example, strains as high as 8% can be completely recovered by heating the alloy above A_f (Cross et al. [28]). Recall that this type of SME phenomenon is termed
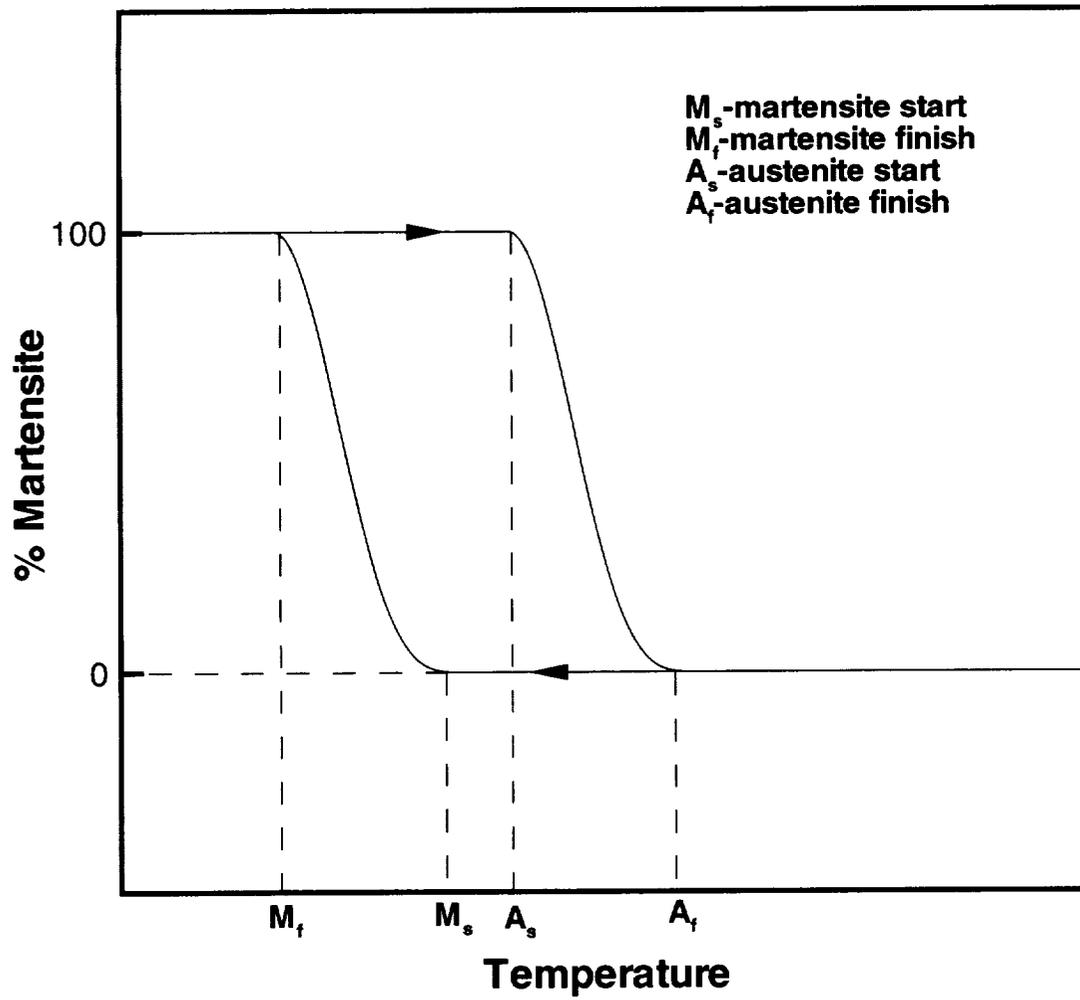
Figure 2.1 Schematic of martensitic and reverse transformations, after Liang and Rogers [13].

Martensite (twinned)

Cool

Deform

Austenite

← Heat

Martensite (deformed)
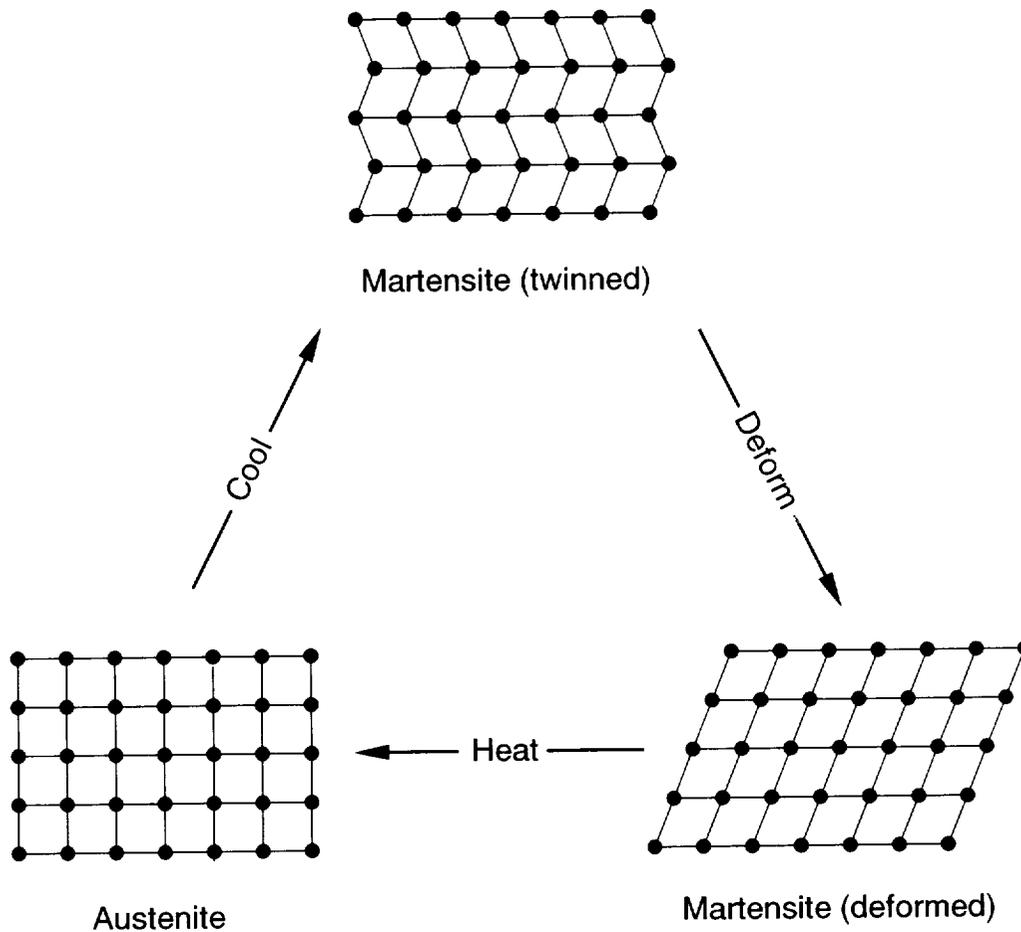
Figure 2.2 Schematic of the shape memory effect, after Wayman and Duerig in [32].

free recovery. This study is primarily concerned with constrained recovery, where the SMA element is prevented from recovering the initial strain and a large recovery stress is induced. The recovery stress is a function of initial strain and temperature, as shown in Figure 2.3 for example.   The recovery stress will approach, but obviously not exceed the austenitic yield stress due to plastic slip or production of stress induced martensite, which will be discussed subsequently. The relationship between these two yield stresses will be discussed subsequently. For example, Cross et al. [28] found that the maximum yield stress for an alloy in a 100 mil diameter rod form was 90 ksi, while the corresponding maximum recovery stress was 80 ksi at 8% initial strain. The austenitic yield stress is approximately a factor of 10 greater than that of the corresponding martensitic phase. The Young's modulus also increases by a factor of three to four under the same conditions (see Figure 2.4).   Note that following a process of free recovery, no shape change is produced in the alloy when it is cooled again below M_f and the specimen must be strained again to repeat the SME. This type of behavior is termed *one-way* shape memory. *Two-way* shape memory, where the alloy "remembers" a low-temperature

9
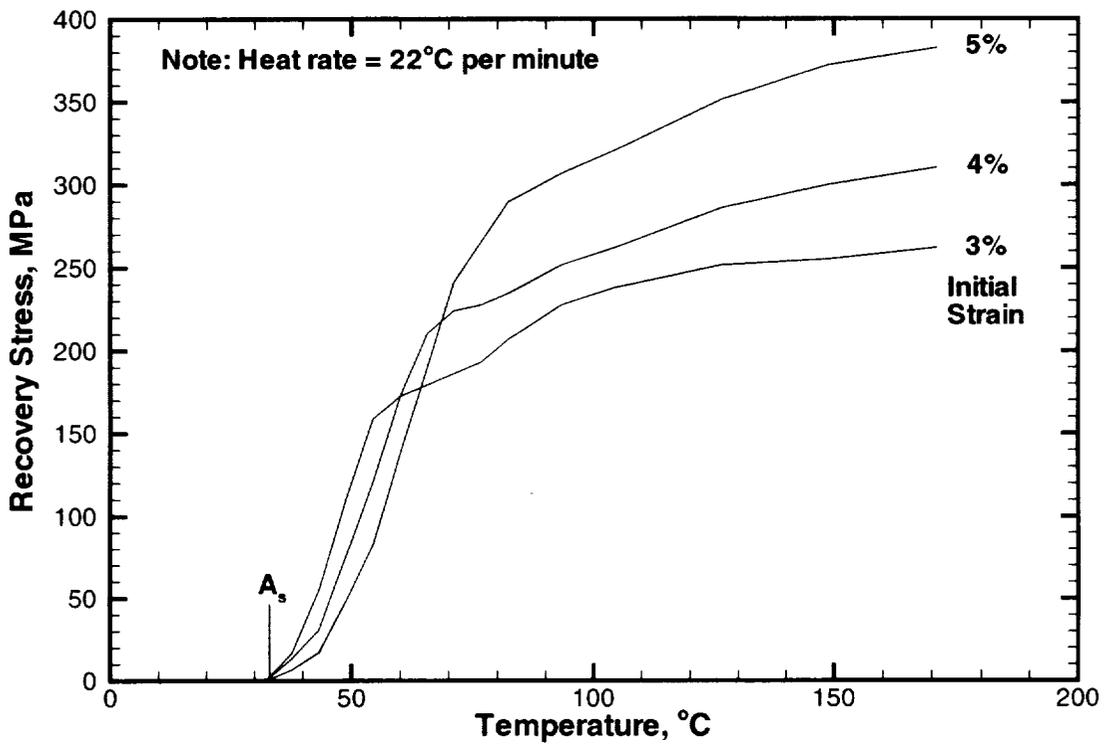
Figure 2.3 Nitinol recovery stress versus temperature and initial strain, after Cross et al. [28].

10
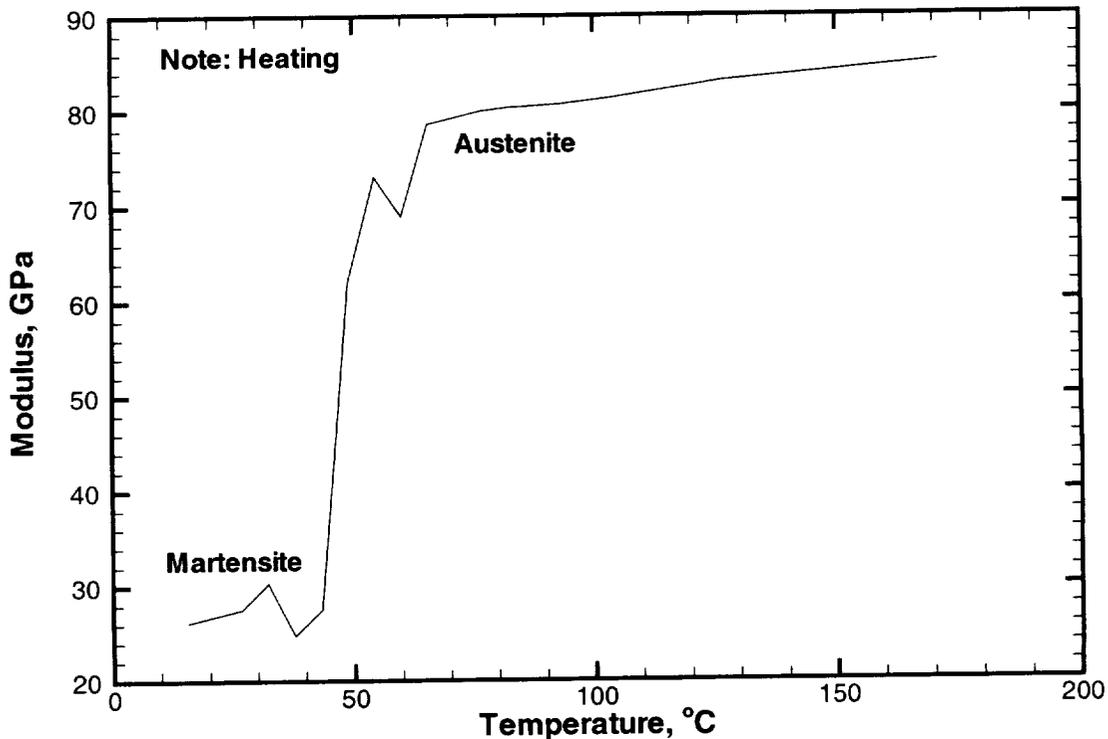
Figure 2.4 Nitinol Young's modulus versus temperature, after Cross et al. [28].

martensitic configuration and a high-temperature austenitic configuration, can be imparted to a SMA with appropriate training, as described by Perkins and Hodgson in [32]. One-way or two-way shape memory behavior can be *trained* (rendered stable and predictable) into a SMA by a number of means. A description of one simple method follows.

One-way training can be accomplished by imparting a specific amount of plastic (detwinning) deformation to the SMA in the low-temperature martensitic condition, heating the material to induce the austenite phase transformation and allowing the alloy to recover the initial strain, and cooling the material to induce the transformation to martensite. This procedure is repeated until the hysteresis becomes stable. Two-way shape memory training can be performed by restraining the SMA element, after being plastically deformed at low temperature, and subjecting it to a number of thermal cycles, alternating between a specific low and high temperature. The benefit of this training method is that the shape memory element "memorizes" two stable shapes (a low-temperature shape and a high-temperature shape) at the expense of some degradation in performance.

There are other means by which a one-way actuator can be returned to a strained state following recovery. Two examples include operating actuators in agonist-antagonist pairs or opposing the actuators with a bias spring. In either case, the active actuators perform work (deform under load). Recall that operation of an actuator in this type of configuration is

termed restrained recovery. Obviously, the amount of force generated in restrained recovery is diminished relative to constrained recovery.

The martensitic transformation can also be stress induced in a shape memory alloy at temperatures above M_s. An increase in the applied stress produces an effect analogous to a decrease in temperature. However, only one martensite variant (*stress induced martensite*, SIM) grows in the direction most favorable for the applied stress. This phenomenon is exemplified in the stress-strain curves for an alloy at various temperatures shown in Figure 2.5. For temperatures in the range $M_s < T < A_s$, SIM will be formed and retained after unloading. Partial reversion to austenite will occur upon stress release for temperatures in the range $A_s < T < A_f$. At temperatures approaching or greater than A_f, the complete reverse transformation ensues immediately upon stress release as the martensite is completely unstable without stress assistance. These phenomena are all classified as pseudoelastic effects. The latter effect of full reverse transformation upon stress release is an example of a subset of pseudoelasticity called superelasticity.

The pseudoelasticity discussed here is called transformation pseudoelasticity. Twinning pseudoelasticity exists as well, which gives rise to *rubber-like* behavior. This phenomenon occurs when a SMA is allowed to age in the martensitic phase and is then stressed to induce prestrain. Instead of maintaining the strain, the strain is recovered upon stress release (in a very similar manner to superelasticity, but entirely in the martensitic phase). This behavior indicates that if one is going to prestrain a SMA actuator, it must be done shortly after inducing the martensitic transformation on cooling, i.e., immediately after removing strain induced in the material during packaging.

Additional insights can be afforded from the stress strain curves shown in Figure 2.5. When the material is in the purely martensitic phase, the yield stress to induce martensite detwinning and produce appreciable strains is quite small. If loading were continued as shown in Figure 2.6, the martensite would eventually become completely detwinned and would deform elastically until plastic slip is induced. Obviously, the amount of reversible strain is limited by the onset of plastic slip in the martensitic phase. Rather complex behavior is involved at intermediate temperatures $M_f < T < A_f$ depending upon the state of the alloy. The stress required to yield the material in the austenitic phase is much higher than that for martensite. At temperatures in the vicinity of A_f, yielding is due to the production of SIM. The stress required to induce SIM continues to increase with increasing temperature above A_f until a critical temperature is reached, at which point plastic slip will be induced in lieu of SIM.

The transformation temperatures of an alloy can be measured by monitoring practically any property of the alloy, such as electrical resistance, but a particularly accurate and insightful means is differential scanning calorimetry (DSC). The transformation temperatures for Nitinol can be altered by changing the composition of the alloy. For example, Buehler and Wang [1] report that A_s for Nitinol can be varied from −50°C to 166°C through changes in the Nickel content from 54.5% to 56.5% by weight (see Figure 2.7). The transformation temperatures are
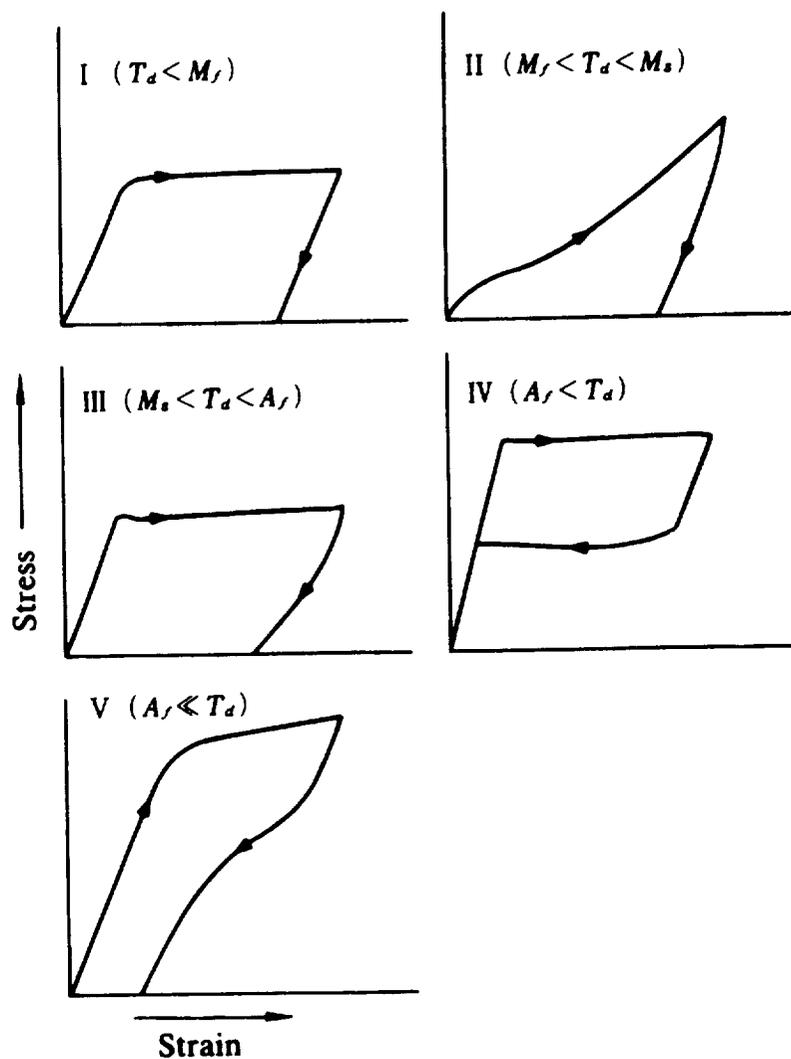
Figure 2.5 Stress-strain curves for a shape memory alloy at various temperatures, after Funakubo [33].
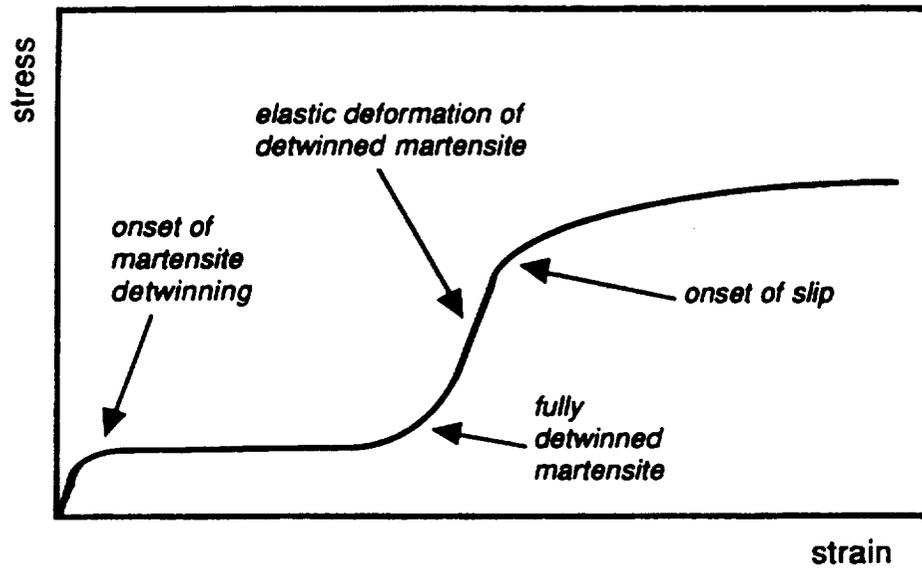
Figure 2.6 Stress-strain curves for a shape memory alloy at various temperatures, after Wayman and Duerig in [32].

200

$^\circ$C

150

Austenite Start Temperature (A$_s$),

100

50

0

-50

-100
53.5   54   54.5   55   55.5   56   56.5

Nickel, weight %
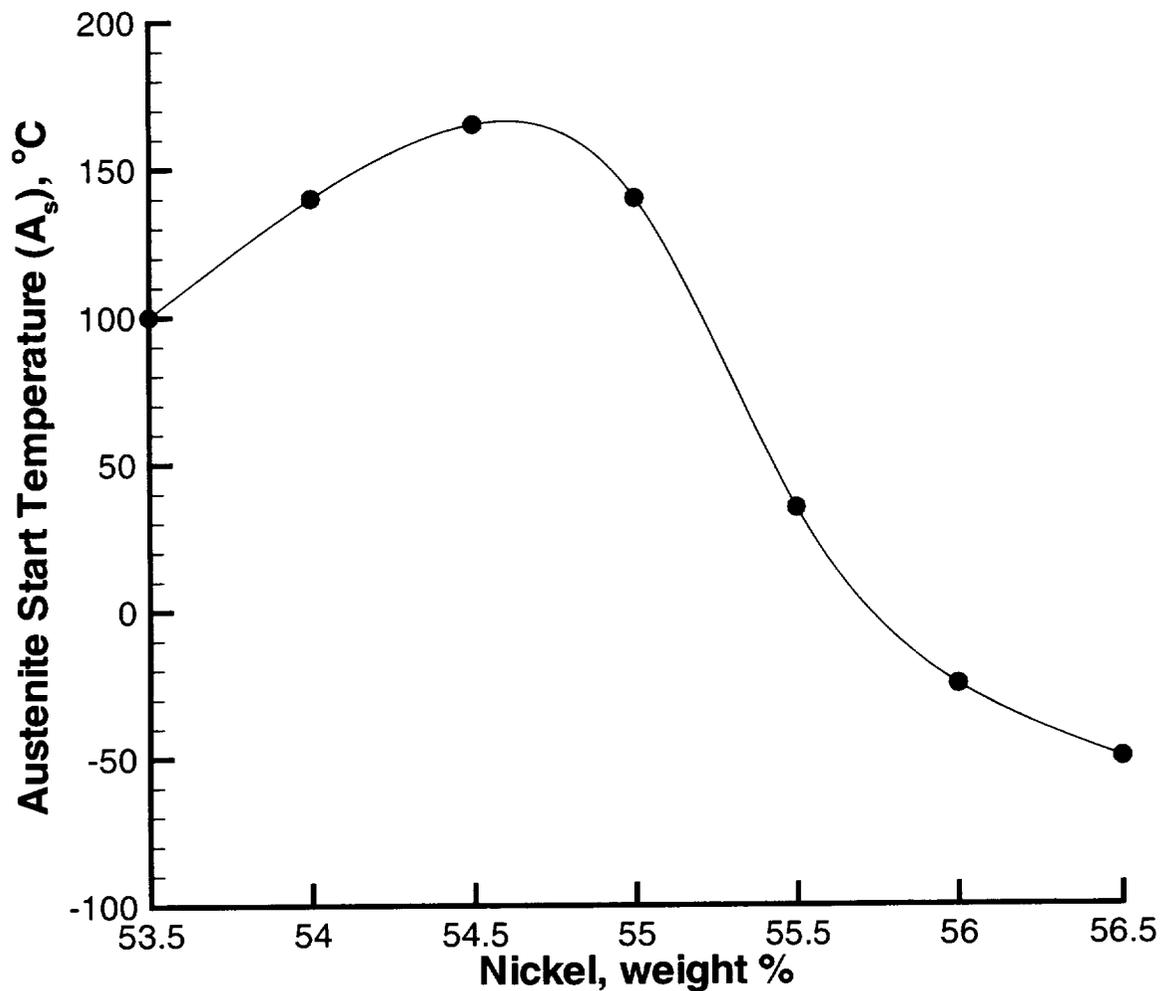
Figure 2.7 Variation in austenite start temperature with
weight % Ni in Nitinol, after Buehler and Wang [1].

also strongly influenced by stress. It is known from early work, such as Cross et al. [28] for example, that the best shape recovery performance for fully annealed Nitinol is achieved with an anneal temperature of approximately 930 °F. Goldstein et al. [38] found that partial annealing of the residual stresses due to cold work can be used to change the transformation temperatures and induce a rhombohedral R phase.

All of the discussions to this point have assumed that the alloy is in a fully annealed state. Some annealing is necessary to remove some of the cold work dislocations which impede the twin boundary movement, but it is usually desirable to only partially anneal the alloy and leave some of the dislocations for strength and durability. Production of the R-phase during cooling from austenite is a direct result of partial annealing, as observed by Saburi in [34]. The R-phase

is itself a product of a thermoelastic martensitic transformation and may be of interest for some applications because of its lesser hysteresis and reversible strain. The R-phase is simply a by-product of circumstances for the focus of the work presented here and does not significantly affect the performance of alloy. The effects of the R-phase are measurably manifested in all aspects of the alloy characteristics, however. For example, stress-strain curves may show an additional knee due to R-phase rearrangement under certain conditions, and DSC plots exhibit an additional endothermic peak due to the formation the R-phase.

The Nitinol actuator material used in this study is partially annealed in the as-received condition, so the material will exhibit the presence of R-phase. The actuators will be used in a one-way mode of constrained recovery operation, but characterization of the dependency of the material on thermal cycle will be quantified in lieu of one-way training. The Nitinol actuators will be embedded within a composite matrix, along the direction of the matrix fibers, and bonded within the matrix during cure. Constrained recovery operation will be insured by mechanical constraint on the resulting SMAHC specimens.

2.2 Constitutive Modeling

A constitutive model of the SMAHC material system is needed in order to predict the thermomechanical behavior of structures manufactured from the SMAHC material. Constitutive theories for SMAHC materials could be developed from micro-structural shape memory models (e.g., [24, 25, 26, 27]), as was done by Boyd and Lagoudas [36] and Birman [37]. However, these models are difficult to use in practice because they are qualitative in nature and depend upon determination of impractical parameters/material properties. An alternative approach is to employ a constitutive model which makes use of experimental measurement of basic engineering properties. Two such models were developed as part of the present study and will be discussed in this section. The models are developed by a mechanics-of-materials approach (see Jones [39]).

A representative volume element of a SMAHC lamina is shown in Figure 2.8. The element is taken to be in the plane of the plate. Note that the matrix material is a composite material itself, for example graphite-epoxy, with principal material directions 1 and 2, and the SMA actuator is embedded in the 1–direction.

Consider the uniaxial state of stress in a SMA actuator along the actuator axis. One form for the thermoelastic constitutive relation of the SMA actuator in the 1–direction was proposed by Jia and Rogers [5] and was extended to include thermal expansion by Turner, Zhong, and Mei [16]:

$$\sigma_{1a} = E_a \epsilon_1 + \sigma_r \qquad\qquad T \geq A_s$$
$$\sigma_{1a} = E_a(\epsilon_1 - \alpha_{1a}\Delta T) \qquad\qquad T < A_s \tag{2.1}$$

where E_a is the Young's modulus of the SMA, ϵ_1 is the strain in the 1–direction, σ_r is the recovery stress of the activated SMA, and α_{1a} is the thermal expansion coefficient for the inactivated SMA. Note that the Young's modulus and recovery stress of the SMA are functions of temperature. The recovery stress is also a function of the initial strain. The thermal expansion coefficient can be treated as essentially constant for temperatures below the phase transformation temperature. A detailed derivation of the constitutive relations for a SMAHC lamina using this approach, referred to as the recovery stress model (RSM), is given in Appendix A. A complete finite element
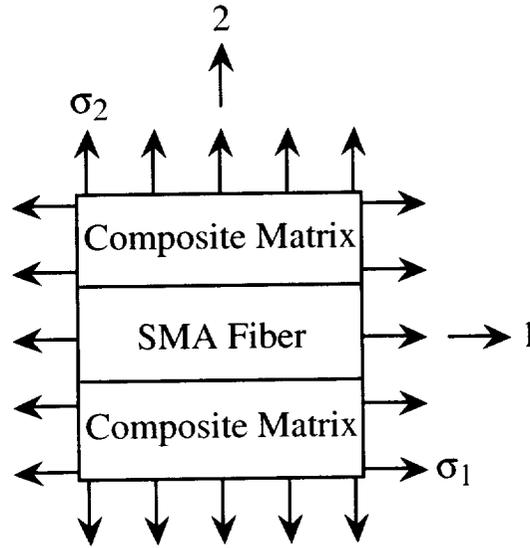
Figure 2.8 Representative volume element for a SMAHC lamina.

formulation was developed by Turner, Zhong, and Mei [16] for the thermomechanical response of SMA hybrid composite panel-type structures based upon the RSM constitutive relations. The RSM constitutive relations and the resulting finite element governing equations are in a form that is physically intuitive, but not consistent with conventional thermoelastic analysis and, therefore, not easily adapted to commercial finite element codes. It will also be shown that the RSM misses some of the mechanics of the material system. Thus, the constitutive relations will be re-cast in a more familiar and robust form.

The uniaxial thermoelastic constitutive relation for the SMA can be written in terms of an effective coefficient of thermal expansion (CTE):

$$\sigma_{1a} = E_a \left[\epsilon_1 - \int_{T_o}^{T} \alpha_{1a}(\tau)d\tau \right]$$ (2.2)

The way in which this relation is used depends upon the application. A measure of the nonlinear CTE $\alpha_{1a}(T)$ over the temperature range of concern would be appropriate for free or restrained recovery applications. For constrained recovery applications, however, one must resort to measurement of the recovery stress.

Comparison of equation (2.2) with equations (2.1) shows the functionality of the effective CTE for constrained recovery applications; it has the usual effect for temperatures below the austenite start temperature

$$\int_{T_0}^{T} \alpha_{1a}(\tau)d\tau = \alpha_{1a}\Delta T$$ (2.3)

17

and is related to the recovery stress at temperatures above A_s by the equation

$$\sigma_r = -E_a \int_{T_0}^{T} \alpha_{1a}(\tau)d\tau \quad \text{or} \quad \int_{T_0}^{T} \alpha_{1a}(\tau)d\tau = -\frac{\sigma_r}{E_a} \tag{2.4}$$

Note that in this case, the nonlinear thermoelastic nature of the SMA is still captured, albeit in a different way, because measurements of recovery stress and modulus versus temperature are inherently cumulative (integrated). Also, note that an experimental approach could be devised to measure appropriate recovery stress σ_r quantities for restrained recovery applications as an alternative to direct measurement of $\alpha_{1a}(T)$.

Thus, the general form for the thermoelastic constitutive relation in the 1-direction for a prestrained SMA actuator can be written as

$$\sigma_{1a} = E_a\left[\epsilon_1 - \int_{T_0}^{T} \alpha_{1a}(\tau)d\tau\right] \quad \text{and} \quad \text{sgn}(\alpha_{1a}) = \begin{cases} +1 & T < A_s \\ -1 & T \geq A_s \end{cases} \tag{2.5}$$

where α_{1a} is due to thermal expansion only for $T < A_s$ and is determined by direct measurement or from equation (2.4) for $T \geq A_s$.

In order to derive the thermoelastic constitutive relation for the 1–direction of a SMA hybrid composite, it is assumed that a stress σ_1 acts alone on the element shown in Figure 2.8 ($\sigma_2 = 0$) and that the SMA and composite matrix are strained by the same amount, ϵ_1 (i.e., plane sections remain plane). The 1-direction thermoelastic constitutive relation of the SMA actuator is given by equation (2.5). Similarly, the one-dimensional, stress-strain relation in the 1-direction for the composite matrix can be expressed as

$$\sigma_{1m} = E_{1m}\left[\epsilon_1 - \int_{T_0}^{T} \alpha_{1m}(\tau)d\tau\right] \tag{2.6}$$

Temperature dependence of the matrix thermal expansion coefficient has been included for generality.

The resultant force in the 1-direction ($\sigma_2 = 0$) is distributed over the SMA and composite matrix and can be written as

$$\sigma_1 A_1 = \sigma_{1a} A_a + \sigma_{1m} A_m \tag{2.7}$$

where (σ_1, A_1), (σ_{1a}, A_a), and (σ_{1m}, A_{1m}) are the (stress, cross-sectional area) of the entire element, SMA actuator, and composite matrix, respectively. Thus, the average stress σ_1 is

$$\sigma_1 = \sigma_{1a} v_a + \sigma_{1m} v_m \tag{2.8}$$

where $v_a = A_a/A_1$ and $v_m = A_m/A_1$ are the volume fractions of SMA and composite matrix, respectively. Substituting for σ_1, σ_{1a}, and σ_{1m} results in

$$E_1\left[\epsilon_1 - \int_{T_0}^{T} \alpha_1(\tau)d\tau\right] = E_a v_a\left[\epsilon_1 - \int_{T_0}^{T} \alpha_{1a}(\tau)d\tau\right] + E_{1m} v_m\left[\epsilon_1 - \int_{T_0}^{T} \alpha_{1m}(\tau)d\tau\right] \tag{2.9}$$

So, the Young's modulus and thermal expansion coefficient for the hybrid composite in the 1-direction have the form

$$E_1 = E_a v_a + E_{1m} v_m \tag{2.10}$$

and

$$\int_{T_0}^{T} \alpha_1(\tau)d\tau = \frac{E_a v_a \int_{T_0}^{T} \alpha_{1a}(\tau)d\tau + E_{1m} v_m \int_{T_0}^{T} \alpha_{1m}(\tau)d\tau}{E_a v_a + E_{1m} v_m} \qquad \operatorname{sgn}(\alpha_{1a}) = \begin{cases} +1 & T < A_s \\ -1 & T \geq A_s \end{cases} \tag{2.11}$$

A similar constitutive relation may be derived for the 2-direction by assuming that the applied stress σ_2 acts upon both the SMA and the matrix $(\sigma_1 = 0)$. The uniaxial thermoelastic constitutive relations in the 2-direction for the SMA actuator and the composite matrix are analogous to those in equations (2.2) and (2.6), i.e.,

$$\sigma_{2a} = \sigma_2 = E_a \left[\epsilon_{2a} - \int_{T_0}^{T} \alpha_{2a}(\tau)d\tau \right] \tag{2.12}$$

and

$$\sigma_{2m} = \sigma_2 = E_{2m} \left[\epsilon_{2m} - \int_{T_0}^{T} \alpha_{2m}(\tau)d\tau \right] \tag{2.13}$$

respectively. The CTE in equation (2.12) for the SMA does not depend on the recovery stress, but is still nonlinear due to the differing martensitic and austenitic properties.

The total elongation is due to strain in the composite matrix and the SMA actuator and may be written in the form

$$A_1 \epsilon_2 = A_m \epsilon_{2m} + A_a \epsilon_{2a} \tag{2.14}$$

Thus, the total strain becomes

$$\epsilon_2 = \epsilon_{2m} v_m + \epsilon_{2a} v_a \tag{2.15}$$

Substituting for ϵ_2, ϵ_{2a}, and ϵ_{2m} results in

$$\frac{\sigma_2}{E_2} + \int_{T_0}^{T} \alpha_2(\tau)d\tau = \frac{\sigma_2 v_a}{E_a} + \frac{\sigma_2 v_m}{E_{2m}} + \int_{T_0}^{T} [\alpha_{2a}(\tau)v_a + \alpha_{2m}(\tau)v_m]d\tau \tag{2.16}$$

Therefore, the Young's modulus and thermal expansion coefficient for the hybrid composite in the 2-direction have the form

$$E_2 = \frac{E_{2m} E_a}{(E_{2m} v_a + E_a v_m)} \tag{2.17}$$

19

and

$$\int_{T_0}^{T} \alpha_2(\tau)d\tau = \int_{T_0}^{T} [\alpha_{2a}(\tau)v_a + \alpha_{2m}(\tau)v_m]d\tau \qquad (2.18)$$

Expressions for the hybrid composite Poisson's ratios and shear moduli follow from similar derivations:

$$\nu_{12} = \nu_a v_a + \nu_{12m} v_m \qquad G_{12} = \frac{G_a G_{12m}}{G_a v_m + G_{12m} v_a} \qquad (2.19)$$

The thermoelastic constitutive relations in principal material coordinates for an orthotropic material have the following form

$$\{\epsilon\} = \{\epsilon\}_M + \{\epsilon\}_T$$
$$= [D]\{\sigma\} + \int_{T_0}^{T} \{\alpha(\tau)\}d\tau \qquad (2.20)$$

where $\{\epsilon\}$ is the total strain, $\{\epsilon\}_M$ is the mechanical strain, $\{\epsilon\}_T$ is the thermal strain, and $[D]$ is the compliance matrix. These relations can be inverted to give

$$\{\sigma\} = [C]\{\epsilon\} - [C]\int_{T_0}^{T} \{\alpha(\tau)\}d\tau \qquad (2.21)$$

where $[C]$ is the stiffness matrix. The constitutive relations, for plane stress, reduce to

$$\begin{Bmatrix} \sigma_1 \\ \sigma_2 \\ \tau_{12} \end{Bmatrix} = \begin{bmatrix} Q_{11} & Q_{12} & 0 \\ Q_{12} & Q_{22} & 0 \\ 0 & 0 & Q_{66} \end{bmatrix} \begin{Bmatrix} \epsilon_1 \\ \epsilon_2 \\ \gamma_{12} \end{Bmatrix} - \begin{bmatrix} Q_{11} & Q_{12} & 0 \\ Q_{12} & Q_{22} & 0 \\ 0 & 0 & Q_{66} \end{bmatrix} \int_{T_0}^{T} \begin{Bmatrix} \alpha_1(\tau) \\ \alpha_2(\tau) \\ 0 \end{Bmatrix} d\tau \qquad (2.22)$$

where $[Q]$ is the reduced stiffness matrix of the composite lamina. The reduced stiffnesses are related to the engineering properties through the following equations

$$Q_{11} = \frac{E_1}{1 - \nu_{12}\nu_{21}} \qquad Q_{12} = \frac{\nu_{12}E_2}{1 - \nu_{12}\nu_{21}} \qquad Q_{22} = \frac{E_2}{1 - \nu_{12}\nu_{21}} \qquad Q_{66} = G_{12} \qquad (2.23)$$

The expressions for the hybrid lamina engineering properties in terms of the properties of the constituent materials are reiterated here for convenience.

$$E_1 = E_a v_a + E_{1m} v_m \qquad E_2 = \frac{E_a E_{2m}}{E_a v_m + E_{2m} v_a}$$

$$\nu_{12} = \nu_a v_a + \nu_{12m} v_m \qquad G_{12} = \frac{G_a G_{12m}}{G_a v_m + G_{12m} v_a}$$

$$\int_{T_0}^{T} \alpha_1(\tau)d\tau = \frac{E_a v_a \int_{T_0}^{T} \alpha_{1s}(\tau)d\tau + E_{1m} v_m \int_{T_0}^{T} \alpha_{1m}(\tau)d\tau}{E_a v_a + E_{1m} v_m} \qquad \mathrm{sgn}(\alpha_{1a}) = \begin{cases} +1 & T < A_s \\ -1 & T \geq A_s \end{cases}$$

$$\int_{T_0}^{T} \alpha_2(\tau)d\tau = \int_{T_0}^{T} [\alpha_{2a}(\tau)v_a + \alpha_{2m}(\tau)v_m]d\tau$$

$$(2.24)$$

20

The thermoelastic constitutive relations for a general k-th orthotropic layer of a laminate with an arbitrary fiber/SMA actuator orientation angle θ, relative to the 1-direction in Figure 2.8, follow from transformation of the relations in principal material coordinates, equation (2.22).

$$\left\{ \begin{array}{c} \sigma_x \\ \sigma_y \\ \tau_{xy} \end{array} \right\}_k = [\bar{Q}]_k \left\{ \begin{array}{c} \epsilon_x \\ \epsilon_y \\ \gamma_{xy} \end{array} \right\}_k - [\bar{Q}]_k \int_{T_0}^{T} \left\{ \begin{array}{c} \alpha_x(\tau) \\ \alpha_y(\tau) \\ \alpha_{xy}(\tau) \end{array} \right\}_k d\tau \qquad (2.25)$$

or

$$\{\sigma\}_k = [\bar{Q}]_k (\{\epsilon\}_k - \{\epsilon\}_{Tk}) \qquad (2.26)$$

The transformed reduced stiffness matrix $[\bar{Q}]_k$ is related to the reduced stiffness matrix in principal material coordinates by

$$[\bar{Q}]_k = [T]^{-1}[Q]_k[T]^{-T} \qquad (2.27)$$

and $[T]$ is the transformation matrix given by

$$[T] = \begin{bmatrix} \cos^2\theta & \sin^2\theta & 2\sin\theta\cos\theta \\ \sin^2\theta & \cos^2\theta & -2\sin\theta\cos\theta \\ -2\sin\theta\cos\theta & 2\sin\theta\cos\theta & \cos^2\theta - \sin^2\theta \end{bmatrix} \qquad (2.28)$$

The constitutive relations given by equations (2.22) or (2.26) will be referred to as the effective coefficient of thermal expansion model (ECTEM).

The constitutive equations in principal material coordinates, equations (2.22), will now be considered further to clarify some advantages of the ECTEM approach. The expressions for the thermal strains in equations (2.24) allow the constitutive relations to be rewritten as

$$\left\{ \begin{array}{c} \sigma_1 \\ \sigma_2 \\ \tau_{12} \end{array} \right\} = \begin{bmatrix} Q_{11} & Q_{12} & 0 \\ Q_{12} & Q_{22} & 0 \\ 0 & 0 & Q_{66} \end{bmatrix} \left\{ \begin{array}{c} \epsilon_1 \\ \epsilon_2 \\ \gamma_{12} \end{array} \right\} - \begin{bmatrix} Q_{11} & Q_{12} & 0 \\ Q_{12} & Q_{22} & 0 \\ 0 & 0 & Q_{66} \end{bmatrix} \int_{T_0}^{T} \left\{ \begin{array}{c} c_{1a}\alpha_{1a}(\tau) \\ v_a\alpha_{2a}(\tau) \\ 0 \end{array} \right\} d\tau$$
$$- \begin{bmatrix} Q_{11} & Q_{12} & 0 \\ Q_{12} & Q_{22} & 0 \\ 0 & 0 & Q_{66} \end{bmatrix} \int_{T_0}^{T} \left\{ \begin{array}{c} c_{1m}\alpha_{1m}(\tau) \\ v_m\alpha_{2m}(\tau) \\ 0 \end{array} \right\} d\tau \qquad (2.29)$$

where the thermal effects of the SMA and matrix material have been separated and

$$c_{1a} = \frac{E_a v_a}{E_a v_a + E_{1m} v_m} \quad \text{and} \quad c_{1m} = \frac{E_{1m} v_m}{E_a v_a + E_{1m} v_m} \qquad (2.30)$$

are constants. These constitutive relations have a form similar to those in the RSM [16], which are rewritten here for convenience of comparison:

$$\left\{ \begin{array}{c} \sigma_1 \\ \sigma_2 \\ \tau_{12} \end{array} \right\} = \begin{bmatrix} Q_{11} & Q_{12} & 0 \\ Q_{12} & Q_{22} & 0 \\ 0 & 0 & Q_{66} \end{bmatrix} \left\{ \begin{array}{c} \epsilon_1 \\ \epsilon_2 \\ \gamma_{12} \end{array} \right\} + \left\{ \begin{array}{c} \sigma_r \\ 0 \\ 0 \end{array} \right\} v_a - [Q]_m \left\{ \begin{array}{c} \alpha_1 \\ \alpha_2 \\ 0 \end{array} \right\}_m v_m \Delta T$$
$$= [Q]\left\{ \begin{array}{c} \epsilon_1 \\ \epsilon_2 \\ \gamma_{12} \end{array} \right\} + \left\{ \begin{array}{c} \sigma_r \\ 0 \\ 0 \end{array} \right\} v_a - \left([Q] \left\{ \begin{array}{c} \alpha_1 \\ \alpha_2 \\ 0 \end{array} \right\} v \right)_m \Delta T \qquad T > A_s \qquad (2.31)$$

21

While the RSM only allows the recovery stress to affect the stress in the 1-direction of a lamina (term 2 of equation (2.31)), the analogous term in the ECTEM (term 2 of equation (2.29)) shows an effect of the 1-direction effective CTE on the stress in the 2-direction of the lamina, through the reduced stiffness Q_{12}. The ECTEM also allows for the fully nonlinear functionality of the 2–direction CTE for the SMA while the RSM neglects it altogether for $T > A_s$. As a result of these differences, the thermal forces calculated by the two formulations are different and the ECTEM more accurately captures the behavior of the material system. The form for the ECTEM constitutive relations given in equation (2.29) will be useful for reference in the thermal buckling discussion of Chapter 5.

In summary, the ECTEM essentially reduces to the RSM for constrained recovery applications, but captures the two-dimensional behavior of SMA actuators and their interaction with a composite matrix more accurately than the RSM. The ECTEM is also capable of modeling restrained or free recovery behavior in a similar manner with experimental measurements of SMA recovery stress, modulus, and/or nonlinear CTE.

2.3 Deformation Behavior and Stress Resultants

A model for the deformation behavior of a SMAHC laminate will be necessary, along with the constitutive relations, to develop the equations governing the static and dynamic response of such structures. Recall that one demand on the formulation is to model the thermoelastic response in the presense of immovable in-plane boundaries, i.e., thermal buckling and post-buckling analysis. Thus, the midplane strain and curvature vectors are defined from the von Kármán strain-displacement relations [40]:

$$
\begin{Bmatrix} \epsilon_x \\ \epsilon_y \\ \gamma_{xy} \end{Bmatrix} = \{\epsilon^o\} + z\{\kappa\}
$$

$$
= \{\epsilon^o_m\} + \{\epsilon^o_b\} + z\{\kappa\} \tag{2.32}
$$

$$
= \begin{Bmatrix} u_{,x} \\ v_{,y} \\ u_{,y} + v_{,x} \end{Bmatrix} + \frac{1}{2}\begin{Bmatrix} w_{,x}^2 \\ w_{,y}^2 \\ 2w_{,x}\,w_{,y} \end{Bmatrix} - z\begin{Bmatrix} w_{,xx} \\ w_{,yy} \\ 2w_{,xy} \end{Bmatrix}
$$

to allow for potential membrane stretching effects due to geometrically nonlinear deflections associated with thermal post-buckling. Note that the midplane strain $\{\epsilon^o\}$ consists of two components; the midplane strain due to membrane displacements $\{\epsilon^o_m\}$ and the nonlinear midplane strain due to bending displacements $\{\epsilon^o_b\}$.

Substitution of the strain-displacement relations in equation (2.26) results in

$$
\{\sigma\}_k = [Q]_k(\{\epsilon^o\} + z\{\kappa\}) - [Q]_k\{\epsilon\}_{Tk} \tag{2.33}
$$

The resultant force and moment vectors of the SMA hybrid composite laminate are defined as

$$
\{N, M\} = \int_{-h/2}^{h/2} \{\sigma\}_k\,(1, z)\,dz \tag{2.34}
$$

22

or

$$\left\{ \begin{array}{c} N \\ M \end{array} \right\} = \left[\begin{array}{cc} A & B \\ B & D \end{array} \right] \left\{ \begin{array}{c} \epsilon^o \\ \kappa \end{array} \right\} - \left\{ \begin{array}{c} N_{\Delta T} \\ M_{\Delta T} \end{array} \right\} \tag{2.35}$$

where the laminate stiffness $[A]$, $[B]$ and $[D]$ and the thermal resultant force and moment vectors $\{N_{\Delta T}\}$ and $\{M_{\Delta T}\}$ are all temperature dependent. The laminate stiffness matrices have the usual form

$$[A] = \int_{-h/2}^{h/2} [Q]_k \, dz = \sum_{k=1}^{N_{lay}} [Q]_k (z_k - z_{k-1})$$

$$[B] = \int_{-h/2}^{h/2} [Q]_k z \, dz = \frac{1}{2} \sum_{k=1}^{N_{lay}} [Q]_k (z_k^2 - z_{k-1}^2) \tag{2.36}$$

$$[D] = \int_{-h/2}^{h/2} [Q]_k z^2 \, dz = \frac{1}{3} \sum_{k=1}^{N_{lay}} [Q]_k (z_k^3 - z_{k-1}^3)$$

and the expression for the thermal resultants is as follows.

$$\{N_{\Delta T}, M_{\Delta T}\} = \int_{-h/2}^{h/2} (1, z) \left([Q]_k \int_{T_0}^{T} \{\alpha(\tau)\}_k \right) d\tau \, dz \tag{2.37}$$

Expanding the resultant force and moment relations, equation (2.35), in terms of the midplane strain and curvature components, equation (2.32), results in

$$\{N\} = [A]\{\epsilon_m^o\} + [A]\{\epsilon_b^o\} + [B]\{\kappa\} - \{N_{\Delta T}\}$$
$$= \{N_m\} + \{N_\theta\} + \{N_b\} - \{N_{\Delta T}\} \tag{2.38}$$

and

$$\{M\} = [B]\{\epsilon_m^o\} + [B]\{\epsilon_b^o\} + [D]\{\kappa\} - \{M_{\Delta T}\}$$
$$= \{M_m\} + \{M_\theta\} + \{M_b\} - \{M_{\Delta T}\} \tag{2.39}$$

where the subscripts m, θ, b, and ΔT indicate components induced by membrane strain, nonlinear membrane strain, bending strain, and thermal expansion, respectively. The resultant force and moment relations and the strain-displacement relations presented in this section will be useful for reference in formulating the equations governing the thermomechanical response of SMAHC panel-type structures in Chapter 4.

A review of the behavior of SMAs was given in this chapter followed by development of a constitutive model for SMA actuators embedded in a composite matrix and used in a constrained-recovery model of the SME for adaptive stiffening. In order to use this model to predict the behavior of the SMAHC material system used in this study, the thermomechanical properties of the constituents must be determined. Results from such characterization testing will be presented in the next chapter, following motivation of the selected materials, description of the SMAHC material system configuration, and discussion of the processes involved in fabricating the SMAHC specimens.

23

Chapter 3
Specimen Fabrication and Material System Characterization

A constitutive model was developed in the previous chapter to describe the mechanics of a SMAHC material system. That model requires measurement of a number of material properties from the constituent materials in order to quantify the behavior of a structure fabricated from such a material. In this chapter, a brief motivation is given for the selected material system, followed by details of the SMAHC specimen fabrication processes and hardware. Processes involved in and results from thermomechanical tests on the constituent materials will be discussed, and the chapter will conclude with disclosure of the final material property data set used to generate the numerical results for SMAHC specimens in this study.

3.1 Material System Selection

In the typical application being considered, such as adaptive stiffening of aerospace structures, the SMA elements would be activated through an inherently elevated temperature of the service environment. Thus, activation of the SMA by surface heat in the planned experiments would be the most accurate simulation. Surface heating could be accomplished through the use of quartz radiant heaters or a number of other sources. These heating methods involve practical problems, however, such as the need for thermal insulation of the test article support structure and other equipment, interference with structural/acoustic/thermal measurements, thickness-direction asymmetry of the thermal load, and a complicated thermal control system. Alternatively, the SMA can be activated electrically through resistive heating. This method has the advantages of simple operation, relatively uniform heating, and excellent controllability. Electrical isolation of the SMA elements may be required for electrical activation of laminates involving carbon-epoxy matrices. Electrical isolation can be achieved through coating techniques, but this could present significant complications. It was decided that a glass-epoxy matrix would be used to circumvent these problems as experiments performed in this study are intended for demonstration and theoretical validation only. This material system also affords the advantage of visual flaw detection due to its translucency.

Most recent SMA hybrid composite structural designs have focused on SMA wire-type actuators distributed uniformly throughout the laminate or individual laminae. There are several disadvantages associated with the use of SMA wire actuators. Integration of wire-type actuators into a composite leads to complicated fabrication procedures because of the relatively large number of actuators usually needed. The small surface area of the actuators makes them very sensitive to actuator/matrix interface flaws because voids can be of significant relative size. Small

size has also been blamed for a relatively high rate of actuator breakage during cure because of sensitivity to stress concentrations at the mechanical restraints. Finally, it is difficult to achieve a desirable overall volume fraction of SMA when trying to optimize the integration of the actuators by placing them in only selected layers. Therefore, the present work will focus on SMA hybrid composite laminates involving ribbon-type SMA elements to simplify the fabrication procedure, allow for more flexibility in fabrication, and hopefully desensitize the actuators to interface voids and stress concentrations. For example, the ribbon-type SMA elements can be placed in strips cut out of particular matrix laminae to result in a rather simple lay-up operation, while keeping the volume fraction high in the desired locations. Another potential benefit of this type of lay-up procedure is that it could potentially be extended directly to e-beam consolidation procedures where spools of SMA ribbon would strategically replace spools of matrix material ribbon.

In summary, the material system used in this study consists of a glass-epoxy matrix material with embedded Nitinol ribbon. Details of the SMAHC specimen fabrication procedures/hardware are given in the following section, followed by a discussion of the thermomechanical testing of the constituent materials.

3.2 Specimen Fabrication

Although a panel-type specimen is closer to the configuration of intended applications, a more simple test specimen will suffice for the objectives of this study; demonstration of the thermomechanical response of a SMAHC laminate and experimental validation of the theoretical model developed in this work. A schematic of the selected beam-type specimen is shown in Figure 3.1. Various constraints, other than the use of ribbon-type actuators, influenced the design of this laminate. These constraints include fabrication tooling geometry and dynamic range of anticipated experimental configurations. The specimen design is by no means optimized, but the predicted performance is in a range that is suitable for the expected loading conditions and to demonstrate significant improvement from the SMA reinforcement.

Note that this specimen design calls for a SMA actuator width of 0.0127 m (0.5 inch) to be embedded within each 0° glass-epoxy layer, i.e., replace a portion of each 0° layer. Material availability limited the procured SMA ribbon cross section to 0.0023x1.5e-4 m (0.09x0.006 inches). This was considered acceptably close to the glass-epoxy unidirectional tape thickness (~1.27e-4 m, ~0.005 inches) and it was planned that five widths of the ribbon would be placed side-by-side to develop a width near the half-inch in the specimen design. Alternatively, in the case that the adjacent SMA actuators prove detrimental because of a weak interface between actuators, the ribbons could be separated within laminae or between laminae.

The SMAHC specimen fabrication procedure used in this study consists of the following steps; prestrain the SMA actuators, lay-up the composite laminate, cure the laminate while restraining the actuators, and machine beam specimens from the consolidated SMAHC laminate. The Nitinol material was packaged on a spool, which subjected the ribbon to significant out-of-plane bending strain. Some in-plane bending, axial, and torsional strain was also imparted to the ribbon during the spooling operation. This *packaging* strain must be removed prior to imparting the actuator prestrain. Packaging strain removal can be conveniently done by inducing the reverse (austenitic) transformation. An apparatus was developed to perform this operation,

22"x1"x0.080" Glass-Epoxy/SMA Hybrid Beam (6 Count)
$(45/0_{SMA}/-45/90)_{2sym}$ Lamination
SMA in 0° Laminae Only
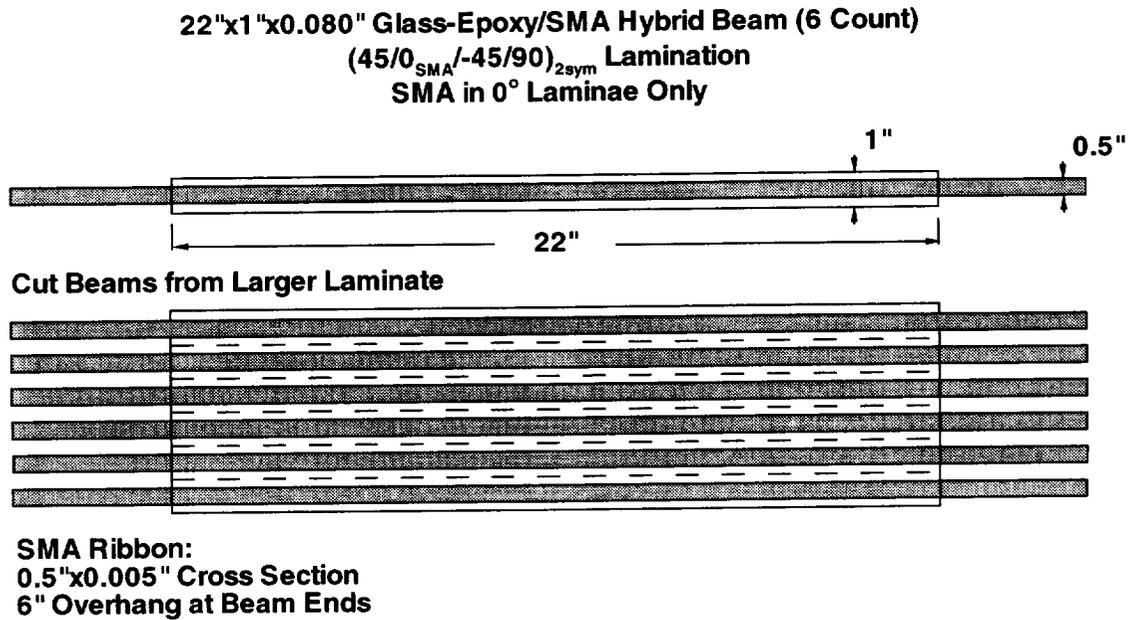
Figure 3.1 Schematic of beam specimens cut from a SMA hybrid composite laminate.

shown in Figure 3.2. It is desirable to induce the martensitic transformation just prior to prestraining in order to avoid aging effects, such as the rubber-like form of pseudoelasticity. Inducing the transformation is also accomplished during the packaging strain recovery process as the ribbon cools to ambient temperature. It will be shown in the next section that, for this particular Nitinol composition in an unrestrained condition, the martensitic transformation is not complete at ambient temperature. However, the martensite will be stress induced during the prestraining operation. Stress–inducing the martensite results in essentially the same state as would be achieved by cooling the ribbon to sub-ambient temperatures prior to prestraining. The main difference is that there may be some austenite remaining in the ribbon after prestraining by the former method, but should be of no consequence because any subsequent thermal cycling (e.g., composite cure) will render the state from the two methods equivalent. The former method, without cooling to sub-ambient temperatures, was selected for simplicity.

The prestraining operation needs to be very precise and repeatable. It was decided that the actuators would be elongated on a mechanical loading machine operated in stroke-control mode. Alignment of the ribbon during elongation is critical to avoid bending strain and to obtain repeatable results. Handling of the ribbon is cumbersome during installation in the test machine, and it is desirable to prestrain multiple strands at once to expedite the process. In

Figure 3.2 Packaging strain recovery rig.

order to rectify these issues, an apparatus was developed to align and maintain proper geometry on three ribbon lengths at once during installation in the test machine. A close-up view of the alignment/gripping apparatus is shown in Figure 3.3. The entire assembly (alignment/gripping apparatus, spacer, and three ribbons) is shown installed in the test machine in the left half of Figure 3.4. The Nitinol ribbons are shown ready for elongation, subsequent to spacer removal, in the right half of Figure 3.4.

The particular spacer length shown was used to maintain a SMA ribbon gage length of 0.635 m (25 in) for manufacture of the beam specimens shown in Figure 3.1. The gage length of the ribbons was elongated to a length of 0.6604 m (26 in), which corresponds to a prestrain of 4%. This gage length was used in order to ensure uniform prestrain over the 0.6604 m (26 in) span between mechanical restraints on the composite lay-up tooling, which will be discussed subsequently. A total of fifty-four ribbon lengths were prestrained 4% using this procedure to prepare for SMAHC laminate fabrication.

A mechanical drawing of the lay-up and cure tooling plate is shown in Figure 3.5. This apparatus was designed to provide a flat surface (± 0.005 inches) and mechanical grips to restrain the SMA during an autoclave cure procedure. Recall that the beam specimen design calls for a lamination of $(45/0/-45/90)_{2s}$ with the Nitinol in the 0° layers. This lamination was accomplished by cutting widths of the 0° layers to size during assembly and filling the void with five ribbon widths laid side-by-side. A picture of the lay-up procedure at the stage of finishing the first 0° layer is shown in Figure 3.6. Note that Kapton release film, fiberglass breather cloth, and teflon-coated fiberglass bleeder cloth are layered between the tooling plate surface and the

28
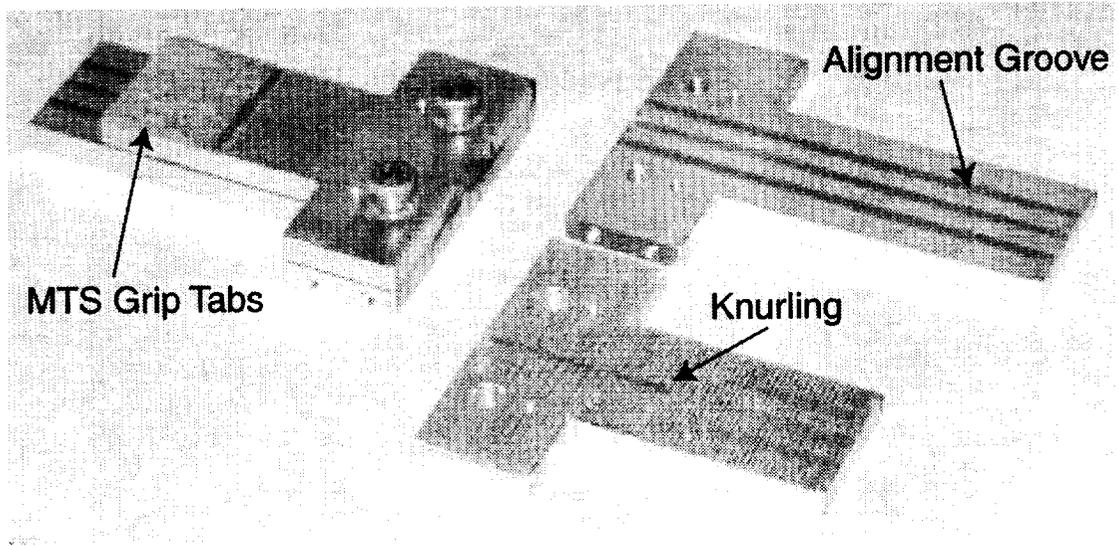
Figure 3.3 Nitinol ribbon gripping apparatus for prestraining and mechanical testing.
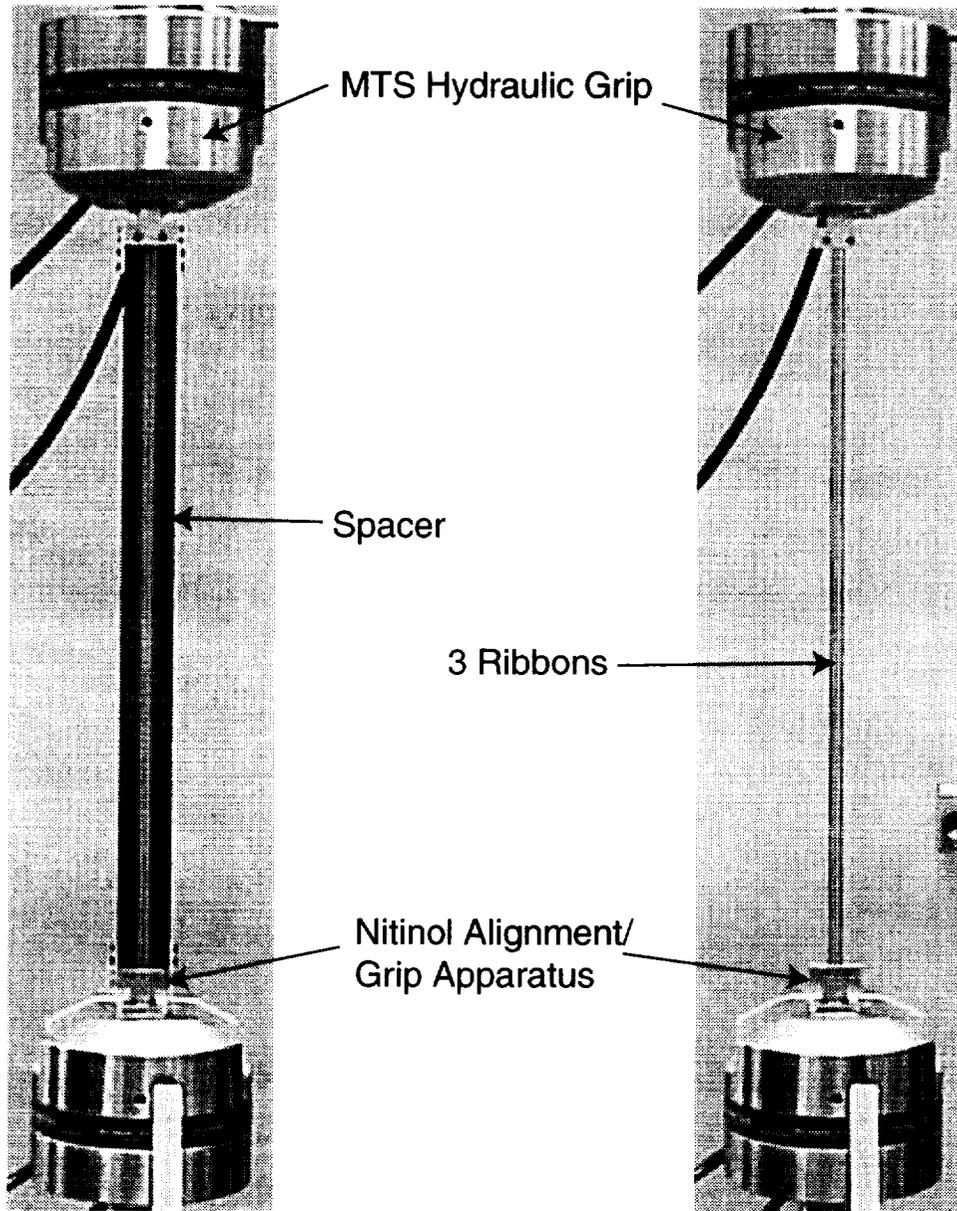
Figure 3.4 Nitinol ribbon prestrain and mechanical testing apparatus.

SMA Hybrid Composite Tooling Plate
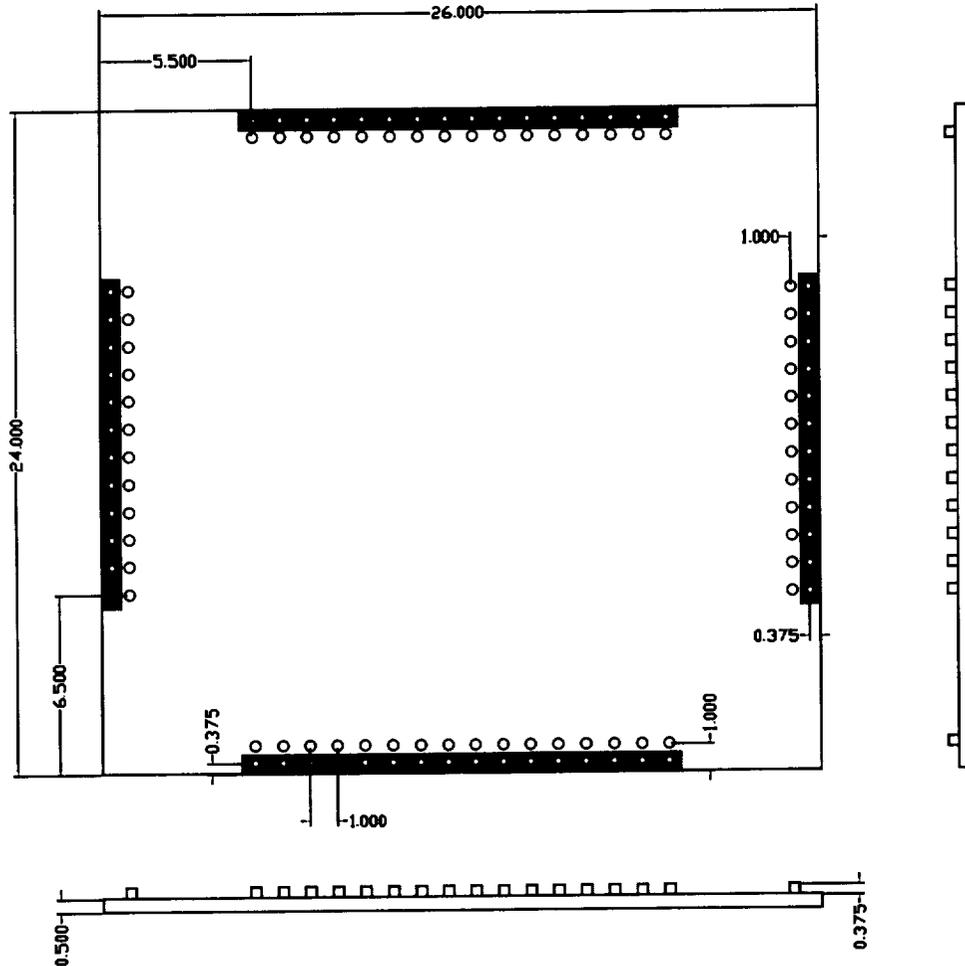
■ Knurled surface between edge of plate and dowels

o 0.375-diameter X 0.750-length dowels

o Tapped holes for 1/4-28 bolts

Material:
Plate, 17-4 PH stainless
Dowels, 300 series stainless

Instructions:
Top surface of plate should be ground

Figure 3.5 Mechanical drawing of the laminate lay-up and cure tooling apparatus (all dimensions in inches).
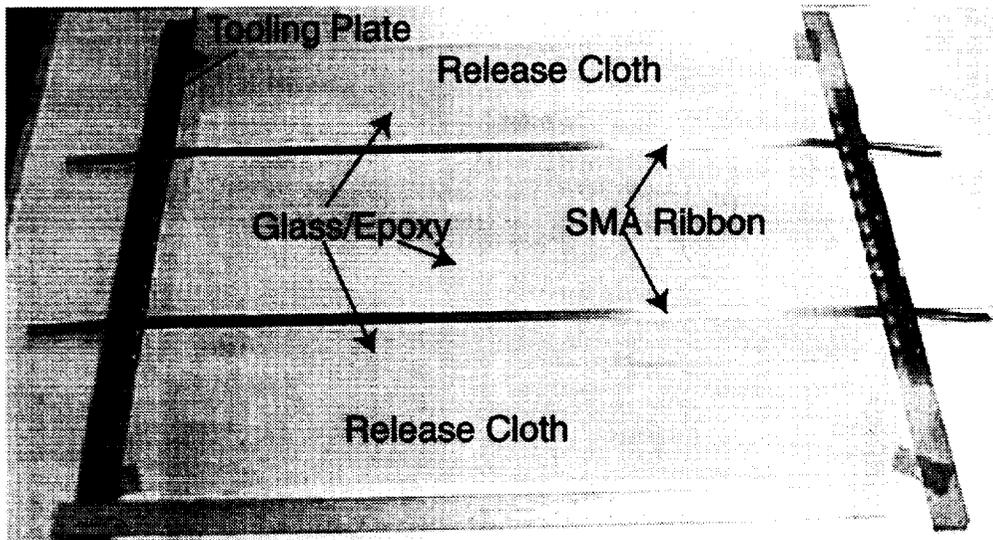
Figure 3.6 Laminate lay-up procedure at the stage of completing layer 2.
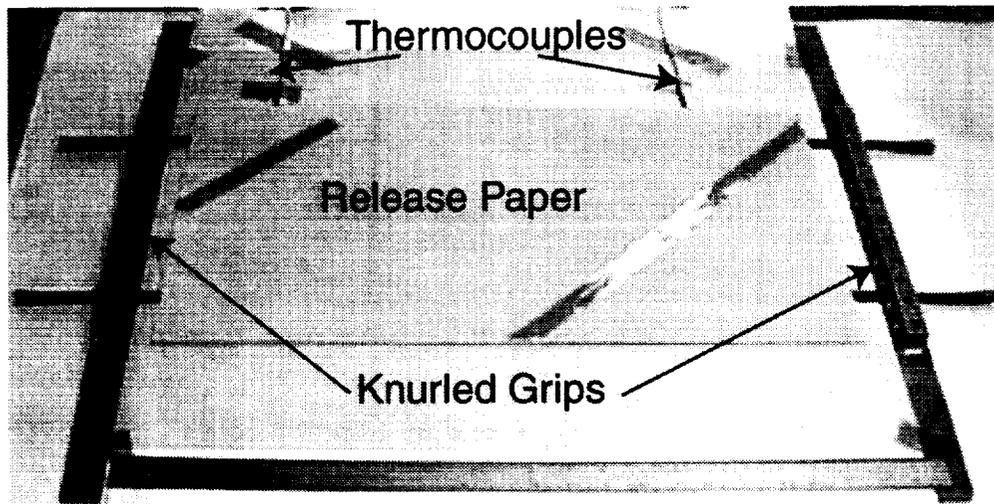
Figure 3.7 Completed laminate with cure control thermocouples and NiTi ribbon grips torqued.

first glass-epoxy layer, in that order. The laminate after complete assembly is shown in Figure 3.7, where the cure cycle control thermocouples have been installed near the laminate and the Nitinol ribbon ends have been secured within the knurled mechanical restraints. The restraints consisted of three parts (tooling plate surface, a thin spacer with knurling on both sides, and the top clamping bar) to minimize bending of the actuators between the laminate boundary and the restraint and to maximize grip for each layer of SMA by minimizing the number of layers gripped together. The mechanical restraint screws were torqued to 11.30 N•m (100 in•lbf). The release paper was subsequently removed from the top layer of glass-epoxy and the laminate was topped with bleeder cloth, Kapton film, a caul plate, bleeder cloth, and breather cloth, in that order. The entire assembly was vacuum bagged as shown in Figure 3.8 and drawn to an internal pressure of 0.0475 atm. The assembly was subjected to the autoclave cure cycle recommended
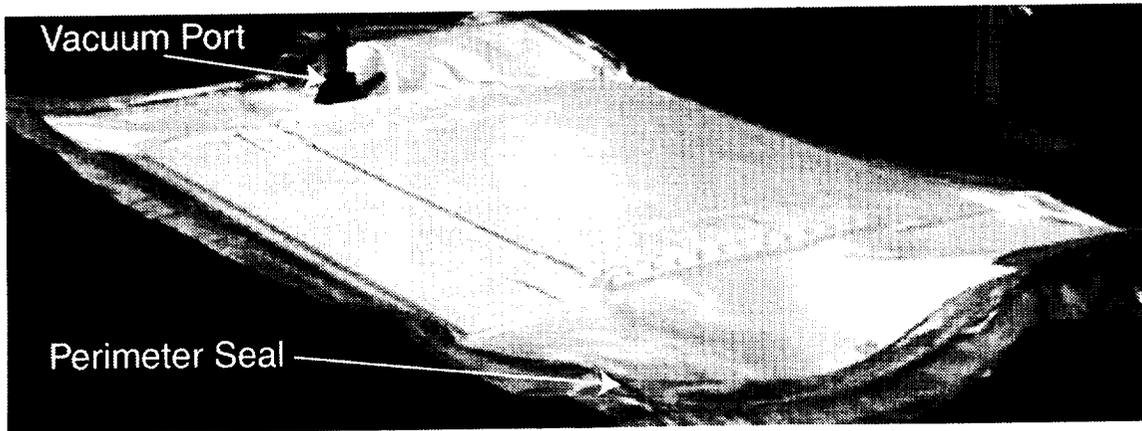
Figure 3.8 Laminate after vacuum-bagging and applying vacuum.
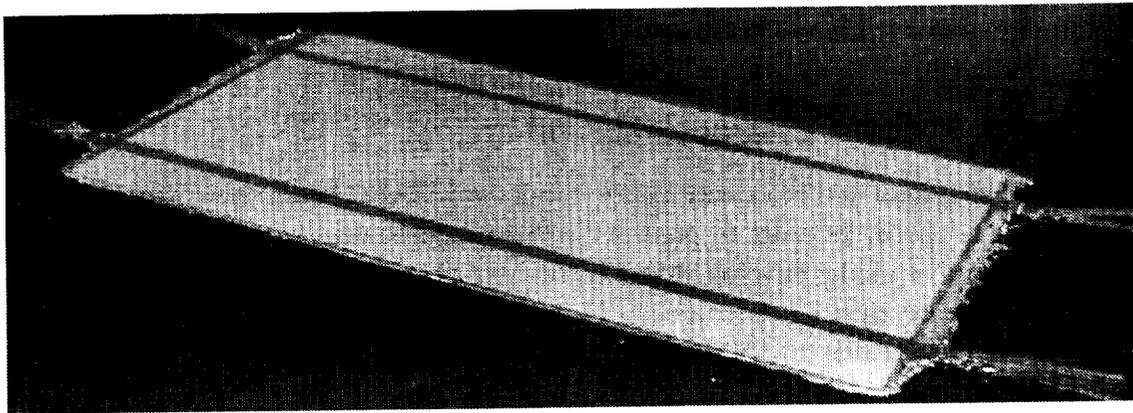
Figure 3.9 Consolidated SMAHC laminated panel.
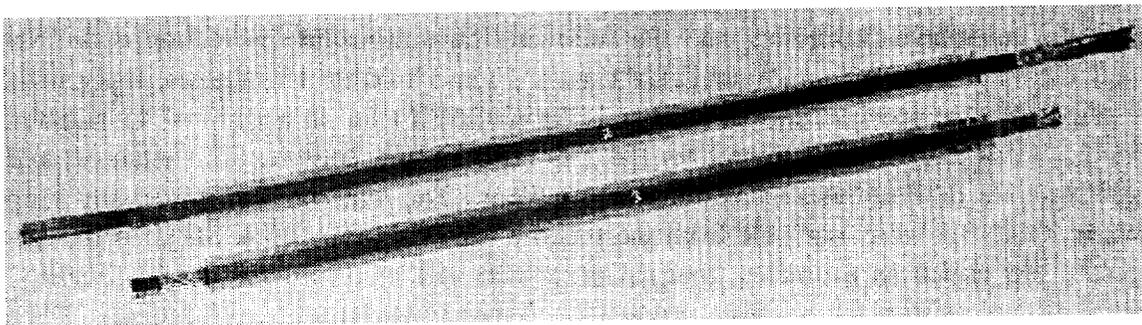
Figure 3.10 SMAHC beam specimens machined from panel.

by the vendor (Fiberite, Inc.) and the resulting consolidated part is shown in Figure 3.9. Details of the cure cycle will be discussed in the following section. Two SMAHC beam specimens were machined from this laminate using the respective centerlines of the embedded Nitinol ribbon. The beam dimensions are shown in Figure 3.10, where it can be seen that the beam marked number 3 has been readied for installation in test fixtures. The beams have dimensions of

Table 3.1 Nominal properties of a Fiberite E-glass/934 epoxy lamina (50–55% fiber volume).

Property	Room Temperature
Young's Modulus, E_1	41.37-55.16 GPa (6-8 Msi)
Poisson's Ratio	0.28-0.32
Density	1.919-1.980e+3 kg/m^3 (1.795-1.852e-4 lbf s^2/in^4)
Cure Temperature	176.7°C (350°F)
Glass Transition	193.3°C (380°F)

0.5588x0.0254x0.0019 m (22x1x0.078 in). The SMA leads of the test-prepared beam were trimmed to an overall length of 0.6604 m (26 in). The overall volume fraction of the SMA within the glass-epoxy dimensions is approximately 13.8%.

3.3 Material System Characterization

The material system and processes used to fabricate SMAHC beam specimens was described in the previous sections. In order to predict the thermomechanical behavior of such a structure using the constitutive model developed in the previous chapter, a number of material properties from the constituents must be determined. Characterization testing that was performed on the glass-epoxy matrix material and Nitinol alloy are described in the following sections.

3.3.1 Glass-Epoxy Matrix

Glass-epoxy unidirectional prepreg tape was obtained from Fiberite, Inc. The material is Hye 8 End/934, an E-glass/934 epoxy resin material system. The resin material is formulated for autoclave processing and the following cure procedure is recommended; heat at 1.1–2.8°C/minute (2–5°F/minute) to 121.1°C (250°F) and hold for 15 minutes, apply 689.5 kPa (100 psig) pressure and continue to hold at 121.1°C (250°F) for an additional 45 minutes, heat at 1.1–2.8°C/minute (2–5°F/minute) to 176.7°C (350°F) and hold for 120 minutes, and cool at 2.8°C/minute (5°F/minute) (maximum) to ambient. The material and processing properties shown in Table 3.1 were available from the Fiberite Materials Handbook [41]. Although these properties are useful as estimates, thermal expansion and more precise elastic property characterization are needed for accurate prediction of thermomechanical performance. Therefore, significant thermomechanical testing of the glass-epoxy material system was performed.

Two laminates were fabricated from the glass-epoxy material system to provide specimens for thermomechanical testing; a unidirectional lay-up $(0)_{20}$ and an angle-ply lay-up $(\pm45)_4$. Tab material was post-cured to the laminates and the resulting structures were machined into uniaxial tensile specimens with dimensions of 0.2286x0.0254 m (9x1 inches) (gage length of 0.1524 m, 6 inches). The tensile specimens were instrumented with a "T-strain gage" at the mid-span and tested on a MTS machine. The unidirectional specimens were tested according to ASTM standard D 3039/D 3039M for estimates of the Young's moduli and Poisson's ratios; E_1, E_2, ν_{12},

and ν_{21}. The angle-ply specimens were tested according to ASTM standard D 3518/D 3518M for estimates of the shear modulus G_{12}. Although the ASTM standards call for modulus estimates to the determined over strain ranges of $\sim$1000–3000 $\mu\epsilon$ and $\sim$2000–6000 $\mu\epsilon$, respectively, the transverse (90°) uniaxial and ±45 angle-ply stress-strain relations showed discernible nonlinearity over those ranges. The maximum normal strain and shear strain for the test configurations considered in this study are not expected to exceed 500 and 250 $\mu\epsilon$, respectively. Therefore, E_2 and G_{12} estimates were determined from $\sim$50–1000 $\mu\epsilon$ and $\sim$50–500 $\mu\epsilon$, respectively, to achieve more representative estimates with ample headroom. Results from these tests/calculations are given in Table 3.2.

Table 3.2 Mechanical properties of Fiberite E-glass/934 epoxy material system in principal material coordinates.

Temperature	E_1	E_2	ν_{12}	G_{21}
°C	GPa	GPa	—	GPa
23.9	49.30	20.00	0.29	9.65
37.8	49.16	19.44	0.29	9.24
65.6	48.75	18.20	0.29	8.41
93.3	48.61	16.20	0.29	7.58
121.1	48.54	14.00	0.29	5.58
148.9	48.82	11.38	0.29	3.45

Specimens for measurement of the coefficient of thermal expansion (CTE) were also machined from the unidirectional laminate $(0)_{20}$ described above. Two CTE specimen geometries were machined for testing by two different methods. Rectangular 0.1524x0.006 m (6x0.25 inch) specimens were tested according to ASTM standard E 228 at Materials Research and Engineering, Inc. A summary of those test results is given in Arvidson et al. [42]. Specimens with the geometry shown in Figure 3.11 were tested by an interferometric dilatometer method at NASA LaRC. Both quadratic and cubic interpolation of the raw thermal expansion data are used in practice to generate linear and quadratic estimates of the CTE with temperature, respectively. Cubic interpolation was employed with the ASTM E 228 test method while quadratic interpolation was used with the interferometer method. The consequence of this difference can be seen in Figures 3.12 and 3.13, where the longitudinal (fiber direction) and transverse CTE estimates versus temperature are shown from the two methods. The two methods are in agreement for the overall trend in the CTE data, but the cubic interpolation of the data collected with the ASTM standard captures higher order effects. Data resulting from both methods are tabulated in Table 3.3, but the quadratically varying CTE data from the ASTM E 228 method will be used in the predictions reported in this study.

Interferometer Dilatometer Specimen
LaRC CTE Specimen

R1.5085

$3.0170 \begin{matrix} +0.0005 \\ -0.0000 \end{matrix}$

1.0000 ±0.005
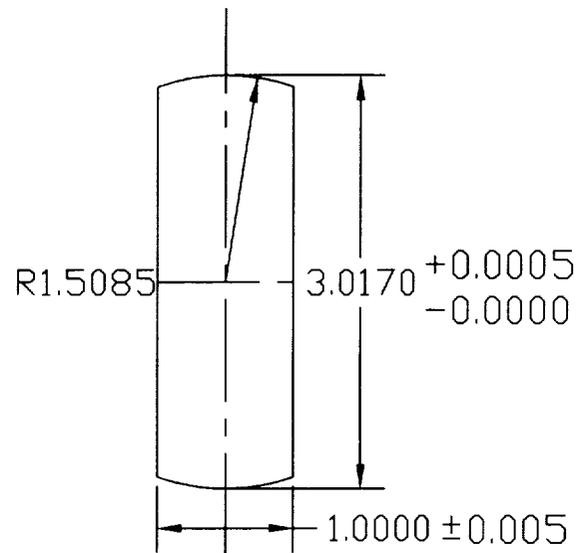
Notes:
1) Specimen length is critical
2) All dimensions in inches

Figure 3.11 Schematic of the CTE specimen geometry for measurement by the interferometric dilatometer method.
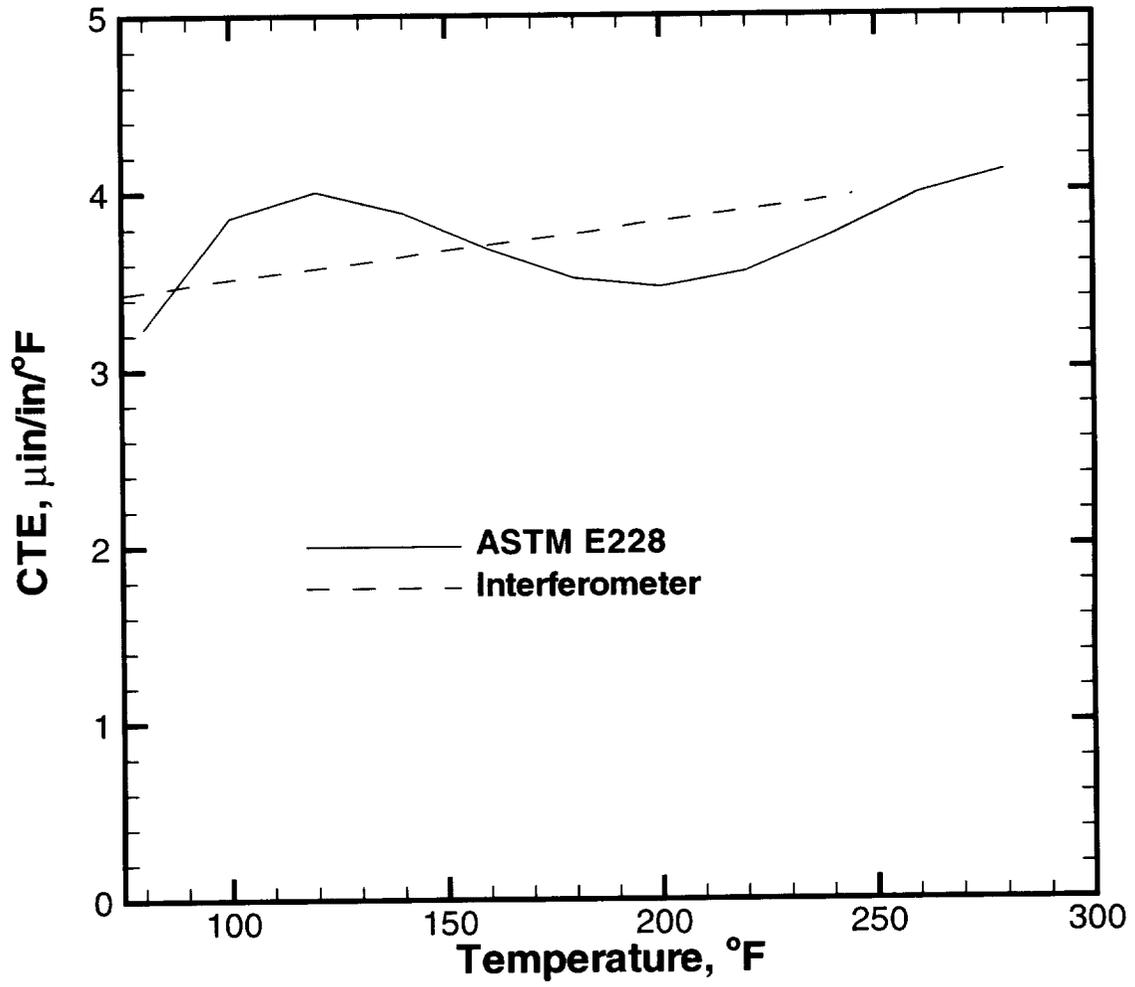
Figure 3.12 Fiberite E-glass/934 epoxy longitudinal
(fiber-direction) CTE vs. temperature by two methods.
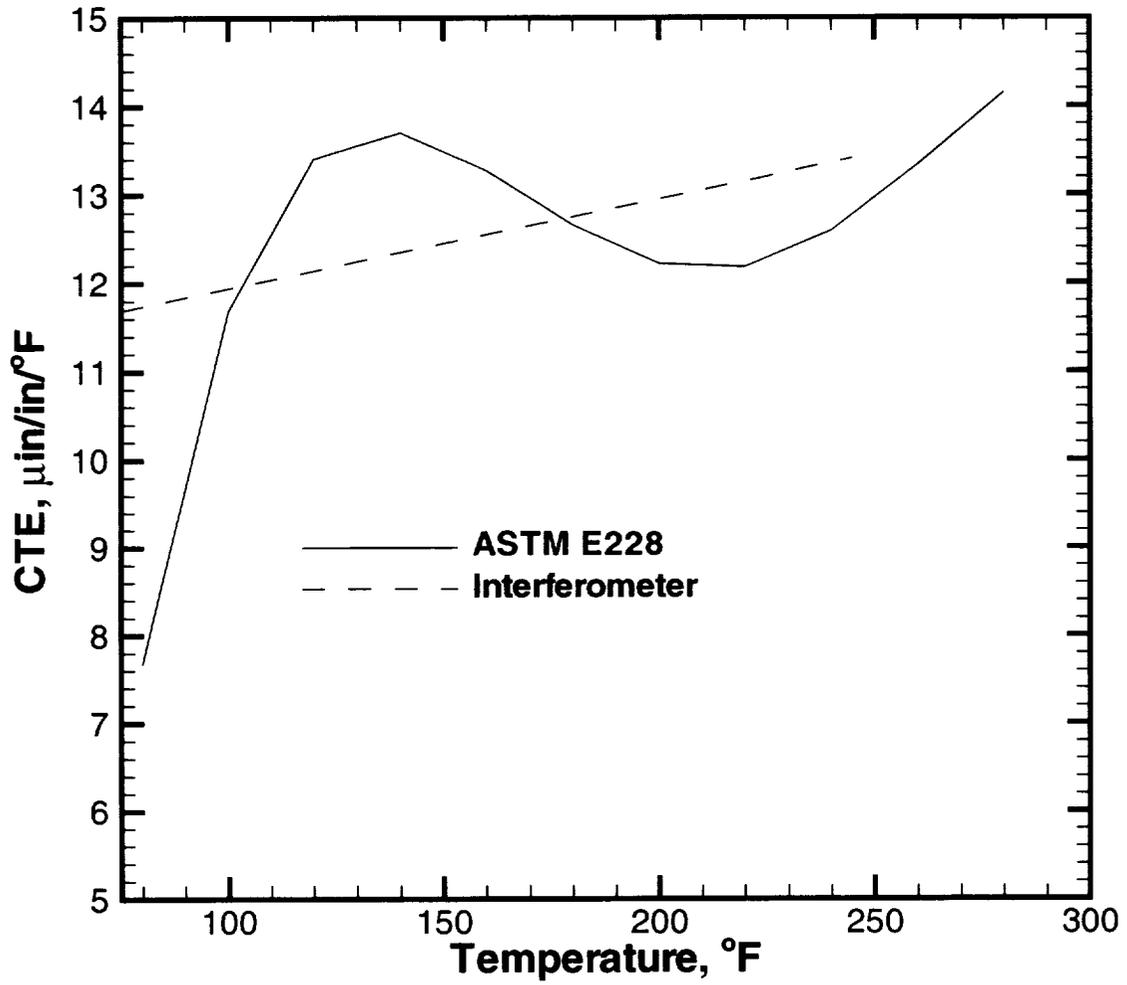
Figure 3.13 Fiberite E-glass/934 epoxy transverse CTE vs. temperature by two methods.

Table 3.3 Fiberite E-glass/934 epoxy CTE in principal
material directions as a function of temperature.

| Temperature | α_1 | | α_2 | |
| | ASTM E228 | Interferometer | ASTM E228 | Interferometer |
°C	$\mu\epsilon/°C$	$\mu\epsilon/°C$	$\mu\epsilon/°C$	$\mu\epsilon/°C$
23.9	—	6.17	—	21.04
26.7	5.83	6.21	13.81	21.13
37.8	6.95	6.34	21.02	21.49
48.9	7.22	6.44	24.14	21.85
60.0	7.00	6.55	24.66	22.23
71.1	6.62	6.68	23.90	22.59
82.2	6.34	6.79	22.79	22.95
93.3	6.25	6.91	22.00	23.31
104.4	6.39	7.02	21.92	23.67
115.6	6.77	7.13	22.66	24.05
126.7	7.18	—	24.01	—
137.8	7.42	—	25.47	—

Tensile specimens with a geometry of 0.1524x0.0127 m (6x0.5 inches) were machined from scrap (glass-epoxy-only) material remaining subsequent to machining SMAHC specimens from the larger quasi-isotropic laminate shown in Figure 3.9. A schematic of the specimen machining organization from the SMAHC panel is shown in Figure 3.14. The tensile specimens were tabbed and instrumented with a "T-strain gage" at the mid-span prior to testing. These quasi-isotropic specimens were tested according to ASTM standard D 3039/D 3039M for estimates of the extensional stiffnesses; A_{11} and A_{22}. A brief discussion of these measurements is given in the following paragraph.

Recall the stress resultant relations given in equation (2.35). In performing the uniaxial tensile tests on the quasi-isotropic specimens, the applied force N_x, axial strain ϵ_x and transverse strain ϵ_y were measured. The transverse and shear force components are zero, $N_y = N_{xy} = 0$. For a symmetric quasi-isotropic laminate, the shear-extension coupling stiffnesses are zero, $A_{16} = A_{26} = 0$ and the extensional stiffnesses are equal $A_{11} = A_{22}$. With these simplifications, the stress resultant equations reduce to

$$N_x = A_{11}\epsilon_x^o + A_{12}\epsilon_y^o$$
$$0 = A_{12}\epsilon_x^o + A_{11}\epsilon_y^o \qquad (3.1)$$
$$0 = A_{66}\gamma_{xy}^o$$

Figure 3.14 Schematic of the machining process for removing tensile, CTE, and SMAHC beam specimens from the SMAHC laminate.

The relationship in the second equation $A_{12} = -A_{11}\epsilon_y^o/\epsilon_x^o$ allows the first equation to be rewritten as

$$N_x/\epsilon_x^o = A_{11}\left[1 - \left(\epsilon_y^o/\epsilon_x^o\right)^2\right] \qquad \text{or} \qquad A_{11} = \frac{N_x/\epsilon_x^o}{\left[1 - \left(\epsilon_y^o/\epsilon_x^o\right)^2\right]} \tag{3.2}$$

Thus, the measured quantities are sufficient to determine the extensional stiffnesses of the quasi-isotropic laminate.

The uniaxial and angle-ply properties discussed previously can be used with classical lamination theory (CLT) to calculate extensional stiffnesses for the quasi-isotropic laminate. The extensional stiffnesses measured from the quasi-isotropic specimens are shown in comparison to those predicted with CLT from the uniaxial and angle-ply properties in Table 3.4. It can be seen that good agreement is achieved. Thus, usage of the properties in Table 3.2 is deemed appropriate for predictions of the glass-epoxy material system behavior.

40

Table 3.4 Comparison of measured and predicted extensional stiffnesses
for a Fiberite E-glass/934 epoxy quasi-isotropic $(45/0/-45/90)_{2s}$ laminate.

| Temperature | Extensional Stiffness, A_{11} | |
| | Measured | Predicted |
°C	MN/m	MN/m
23.9	69.2	63.5
37.8	63.3	62.4
65.6	60.1	60.1
93.3	57.5	57.3
121.1	53.8	53.2
148.9	50.7	48.9

A variety of test procedures and results have been presented in this section. A summary of the properties to be used in the numerical predictions later in this study are shown in Table 3.5. Note that slight extrapolation of the CTE data and linear interpolation of the CTE and elastic property data was performed to result in a common temperature resolution.

3.3.2 Nitinol Alloy

Nitinol ribbon material was provided by Shape Memory Applications, Inc. A Nitinol alloy was specified with an appropriate composition to give a martensite finish M_f temperature above the expected ambient temperature while maintaining an austenite finish temperature well below the glass-transition temperature of the Fiberite 934 epoxy matrix. The achievable ribbon cross section was 0.0023x0.00015 m (9x0.006 inches). The nominal transformation temperatures of the provided alloy, in a fully annealed state, were reported by the vendor as shown in Table 3.6. These temperatures were reportedly determined by differential scanning calorimetry (DSC). As the provided material is not in a fully annealed state, it was expected that all of the transformation temperatures would be somewhat lower than those in the table due to dislocations remaining from the cold work performed to generate the final geometry. Conversely, mechanical restraint in the planned test configurations will increase phase transformation temperatures. In any case, it was decided that additional DSC measurements should be performed on samples of the provided material to determine the baseline phase transformation temperatures.

Small samples (<10mg) were cut from the ribbon material in the as-received condition for the DSC testing. Initial scans showed irregularities in the endothermic peak during heating and a disproportionately small-sized exothermic peak during the cooling, which indicated a potential for unexpected additional activity below ambient temperature. As a result of these initial findings, two more-rigorous scanning procedures were defined in an effort to differentiate between several effects seen in the initial scans. The first scan procedure, termed the *heat-first* procedure, entailed heating from ambient temperature to 150°C at 5°C/minute, cooling from 150°C to –20°C at 5°C/minute, and repeating this entire profile once the sample was returned to ambient from –20°C (also at 5°C/minute). For future reference, the first cycle will be called *first*

Table 3.5 Summary of the thermomechanical properties of Fiberite
E-glass/934 epoxy material system in principal material coordinates.

Temperature	E_1	E_2	ν_{12}	G_{21}	α_1	α_2
°C	GPa	GPa	—	GPa	$\mu\epsilon/°C$	$\mu\epsilon/°C$
21.1	49.30	20.00	0.29	9.65	5.22	10.80
26.7	49.30	19.86	0.29	9.58	5.83	13.81
37.8	49.16	19.44	0.29	9.24	6.95	21.02
48.9	49.02	18.96	0.29	8.89	7.22	24.14
60.0	48.82	18.48	0.29	8.55	7.00	24.66
65.6	48.75	18.20	0.29	8.41	6.80	24.28
71.1	48.75	17.79	0.29	8.27	6.62	23.90
82.2	48.68	17.03	0.29	7.93	6.34	22.79
93.3	48.61	16.20	0.29	7.58	6.25	22.00
104.4	48.61	15.31	0.29	6.76	6.39	21.92
115.6	48.54	14.41	0.29	6.00	6.77	22.66
121.1	48.54	14.00	0.29	5.58	6.97	23.33
126.7	48.61	13.45	0.29	5.17	7.18	24.01
137.8	48.68	12.41	0.29	4.27	7.42	25.47
148.9	48.82	11.38	0.29	3.45	7.63	26.28

Table 3.6 Transformation temperatures for the provided Nitinol alloy in a fully-annealed state.

	Temperature	
Transformation Marker	°C	°F
Austenite Start	67.2	153
Austenite Peak	80.0	176
Austenite Finish	85.0	185
Martensite Start	46.1	115
Martensite Peak	40.0	104
Martensite Finish	32.2	90

heat and the repeat cycle will be called second heat. The second procedure (cool-first) consisted of cooling from ambient temperature to –20°C at 5°C/minute, heating from –20°C to 150°C at 5°C/minute, cooling from 150°C to ambient temperature at 5°C/minute, and repeating this entire profile once the sample was returned to ambient. For this case, the first cycle will be called first
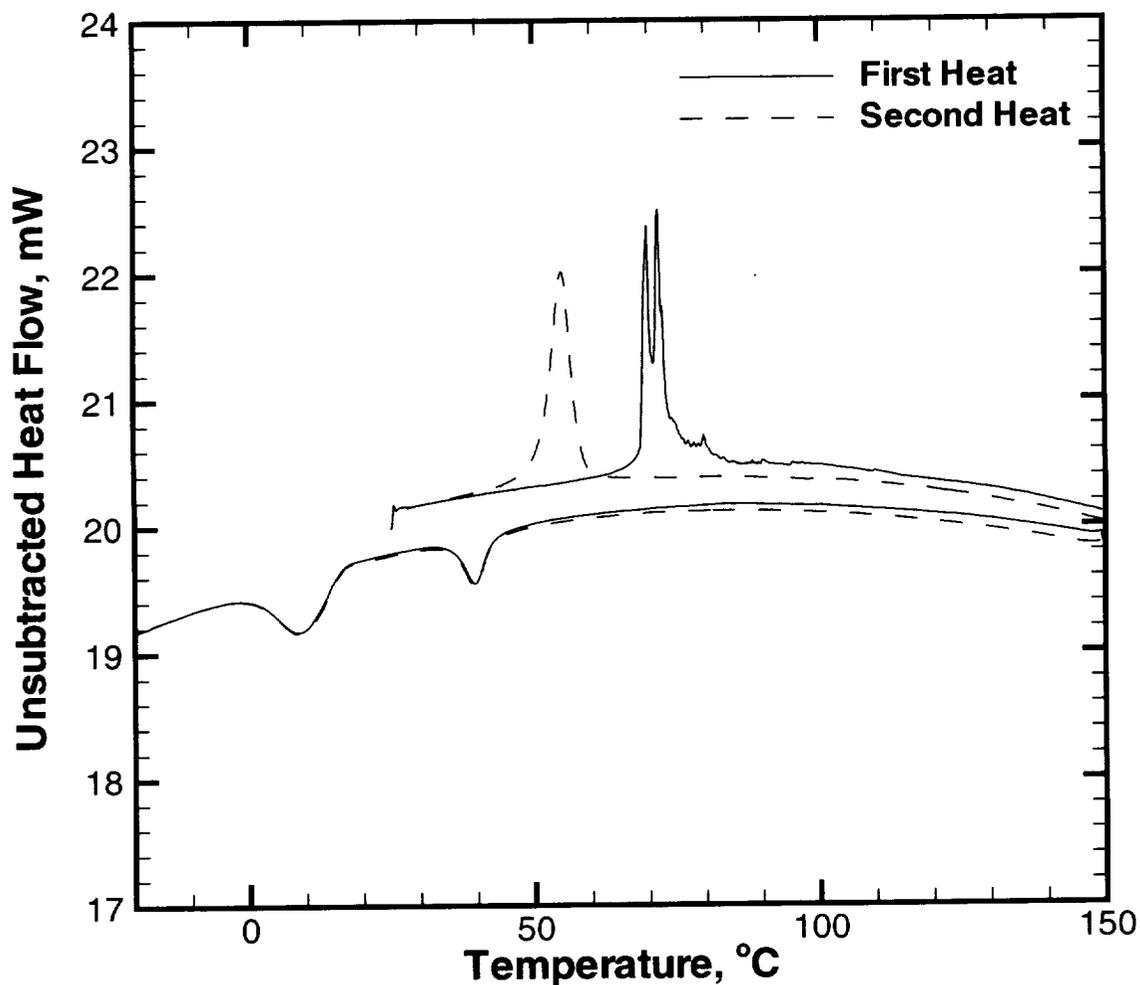
Figure 3.15 Heat-first DSC signatures for first- and second-heat of as-received material.

cool and the repeat cycle will be called *second cool*. Repeatability tests were also performed on each sample type and with each scan procedure.

Representative results from heat-first DSC tests are shown in Figure 3.15. The shape of the first-heat endotherms were ill-behaved and not repeatable, while the analogous second-heat endotherms were repeatable. Similar results with regard to the first-heat and second-heat endotherms are evident in the representative cool-first signatures shown in Figure 3.16. These effects are attributable to first-heat recovery of the mechanical deformation induced by shearing the small samples needed for DSC measurements from longer lengths.

Note that both cycles of the heat-first test show two distinct exothermic peaks during the cool-down portion of the cycles; one peaking at approximately 39°C and attributable to the *R-phase* transformation, the other peaking at approximately 9°C due to the usual twinned martensitic
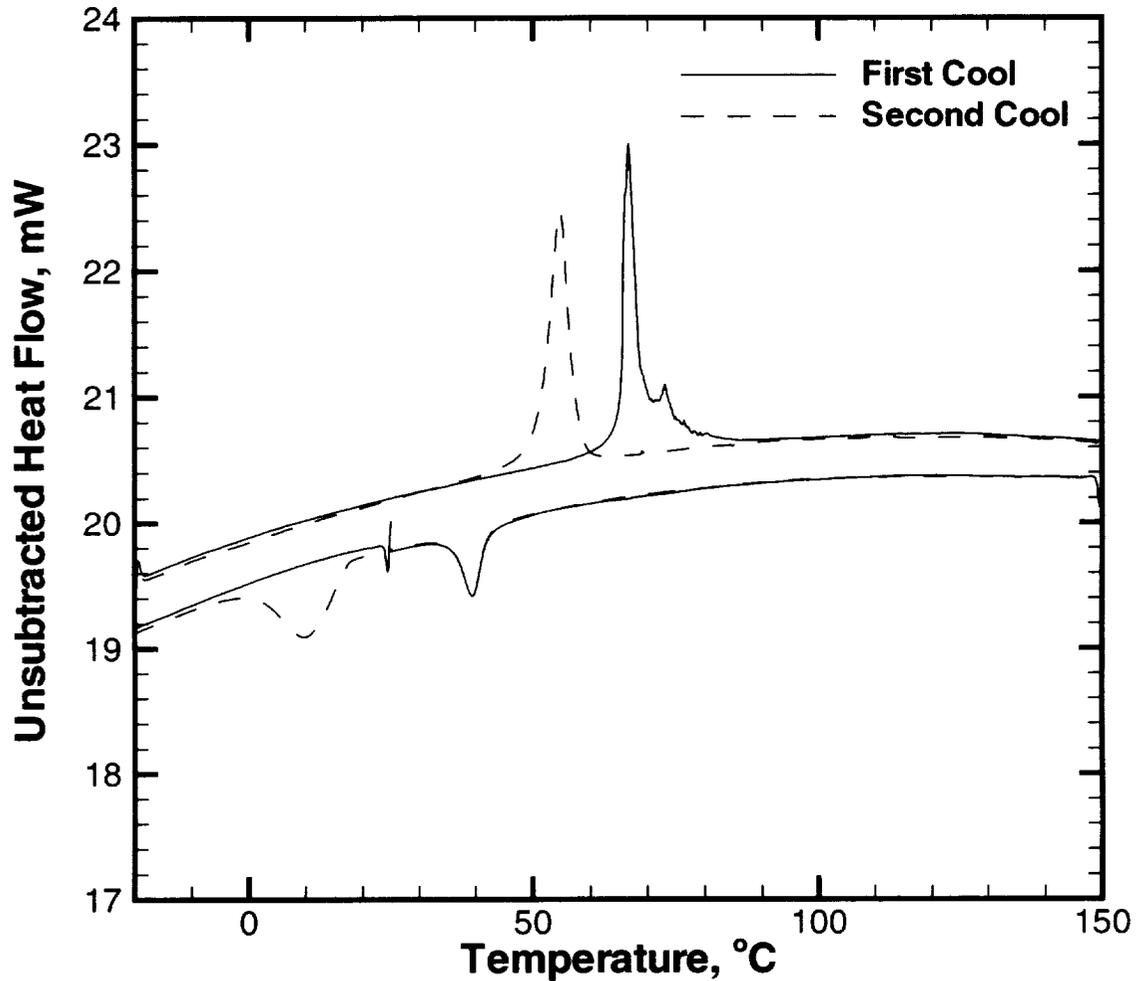
Figure 3.16 Cool-first DSC signatures for first- and second-cool of as-received material.

transformation. The R-phase is a by-product of a partially annealed condition and does not adversely affect performance, as observed by Otsuka and Wayman [34]. Note that the cool-first signature does not show the martensitic transformation on the first-cool portion of the cycle, indicating that the alloy was delivered in a fully transformed state. From these DSC tests it can be seen that the transformation temperatures for the Nitinol in the as-received condition and in a free configuration are approximately A_s=45°C (113°F), A_f=60°C (140°F), M_s=17°C (62.6°F), and M_f=0°C (32°F). Note that the transformation start and finish temperatures indicated here mark the onset/termination of substantial phase transformation activity. Measurable activity can be seen in the tails of the exothermic and endothermic peaks of the DSC signatures. This observation will be revisited later in this section. The DSC results give significant insight into the state of the alloy, but mechanical properties are needed to model the behavior of the material.

Data pertaining to the material property and performance characteristics of the alloy were acquired through mechanical testing performed at Lockheed Martin Astronautics (LMA) [43] and at NASA LaRC. Although rigorous training could have been performed on the alloy to generate a thermomechanically stable actuator material, the elevated cure temperature of the glass-epoxy matrix material (176.7°C, 350°F) was considered to be high enough to risk degrading the expensive training. Thus, thermomechanical testing was performed to quantify the material characteristics as a function of thermal cycle. Discussion will focus on testing performed at Lockheed Martin first, followed by the testing performed at NASA LaRC.

Isolength (constant strain) and isothermal tests were performed on nominal 0.254 m (10 inch) lengths of the material. Isolength tests were performed to measure the maximum recovery stress generated by the actuator material as a function of thermal cycle and initial strain. The results of this test are shown in Figure 3.17 for prestrain values of 2%, 3% and 4%. It can be seen that in all cases the recovery stress diminishes rapidly out to about 10 thermal cycles and approaches an asymptotic value at 50 cycles. Additional isolength tests were performed with the 2% and 4% prestrain samples after the thermal cycling tests to measure the variation of the stabilized recovery stress with temperature. These results are presented in Figure 3.18. Note that the recovery force starts to increase at a temperature very near ambient ($\sim$24°C, 75°F). This phenomenon appears to be in disagreement with the DSC results, but closer inspection reveals that it is not. The initial increase in the recovery force is associated with the transformation activity in the low-temperature "tail", below the so-called A_s, of the exothermic peak in Figures 3.15 and 3.16. The abrupt change in the slope of the recovery stress vs. temperature curve, near 40°C (104°F), is associated with A_s. Also note that the higher prestrain level generates greater recovery stress as expected. A couple of more subtle points can also be seen in this plot. Although the increased recovery stress at 4% prestrain does inhibit completion of the reverse transformation more than at 2%, as evidenced by the higher temperature as which it approaches an asymptotic value, the maximum slope of the 2% recovery stress vs. temperature curve is not as great as that for 4%. This trend is interesting in contrast to the data presented by Cross et al. [28], where reduction in the peak values of the recovery stress at lower prestrain levels is accompanied by higher maximum slope of the recovery stress vs. temperature curve. These insights will be revisited later in this chapter as well as in Chapter 8.

A couple of options exist, with the available data from LMA, for modeling the behavior of the SMA material in the hybrid composite for comparison to experiment. The specimens could be thermally cycled enough (e.g., 50 times) to render the structure's properties stable and simply model the SMA recovery stress behavior according to Figure 3.18. Alternatively, an estimate of the variation of recovery stress with thermal cycle number and temperature can be calculated from the available data. Construction of such a data set can be accomplished by normalizing the recovery stress versus temperature data to the corresponding maximum recovery stress versus cycle data set. The resulting carpet plots are shown in Figures 3.19 and 3.20 for the samples with 2% and 4% prestrain, respectively. Usage of these data sets allows modeling of the material system without any requirement on thermal cycling of the SMAHC specimens.

Isothermal tests were conducted to measure load versus deflection on all of the previously described specimens, as well as a specimen in the as-received condition, at ambient and elevated temperature (120°C) to obtain estimates of the Young's modulus. Representative plots, converted
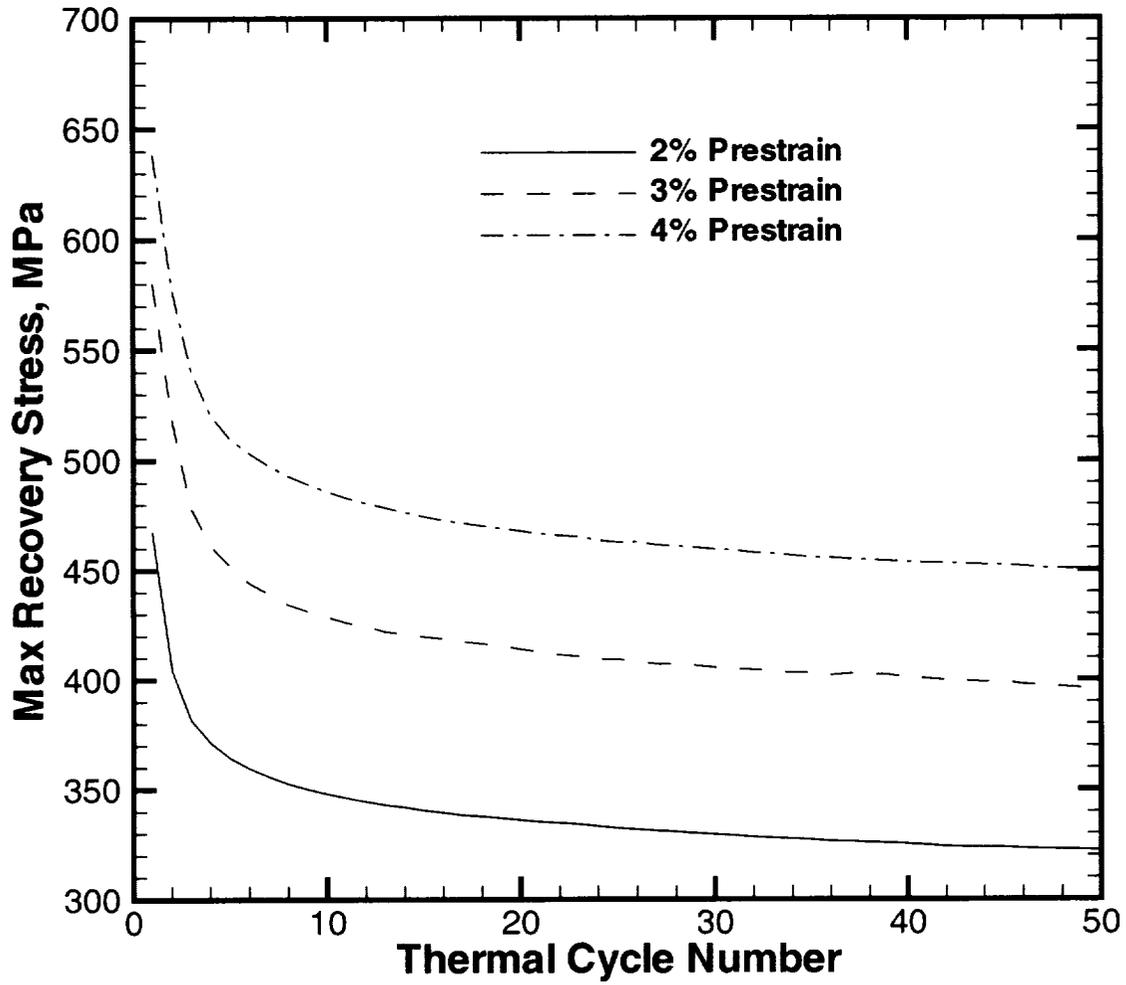
Figure 3.17 Max recovery stress versus thermal cycle number
for Nitinol ribbon samples with 2%, 3%, and 4% prestrain.
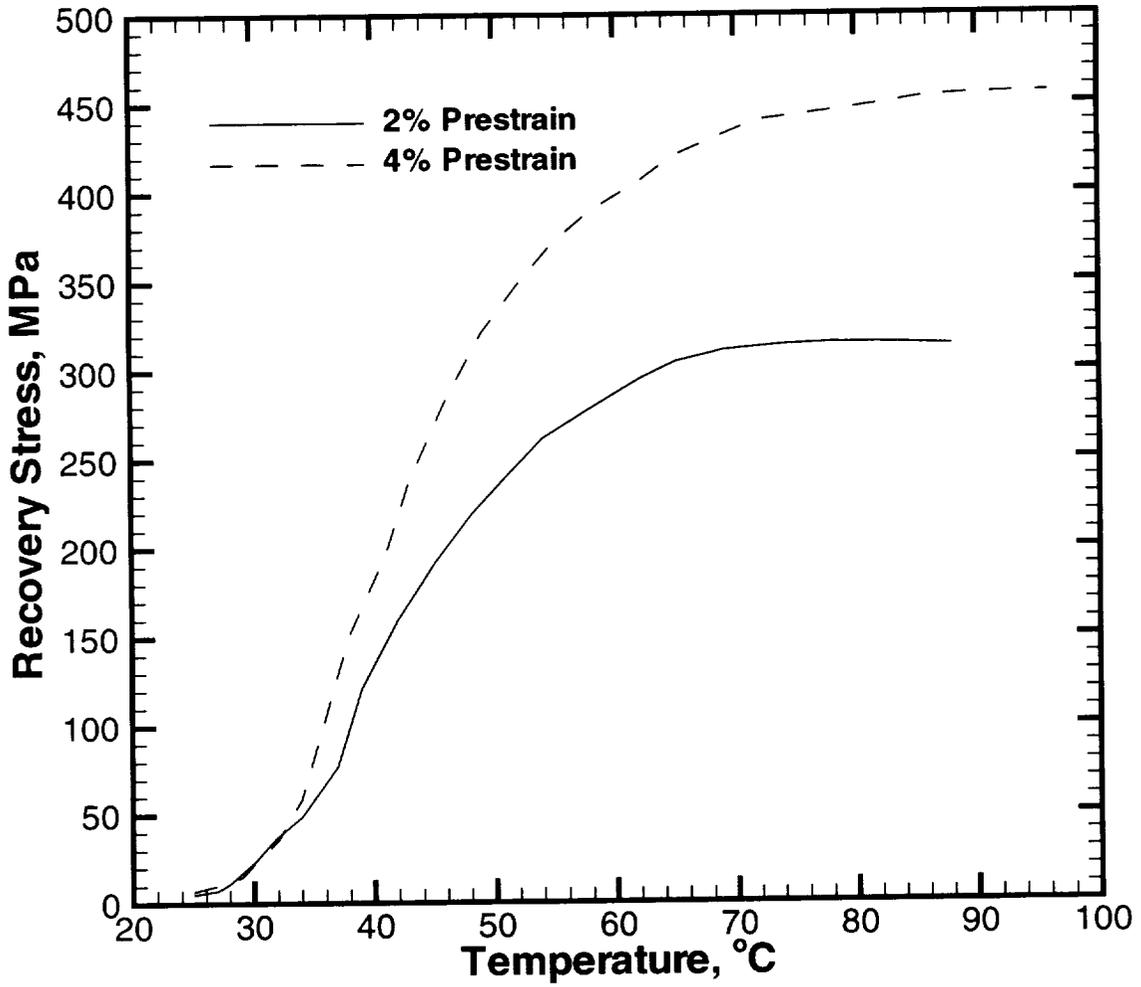
Figure 3.18 Recovery stress versus temperature for Nitinol
ribbon samples with 2% and 4% prestrain, after 50 cycles.
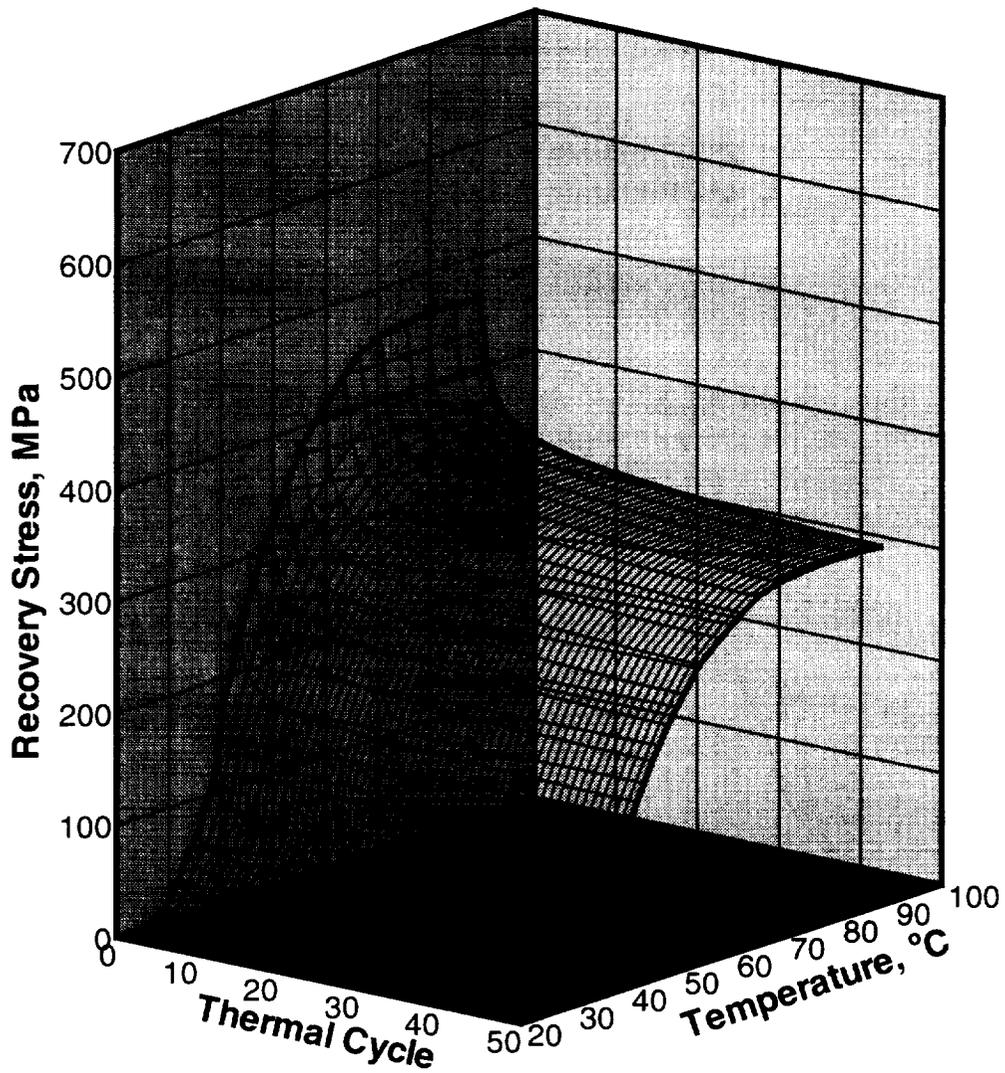
Figure 3.19 Recovery stress versus thermal cycle and temperature for sample with 2% prestrain.
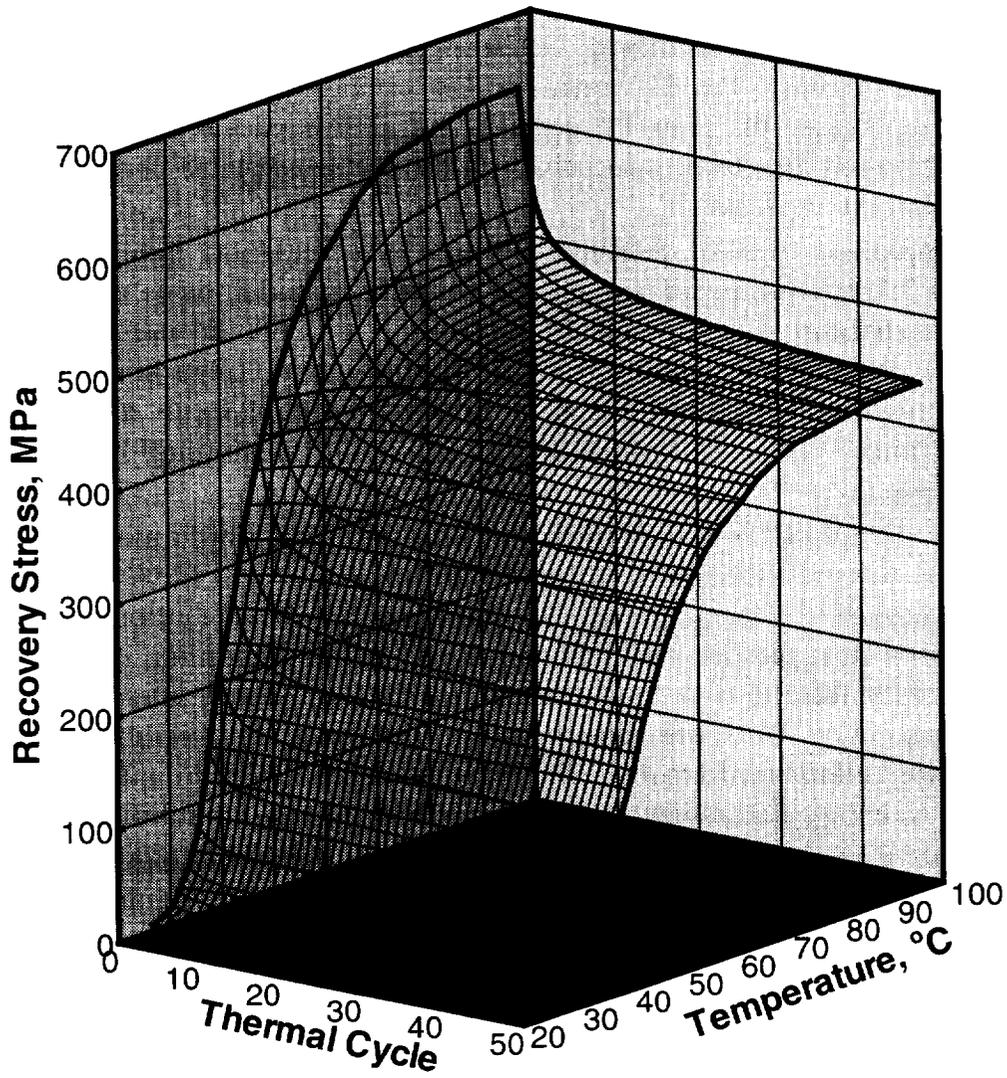
Figure 3.20 Recovery stress versus thermal cycle temperature for sample with 4% prestrain.

to units of stress versus strain, are shown for the cases of 0% (as-received) and 4% prestrain at ambient and elevated temperatures in Figures 3.21 and 3.22. The martensite variant re-orientation yield stress and initiation of linear elastic behavior of the martensitic phase are evident in the ambient temperature curves. Note the contrast between the as-received and 4% ambient temperature results. The 4% curve does not exhibit the long martensite variant re-orientation plateau because the prior 4% prestrain has diminished the available variants for re-orientation. However, the curves associated with the unique austenitic phase are linear and practically identical, as expected.

Ambient temperature Young's modulus estimates were calculated from only the initial (0–25.5 MPa, 0–3.7 ksi) portion of the ambient temperature curve, while the overall slope of the elevated temperature data was used for hot Young's modulus estimates. Recall that the maximum normal strain is not expected to exceed 500 $\mu\epsilon$ in the configurations considered in this study. Therefore, evaluation of the ambient temperature modulus over the small range is considered appropriate. The resulting modulus data and values summarizing the isolength tests are shown in Table 3.7.

Recall that in the SMAHC specimen fabrication procedures, described earlier in this chapter, the Nitinol ribbon was prestrained 4%. Although data was collected at LMA for this prestrain level, there is a fundamental inconsistency. The ribbon used in the fabrication procedures was necessarily released from tension after prestraining and before embedding in the composite, whereas the recovery force tests at LMA were performed immediately after prestraining and without regripping. Also, there was some suspicion that aging, after prestraining, may have some effect on the actuator performance. Therefore, additional isolength and isothermal tests were performed on excess ribbon with 4% prestrain remaining from the fabrication process.

Isolength tests were performed on 0.127 m (5 inch) gage lengths to measure the recovery force versus temperature and thermal cycle. An adaptation of the prestraining apparatus was used to configure the Nitinol ribbon for measurement of recovery force. The apparatus, shown in Figure 3.23, allowed for convenient and repeatable installation of ribbon samples in the test machine. A picture of a sample installed in the test machine, after spacer removal, is shown in Figure 3.24. The ribbon was subjected to a slight preload ∼4.45 N (1 lbf) to keep the sample taut prior to fixing the test machine grips (stroke control) and exposing the sample to thermal cycling. The ribbon was electrically heated to expedite the thermal cycling process. The recovery force and ribbon temperature at three locations were measured at 2–second intervals during each thermal cycle, each of which was completed in approximately 15 minutes. The raw data was then processed to estimate the recovery stress with a common temperature resolution and averaged over three samples. The resulting recovery stress versus temperature data corresponding to the second through fourth thermal cycle are shown in Figure 3.25. The data for the first thermal cycle are not included as that information is applicable only to the SMAHC cure cycle. The fiftieth cycle data is included for comparison with the LMA data.

It can be seen by comparing the maximum recovery force with the data in Figure 3.17 that the performance of the Nitinol ribbon that was prestrained 4% and released is similar to that of the 3% prestrain data collected at LMA. Analogous curves were generated from the LMA data by averaging 2% and 4% prestrain data sets in Figure 3.18 and scaling the resulting load vs. temperature data by the maximum load for 3% prestrain at cycle numbers 2, 3, 4 and 50
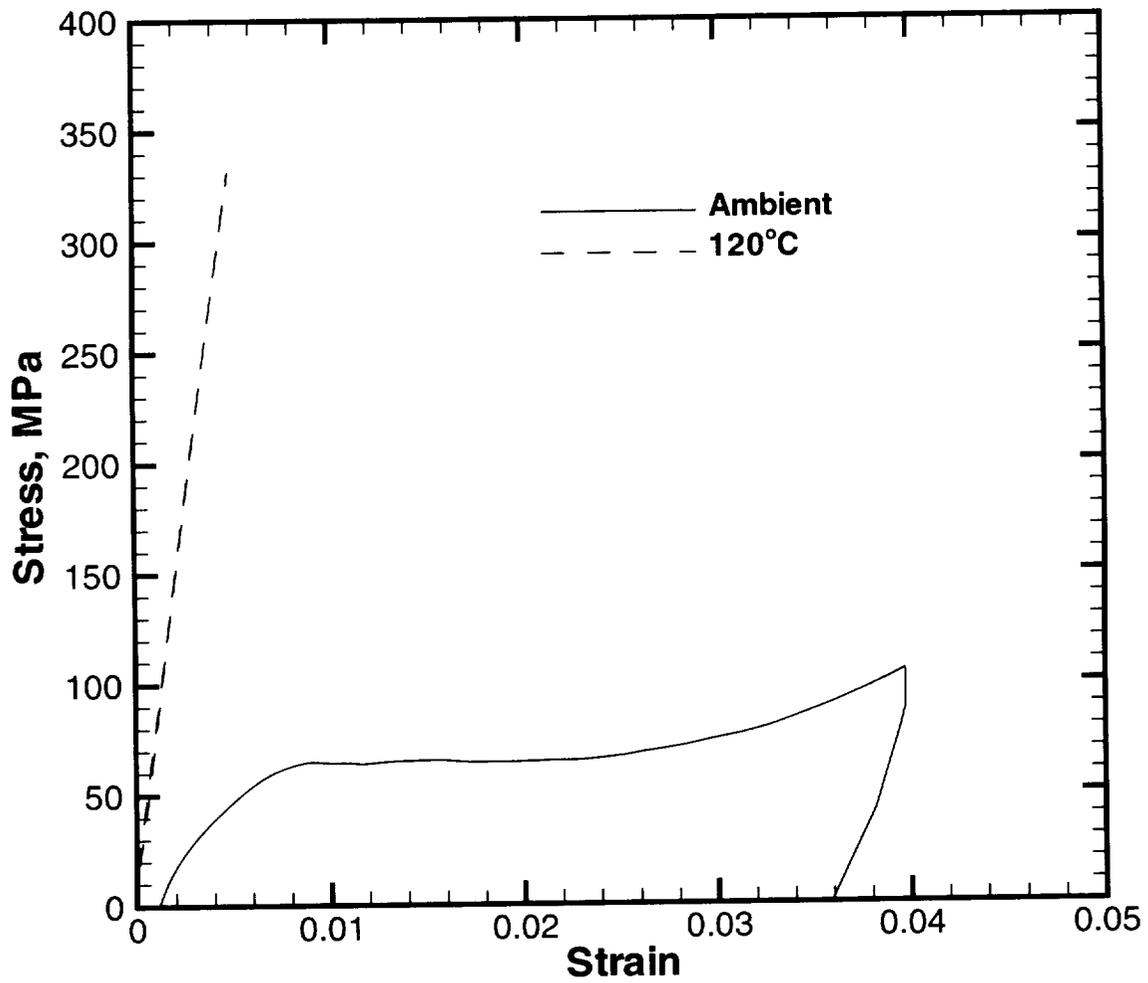
Figure 3.21 Applied stress versus strain for 0.09x0.006x10 inch sample with 0% prestrain (as-received) at ambient temperature and 120°C.
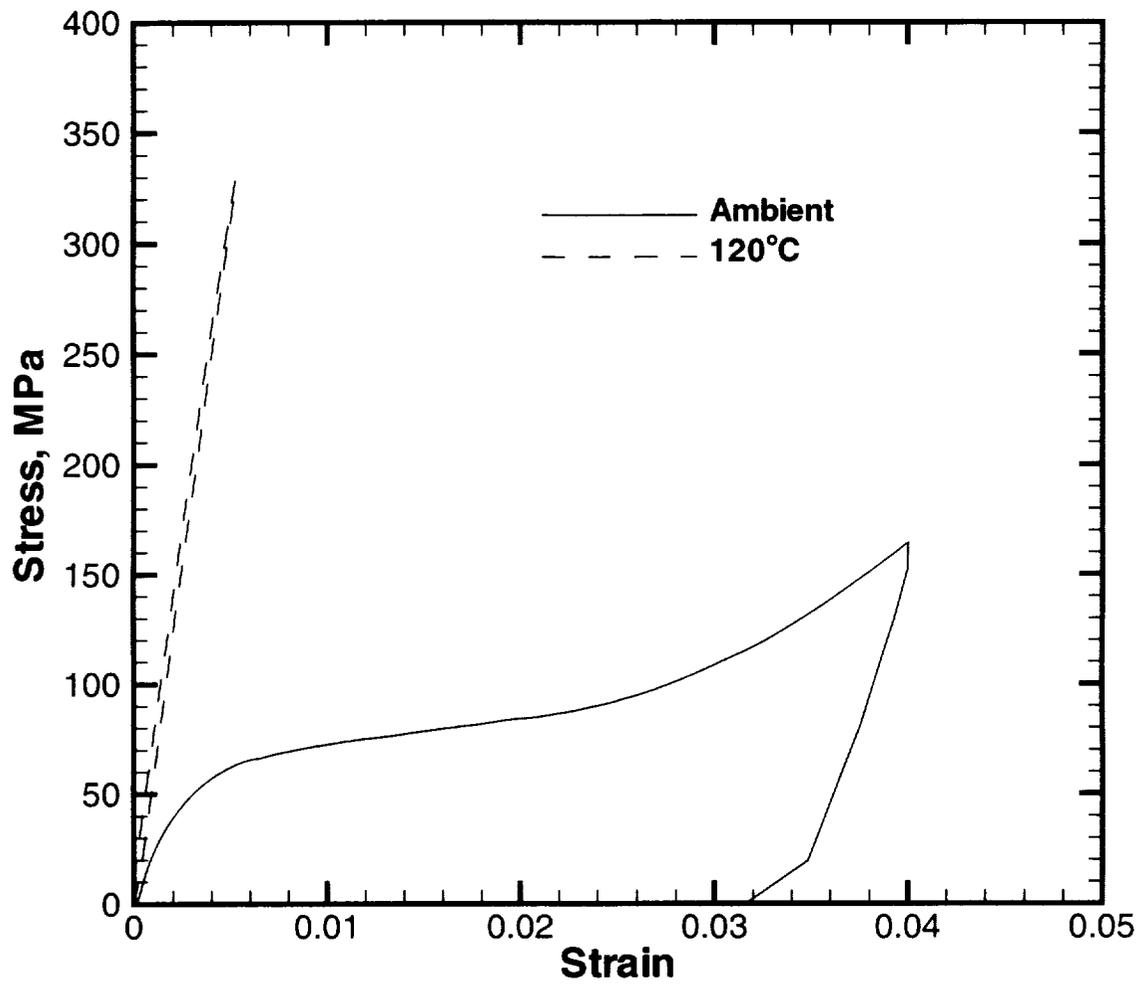
Figure 3.22 Applied stress versus strain for 0.09x0.006x10 inch
sample with 4% prestrain at ambient temperature and 120°C.

Table 3.7 Summary of Nitinol characterization tests.

Sample	Prestrain, %	# of Cycles	Maximum Stress, MPa		Young's Modulus, GPa	
			Initial	Final	120°C	Ambient
1	1.99	50	429.4	296.0	55.50	22.75
2	3.08	50	533.0	363.3	62.47	25.10
3	3.07	10	517.1	396.3	56.06	24.41
4	4.00	50	586.3	412.7	55.64	24.34
5	3.95	10	579.2	442.1	55.92	24.20
6	N/A	0	N/A	N/A	59.78	14.41
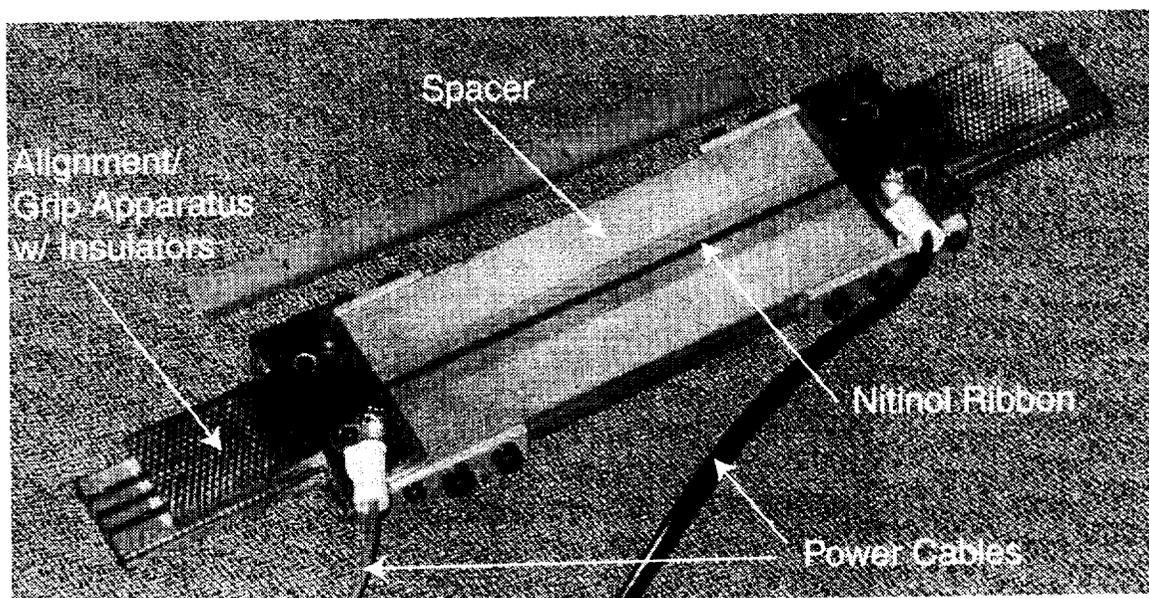
Figure 3.23 Apparatus for installation of a Nitinol ribbon sample
in a tensile test machine for recovery force measurement.

MTS Hydraulic Grip

Nitinol Alignment/ Grip Apparatus

Nitinol Ribbon

Thermocouples
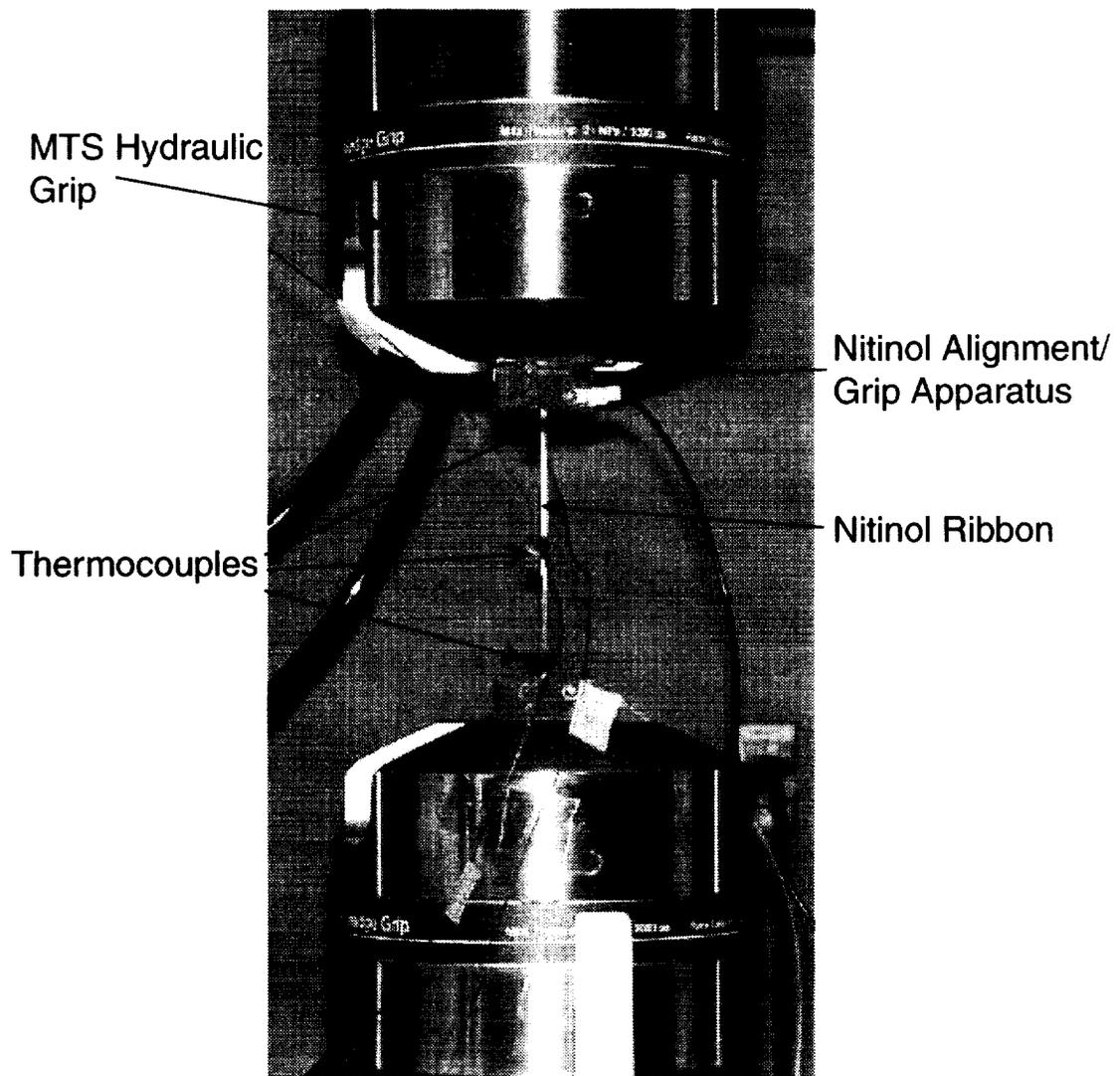
Figure 3.24 Recovery force measurement in progress.
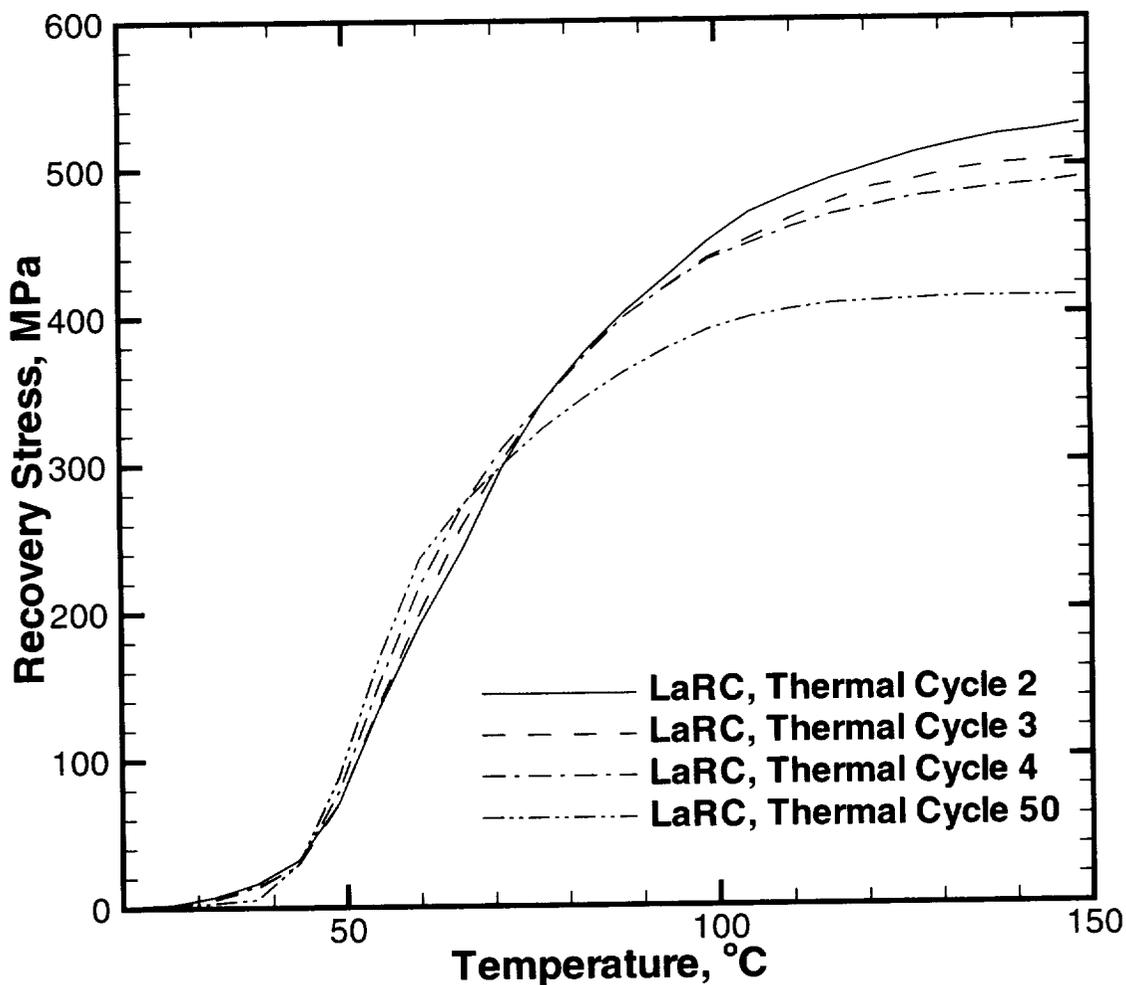
Figure 3.25 Recovery stress versus temperature of the Nitinol ribbon (prestrained 4% and released) for thermal cycles 2–4 and 50.

in Figure 3.17. The resulting curves are shown in Figure 3.26. Note that the 3% prestrain case "constructed" from the LMA data achieves roughly the same maximum recovery force, but over a much more narrow temperature range. This trend is a real physical phenomenon and is apparently attributable to aging effects. Also note the shape change with thermal cycle of the recovery stress vs. temperature curve, evident in Figure 3.25. This effect is not reflected in the data set constructed from the LMA data and expresses the importance of quantifying the recovery stress functionality with temperature vs. thermal cycle.

Isothermal tests were conducted using 0.127 m (5 inch) gage lengths with the same gripping apparatus as shown previously. The entire assembly, including high-temperature MTS grips, was contained within a box furnace. Modulus tests were conducted on 3 ribbon samples at
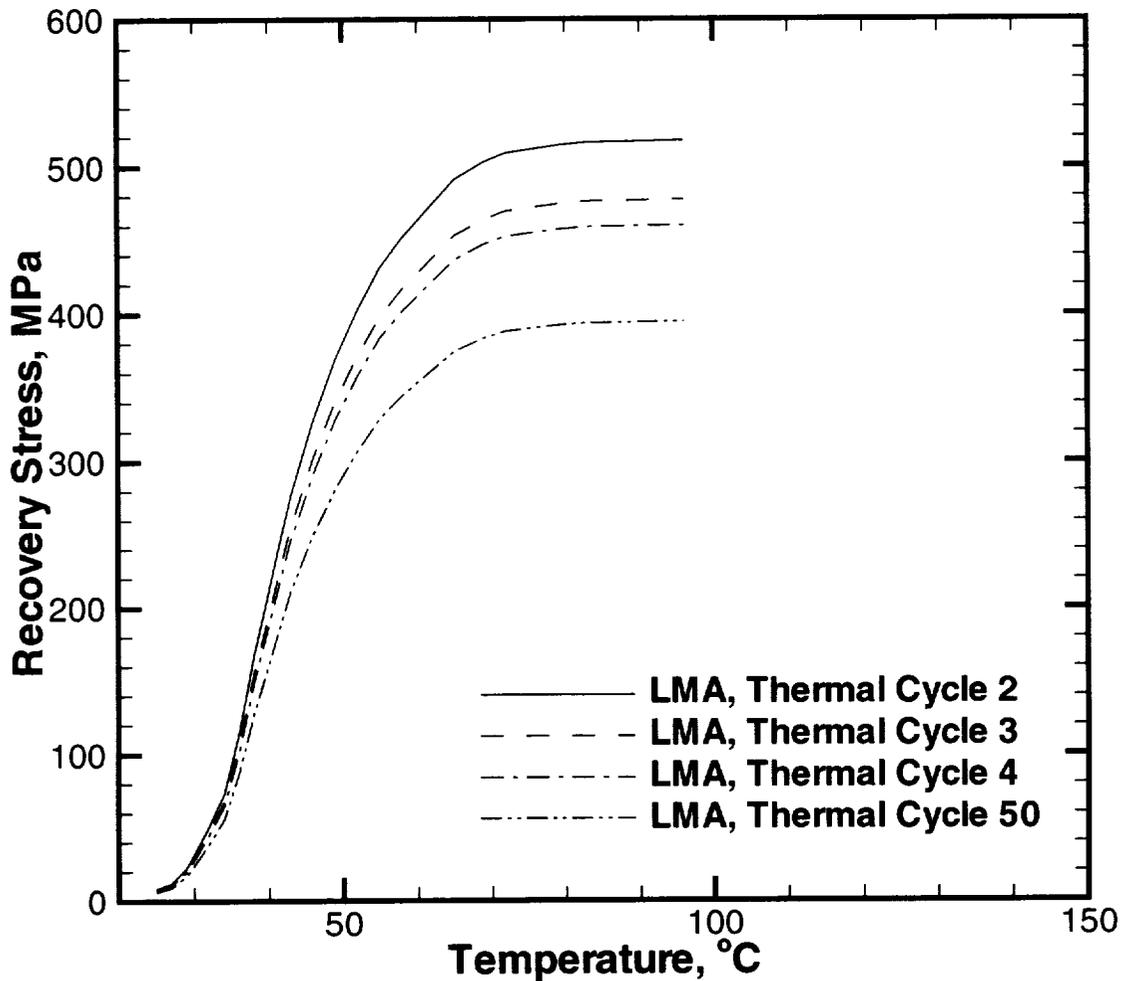
Figure 3.26 Recovery stress versus temperature of the Nitinol ribbon for 3%
prestrain constructed from the LMA data for thermal cycles 2–4 and 50.

each of 6 temperatures; 21.11°C (70°F), 37.78°C (100°F), 65.56°C (150°F), 93.33°C (200°F),
121.1°C (250°F), and 148.9°C (300°F). Estimates from the three samples were averaged and the
resulting modulus versus temperature behavior is shown in Figure 3.27. Stress-strain behavior
similar to that shown in Figure 3.22 was observed, but the modulus estimates are somewhat
different. These differences are also probably attributable to aging effects, akin to the rubber-
like pseudoelasticity behavior.

Note that the temperature range over which the modulus exhibits the most variation in
Figure 3.27 is more narrow than the A_s–A_f range interpreted from Figure 3.25. This obervation
is consistent with the data collected by Cross et al. [28]. The low-temperature transition
point is associated with the temperature at which there is significant austenite and high-enough
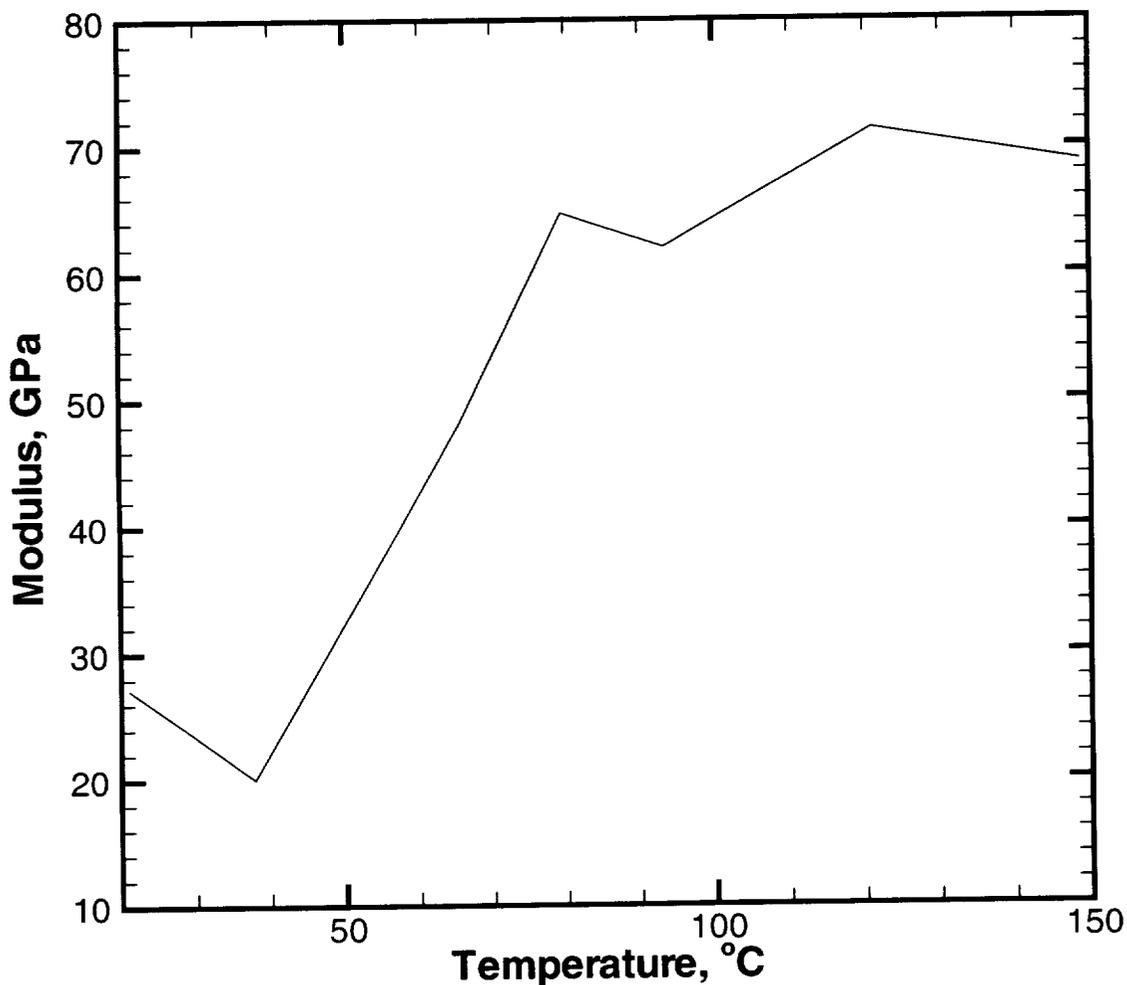
Figure 3.27 Modulus for the Nitinol ribbon prestrained
4% and released as a function of temperature.

temperature to not allow immediate transformation to martensite upon stress application. The high-temperature transition point corresponds to the temperature at which the austenite volume fraction begins to dominate.

Published data will be used for Poisson's ratio (0.3) and the transverse direction CTE for the martensitic 6.6e-6 /°C (3.67e-6 /°F) and austenitic 11e-6 /°C (6.11e-6 /°F) as measurement of these properties as a function of temperature would require significant additional effort/development. In light of the previous discussions concerning the differences between the data collected at LaRC and LMA, the data collected at LaRC are more representative of the thermomechanical properties of the Nitinol ribbon actually embedded in the composite and is more accurate. Therefore, the properties interpreted from this data were used in making the

predictions shown later in this document. These properties are tabulated in Table 3.8. Note that the modulus data has been linearly interpolated within the more coarse temperature resolution. The 2-direction CTE has been interpolated between two transition points noted in regard to Figure 3.27, 43.33°C (110°F) and 82.22°C (180°F), to approximate the variation within the reverse transformation temperature range. The "in-service" austenite start and finish temperatures, as interpreted from the recovery stress versus temperature data, are 26.7°C (80°F) and 148.9°C (300°F), respectively. However, the temperature range of property variation is better modeled by the temperatures at which the recovery stress vs. temperature curve rapidly changes slope, as discussed previously.

In this chapter, the glass-epoxy and Nitinol ribbon material system selected for this study was described. Discussion of the procedures for fabricating the SMAHC beam specimens was followed by results from thermomechanical characterization tests on the constituent materials. A full set of temperature dependent material properties were generated to quantify the constitutive model developed in the previous chapter. This constitutive model can now be incorporated in a thermomechanical model to predict the behavior of structures fabricated from this material system. One such model is developed using a finite element approach in the following chapter.

Table 3.8 Summary of the thermomechanical properties of the Nitinol ribbon.

| Temperature | Recovery Stress | | | E | α_2 |
| | Cycle 2 | Cycle 3 | Cycle 4 | | |
°C	MPa	MPa	MPa	GPa	$\mu\epsilon/°C$
21.1	0	0	0	27.17	6.606
26.7	2.130	1.276	2.130	24.82	6.606
32.2	7.233	5.530	7.233	22.41	6.606
37.8	16.18	13.20	14.05	20.06	6.606
43.3	31.92	28.95	28.52	25.72	6.606
48.9	70.65	70.23	78.74	31.37	7.236
54.4	135.4	137.9	151.9	36.96	7.866
60.0	192.0	199.6	217.9	42.61	8.496
65.6	240.5	256.6	269.4	48.27	9.108
71.1	297.1	301.8	309.8	54.88	9.738
76.7	341.8	341.8	341.3	61.43	10.37
82.2	374.5	373.7	372.0	64.19	11.00
87.8	402.2	399.2	399.2	63.16	11.00
93.3	425.6	419.2	418.8	62.06	11.00
98.9	449.9	438.8	437.5	63.92	11.00
104.4	469.0	451.6	448.2	65.78	11.00
110.0	481.0	464.8	458.8	67.64	11.00
115.6	491.6	475.8	467.3	69.50	11.00
121.1	500.1	485.6	472.9	71.36	11.00
126.7	508.6	490.3	478.8	70.81	11.00
132.2	515.0	496.7	481.8	70.33	11.00
137.8	520.5	500.5	485.2	69.78	11.00
143.3	523.5	502.2	487.3	69.29	11.00
148.9	527.8	503.9	490.7	68.74	11.00

Chapter 4
Finite Element Formulation

Previous models have been limited in their ability to predict the behavior of SMAHC structures because of inaccurate/impractical constitutive models and/or classical formulation approach. The present formlulation incorporates the ECTEM and will be developed using a finite element approach. This combination will later be shown to accurately capture the mechanics of the system and to afford the generality/versatility to allow comparison with experiment.

The governing equations for the geometrically nonlinear, static thermal response and the geometrically linear dynamic response of a rectangular panel-type structure subjected to combined thermal and mechanical loads is derived in this chapter. It is necessary to account for geometrically nonlinear out-of-plane deflection because of the potential for large static deflections due to thermal buckling. Therefore, a finite element with cubic out-of-plane interpolation functions is deemed necessary.

4.1 Element Displacement Functions

A rectangular 24 degree-of-freedom (dof) plate element [44] was chosen for the subsequent finite element formulation. The element has four nodes with two in-plane and four out-of-plane dof per node, and is shown schematically in Figure 4.1. The in-plane displacement functions are bilinear and that for the out-of-plane displacement is bi-cubic:

$$u(x,y) = a_1 + a_2 x + a_3 y + a_4 xy$$
$$v(x,y) = a_5 + a_6 x + a_7 y + a_8 xy$$

(4.1)

and

$$w(x,y) = c_1 + c_2 x + c_3 y + c_4 x^2 + c_5 xy + c_6 y^2 + c_7 x^3 + c_8 x^2 y + c_9 xy^2 + c_{10} y^3$$
$$+ c_{11} x^3 y + c_{12} x^2 y^2 + c_{13} xy^3 + c_{14} x^3 y^2 + c_{15} x^2 y^3 + c_{16} x^3 y^3$$

(4.2)

where the a_i and c_i are generalized coordinates.

The displacement functions can also be written in a form particularly suited to numerical implementation in terms of the nodal degrees of freedom and appropriate bilinear and bi-cubic interpolation functions of the element coordinates :

$$u(x,y) = \sum_{i=1}^{4} L_i(\xi, \eta) u_i = \frac{1}{ab}[(a - x)(b - y)u_1 + x(b - y)u_2 + xy u_3 + (a - x)y u_4]$$

(4.3)

$$v(x,y) = \sum_{i=1}^{4} L_i(\xi, \eta) v_i = \frac{1}{ab}[(a - x)(b - y)v_1 + x(b - y)v_2 + xy v_3 + (a - x)y v_4]$$
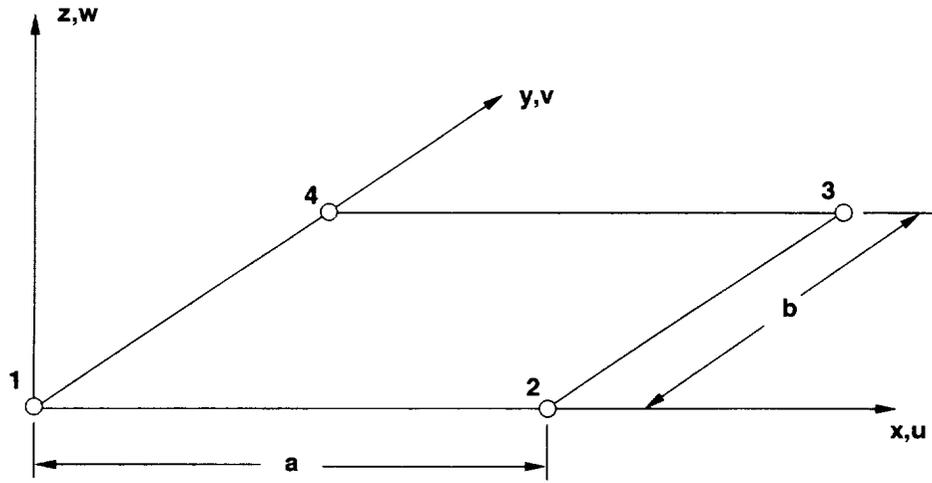
Figure 4.1 Schematic of 24 dof rectangular plate element.

and

$$w(x,y) = \sum_{i=4}^{20} L_i(x,y)\, q_i$$

$$= \frac{1}{a^3 b^3}\Big[(a^3 + 2x^3 - 3ax^2)(b^3 + 2y^3 - 3by^2)w_1 + (3ax^2 - 2x^3)(b^3 + 2y^3 - 3by^2)w_2$$

$$+ (3ax^2 - 2x^3)(3by^2 - 2y^3)w_3 + (a^3 + 2x^3 - 3ax^2)(3by^2 - 2y^3)w_4$$

$$+ ax(x-a)^2(b^3 + 2y^3 - 3by^2)\left(\frac{\partial w}{\partial x}\right)_1 + a(x^3 - ax^2)(b^3 + 2y^3 - 3by^2)\left(\frac{\partial w}{\partial x}\right)_2$$

$$+ a(x^3 - ax^2)(3by^2 - 2y^3)\left(\frac{\partial w}{\partial x}\right)_3 + ax(x-a)^2(3by^2 - 2y^3)\left(\frac{\partial w}{\partial x}\right)_4$$

$$+ b(a^3 + 2x^3 - 3ax^2)y(y-b)^2\left(\frac{\partial w}{\partial y}\right)_1 + b(3ax^2 - 2x^3)y(y-b)^2\left(\frac{\partial w}{\partial y}\right)_2$$

$$+ b(3ax^2 - 2x^3)(y^3 - by^2)\left(\frac{\partial w}{\partial y}\right)_3 + b(a^3 + 2x^3 - 3ax^2)(y^3 - by^2)\left(\frac{\partial w}{\partial y}\right)_4$$

$$+ abxy(x-a)^2(y-b)^2\left(\frac{\partial^2 w}{\partial x\partial y}\right)_1 + abxy(x^2 - ax)(y-b)^2\left(\frac{\partial^2 w}{\partial x\partial y}\right)_2$$

$$+ abxy(x^2 - ax)(y^2 - by)\left(\frac{\partial^2 w}{\partial x\partial y}\right)_3 + abxy(x-a)^2(y^2 - by)\left(\frac{\partial^2 w}{\partial x\partial y}\right)_4 \Big]$$

(4.4)

where u_i and v_i are the in-plane dof, q_i denotes the out-of-plane dof ($w_1 \rightarrow \left(\frac{\partial^2 w}{\partial x\partial y}\right)_4$), and a/b are the element length/width, respectively. It will be advantageous for discussions that follow to cast these equations in matrix form

$$\left\{ \begin{array}{c} u \\ v \\ w \end{array} \right\} = \left[\begin{array}{cc} \lfloor L_u \rfloor & 0 \\ \lfloor L_v \rfloor & 0 \\ 0 & \lfloor L_w \rfloor \end{array} \right] \left\{ \begin{array}{c} a_m \\ a_b \end{array} \right\} = [L_{uvw}]\{a_{mb}\}$$

(4.5)

where the nodal degrees of freedom have been collected into membrane $\{a_m\}$ and bending $\{a_b\}$ components

$$\lfloor a_m \rfloor = \lfloor u_1 \quad u_2 \quad u_3 \quad u_4 \quad v_1 \quad v_2 \quad v_3 \quad v_4 \rfloor$$

$$\lfloor a_b \rfloor = \lfloor w_1 \quad \ldots \quad w_4 \quad w_{,x1} \quad \ldots \quad w_{,x4} \quad w_{,y1} \quad \ldots \quad w_{,y4} \quad w_{,xy1} \quad \ldots \quad w_{,xy4} \rfloor$$

(4.6)

Also, the displacement shape functions have been collected into vectors

$$\lfloor L_u \rfloor = \lfloor L_1 \quad L_2 \quad L_3 \quad L_4 \quad 0 \quad 0 \quad 0 \quad 0 \rfloor$$

$$\lfloor L_v \rfloor = \lfloor 0 \quad 0 \quad 0 \quad 0 \quad L_1 \quad L_2 \quad L_3 \quad L_4 \rfloor$$

$$\lfloor L_w \rfloor = \lfloor L_5 \quad L_6 \quad \ldots \quad L_{20} \rfloor$$

(4.7)

Recall the von Kármán strain displacement relations, equation (2.32). The membrane midplane strains and midplane curvatures can be written in terms of the nodal degrees of freedom

63

and interpolation functions by substituting from equations (4.5) and (4.7):

$$\{\epsilon_m^o\} = \left\{ \begin{array}{c} u_{,x} \\ v_{,y} \\ u_{,y} + v_{,x} \end{array} \right\} = \left\{ \begin{array}{c} \lfloor L_{u,x} \rfloor \\ \lfloor L_{v,y} \rfloor \\ \lfloor L_{u,y} \rfloor + \lfloor L_{v,x} \rfloor \end{array} \right\} \{a_m\} = [C_m]\{a_m\}$$

$$\{\kappa\} = -\left\{ \begin{array}{c} w_{,xx} \\ w_{,yy} \\ 2w_{,xy} \end{array} \right\} = -\left\{ \begin{array}{c} \lfloor L_{w,xx} \rfloor \\ \lfloor L_{w,yy} \rfloor \\ 2\lfloor L_{w,xy} \rfloor \end{array} \right\} \{a_b\} = [C_b]\{a_b\}$$

(4.8)

where

$$[C_m] = \begin{bmatrix} L_{1,x} & L_{2,x} & L_{3,x} & L_{4,x} & 0 & 0 & 0 & 0 \\ 0 & 0 & 0 & 0 & L_{1,y} & L_{2,y} & L_{3,y} & L_{4,y} \\ L_{1,y} & L_{2,y} & L_{3,y} & L_{4,y} & L_{1,x} & L_{2,x} & L_{3,x} & L_{4,x} \end{bmatrix}$$

(4.9)

and

$$[C_b] = -\begin{bmatrix} L_{5,xx} & L_{6,xx} & \dots & L_{20,xx} \\ L_{5,yy} & L_{6,yy} & \dots & L_{20,yy} \\ 2L_{5,xy} & 2L_{6,xy} & \dots & L_{20,xy} \end{bmatrix}$$

(4.10)

The bending midplane strain requires some manipulation to obtain a useful form. One approach follows from recognition that the second-order (nonlinear) terms can be expressed as the product of first-order terms:

$$\{\epsilon_b^o\} = \frac{1}{2} \left\{ \begin{array}{c} w_{,x}^2 \\ w_{,y}^2 \\ 2w_{,x}\, w_{,y} \end{array} \right\} = \frac{1}{2} \begin{bmatrix} w_{,x} & 0 \\ 0 & w_{,y} \\ w_{,y} & w_{,x} \end{bmatrix} \left\{ \begin{array}{c} w_{,x} \\ w_{,y} \end{array} \right\}$$

(4.11)

It will be useful later to make the definition

$$[\theta] = \begin{bmatrix} w_{,x} & 0 \\ 0 & w_{,y} \\ w_{,y} & w_{,x} \end{bmatrix}$$

(4.12)

$$\{G\} = \left\{ \begin{array}{c} w_{,x} \\ w_{,y} \end{array} \right\}$$

The vector $\{G\}$ can be written in terms of nodal degrees of freedom as before in equations (4.8) to give

$$\{G\} = \left\{ \begin{array}{c} \lfloor L_{w,x} \rfloor \\ \lfloor L_{w,y} \rfloor \end{array} \right\} \{a_b\} = [C_\theta]\{a_b\}$$

(4.13)

where

$$[C_\theta] = \begin{bmatrix} L_{5,x} & L_{6,x} & \dots & L_{20,x} \\ L_{5,y} & L_{6,y} & \dots & L_{20,y} \end{bmatrix}$$

(4.14)

Thus, the (nonlinear) bending midplane strain can be written as follows

$$\{\epsilon_b^o\} = \frac{1}{2}[\theta][C_\theta]\{a_b\}$$

(4.15)

where $[\theta]$ is a constant matrix whose entries are evaluated based upon the nodal degrees of freedom from the previous iteration in an iterative procedure. Such a procedure will be described in Chapter 5.

$$[\theta]_{i+1} = \begin{bmatrix} \lfloor L_{w,x} \rfloor & 0 \\ 0 & \lfloor L_{w,y} \rfloor \\ \lfloor L_{w,y} \rfloor & \lfloor L_{w,x} \rfloor \end{bmatrix} \{a_b\}_i \tag{4.16}$$

The form for the von Kármán midplane strain and curvature can be summarized as follows.

$$
\begin{aligned}
\{\epsilon\} &= \{\epsilon^o\} + z\{\kappa\} \\
&= \{\epsilon_m^o\} + \{\epsilon_b^o\} + z\{\kappa\} \\
&= [C_m]\{a_m\} + \frac{1}{2}[\theta][C_\theta]\{a_b\} + z[C_b]\{a_b\}
\end{aligned}
\tag{4.17}
$$

Finally, it will be useful in subsequent discussions to write the resultant force components from equation (2.38) in terms of the nodal degrees of freedom:

$$
\begin{aligned}
\{N_m\} &= [A][C_m]\{a_m\} \\
\{N_\theta\} &= \frac{1}{2}[A][\theta][C_\theta]\{a_b\} \\
\{N_b\} &= [B][C_b]\{a_b\}
\end{aligned}
\tag{4.18}
$$

4.2 Euler-Lagrange Equations

The equations of motion for a mechanical system can be derived following a Newtonian approach or a variational approach. Variational methods have proven to be very effective tools in deriving the equations of motion for complex mechanical systems. The governing equations for the mechanical system considered in this study will be derived using the extended Hamilton's principle, as described in Meirovitch [45] for example. Hamilton's principle states that the path satisfying Newton's law extremizes the time integral of the Lagrangian with respect to all possible paths between the limits of the time interval defining prescribed initial and final configurations. The extended Hamilton's principle simply extends this idea to systems with non-conservative forces:

$$\delta \int_{t_1}^{t_2} (T - V + W)dt = 0 \tag{4.19}$$

and

$$
\begin{aligned}
T &= \int_D \frac{1}{2}\rho\{\dot{u}_s\}^T \{\dot{u}_s\}dD \\
V &= \int_D v\,dD \\
W &= \int_D \{b\}^T\{u_s - u_g\}dD + \int_S \{t\}^T\{u_s - u_g\}dS
\end{aligned}
\tag{4.20}
$$

65

where δ is the variational operator, T is the kinetic energy, V is the elastic potential (strain) energy, W is the work done by non-conservative forces, ρ is the mass density of the structure, v is the strain energy density, $\{b\}$ is the body force vector, $\{t\}$ is the surface traction vector, $\{u_s\}$ is the displacement vector of the structure, $\{u_g\}$ is the displacement vector of the grip/boundary (assumed uniform over the boundary to allow for base excitation of the structure through a fixture), D indicates the domain (volume) of the structure, and S indicates the surface of the structure. The displacement of the structure relative to the boundary can be expressed as

$$\{u\} = \{u_s - u_g\} \tag{4.21}$$

such that the energy terms can be rewritten in terms of the relative displacements:

$$T = \int_D \frac{1}{2}\rho\{\dot{u} + \dot{u}_g\}^T\{\dot{u} + \dot{u}_g\}dD$$

$$V = \int_D v\,dD \tag{4.22}$$

$$W = \int_D \{b\}^T\{u\}dD + \int_S \{t\}^T\{u\}dS$$

Consideration is restricted to a panel-type structure subjected to a steady-state thermal excitation and mechanical excitation consisting of surface pressure, out-of-plane concentrated forces, and/or inertial loading. The following assumptions are made for the development of the governing equations:

1. Body forces other than inertia are negligible.
2. The structure is in a state of plane stress.
3. von Kármán deformation relations are valid.
4. Linear elastic material properties are valid.

Assumptions 1 and 4, and the above-mentioned restrictions allow the potential energy and non-conservative work terms to be simplified as follows.

$$V = \int_D \frac{1}{2}\{\sigma\}^T\{\epsilon\}_M dD = \int_D \frac{1}{2}\{\epsilon\}_M^T\{\sigma\}dD$$

$$W = \int_S \left[pw + \sum_{i=1}^{N_f} f_i'w\,\delta(\{x\} - \{x\}_i)\right]dS \tag{4.23}$$

where $\{\sigma\}$ and $\{\epsilon\}_M$ are the stress and mechanical strain vectors, respectively, w is the out-of-plane displacement of the structure, p is the surface pressure, f_i' are concentrated forces applied normal to the plane of the structure, N_f is the number of concentrated forces, $\{x\}$ is the coordinate vector in the plane of the structure, $\{x\}_i$ designates the point(s) of concentrated force application, and $\delta(\{x\} - \{x\}_i)$ is a spatial Dirac delta function defined by

$$\delta(\{x\} - \{x\}_i) = 0 \qquad \text{for} \qquad \{x\} \neq \{x\}_i \tag{4.24}$$

Assumptions 2 and 3 allow the constitutive relations for a single lamina to be written as shown in the previous chapter, equation (2.26):

$$\{\sigma\}_k = [Q]_k(\{\epsilon\}_k - \{\epsilon\}_{Tk})$$

$$= [Q]_k(\{\epsilon^0\} + z\{\kappa\} - \int_{T_0}^{T} \{\alpha(\tau)\}_k dT) \qquad (4.25)$$

Recall that the mechanical strain is equal to the difference between the total strain and the thermal strain ($\{\epsilon\}_M = \{\epsilon\} - \{\epsilon\}_T$). Substituting this expression into the form for the strain energy in equation (4.23) gives

$$V = \int_S \int_{-\frac{h}{2}}^{\frac{h}{2}} \frac{1}{2}\left(\{\epsilon\}_k^T - \{\epsilon\}_{Tk}^T\right)[Q]_k(\{\epsilon\}_k - \{\epsilon\}_{Tk})dD$$

$$= \int_S \int_{-\frac{h}{2}}^{\frac{h}{2}} \frac{1}{2}\left(\{\epsilon\}_k^T [\bar{Q}]_k \{\epsilon\}_k - 2\{\epsilon\}_k^T [\bar{Q}]_k \{\epsilon\}_{Tk} - \{\epsilon\}_{Tk}^T [\bar{Q}]_k \{\epsilon\}_{Tk}\right)dD \qquad (4.26)$$

Commuting the variation and integration operations in equation (4.19) results in the following expression for Hamilton's principle.

$$\int_{t_1}^{t_2} (\delta T - \delta V + \delta W)dt = 0 \qquad (4.27)$$

Consider the first variation of the kinetic energy, from equations (4.22):

$$\delta T = \delta \int_D \frac{1}{2}\rho\{\dot{u} + \dot{u}_g\}^T \{\dot{u} + \dot{u}_g\}dD \qquad (4.28)$$

Commuting the variation and integration operations again and integrating through the thickness results in the expression

$$\delta T = \int_D \frac{1}{2}\rho\left(\{\delta\dot{u}\}^T\{\dot{u} + \dot{u}_g\} + \{\dot{u} + \dot{u}_g\}^T\{\delta\dot{u}\}\right)dD$$

$$= \int_D \rho\{\delta\dot{u}\}^T\{\dot{u} + \dot{u}_g\}dD \qquad (4.29)$$

$$= \int_S \rho h\{\delta\dot{u}\}^T\{\dot{u} + \dot{u}_g\}dS$$

where $\delta\dot{u}_g$ has been omitted because the instantaneous constraints are assumed to be held constant during application of a virtual displacement to achieve the varied path. Similarly, the first

67

variation of the strain energy in equation (4.26) can be written as

$$\delta V = \delta \int_S \int_{-\frac{h}{2}}^{\frac{h}{2}} \frac{1}{2}\left(\{\epsilon\}_k^T [Q]_k \{\epsilon\}_k - 2\{\epsilon\}_k^T [Q]_k \{\epsilon\}_{Tk} - \{\epsilon\}_{Tk}^T [Q]_k \{\epsilon\}_{Tk}\right) dD$$

$$= \int_S \int_{-\frac{h}{2}}^{\frac{h}{2}} \frac{1}{2}\left(\{\delta\epsilon\}_k^T [Q]_k \{\epsilon\}_k + \{\epsilon\}_k^T [Q]_k \{\delta\epsilon\}_k - 2\{\delta\epsilon\}_k^T [\bar{Q}]_k \{\epsilon\}_{Tk}\right) dD \qquad (4.30)$$

$$= \int_S \int_{-\frac{h}{2}}^{\frac{h}{2}} \left(\{\delta\epsilon\}_k^T [Q]_k \{\epsilon\}_k - \{\delta\epsilon\}_k^T [Q]_k \{\epsilon\}_{Tk}\right) dD$$

Incorporating the von Kármán strain-displacement relations, equations (2.32), gives

$$\delta V = \int_S \int_{-\frac{h}{2}}^{\frac{h}{2}} \left[\left(\{\delta\epsilon^0\}^T + z\{\delta\kappa\}^T \right)[\bar{Q}]_k \left(\{\epsilon^0\} + z\{\kappa\}\right) - \left(\{\delta\epsilon^0\}^T + z\{\delta\kappa\}^T\right)[\bar{Q}]_k \int_{T_0}^{T} \{\alpha(\tau)\}_k d\tau \right] dD$$

$$(4.31)$$

Expanding the integrand results in

$$\delta V = \int_S \int_{-\frac{h}{2}}^{\frac{h}{2}} \left[\{\delta\epsilon^0\}^T [Q]_k \{\epsilon^0\} + z\{\delta\epsilon^0\}^T [\bar{Q}]_k \{\kappa\} + z\{\delta\kappa\}^T [Q]_k \{\delta\epsilon^0\} + z^2\{\delta\kappa\}^T [Q]_k \{\delta\kappa\} \right.$$

$$\left. - \{\delta\epsilon^0\}^T [Q]_k \int_{T_0}^{T} \{\alpha(\tau)\}_k d\tau - z\{\delta\kappa\}^T [Q]_k \int_{T_0}^{T} \{\alpha(\tau)\}_k d\tau \right] dD$$

$$(4.32)$$

and integrating through the thickness generates the stress resultant notation from equations (2.35). The following form for the first variation of the strain energy results.

$$\delta V = \int_S \left(\{\delta\epsilon^0\}^T [A]\{\epsilon^0\} + \{\delta\epsilon^0\}^T [B]\{\kappa\} + \{\delta\kappa\}^T [B]\{\epsilon^0\} + \{\delta\kappa\}^T [D]\{\kappa\} \right.$$

$$(4.33)$$

$$\left. - \{\delta\epsilon^0\}^T \{N_{\Delta T}\} - \{\delta\kappa\}^T \{M_{\Delta T}\} \right) dS$$

Finally, referring to equation (4.23) the first variation of the non-conservative work has the form

$$\delta W = \delta \int_S \left[pw + \sum_{i=1}^{N_f} f_i' w \, \delta(\{x\} - \{x\}_i) \right] dS$$

$$(4.34)$$

$$= \int_S \left[p\delta w + \sum_{i=1}^{N_f} f_i' \delta w \, \delta(\{x\} - \{x\}_i) \right] dS$$

68

Recall that $\delta(\{x\} - \{x\}_i)$ is a spatial Dirac delta function and shouldn't be confused with the variational operator.

The form of Hamilton's principle given in equation (4.27) can now be rewritten by substituting from equations (4.29), (4.33), and (4.34):

$$\int_{t_1}^{t_2} \left[\int_S \{\rho h \{\delta u\}^T \{\ddot{u} + \ddot{u}_g\} - \{\delta \epsilon^0\}^T [A]\{\epsilon^0\} - \{\delta \epsilon^0\}^T [B]\{\kappa\} - \{\delta \kappa\}^T [B]\{\epsilon^0\} - \{\delta \kappa\}^T [D]\{\kappa\} \right.$$

$$\left. + \{\delta \epsilon^0\}^T \{N_{\Delta T}\} + \{\delta \kappa\}^T \{M_{\Delta T}\} + p \delta w + \sum_{i=1}^{N_f} f_i' \delta w \, \delta(\{x\} - \{x\}_i)\} dS \right] dt = 0$$

(4.35)

The first term can be integrated by parts to give

$$\int_S \rho h \{\delta u\}^T \Big|_{t_1}^{t_2} \{\dot{u} + \dot{u}_g\} dS - \int_{t_1}^{t_2} \left[\int_S \{\rho h \{\delta u\}^T \{\ddot{u} + \ddot{u}_g\} - \{\delta \epsilon^0\}^T [A]\{\epsilon^0\} - \{\delta \epsilon^0\}^T [B]\{\kappa\} \right.$$

$$- \{\delta \kappa\}^T [B]\{\epsilon^0\} - \{\delta \kappa\}^T [D]\{\kappa\} + \{\delta \epsilon^0\}^T \{N_{\Delta T}\}$$

$$\left. + \{\delta \kappa\}^T \{M_{\Delta T}\} + p \delta w + \sum_{i=1}^{N_f} f_i' \delta w \, \delta(\{x\} - \{x\}_i)\} dS \right] dt = 0$$

(4.36)

Note that the first term in the latter equation is equal to zero because the integrand vanishes as the virtual displacements $\{\delta u\}$ are defined to be zero at times t_1 and t_2.

The expression given in equation (4.36) resulted from application of extended Hamilton's principle to the energy terms associated with the entire structure. The same approach is applicable to any portion of the structure, e.g., finite element, due to physical constraints. Therefore, the following development will focus on the element level. Recall that expressions for the midplane membrane strains $\{\epsilon^0\}$ and curvatures $\{\kappa\}$ were given in terms of element degrees of freedom in equations (4.17). The variation of the midplane strain within the element would then be written as

$$\{\delta \epsilon^0\} = [C_m]\{\delta a_m\} + \frac{1}{2}[\delta \theta][C_\theta]\{a_b\} + \frac{1}{2}[\theta][C_\theta]\{\delta a_b\}$$

(4.37)

or

$$\{\delta \epsilon^0\} = [C_m]\{\delta a_m\} + \frac{1}{2}[\delta \theta]\{G\} + \frac{1}{2}[\theta]\{\delta G\}$$

(4.38)

by substituting from equation (4.13). The components of the second and third terms can be examined as follows

$$\frac{1}{2}[\delta \theta][C_\theta]\{a_b\} + \frac{1}{2}[\theta][C_\theta]\{\delta a_b\} = \frac{1}{2}\left(\delta \begin{bmatrix} w,_x & 0 \\ 0 & w,_y \\ w,_y & w,_x \end{bmatrix}\right)\begin{Bmatrix} w,_x \\ w,_y \end{Bmatrix} + \frac{1}{2}\left(\begin{bmatrix} w,_x & 0 \\ 0 & w,_y \\ w,_y & w,_x \end{bmatrix}\right)\delta\begin{Bmatrix} w,_x \\ w,_y \end{Bmatrix}$$

$$= \frac{1}{2}\begin{Bmatrix} \delta w,_x \, w,_x \\ \delta w,_y \, w,_y \\ \delta w,_y \, w,_x + \delta w,_x \, w,_y \end{Bmatrix} + \frac{1}{2}\begin{Bmatrix} w,_x \, \delta w,_x \\ w,_y \, \delta w,_y \\ w,_y \, \delta w,_x + w,_x \, \delta w,_y \end{Bmatrix}$$

(4.39)

69

It can be seen that

$$\frac{1}{2}[\delta\theta][C_\theta]\{a_b\} + \frac{1}{2}[\theta][C_\theta]\{\delta a_b\} = \frac{1}{2}[\theta]\{\delta G\} + \frac{1}{2}[\theta]\{\delta G\}$$
$$= [\theta]\{\delta G\}$$
$$= [\theta][C_\theta]\{\delta a_b\}$$

(4.40)

So, the final forms for the membrane strain and curvature vectors in terms of element degrees of freedom are as follows.

$$\{\delta\epsilon^0\} = [C_m]\{\delta a_m\} + [\theta][C_\theta]\{\delta a_b\}$$
$$\{\delta\kappa\} = [C_b]\{\delta a_b\}$$

(4.41)

The structural displacement-related quantities in equation (4.36) can be written in terms of the element degrees of freedom from equation (4.5):

$$\{\delta u\}^T\{\ddot{u} + \ddot{u}_g\} = \{\delta a_{mb}\}^T[L_{uvw}]^T[L_{uvw}]\{\ddot{a}_{mb} + \ddot{u}_g\}$$

$$= \left\{\begin{matrix}\delta a_m\\\delta a_b\end{matrix}\right\}^T\begin{bmatrix}\{L_u\} & \{L_v\} & 0\\0 & 0 & \{L_w\}\end{bmatrix}\begin{bmatrix}\lfloor L_u\rfloor & 0\\\lfloor L_v\rfloor & 0\\0 & \lfloor L_w\rfloor\end{bmatrix}\left\{\begin{matrix}\ddot{a}_m\\\ddot{a}_b\end{matrix} + \begin{matrix}0\\\ddot{u}_g\end{matrix}\right\}$$

$$= \left\{\begin{matrix}\delta a_m\\\delta a_b\end{matrix}\right\}^T\begin{bmatrix}\{L_u\}\{L_u\}^T + \{L_v\}\{L_v\}^T & 0\\0 & \{L_w\}\{L_w\}^T\end{bmatrix}\left\{\begin{matrix}\ddot{a}_m\\\ddot{a}_b\end{matrix} + \begin{matrix}0\\\ddot{u}_g\end{matrix}\right\}$$

$$= \{\delta a_m\}^T\left(\{L_u\}\{L_u\}^T + \{L_v\}\{L_v\}^T\right)\{\ddot{a}_m\} + \{\delta a_b\}^T\{L_w\}\{L_w\}^T\{\ddot{a}_b + \ddot{u}_g\}$$

(4.42)

and

$$\delta w = \{L_w\}^T\{\delta a_b\} = \{\delta a_b\}^T\{L_w\}$$

(4.43)

where it has been assumed that the base acceleration component $\ddot{u}_g$ is normal to the plane of the structure. The expressions in equations (4.41), (4.42), and (4.43) can be substituted into Hamilton's principle, equation (4.36), to give

$$\int_{t_1}^{t_2}\left[\int_{A_e}\{\rho h(\{\delta a_m\}^T\left(\{L_u\}\{L_u\}^T + \{L_v\}\{L_v\}^T\right)\{\ddot{a}_m\} + \{\delta a_b\}^T\{L_w\}\{L_w\}^T\{\ddot{a}_b + \ddot{u}_g\})\right.$$

$$+ ([C_m]\{\delta a_m\} + [\theta][C_\theta]\{\delta a_b\})^T[A]([C_m]\{a_m\} + \frac{1}{2}[\theta][C_\theta]\{a_b\})$$

$$+ ([C_m]\{\delta a_m\} + [\theta][C_\theta]\{\delta a_b\})^T[B][C_b]\{a_b\} + \{\delta a_b\}^T[C_b]^T[B]([C_m]\{a_m\} + \frac{1}{2}[\theta][C_\theta]\{a_b\})$$

$$+ \{\delta a_b\}^T[C_b]^T[D][C_b]\{a_b\} - ([C_m]\{\delta a_m\} + [\theta][C_\theta]\{\delta a_b\})^T\{N_{\Delta T}\} - \{\delta a_b\}^T[C_b]^T\{M_{\Delta T}\}$$

$$\left. - p\delta w - \sum_{i=1}^{n_f} f_i^t\delta w\,\delta(\{x\} - \{x\}_i)\}dA_e\right]dt = 0$$

(4.44)

where the spatial integration has been limited to the area A_e of the finite element in concern and the number of concentrated forces in the summation has been limited to that number n_f within

70

the element area. Expanding the integrand results in the following expression.

$$\int_{t_1}^{t_2} \left[\int_{A_e} \left\{ \rho h \left[\{\delta a_m\}^T \left(\{L_u\}\{L_u\}^T + \{L_v\}\{L_v\}^T \right) \{\ddot{a}_m\} + \{\delta a_b\}^T \{L_w\}\{L_w\}^T \{\ddot{a}_b + \ddot{u}_g\} \right] \right. \right.$$

$$+ \{\delta a_m\}^T [C_m]^T [A][C_m]\{a_m\} + \frac{1}{2}\{\delta a_m\}^T [C_m]^T [A][\theta][C_\theta]\{a_b\}$$

$$+ \{\delta a_b\}^T [C_\theta]^T [\theta]^T [A][C_m]\{a_m\} + \frac{1}{2}\{\delta a_b\}^T [C_\theta]^T [\theta]^T [A][\theta][C_\theta]\{a_b\}$$

$$+ \{\delta a_m\}^T [C_m]^T [B][C_b]\{a_b\} + \{\delta a_b\}^T [C_\theta]^T [\theta]^T [B][C_b]\{a_b\} + \{\delta a_b\}^T [C_b]^T [B][C_m]\{a_m\}$$

$$+ \frac{1}{2}\{\delta a_b\}^T [C_b]^T [B][\theta][C_\theta]\{a_b\} + \{\delta a_b\}^T [C_b]^T [D][C_b]\{a_b\} - \{\delta a_m\}^T [C_m]^T \{N_{\Delta T}\}$$

$$- \{\delta a_b\}^T [C_\theta]^T [\theta]^T \{N_{\Delta T}\} - \{\delta a_b\}^T [C_b]^T \{M_{\Delta T}\}$$

$$- \{\delta a_b\}^T \{L_w\}p - \{\delta a_b\}^T \{L_w\} \sum_{i=1}^{n_f} f_i' \delta w \, \delta(\{x\} - \{x\}_i) \} dA_e \right] dt = 0$$

(4.45)

Consider the product $[\theta]^T \{N\}$. Expanding the product in terms of the matrix components results in the following identity.

$$[\theta]^T \{N\} = \begin{bmatrix} w_{,x} & 0 & w_{,y} \\ 0 & w_{,y} & w_{,x} \end{bmatrix} \begin{Bmatrix} N_x \\ N_y \\ N_{xy} \end{Bmatrix} = \begin{bmatrix} N_x & N_{xy} \\ N_{xy} & N_y \end{bmatrix} \begin{Bmatrix} w_{,x} \\ w_{,y} \end{Bmatrix}$$

$$= [N]\{G\}$$

$$= [N][C_\theta]\{a_b\}$$

(4.46)

This identity is useful for further manipulation of equation (4.45). Note that the terms

$$\{\delta a_b\}^T [C_\theta]^T [\theta]^T [A][C_m]\{a_m\} \quad \text{and} \quad \{\delta a_b\}^T [C_\theta]^T [\theta]^T [B][C_b]\{a_b\} \quad (4.47)$$

in equation (4.45) do not have symmetric counterparts. However, noting that from equations (4.18) $[A][C_m]\{a_m\} = \{N_m\}$, the former of the two terms in equation (4.47) can be split as follows

$$\{\delta a_b\}^T [C_\theta]^T [\theta]^T [A][C_m]\{a_m\} = \frac{1}{2}\{\delta a_b\}^T [C_\theta]^T [\theta]^T [A][C_m]\{a_m\}$$

$$+ \frac{1}{2}\{\delta a_b\}^T [C_\theta]^T [\theta]^T \{N_m\}$$

(4.48)

and the identity in equation (4.46) can be employed to give

$$\{\delta a_b\}^T [C_\theta]^T [\theta]^T [A][C_m]\{a_m\} = \frac{1}{2}\{\delta a_b\}^T [C_\theta]^T [\theta]^T [A][C_m]\{a_m\}$$

$$+ \frac{1}{2}\{\delta a_b\}^T [C_\theta]^T [N_m][C_\theta]\{a_b\}$$

(4.49)

Now, the first half of the term has a symmetric counterpart in equation (4.45) and the second half is symmetric itself. Similarly, noting that $[B][C_b]\{a_b\} = \{N_b\}$, the latter of the two terms

71

in equation (4.47) can be split as follows

$$\{\delta a_b\}^T [C_\theta]^T [\theta]^T [B][C_b]\{a_b\} = \frac{1}{2}\{\delta a_b\}^T [C_\theta]^T [\theta]^T [B][C_b]\{a_b\}$$
$$+ \frac{1}{2}\{\delta a_b\}^T [C_\theta]^T [\theta]^T \{N_b\} \tag{4.50}$$

and the identity in equation (4.46) can be employed to give

$$\{\delta a_b\}^T [C_\theta]^T [\theta]^T [B][C_b]\{a_b\} = \frac{1}{2}\{\delta a_b\}^T [C_\theta]^T [\theta]^T [B][C_b]\{a_b\}$$
$$+ \frac{1}{2}\{\delta a_b\}^T [C_\theta]^T [N_b][C_\theta]\{a_b\} \tag{4.51}$$

So, both terms in equation (4.47) have been transformed into symmetric forms. Finally, the identity in equation (4.46) can be used to rewrite another term in equation (4.45) as follows.

$$\{\delta a_b\}^T [C_\theta]^T [\theta]^T \{N_{\Delta T}\} = \{\delta a_b\}^T [C_\theta]^T [N_{\Delta T}][C_\theta]\{a_b\} \tag{4.52}$$

Substituting the expressions from equations (4.49), (4.51), and (4.52) into Hamilton's principle for the element, equation (4.45), and separating terms involving $\{\delta a_m\}^T$ and $\{\delta a_b\}^T$ results in the following expression.

$$\int_{t_1}^{t_2} \left[\int_A \{ \{\delta a_m\}^T [\rho h \left(\{L_u\}\{L_u\}^T + \{L_v\}\{L_v\}^T \right) \{\ddot{a}_m\} + [C_m]^T [A][C_m]\{a_m\}$$

$$+ \frac{1}{2}[C_m]^T [A][\theta][C_\theta]\{a_b\} + [C_m]^T [B][C_b]\{a_b\} - [C_m]^T \{N_{\Delta T}\}]$$

$$+ \{\delta a_b\}^T [\rho h \{L_w\}\{L_w\}^T \{\ddot{a}_b + \ddot{u}_g\} + \frac{1}{2}[C_\theta]^T [\theta]^T [A][C_m]\{a_m\} + \frac{1}{2}[C_\theta]^T [N_m][C_\theta]\{a_b\}$$

$$+ \frac{1}{2}[C_\theta]^T [\theta]^T [A][\theta][C_\theta]\{a_b\} + [C_\theta]^T [B][C_m]\{a_m\} + \frac{1}{2}[C_\theta]^T [\theta]^T [B][C_b]\{a_b\}$$

$$+ \frac{1}{2}[C_\theta]^T [N_b][C_\theta]\{a_b\} + \frac{1}{2}[C_b]^T [B][\theta][C_\theta]\{a_b\} + [C_b]^T [D][C_b]\{a_b\} - [C_\theta]^T [N_{\Delta T}][C_\theta]\{a_b\}$$

$$- [C_b]^T \{M_{\Delta T}\} - \{L_w\}p - \{L_w\} \sum_{i=1}^{n_f} f_i' \delta w\, \delta(\{x\} - \{x\}_i)\} dA_e \right] dt = 0 \tag{4.53}$$

The virtual displacements $\{\delta a_m\}$ and $\{\delta a_b\}$ are arbitrary and independent, so the corresponding components of the integrand in equation (4.53) must each equal zero. The two resulting equations can be written in matrix form:

$$\begin{bmatrix} m_b & 0 \\ 0 & m_m \end{bmatrix} \begin{Bmatrix} \ddot{a}_b \\ \ddot{a}_m \end{Bmatrix} + \left(\begin{bmatrix} k_b & k_{bm} \\ k_{mb} & k_m \end{bmatrix} - \begin{bmatrix} k_{\Delta T} & 0 \\ 0 & 0 \end{bmatrix} + \frac{1}{2}\begin{bmatrix} n1_b + (n1_b)_B & n1_{bm} \\ n1_{mb} & 0 \end{bmatrix} \right.$$

$$\left. + \frac{1}{3}\begin{bmatrix} n2_b & 0 \\ 0 & 0 \end{bmatrix} \right) \begin{Bmatrix} a_b \\ a_m \end{Bmatrix} = \begin{Bmatrix} p_b(t) \\ 0 \end{Bmatrix} + \begin{Bmatrix} f_b(t) \\ 0 \end{Bmatrix} + \begin{Bmatrix} p_{b\Delta T} \\ p_{m\Delta T} \end{Bmatrix} - \begin{bmatrix} m_b & 0 \\ 0 & m_m \end{bmatrix} \begin{Bmatrix} \ddot{u}_g \\ 0 \end{Bmatrix} \tag{4.54}$$

where the element matrices are as follows.

$$[m_b] = \int_{A_e} \rho h \{L_w\}\{L_w\}^T dA_e \qquad [m_m] = \int_{A_e} \rho h \left(\{L_u\}\{L_u\}^T + \{L_v\}\{L_v\}^T\right) dA_e$$

$$[k_b] = \int_{A_e} [C_b]^T [D][C_b] dA_e \qquad [k_m] = \int_{A_e} [C_m]^T [A][C_m] dA_e$$

$$[k_{bm}] = \int_{A_e} [C_b]^T [B][C_m] dA_e \qquad [k_{mb}] = [k_{bm}]^T$$

$$[k_{\Delta T}] = \int_{A_e} [C_\theta]^T [N_{\Delta T}][C_\theta] dA_e \qquad [n1_b] = \int_{A_e} [C_\theta]^T [N_m][C_\theta] dA_e$$

$$[(n1_b)_B] = \int_{A_e} ([C_\theta]^T [\theta]^T [B][C_b] + [C_\theta]^T [N_b][C_\theta] + [C_b]^T [B][\theta][C_\theta]) dA_e$$

$$[n1_{bm}] = \int_{A_e} [C_\theta]^T [\theta]^T [A][C_m] dA_e \qquad [n1_{mb}] = [n1_{bm}]^T$$

$$[n2_b] = \frac{3}{2} \int_{A_e} [C_\theta]^T [\theta]^T [A][\theta][C_\theta] dA_e$$

$$\{p_b(t)\} = \int_{A_e} p(x,y,t)\{L_w\} dA_e \qquad \{f_b(t)\} = \sum_{i=1}^{n_f} \int_{A_e} f_i'(t)\,\delta(\{x\} - \{x\}_i)\{L_w\} dA_e$$

$$\{p_{b\Delta T}\} = \int_{A_e} [C_b]^T \{M_{\Delta T}\} dA_e \qquad \{p_{m\Delta T}\} = \int_{A_e} [C_b]^T \{N_{\Delta T}\} dA_e$$

$$(4.55)$$

The element area integrations can be conveniently and efficiently evaluated though Gauss-Legendre numerical integration, as demonstrated in Appendix B. The governing equations for each element can be assembled to form the Euler-Lagrange equations for the entire system:

$$\begin{bmatrix} M_b & 0 \\ 0 & M_m \end{bmatrix}\left\{\begin{array}{c} \ddot{A}_b \\ \ddot{A}_m \end{array}\right\} + \left(\begin{bmatrix} K_b & K_B \\ K_B^T & K_m \end{bmatrix} - \begin{bmatrix} K_{\Delta T} & 0 \\ 0 & 0 \end{bmatrix}\right.$$
$$\left. + \frac{1}{2}\begin{bmatrix} N1_b + (N1_b)_B & N1_{bm} \\ N1_{mb} & 0 \end{bmatrix} + \frac{1}{3}\begin{bmatrix} N2_b & 0 \\ 0 & 0 \end{bmatrix}\right)\left\{\begin{array}{c} A_b \\ A_m \end{array}\right\} \qquad (4.56)$$
$$= \left\{\begin{array}{c} P_b(t) \\ 0 \end{array}\right\} + \left\{\begin{array}{c} F_b(t) \\ 0 \end{array}\right\} + \left\{\begin{array}{c} P_{b\Delta T} \\ P_{m\Delta T} \end{array}\right\} - \begin{bmatrix} M_b & 0 \\ 0 & M_m \end{bmatrix}\left\{\begin{array}{c} \ddot{U}_g \\ 0 \end{array}\right\}$$

or

$$[M]\{\ddot{A}\} + ([K] - [K_{\Delta T}] + \frac{1}{2}[N1] + \frac{1}{3}[N2])\{A\} = \{P(t)\} + \{F(t)\} + \{P_{\Delta T}\} - [M]\{\ddot{U}_g(t)\}$$
$$(4.57)$$

where $[M]$ and $[K]$ are the usual system mass and linear stiffness matrices; $[K_{\Delta T}]$ is the geometric stiffness matrix due to the thermal in-plane force vector $\{N_{\Delta T}\}$; $[N1]$ and $[N2]$ are the first- and second-order nonlinear stiffness matrices which depend linearly and quadratically

73

upon displacement $\{A\}$, respectively; $\{P(t)\}$ is the surface pressure excitation load vector, $\{F(t)\}$ is the concentrated force excitation load vector, $\{P_{\Delta T}\}$ is the thermal force vector, and $\{\ddot{U}_g(t)\}$ is the inertial excitation base acceleration vector. The subscripts b and m denote bending and membrane components, respectively, and the subscript B indicates that the corresponding stiffness matrix is due to the laminate bending-membrane coupling stiffness matrix $[B]$. Note that the stiffness matrices $[K]$, $[K_{\Delta T}]$, $[N1]$, $[N2]$ and the thermal force vector $\{P_{\Delta T}\}$ are all temperature dependent.

4.2.1 Separation of Static and Dynamic Components

Recall that the system is restricted to be thermally steady-state. It is assumed that the structure will undergo small dynamic motions about a stable static shape (flat or thermally buckled) so that the system degrees of freedom will consist of static and dynamic components

$$\{A\} = \{A\}_s + \{A\}_d \tag{4.58}$$

such that

$$\{A\}_d << \{A\}_s \rightarrow \{A\}_d^2 \approx 0 \tag{4.59}$$

Consider the effect, on the element level, of equation (4.58) on the form of $[\theta]$ in equation (4.12):

$$[\theta] = [\theta]_s + [\theta]_d = \begin{bmatrix} w_{s,x} & 0 \\ 0 & w_{s,y} \\ w_{s,y} & w_{s,x} \end{bmatrix} + \begin{bmatrix} w_{d,x} & 0 \\ 0 & w_{d,y} \\ w_{d,y} & w_{d,x} \end{bmatrix} \tag{4.60}$$

It can be seen from equations (4.55) that the nonlinear stiffness matrices, $[n1]$ and $[n2]$, are thus affected. For example,

$$
\begin{aligned}
[n1_{bm}] &= \int_S [C_\theta]^T [\theta]^T [A][C_m] dS \\
&= \int_S [C_\theta]^T ([\theta]_s^T + [\theta]_d^T)[A][C_m] dS \\
&= \int_S [C_\theta]^T [\theta]_s^T [A][C_m] dS + \int_S [C_\theta]^T [\theta]_d^T [A][C_m] dS \\
&= [n1_{bm}]_s + [n1_{bm}]_d
\end{aligned}
\tag{4.61}
$$

Similarly,

$$[n1_{mb}] = [n1_{mb}]_s + [n1_{mb}]_d \tag{4.62}$$

Note that the resultant forces due to membrane and bending strain, equations (4.18), are also affected. So, these forces can be written as

$$\{N_m\} = \{N_m\}_s + \{N_m\}_d \quad \text{and} \quad \{N_b\} = \{N_b\}_s + \{N_b\}_d \tag{4.63}$$

or

$$[N_m] = [N_m]_s + [N_m]_d \quad \text{and} \quad [N_b] = [N_b]_s + [N_b]_d \tag{4.64}$$

Therefore,

$$[n1_b] = [n1_b]_s + [n1_b]_d \quad \text{and} \quad [(n1_b)_B] = [(n1_b)_B]_s + [(n1_b)_B]_d \quad (4.65)$$

Finally, the second-order nonlinear element stiffness matrix takes the form

$$
\begin{aligned}
[n2_b] &= \frac{3}{2} \int_S [C_\theta]^T [\theta]^T [A][\theta][C_\theta] dS \\
&= \frac{3}{2} \int_S [C_\theta]^T ([\theta]_s^T + [\theta]_d^T)[A]([\theta]_s + [\theta]_d)[C_\theta] dS \\
&= \frac{3}{2} \int_S ([C_\theta]^T [\theta]_s^T [A][\theta]_s [C_\theta] + [C_\theta]^T [\theta]_s^T [A][\theta]_d [C_\theta] \\
&\qquad + [C_\theta]^T [\theta]_d^T [A][\theta]_s [C_\theta] + [C_\theta]^T [\theta]_d^T [A][\theta]_d [C_\theta]) dS \\
&= [n2_b]_s + [n2_b]_{sd} + [n2_b]_{ds} + [n2_b]_d
\end{aligned} \quad (4.66)
$$

This distributive property conveys to the system matrices:

$$
\begin{aligned}
[N1] &= [N1]_s + [N1]_d \\
[N2] &= [N2]_s + [N2]_{sd} + [N2]_{ds} + [N2]_d
\end{aligned} \quad (4.67)
$$

and the system equations of motion, equation (4.57), become

$$
\begin{aligned}
[M]\{\ddot{A}\}_d &+ ([K] - [K_{\Delta T}])(\{A\}_s + \{A\}_d) + \frac{1}{2}([N1]_s + [N1]_d)(\{A\}_s + \{A\}_d) \\
&+ \frac{1}{3}([N2]_s + [N2]_{sd} + [N2]_{ds} + [N2]_d)(\{A\}_s + \{A\}_d) \\
&= \{P(t)\} + \{F(t)\} + \{P_{\Delta T}\} - [M]\{\ddot{r}_g\}
\end{aligned} \quad (4.68)
$$

It is desirable to separate the equations governing the static and dynamic response. However, there are terms which couple the static and dynamic displacements. The term $[N2]_d$ can be neglected because it is second order with respect to $\{A\}_d$. The form of other coupling terms can be clarified as follows.

Consider the product of the first-order nonlinear dynamic stiffness and the static displacement vector. On the element level, referring to equations (4.55), the four components of this matrix can be manipulated as follows in discussions designated by numbers 1) through 4).

1) The product of the first-order dynamic bending stiffness and static bending nodal degrees of freedom has the form

$$[n1_b]_d \{a_b\}_s = \int_S [C_\theta]^T [N_m]_d [C_\theta] dS \{a_b\}_s \quad (4.69)$$

This integrand can be rewritten by noting the following

$$
\begin{aligned}
[N_m]_d [C_\theta]\{a_b\}_s &= [\theta]_s^T \{N_m\}_d \\
&= [\theta]_s^T [A][C_m]\{a_m\}_d
\end{aligned} \quad (4.70)
$$

75

so the expression given by equation (4.69) can be rewritten as

$$[n1_d]_d\{a_b\}_s = \int_S [C_\theta]^T [\theta]_s^T [A][C_m]dS\{a_m\}_d \tag{4.71}$$

The form of the integral in equation (4.71) can be immediately recognized as the product of the first-order static coupling stiffness and the dynamic membrane displacements. Therefore, the expression in equation (4.71) can be written as follows.

$$[n1_b]_d\{a_b\}_s = [n1_{bm}]_s\{a_m\}_d \tag{4.72}$$

2a) The product of the first-order dynamic bending stiffness due to the $[B]$ matrix and static bending nodal degrees of freedom has the form

$$[(n1_b)_B]_d\{a_b\}_s = \int_S ([C_\theta]^T [\theta]_d^T [B][C_b] + [C_\theta]^T [N_b]_d[C_\theta] + [C_b]^T [B][\theta]_d[C_\theta])dS\{a_b\}_s \tag{4.73}$$

but recall from equations (4.18) and (4.46) that the substitutions

$$[B][C_b]\{a_b\}_s = \{N_b\}_s, \quad \text{and} \quad [\theta]_d^T \{N_b\}_s = [N_b]_s[C_\theta]\{a_b\}_d \tag{4.74}$$

can be made. It follows that the expression given in equation (4.73) can be rewritten as

$$[(n1_b)_B]_d\{a_b\}_s = \int_S [C_\theta]^T [N_b]_s[C_\theta]dS\{a_b\}_d + \int_S [C_\theta]^T [N_b]_d[C_\theta]dS\{a_b\}_s$$
$$+ \int_S [C_b]^T [B][\theta]_d[C_\theta]dS\{a_b\}_s \tag{4.75}$$

2b) Conversely, the product of the first-order static bending stiffness due to the $[B]$ matrix and dynamic bending nodal degrees of freedom has the form

$$[(n1_b)_B]_s\{a_b\}_d = \int_S ([C_\theta]^T [\theta]_s^T [B][C_b] + [C_\theta]^T [N_b]_s[C_\theta] + [C_b]^T [B][\theta]_s[C_\theta])dS\{a_b\}_d \tag{4.76}$$

but equations (4.18) and (4.46) allow the substitutions

$$[B][C_b]\{a_b\}_d = \{N_b\}_d \quad \text{and} \quad [\theta]_s^T \{N_b\}_d = [N_b]_d[C_\theta]\{a_b\}_s \tag{4.77}$$

It follows that equation (4.76) can be rewritten as

$$[(n1_b)_B]_s\{a_b\}_d = \int_S [C_\theta]^T [N_b]_d[C_\theta]dS\{a_b\}_s + \int_S [C_\theta]^T [N_b]_s[C_\theta]dS\{a_b\}_d$$
$$+ \int_S [C_b]^T [B][\theta]_s[C_\theta]dS\{a_b\}_d \tag{4.78}$$

The first two terms of equations (4.75) and (4.78) are obviously identical, but the third term requires further investigation. Recall from equation (4.13) that $[\theta][C_\theta]\{a_b\} = [\theta]\{G\}$. Therefore, term three in equation (4.75) can be rewritten in terms of out-of-plane displacement derivatives:

$$[\theta]_d[C_\theta]\{a_b\}_s = [\theta]_d\{G\}_s = \begin{bmatrix} w_{d \cdot x} & 0 \\ 0 & w_{d \cdot y} \\ w_{d \cdot y} & w_{d \cdot x} \end{bmatrix} \begin{Bmatrix} w_{s \cdot x} \\ w_{s \cdot y} \end{Bmatrix} = \begin{Bmatrix} w_{d \cdot x}\, w_{s \cdot x} \\ w_{d \cdot y}\, w_{s \cdot y} \\ w_{d \cdot y}\, w_{s \cdot x} + w_{d \cdot x}\, w_{s \cdot y} \end{Bmatrix} \tag{4.79}$$

It is clear that the previous expression is the same as the following.

$$[\theta]_s[C_\theta]\{a_b\}_d = [\theta]_s\{G\}_d = \begin{bmatrix} w_{s \cdot x} & 0 \\ 0 & w_{s \cdot y} \\ w_{s \cdot y} & w_{s \cdot x} \end{bmatrix} \begin{Bmatrix} w_{d \cdot x} \\ w_{d \cdot y} \end{Bmatrix} = \begin{Bmatrix} w_{s \cdot x}\, w_{d \cdot x} \\ w_{s \cdot y}\, w_{d \cdot y} \\ w_{s \cdot y}\, w_{d \cdot x} + w_{s \cdot x}\, w_{d \cdot y} \end{Bmatrix} \tag{4.80}$$

Thus, the third term in equations (4.75) and (4.78) are identical, and the final result gives the following equality.

$$[(n1_b)B]_d\{a_b\}_s = [(n1_b)B]_s\{a_b\}_d \tag{4.81}$$

3) The product of the first-order dynamic coupling stiffness and the static membrane displacements has the form

$$[n1_{bm}]_d\{a_m\}_s = \int_S [C_\theta]^T[\theta]_d^T[A][C_m]dS\{a_m\}_s \tag{4.82}$$

Equations (4.18) and (4.46) allow the substitutions

$$[A][C_m]\{a_m\}_s = \{N_m\}_s \quad \text{and} \quad [\theta]_d^T\{N_m\}_s = [N_m]_s[C_\theta]\{a_b\}_d \tag{4.83}$$

So, equation (4.82) can be rewritten as

$$[n1_{bm}]_d\{a_m\}_s = \int_S [C_\theta]^T[N_m]_s^T[C_\theta]dS\{a_b\}_d \tag{4.84}$$

The form of the integral in equation (4.84) is easily recognized as the product of the first-order static bending stiffness and the dynamic bending nodal degrees of freedom. Thus, the final equality becomes

$$[n1_{bm}]_d\{a_m\}_s = [n1_b]_s\{a_b\}_d \tag{4.85}$$

4) The product of the first-order dynamic coupling stiffness and the static bending nodal degrees of freedom has the form

$$[n1_{mb}]_d\{a_b\}_s = \int_S [C_m]^T[A][\theta]_d[C_\theta]dS\{a_b\}_s \tag{4.86}$$

but recall from equation (4.13) that $[\theta][C_\theta]\{a_b\} = [\theta]\{G\}$. So, the analogous product in equation (4.86) can be written in terms of out-of-plane displacement derivatives:

$$[\theta]_d[C_\theta]\{a_b\}_s = [\theta]_d\{G\}_s = \begin{bmatrix} w_{d \cdot x} & 0 \\ 0 & w_{d \cdot y} \\ w_{d \cdot y} & w_{d \cdot x} \end{bmatrix} \begin{Bmatrix} w_{s \cdot x} \\ w_{s \cdot y} \end{Bmatrix} = \begin{Bmatrix} w_{d \cdot x}\, w_{s \cdot x} \\ w_{d \cdot y}\, w_{s \cdot y} \\ w_{d \cdot y}\, w_{s \cdot x} + w_{d \cdot x}\, w_{s \cdot y} \end{Bmatrix} \tag{4.87}$$

This expression can be manipulated into the following equivalent form

$$[\theta]_s[C'_\theta]\{a_b\}_d = [\theta]_s\{G\}_d = \begin{bmatrix} w_{s,x} & 0 \\ 0 & w_{s,y} \\ w_{s,y} & w_{s,x} \end{bmatrix} \begin{Bmatrix} w_{d,x} \\ w_{d,y} \end{Bmatrix} = \begin{Bmatrix} w_{s,x}\, w_{d,x} \\ w_{s,y}\, w_{d,y} \\ w_{s,y}\, w_{d,x} + w_{s,x}\, w_{d,y} \end{Bmatrix} \qquad (4.88)$$

which provides the final needed equality.

$$[n1_{mb}]_d\{a_b\}_s = [n1_{mb}]_s\{a_b\}_d \qquad (4.89)$$

The four equalities given in equations (4.72), (4.81), (4.85), and (4.89) can be written in the matrix form

$$\begin{bmatrix} n1_{b,d} + (n1_b)_{B,d} & n1_{bm,d} \\ n1_{mb,d} & 0 \end{bmatrix} \begin{Bmatrix} a_{b,s} \\ a_{m,s} \end{Bmatrix} = \begin{bmatrix} n1_{b,s} + (n1_b)_{B,s} & n1_{bm,s} \\ n1_{mb,s} & 0 \end{bmatrix} \begin{Bmatrix} a_{b,d} \\ a_{m,d} \end{Bmatrix} \qquad (4.90)$$

from which it is easily seen that the assembled system matrices share the analogous equality:

$$[N1]_d\{A\}_s = [N1]_s\{A\}_d \qquad (4.91)$$

The cross-terms generated by the expansion of the second-order nonlinear stiffness into static and dynamic components need manipulation as well. The product of each cross term with the corresponding displacement vector, on the element level, can be manipulated as follows in the discussions designated by numbers 1') through 4').

1') The product of the second-order bending stiffness cross-term $[n2_b]_{sd}$ and static bending nodal degrees of freedom $\{a_b\}_s$ is written as

$$[n2_b]_{sd}\{a_b\}_s = \int_S [C'_\theta]^T[\theta]_s^T[A][\theta]_d[C'_\theta]dS\{a_b\}_s \qquad (4.92)$$

but recall from the previous manipulations designated by 2b) and 4) that

$$[\theta]_i\{G\}_j = [\theta]_j\{G\}_i \qquad \Rightarrow \qquad [\theta]_d[C'_\theta]\{a_b\}_s = [\theta]_s[C'_\theta]\{a_b\}_d \qquad (4.93)$$

Thus, the following substitution can be made.

$$[n2_b]_{sd}\{a_b\}_s = [n2_b]_s\{a_b\}_d \qquad (4.94)$$

2') The product of the second-order bending stiffness cross-term $[n2_b]_{sd}$ and dynamic bending nodal degrees of freedom $\{a_b\}_d$ has the form

$$[n2_b]_{sd}\{a_b\}_d = \int_S [C'_\theta]^T[\theta]_s^T[A][\theta]_d[C'_\theta]dS\{a_b\}_d \qquad (4.95)$$

but recall from numbers 1) and 2a) that

$$[A][\theta]_d[C'_\theta]\{a_b\}_d = \{N_\theta\}_d \qquad \text{and} \qquad [\theta]_s^T\{N_\theta\}_d = [N_\theta]_d[C'_\theta]\{a_b\}_s \qquad (4.96)$$

78

Thus, the expression can be rewritten as follows.

$$[n2_b]_{sd}\{a_b\}_d = \int_S [C_\theta]^T [N_\theta]_d [C_\theta] dS \{a_b\}_s$$

$$= [n2_b]_d \{a_b\}_s \tag{4.97}$$

3') Similarly, the product of the second-order bending stiffness cross-term $[n2_b]_{ds}$ and static bending nodal degrees of freedom $\{a_b\}_s$ has the form

$$[n2_b]_{ds}\{a_b\}_s = \int_S [C_\theta]^T [\theta]_d^T [A][\theta]_s [C_\theta] dS \{a_b\}_s \tag{4.98}$$

With the following substitutions

$$[A][\theta]_s [C_\theta]\{a_b\}_s = \{N_\theta\}_s \qquad \text{and} \qquad [\theta]_d^T \{N_\theta\}_s = [N_\theta]_s [C_\theta]\{a_b\}_d \tag{4.99}$$

the expression can be rewritten as

$$[n2_b]_{ds}\{a_b\}_s = \int_S [C_\theta]^T [N_\theta]_s [C_\theta] dS \{a_b\}_d$$

$$= [n2_b]_s \{a_b\}_d \tag{4.100}$$

4') Finally, the product of the second-order bending stiffness cross-term $[n2_b]_{ds}$ and dynamic bending nodal degrees of freedom $\{a_b\}_d$ can be written as

$$[n2_b]_{ds}\{a_b\}_d = \int_S [C_\theta]^T [\theta]_d^T [A][\theta]_s [C_\theta] dS \{a_b\}_d \tag{4.101}$$

but from number 1') it is known that

$$[\theta]_i \{G\}_j = [\theta]_j \{G\}_i \qquad \Rightarrow \qquad [\theta]_s [C_\theta]\{a_b\}_d = [\theta]_d [C_\theta]\{a_b\}_s \tag{4.102}$$

Thus, this term can be rewritten in the following form.

$$[n2_b]_{ds}\{a_b\}_d = [n2_b]_d \{a_b\}_s \tag{4.103}$$

So, on the system level, implementation of the manipulations designated by 1') through 4') gives

$$[N2]_{sd}\{A\}_s = [N2]_s \{A\}_d$$
$$[N2]_{sd}\{A\}_d = [N2]_d \{A\}_s$$
$$[N2]_{ds}\{A\}_s = [N2]_s \{A\}_d$$
$$[N2]_{ds}\{A\}_d = [N2]_d \{A\}_s \tag{4.104}$$

Expanding the system equations of motion, equations (4.68), results in

$$[M]\{\ddot{A}\}_d + [K]\{A\}_s + [K]\{A\}_d - [K_{\Delta T}]\{A\}_s - [K_{\Delta T}]\{A\}_d + \frac{1}{2}[N1]_s \{A\}_s$$

$$+ \frac{1}{2}[N1]_s \{A\}_d + \frac{1}{2}[N1]_d \{A\}_s + \frac{1}{2}[N1]_d \{A\}_d + \frac{1}{3}[N2]_s \{A\}_s + \frac{1}{3}[N2]_s \{A\}_d$$

$$+ \frac{1}{3}[N2]_{sd}\{A\}_s + \frac{1}{3}[N2]_{sd}\{A\}_d + \frac{1}{3}[N2]_{ds}\{A\}_s + \frac{1}{3}[N2]_{ds}\{A\}_d + \frac{1}{3}[N2]_d \{A\}_s$$

$$+ \frac{1}{3}[N2]_d \{A\}_d = \{P(t)\} + \{F(t)\} + \{P_{\Delta T}\} - [M]\{\ddot{U}_g\} \tag{4.105}$$

79

and making the substitutions from equations (4.91) and (4.104) gives the following expression.

$$[M]\{\ddot{A}\}_d + [K]\{A\}_s + [K]\{A\}_d - [K_{\Delta T}]\{A\}_s - [K_{\Delta T}]\{A\}_d + \frac{1}{2}[N1]_s\{A\}_s$$

$$+ \frac{1}{2}[N1]_s\{A\}_d + \frac{1}{2}[N1]_s\{A\}_d + \frac{1}{2}[N1]_d\{A\}_d + \frac{1}{3}[N2]_s\{A\}_s + \frac{1}{3}[N2]_s\{A\}_d$$

$$+ \frac{1}{3}[N2]_s\{A\}_d + \frac{1}{3}[N2]_d\{A\}_s + \frac{1}{3}[N2]_s\{A\}_d + \frac{1}{3}[N2]_d\{A\}_s + \frac{1}{3}[N2]_d\{A\}_s$$

$$+ \frac{1}{3}[N2]_d\{A\}_d = \{P(t)\} + \{F(t)\} + \{P_{\Delta T}\} - [M]\{\ddot{U}_g\}$$

(4.106)

Separating the terms involving the static displacements $\{A\}_s$ from those involving the dynamic displacements$\{A\}_d$ results in the following static and dynamic governing equations.

$$([K] - [K_{\Delta T}] + \frac{1}{2}[N1]_s + \frac{1}{3}[N2]_s + [N2]_d)\{A\}_s = \{P_{\Delta T}\}$$

$$[M]\{\ddot{A}\}_d + ([K] - [K_{\Delta T}] + [N1]_s + \frac{1}{2}[N1]_d + [N2]_s$$

(4.107)

$$+ \frac{1}{3}[N2]_d)\{A\}_d = \{P(t)\} + \{F(t)\} - [M]\{\ddot{U}_g\}$$

The matrix $[N2]_d$, appearing in both equations, can be neglected because it is second order with respect to the small dynamic displacements $\{A\}_d$. The matrix $[N1]_d$, appearing in the dynamic equation, can be neglected also because the product $[N1]_d\{A\}_d$ is second-order in $\{A\}_d$ as well. Therefore, the final static and dynamic governing equations are as follows.

$$([K] - [K_{\Delta T}] + \frac{1}{2}[N1]_s + \frac{1}{3}[N2]_s)\{A\}_s = \{P_{\Delta T}\} \qquad \text{Static}$$

$$[M]\{\ddot{A}\}_d + ([K] - [K_{\Delta T}] + [N1]_s + [N2]_s)\{A\}_d$$

(4.108)

$$= \{P(t)\} + \{F(t)\} - [M]\{\ddot{U}_g\} \qquad \text{Dynamic}$$

In the applications being considered for this technology, there is often a combination of a flexible structures with a rigid boundary and combined thermal and mechanical loads. Thus, there is an opportunity for thermal buckling and an analysis capable of predicting such an event is necessary. Often it is also desirable to predict the post-buckled deflection of a structure subsequent to such an event. It will be shown later in this document that certain combinations of constituent materials in a SMAHC structure can exhibit a thermal buckling event and return the post-buckling deflection to zero. In order to capture and better understand this behavior, thermal buckling and post-buckling analyses are necessary.

Thus, three types of analyses are required to study the response of the structures considered in this study: (1) thermal buckling analysis, (2) thermal post-buckling analysis, and (3) dynamic analysis. Each of these analyses are discussed in the following two chapters. Acoustic radiation analysis is presented in Chapter 7 to study the structural-acoustic response and noise transmission characteristics of panel-type structures. A flowchart of the overall thermomechanical analysis procedure is given in Figure 4.2.
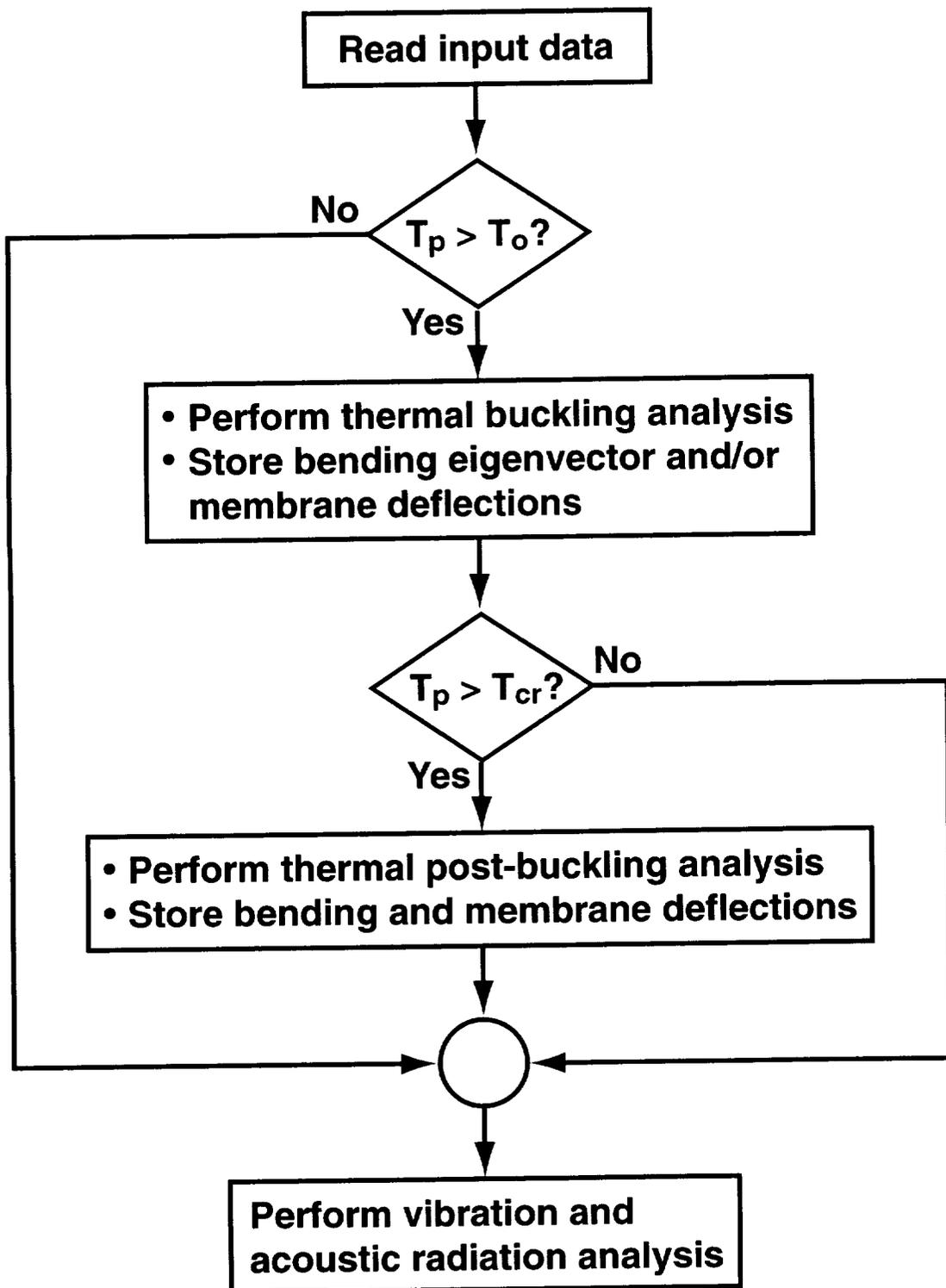
Figure 4.2 Overall thermomechanical analysis flowchart.

Chapter 5
Static Response

The static response considered in this study is assumed to be solely due to a thermal load. Two analysis types are potentially needed to determine this response: (1) thermal buckling analysis and (2) thermal post-buckling analysis. Each analysis will be discussed in this chapter. Thermal buckling and post-buckling considerations necessitate the investigation of static stability. Therefore, the fundamental equations governing this behavior will be derived first.

5.1 Static Stability and Nonlinear Analysis

The idea of static stability commonly arises in the context of a structure subjected to compressive mechanical loads in an axial direction. The goal is typically to determine the critical load for which the structure loses stability and may be deflected significantly by a lateral load, from which it will not return upon lateral load removal (commonly referred to as buckling). In practice, a structure in such a condition often deflects (buckles) as a result of imperfections, without the application of lateral loads. Whether buckled by mechanical loads and/or imperfections, it is often desirable to calculate the deflected shape of a structure subsequent to buckling (often termed post-buckling deflected shape). Such an analysis usually involves geometrically nonlinear analysis as the deflections are typically large.

In the case of thermoelastic response analysis, such as that considered here, a compressive load is generated by thermal expansion of a structure in the presence of mechanical boundary constraints. Thus, the goal is to determine the critical temperature at which the structure becomes unstable (also called the buckling temperature). Analysis of the thermal post-buckling deflection will also be of particular value.

Stability of an equilibrium configuration can be investigated through the use of the adjacent equilibrium method [46, 47]. Application of this method entails imposing small increments to the displacements of a system in static equilibrium and examining the resulting adjacent configuration. Let $\{\Psi(A)\}$ denote an equilibrium configuration for a structure with a displacement field given by $\{A\}$. Now, let the static displacements be given an increment

$$\{A\} \rightarrow \{A\} + \{\delta A\} \qquad \text{such that} \qquad \{\delta A^2\} \approx \{0\} \tag{5.1}$$

where the $\{\delta A\}$ are infinitesimal displacements. The adjacent static configuration $\{\Psi(A + \delta A)\}$ can be approximated by a truncated Taylor Series expansion:

$$\{\Psi(A + \delta A)\} = \{\Psi(A)\} + \frac{d\{\Psi(A)\}}{d\{A\}}\{\delta A\} + O(\{\delta A^2\}) \tag{5.2}$$

One could proceed to determine the derivative of the static configuration with respect to the static displacements, but the necessary ingredients for an equivalent procedure has already been developed in the previous chapter and can be employed here.

Recall that the equilibrium configuration $\{\Psi(A)\}$ is governed by the static system in equations (4.108):

$$\{\Psi(A)\} = ([K] - [K_{\Delta T}] + \frac{1}{2}[N1] + \frac{1}{3}[N2])\{A\} - \{P_{\Delta T}\} = \{0\} \tag{5.3}$$

where the static subscript s has been omitted for simplicity. The expression for the increment in the static displacements, equation (5.1), is analogous to the separation of the static and dynamic components of the total displacements given in equation (4.58). Substitution of $\{A\} + \{\delta A\}$ into equation (5.3) gives the adjacent static configuration that is not necessarily in equilibrium:

$$\{\Psi(A + \delta A)\} = ([K] - [K_{\Delta T}] + \frac{1}{2}[N1(A + \delta A)] + \frac{1}{3}[N2(A + \delta A)])(\{A\} + \{\delta A\}) - \{P_{\Delta T}\} \tag{5.4}$$

The manipulation of terms in the discussion following equation (4.58) allows the first- and second-order nonlinear stiffness matrices for the static system in equation (5.4) to be written as

$$[N1] = [N1]_0 + [N1]_\delta$$
$$[N2] = [N2]_0 + [N2]_{0\delta} + [N2]_{\delta0} + [N2]_\delta \tag{5.5}$$

where the subscripts 0 and δ indicate the influence of the displacements $\{A\}$ and $\{\delta A\}$, respectively.

Expanding $[N1]$ and $[N2]$ in equation (5.4) gives the following expression for the adjacent configuration.

$$\{\Psi(A + \delta A)\} = \left[[K] - [K_{\Delta T}] + \frac{1}{2}([N1]_0 + [N1]_\delta)\right.$$
$$\left. + \frac{1}{3}([N2]_0 + [N2]_{0\delta} + [N2]_{\delta0} + [N2]_\delta)\right](\{A\} + \{\delta A\}) - \{P_{\Delta T}\} \tag{5.6}$$

Further manipulation allows several terms in equation (5.6) to be written in forms analogous to equations (4.91) and (4.104):

$$[N1]_\delta\{A\} = [N1]_0\{\delta A\}$$
$$[N2]_{0\delta}\{A\} = [N2]_0\{\delta A\}$$
$$[N2]_{0\delta}\{\delta A\} = [N2]_\delta\{A\} \tag{5.7}$$
$$[N2]_{\delta0}\{A\} = [N2]_0\{\delta A\}$$
$$[N2]_{\delta0}\{\delta A\} = [N2]_\delta\{A\}$$

Expanding equation (5.6) gives

$$\{\Psi(A + \delta A)\} = [K]\{A\} + [K]\{\delta A\} - [K_{\Delta T}]\{A\} - [K_{\Delta T}]\{\delta A\} + \frac{1}{2}[N1]_0\{A\}$$
$$+ \frac{1}{2}[N1]_0\{\delta A\} + \frac{1}{2}[N1]_\delta\{A\} + \frac{1}{2}[N1]_\delta\{\delta A\} + \frac{1}{3}[N2]_0\{A\}$$
$$+ \frac{1}{3}[N2]_0\{\delta A\} + \frac{1}{3}[N2]_{0\delta}\{A\} + \frac{1}{3}[N2]_{0\delta}\{\delta A\} + \frac{1}{3}[N2]_{\delta0}\{A\}$$
$$+ \frac{1}{3}[N2]_{\delta0}\{\delta A\} + \frac{1}{3}[N2]_\delta\{A\} + \frac{1}{3}[N2]_\delta\{\delta A\} - \{P_{\Delta T}\} \tag{5.8}$$

84

and making the substitutions from equations (5.7) results in

$$
\begin{aligned}
\{\Psi(A + \delta A)\} = {} & [K]\{A\} + [K]\{\delta A\} - [K_{\Delta T}]\{A\} - [K_{\Delta T}]\{\delta A\} + \frac{1}{2}[N1]_0\{A\} \\
& + \frac{1}{2}[N1]_0\{\delta A\} + \frac{1}{2}[N1]_0\{\delta A\} + \frac{1}{2}[N1]_\delta\{\delta A\} + \frac{1}{3}[N2]_0\{A\} \\
& + \frac{1}{3}[N2]_0\{\delta A\} + \frac{1}{3}[N2]_0\{\delta A\} + \frac{1}{3}[N2]_\delta\{A\} + \frac{1}{3}[N2]_0\{\delta A\} \\
& + \frac{1}{3}[N2]_\delta\{A\} + \frac{1}{3}[N2]_\delta\{A\} + \frac{1}{3}[N2]_\delta\{\delta A\} - \{P_{\Delta T}\} = \{0\}
\end{aligned}
\tag{5.9}
$$

Separating terms in $\{A\}$ and $\{\delta A\}$, neglecting second- and higher-order terms in $\{\delta A\}$, and omitting the subscript 0 gives

$$
\begin{aligned}
\{\Psi(A + \delta A)\} = {} & ([K] - [K_{\Delta T}] + \frac{1}{2}[N1] + \frac{1}{3}[N2])\{A\} - \{P_{\Delta T}\} \\
& + ([K] - [K_{\Delta T}] + [N1] + [N2])\{\delta A\}
\end{aligned}
\tag{5.10}
$$

In order for this adjacent static configuration to be in equilibrium we must have $\{\Psi(A + \delta A)\} = \{0\}$. Then, the form for the *incremental* static system of equations becomes evident when the relations in equations (5.2) and (5.3) are compared to that in equation (5.10):

$$
([K] - [K_{\Delta T}] + [N1] + [N2])\{\delta A\} = \{0\}
\tag{5.11}
$$

as the original equilibrium configuration $\{\Psi(A)\}$ is identically satisfied. It can also be seen that the first-order derivative of the original equilibrium configuration with respect to the static displacement vector is given by

$$
\frac{d\{\Psi(A)\}}{d\{A\}} = [K_{tan}] = [K] - [K_{\Delta T}] + [N1] + [N2]
\tag{5.12}
$$

which is called the *tangent* stiffness matrix.

It will be shown in the following sections that Equations (5.10)–(5.12) are useful for thermal buckling and post-buckling analyses. The incremental static system of equations will be useful for investigation of thermal buckling as the expression must be satisfied for an adjacent equilibrium to exist. The tangent stiffness matrix will be useful in calculation of static deflections due to thermal moments/bending-membrane coupling or post-buckling deflections, where a Newton-Raphson approach will require the derivative of the stiffness coefficients. These procedures will be described subsequently.

5.2 Thermal Buckling Analysis

A thermal buckling analysis is carried out to determine the critical (buckling) temperature distribution of a structure $T_{cr}(x, y) = \Delta T_{cr}(x, y) + T_o$, where T_o is the uniform reference or ambient temperature distribution. This type of analysis is useful for determination of a need for thermal post-buckling analysis for a particular configuration and loading condition. Although buckling analyses are inherently linear, and the system in concern is decidedly

nonlinear (temperature-dependent properties), there is at least one way to seek a solution within the framework of the present formulation. Furthermore, a thermal buckling solution is very desirable because of the insight it affords, the computational efficiency for cases when thermal post-buckling analyses are not warranted, and the ability to provide an initial trial solution for thermal post-buckling analyses when they are necessary. All of these points will be made more evident in the following discussions.

Equations governing thermal buckling can be obtained from the static equations of equilibrium, equations (4.108), and the incremental static system of equations, equation (5.11). As stated previously, thermal buckling is a stability problem, indicating a condition for the onset of buckling. Therefore, the nonlinear stiffness terms due to out-of-plane deflection can be neglected. The stiffness terms involving bending-membrane coupling can also be neglected because any increase in temperature will result in out-of-plane deflection. An exception to this exists for antisymmetric angle-ply laminates which is a special case that will not be treated here. Moment resultant terms are also neglected for similar reasons, i.e., the thermal load is assumed constant through the thickness of the structure. Cases for which there is either bending-membrane coupling or thermal moment effects should be treated with a thermal post-buckling procedure, described in the next section, to determine the buckling temperature and static thermal deflections. The static governing equations from (4.108), with the aforementioned restrictions, simplify to the following.

$$
\left(\begin{bmatrix} K_b & 0 \\ 0 & K_m \end{bmatrix} - \begin{bmatrix} K_{\Delta T} & 0 \\ 0 & 0 \end{bmatrix} + \frac{1}{2} \begin{bmatrix} N1_b & 0 \\ 0 & 0 \end{bmatrix} \right) \begin{Bmatrix} A_b \\ A_m \end{Bmatrix} = \begin{Bmatrix} 0 \\ P_{m\Delta T} \end{Bmatrix}
\tag{5.13}
$$

The term $[N1_b]$ is retained because it is dependent upon the membrane displacements $\{A_m\}$ only.

5.2.1 Constant Matrix Material Properties

The proposed solution to the thermal buckling problem, discussed subsequently, entails separation of the SMA and matrix material thermal effects. Recall the SMA hybrid composite lamina constitutive relations in principal material coordinates, after separating the SMA and matrix thermal effects, given in equation (2.29). It is noted that the material system constituents are not fully separated in that equation because of their combined effects in the reduced stiffness matrix. However, the coefficients c_{1a} and c_{1m} essentially render them separate in the 1–direction and will lead to a useful form for the governing equations. Incorporation of those constitutive relations into the finite element formulation results in a system of static governing equations analogous to those in equations (4.108). The aforementioned assumptions inherent to thermal buckling analysis reduce this static system to the following.

$$
\left(\begin{bmatrix} K_b & 0 \\ 0 & K_m \end{bmatrix} - \begin{bmatrix} K_{\Delta T} & 0 \\ 0 & 0 \end{bmatrix}_a - \begin{bmatrix} K_{\Delta T} & 0 \\ 0 & 0 \end{bmatrix}_m + \frac{1}{2} \begin{bmatrix} N1_b & 0 \\ 0 & 0 \end{bmatrix} \right) \begin{Bmatrix} A_b \\ A_m \end{Bmatrix} = \begin{Bmatrix} 0 \\ P_{m\Delta T} \end{Bmatrix}_a + \begin{Bmatrix} 0 \\ P_{m\Delta T} \end{Bmatrix}_m
\tag{5.14}
$$

The subscripts a and m indicate SMA and matrix material, respectively. It is obvious that the bending and membrane equations of the static problem are now de-coupled. The membrane displacements due to an applied thermal load that varies only in the plane of the structure can thus be determined from the equation

$$
[K_m]\{A_m\} = \{P_{m\Delta T}\}_a + \{P_{m\Delta T}\}_m
\tag{5.15}
$$

For a given applied temperature distribution $\Delta T(x, y)$, equation (4.55) can be used to form the thermal force vectors $\{P_{m\Delta T}\}_a$ and $\{P_{m\Delta T}\}_m$ and equation (5.15) can be solved for the membrane displacements:

$$\{A_m\} = [K_m]^{-1}(\{P_{m\Delta T}\}_a + \{P_{m\Delta T}\}_m)$$
$$= \{A_m\}_a + \{A_m\}_m \tag{5.16}$$

The stability of this thermoelastic equilibrium configuration can be investigated through the use of the incremental static equations (5.11).

The incremental static system of equations can be simplified as above by neglecting nonlinear stiffness terms due to out-of-plane displacements, bending-membrane coupling stiffnesses, and moment resultants:

$$\left(\begin{bmatrix} K_b & 0 \\ 0 & K_m \end{bmatrix} - \begin{bmatrix} K_{\Delta T} & 0 \\ 0 & 0 \end{bmatrix}_a - \begin{bmatrix} K_{\Delta T} & 0 \\ 0 & 0 \end{bmatrix}_m + \begin{bmatrix} N1_b & 0 \\ 0 & 0 \end{bmatrix}_a + \begin{bmatrix} N1_b & 0 \\ 0 & 0 \end{bmatrix}_m \right) \begin{Bmatrix} \delta A_b \\ \delta A_m \end{Bmatrix} = \begin{Bmatrix} 0 \\ 0 \end{Bmatrix} \tag{5.17}$$

Note that the first-order nonlinear stiffness matrix due to membrane displacements has been separated into components evaluated with membrane displacements caused by SMA and matrix material thermal effects, respectively. Thus, the equations governing the stability of the out-of-plane displacements can be written as

$$([K_b] - [K_{\Delta T}]_a - [K_{\Delta T}]_m + [N1_b]_a + [N1_b]_m)\{\delta A_b\} = \{0\} \tag{5.18}$$

Consider a temperature distribution change of the following form

$$\Delta T(x, y) = \lambda \Delta T_1(x, y) \tag{5.19}$$

where λ is a scalar. For a matrix material with constant material properties, the thermal force vector and geometric stiffness matrix due to the thermal effects are linear functions of the temperature change:

$$\{P_{m\Delta T}\}_{m\Delta T(x,y)} = \lambda\{P_{m\Delta T}\}_{m\Delta T_1(x,y)}$$
$$[K_{\Delta T}]_{m\Delta T(x,y)} = \lambda[K_{\Delta T}]_{m\Delta T_1(x,y)} \tag{5.20}$$

A similar relation can be written for the corresponding first-order nonlinear stiffness matrix

$$[N1_b]_{m\Delta T(x,y)} = \lambda[N1_b]_{m\Delta T_1(x,y)} \tag{5.21}$$

because equations (5.15) are linear and $[N1_b]_m$ is linearly dependent upon the membrane displacements due to matrix material thermal effects.

Analogous expressions cannot be written for the thermal force vector $\{P_{m\Delta T}\}_{a\Delta T(x,y)}$, geometric stiffness matrix $[K_{\Delta T}]_{a\Delta T(x,y)}$, and first-order nonlinear stiffness matrix $[N1_b]_{a\Delta T(x,y)}$ associated with the SMA thermal effects over the same temperature change $\Delta T(x, y) = \lambda \Delta T_1(x, y)$ as they are all nonlinear functions of temperature. The stiffness matrix $[K_b]$ is also nonlinear with temperature because of the influence of the SMA constituent. At the present, let all of the terms involving the SMA thermal effects be simply evaluated at the imposed temperature distribution and taken as constant; the rationale for this approach will be explained

subsequently. In this case, equation (5.18) can be rewritten for the temperature distribution change $\Delta T(x,y) = \lambda \Delta T_1(x,y)$ as

$$([K_b] - [K_{\Delta T}]_a - \lambda[K_{\Delta T}]_m + [N1_b]_a + \lambda[N1_b]_m)\{\delta A_b\} = \{0\} \qquad (5.22)$$

which can be expressed as an eigenvalue problem

$$([K_b] - [K_{\Delta T}]_a + [N1_b]_a)\{\phi\} = \lambda([K_{\Delta T}]_m - [N1_b]_m)\{\phi\} \qquad (5.23)$$

A critical temperature change exists if there is a solution to equation (5.23) for which $\{\phi\}$ is nontrivial. The first eigen-solution gives the critical temperature change from the expression $\Delta T_{cr}(x,y) = \lambda_1 \Delta T_1(x,y)$ and the corresponding buckling mode shape $\{\phi\}_1$.

An iterative procedure can be employed to account for the nonlinear functionality of the terms involving the SMA thermal effects in equation (5.23). The iterative procedure entails imposing any desired temperature distribution $T_1(x,y) = T_0 + \Delta T_1(x,y)$ to evaluate the material properties. Then, equations (2.37) and (4.55) an be used to evaluate the SMA and matrix material thermal force vectors $\{P_{m\Delta T}\}_a$ and $\{P_{m\Delta T}\}_m$ and the corresponding geometric stiffness matrices $[K_{\Delta T}]_a$ and $[K_{\Delta T}]_m$. Equations (5.15) can be solved for the membrane displacements $\{A_m\}_s$ and $\{A_m\}_m$, which can then be used in equations (4.18) and (4.55) to form the first-order nonlinear stiffness matrices $[N1_b]_a$ and $[N1_b]_m$. Subsequently, the bending eigenvalue problem, equation (5.23), can be formed and solved for an estimate of the buckling temperature $T_2(x,y) = \lambda_1^1 T_1(x,y) = \lambda_1^1[T_0 + \Delta T_1(x,y)]$ and mode shape $\{\phi\}_1^1$, where the superscript indicates iteration number. This process is repeated until convergence is achieved $(\lambda_1^n = 1.000 \pm .001)$, at which point usage of the linearized eigenvalue problem has been rendered appropriate and accurate because $\Delta T_n(x,y)$ is such a small quantity that the material properties are essentially constant.

5.2.2 Non-Constant Matrix Material Properties

The assumption that the matrix material properties were constant with temperature was implicit to the equations and solution methodology developed in the previous section. Under such conditions, a rationale was developed to separate the linear and nonlinear components of the governing equations and use an iterative approach to compensate for the nonlinearity. Recall that during the linear/nonlinear separation process, a comment was made that the reduced stiffness matrix disallowed complete separation of the constituent material effects. This point was also made in Chapter 2. Thus, some nonlinear effects (e.g., modulus of the SMA) do appear on the right-hand side of equation (5.23) and the solution method of the previous section must be applicable for at least some forms of temperature dependence in the matrix material.

This has, in fact, been observed for all of the cases considered in this study, which include cases for which all of the matrix material properties vary significantly with temperature. The validity of the thermal buckling solution for such cases was established by comparing with a thermal post-buckling method. The thermal post-buckling method serves as another means of determining a buckling temperature, as the temperature at which the thermal post-buckling deflection departs from zero. In the event that a thermal buckling solution could not be achieved, an initial guess would be formulated from the thermal buckling problem and used to start a

thermal post-buckling solution. More detail on this approach will be given following the post-buckling solution method description at the end of the next section. A flow chart exemplifying the thermal buckling solution procedure is shown in Figure 5.1.
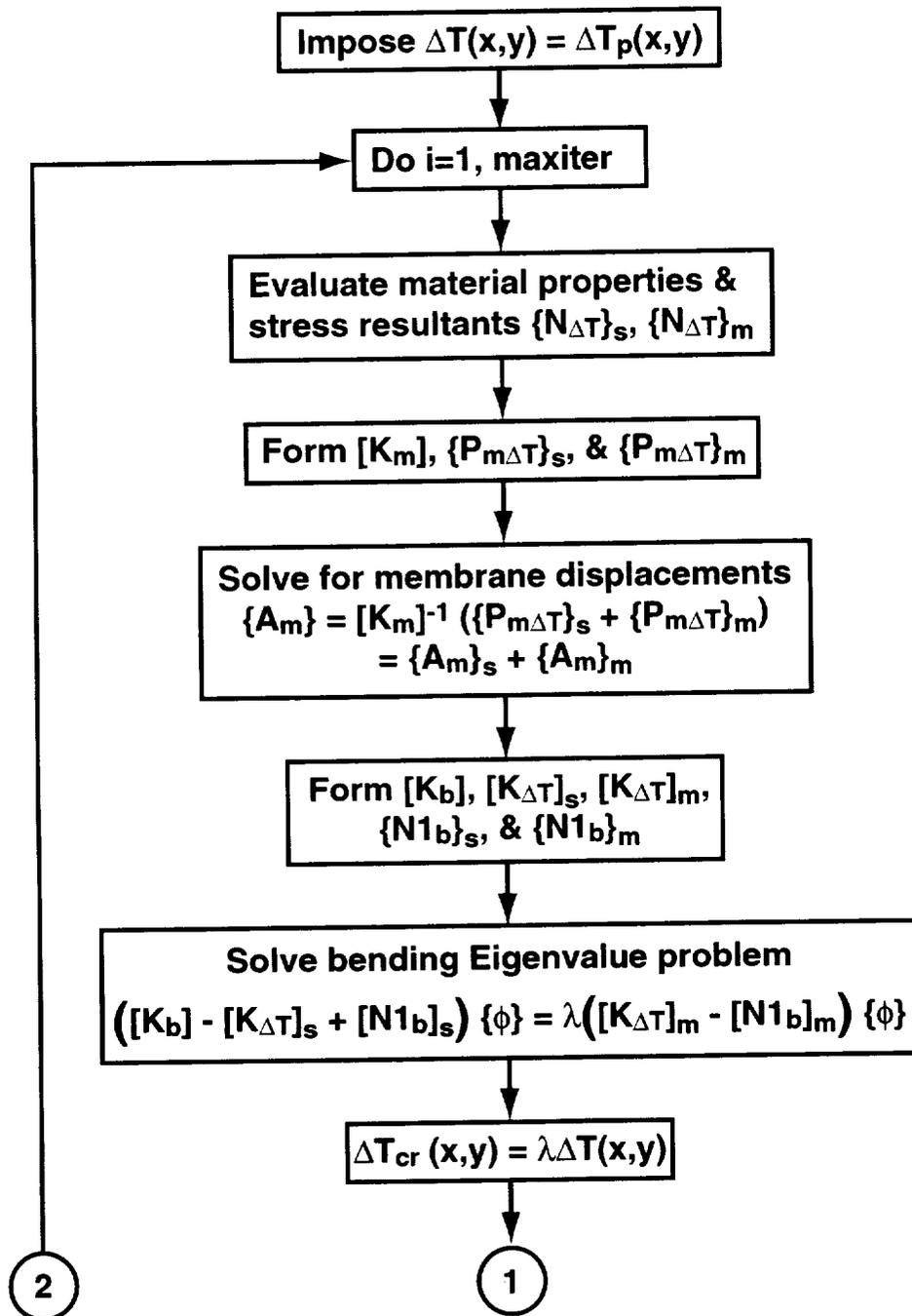
Figure 5.1 Thermal buckling calculation flowchart. (Continued) . . .

89
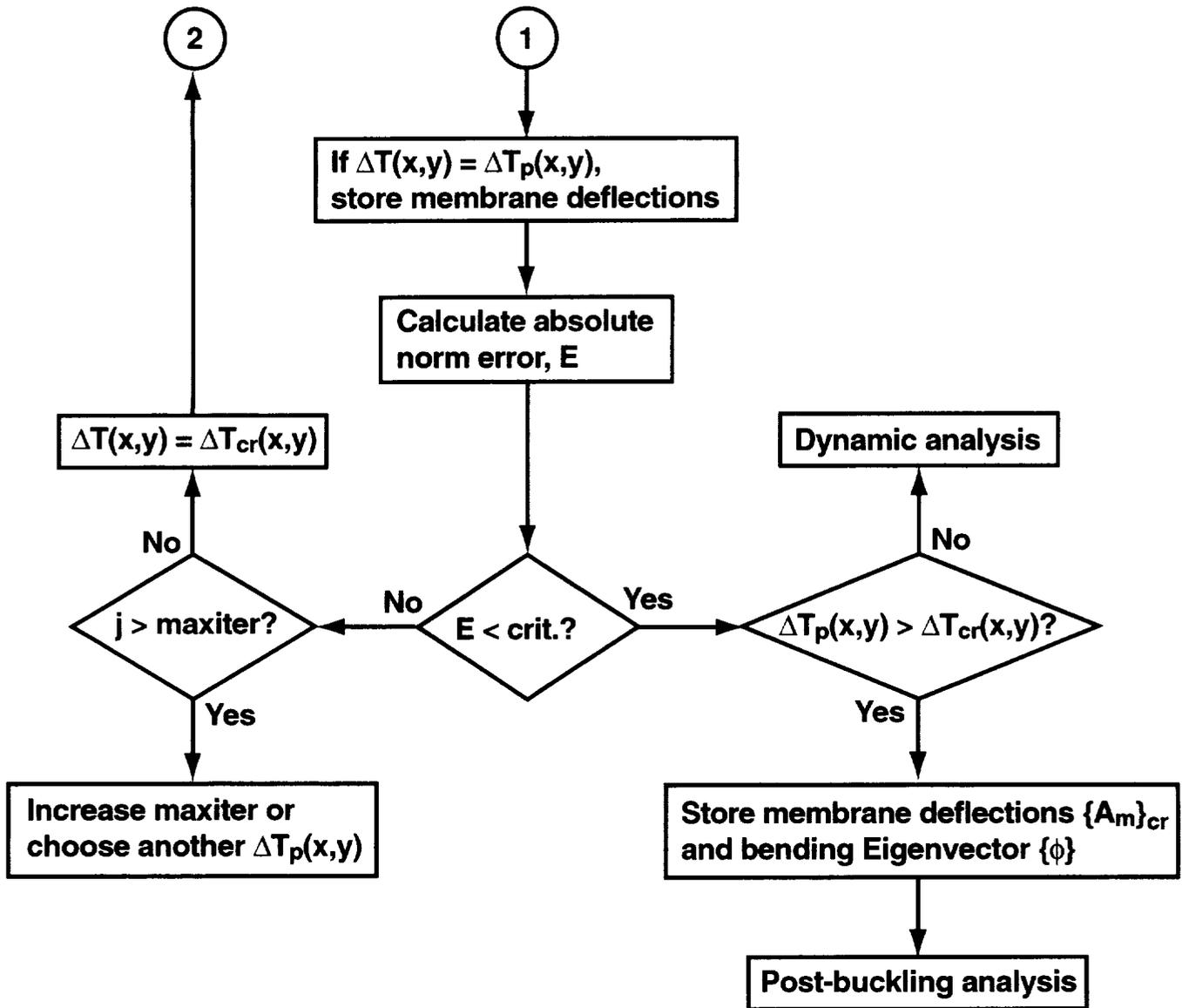
Figure 5.1 Thermal buckling calculation flowchart.

It will be shown in Chapter 8 that two buckling temperatures can exist for some SMA hybrid composite structures. Details will be deferred to that discussion, but some general comments are useful here. This effect is a manifestation of a material system with a SMA constituent that has an austenite start temperature A_s greater than ambient temperature and is not to be confused with higher-order buckling modes occurring at temperatures above initial thermal buckling. A typical sequence of events in such a case can be described as follows. At temperatures less than A_s, the SMA is not activated and behaves like a conventional linear thermoelastic material. So the SMAHC structure will buckle if a critical temperature exists below A_s. The SMA becomes activated at A_s and the recovery stress rapidly increases with temperature, which overcomes the compressive thermal stress and reduces the thermal deflection (potentially eliminating it). At

90

higher temperatures, the rate of increase of the recovery stress with temperature diminishes and may be surpassed by the rate of increase in matrix compressive thermal stress. Further increases in temperature will cause net-compressive stress development, causing the thermal deflection to grow again or lead to a second incidence of thermal buckling for a structure that was rendered flat.

5.3 Thermal Post-buckling Analysis

Once the buckling temperature is determined, the next step will depend on the temperature for the particular application of concern. For temperatures greater than the critical temperature $(T(x,y) > T_{cr}(x,y))$, a post-buckling analysis must be performed to determine the thermal deflection. The thermal post-buckling solution is started at the buckling temperature $T_{cr}(x,y)$ for expediency and ease of solution. Starting at the ambient temperature can be much more computationally intensive (for cases with large $\Delta T_{cr}(x,y)$) and is numerically ill-conditioned. Further remarks about initiating the post-buckling solution will be given later in this section. For the cases described above, where two buckling temperatures can exist, it is advisable (although not necessary) to initiate a thermal post-buckling analysis at the first buckling temperature to assess the evolution of the static deflection in arriving at the desired operating temperature. The governing equations for thermal post-buckling deflection are given in equations (4.108)

$$\left([K] - [K_{\Delta T}] + \frac{1}{2}[N1] + \frac{1}{3}[N2] \right)\{A\} = \{P_{\Delta T}\} \tag{5.24}$$

where the *static* subscript s has been omitted. Note that there is no need to separate the SMA and matrix material thermal effects in thermal post-buckling analysis. One effective approach for solving this nonlinear system of equations is the Newton-Raphson iterative method.

Consider a static system described by equation (5.24) at the buckling temperature distribution $T_{cr}(x,y)$ and denote this equilibrium configuration by $\{\Psi(A)\}$. A small increment in the temperature distribution $T(x,y) = T_{cr}(x,y) + \delta T(x,y)$ will result in the formation of an adjacent equilibrium configuration denoted by $\{\Psi(A+\delta A)\}$. This adjacent equilibrium configuration can be derived from a truncated Taylor series expansion as shown in equation (5.10):

$$\{\Psi(A+\delta A)\} = ([K] - [K_{\Delta T}] + \frac{1}{2}[N1] + \frac{1}{3}[N2])\{A\} - \{P_{\Delta T}\}$$
$$+ ([K] - [K_{\Delta T}] + [N1] + [N2])\{\delta A\} = \{0\} \tag{5.25}$$

The first collection of terms on the right-hand side of this equation is no longer a statement of static equilibrium

$$\{\Psi(A)\} \neq ([K] - [K_{\Delta T}] + \frac{1}{2}[N1] + \frac{1}{3}[N2])\{A\} - \{P_{\Delta T}\} \neq \{0\} \tag{5.26}$$

as the stiffnesses and thermal load vector are evaluated at $T(x,y) = T_{cr}(x,y) + \delta T(x,y)$, while $\{A\}$ is associated with the system at temperature $T_{cr}(x,y)$. So, the expression for the adjacent equilibrium configuration can be rewritten in terms of the tangent stiffness matrix, equation (5.12), and an incremental load vector

$$[K_{tan}]\{\delta A\} = \{\delta P_{\Delta T}\} \tag{5.27}$$

where the incremental load vector is defined by

$$\{\delta P_{\Delta T}\} = \{P_{\Delta T}\} - ([K] - [K_{\Delta T}] + \frac{1}{2}[N1] + \frac{1}{3}[N2])\{A\}$$ (5.28)

Although a small increment in temperature may render the static system essentially linear with temperature, the new equilibrium configuration is also governed by the geometric nonlinearity of the first- and second-order nonlinear stiffness matrices, which are linearly and quadratically dependent upon the out-of-plane displacements. Thus, an iterative procedure is necessary to converge on the new equilibrium configuration.

The incremental form of equation (5.24) for the j-th iteration can be written as

$$[K_{tan}]_j\{\delta A\}_j = \{\delta P_{\Delta T}\}_j$$ (5.29)

The tangent stiffness and incremental load vector for the subsequent iteration $[K_{tan}]_{j+1}$ and $\{\delta P_{\Delta T}\}_{j+1}$ are updated by using the updated thermal deflections

$$\{A\} = \{A\} + \{\delta A\}_j$$ (5.30)

The iteration procedure is continued, with the previous iteration's deflections as an estimate, until the deflection estimate approaches the true equilibrium configuration. As the deflection estimate approaches the equilibrium configuration, the expression for the incremental load vector approaches an expression of equilibrium, at which point the incremental load vector $\{\delta P_{\Delta T}\}_j$ and, consequently, the incremental displacements $\{\delta A\}_j$ approach zero. Convergence is achieved when either incremental values are reduced to a specified small quantity defined by the error criterion. A *maximum norm* error criterion was used in this study, as described by Bergan and Clough [48].

As mentioned previously, the thermal post-buckling analysis is sensitive to the starting temperature and the corresponding trial solution. An initial trial solution for the thermal post-buckling procedure, starting at the buckling temperature, can be constructed from the thermal buckling solution. The membrane deflections, determined from equations (5.16) evaluated at the (first) buckling temperature, are used directly. The buckling mode shape, determined from equation (5.23), is normalized to its maximum displacement entry and to a fraction of the structure thickness (half-thickness was found to perform well) to give the out-of-plane portion of the initial trial solution a physically scaled value:

$$\{A\} = \left\{ \begin{array}{c} A_b \\ A_m \end{array} \right\} = \left\{ \begin{array}{c} 0.5h\{\phi\}/\phi_{w_{max}} \\ \{A_m\}_{cr} \end{array} \right\}$$ (5.31)

Convergence on the displacements due to a rather large temperature increment $\Delta T(x,y)$ can typically be improved by splitting the large temperature increment into a number of smaller increments:

$$\Delta T_i(x,y) = \frac{\Delta T(x,y)}{N_{\Delta T}}$$ (5.32)

Iteration is performed at each of the smaller temperature increments in succession until the converged equilibrium configuration (post-buckled static solution) is achieved for the desired

temperature. The converged displacement vector at each of the smaller temperature increments is scaled and used as a trial vector for the next temperature increment :

$$\{A\}_i = \{A\}_{i-1} \frac{T_i(x,y) - T_o(x,y)}{T_{i-1}(x,y) - T_o(x,y)} \tag{5.33}$$

Note that a mechanism for re-initialization of the out-of-plane displacements is necessary because of the potential for elimination of the post-buckling deflection due to SMA recovery forces for the cases with two buckling temperatures. A flow chart demonstrating the thermal post-buckling solution procedure is shown in Figure 5.2.

One final remark concerns any potential cases for which convergence on a thermal buckling solution is not possible. In such cases, a thermal post-buckling solution should be initiated from the reference temperature and should proceed at temperature increments until a thermal post-buckling deflection is developed. At each increment in temperature, the in-plane problem of the buckling solution should be solved for the in-plane deflections. The in-plane deflections will be used to form the thermal buckling eigenvalue problem. The eigenvector resulting from a single eigen-solution would then be used, along with the in-plane deflections, to form an initial guess for the post-buckling solution at that temperature. Once a thermal post-buckling deflection is achieved, a refined estimate of the buckling temperature can be determined by restarting the post-buckling solution in the vicinity of the first solution with a smaller temperature increment.
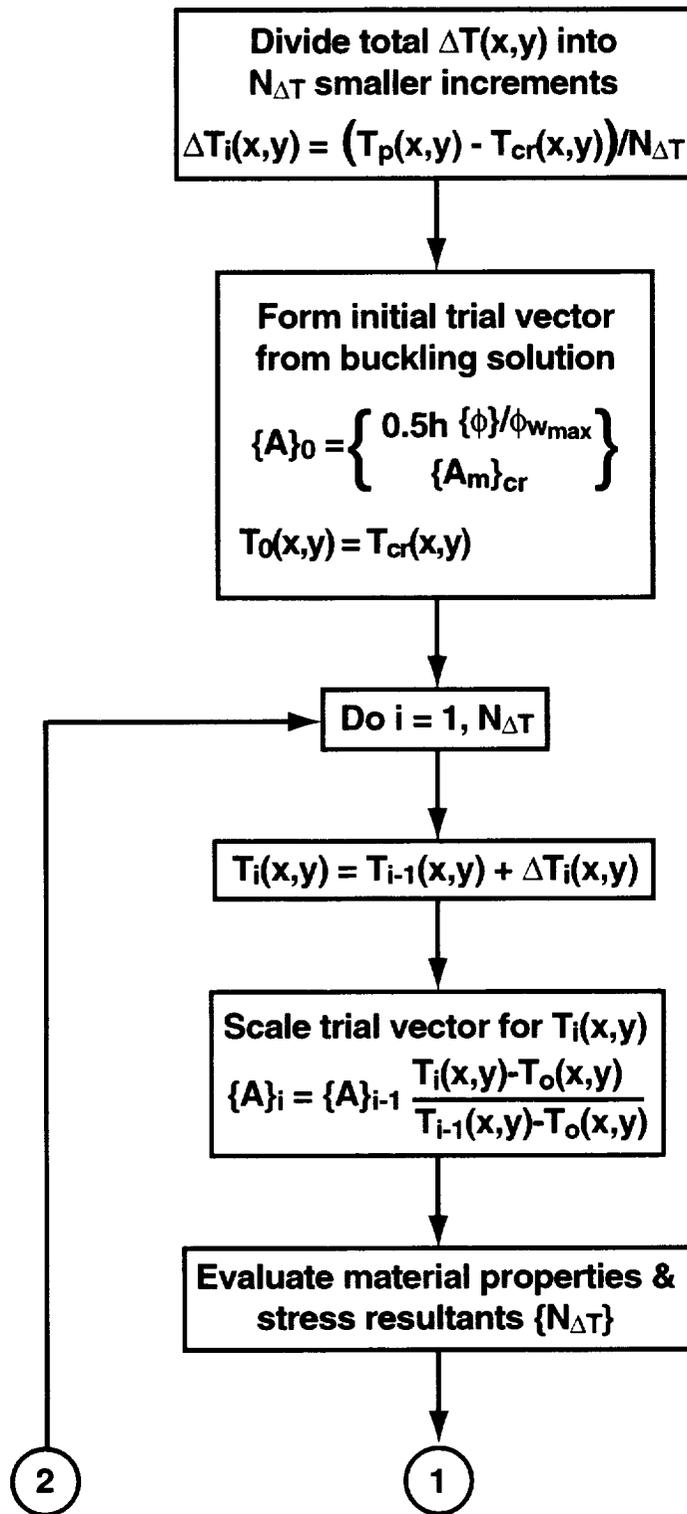
Figure 5.2   Thermal post-buckling calculation flowchart.   (Continued) . . .
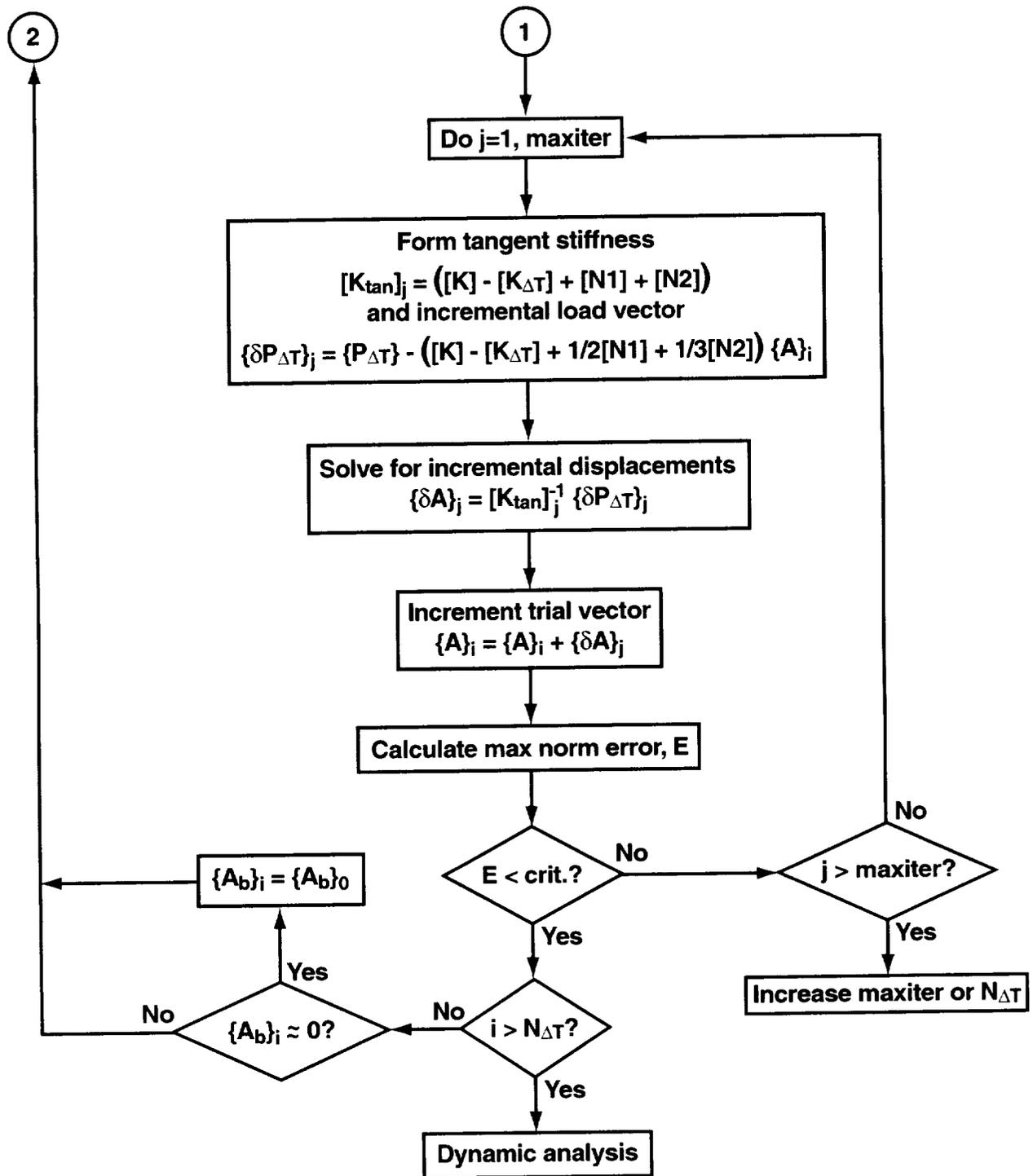
Figure 5.2 Thermal post-buckling calculation flowchart.

5.4 Analytical Validation

In the previous sections, a formulation and approach for prediction of the static stability (thermal buckling) and large-deflection (thermal post-buckling) of SMA hybrid composite panel-type structures was derived. The formulation and implementation will now be validated through comparison with fundamental cases and experimental measurements. Comparisons will be made with known solutions for the cases of a simply-supported isotropic beam, simply-supported and clamped isotropic plates, and a simply-supported symmetrically-laminated composite plate to benchmark the analysis. Comparisons will be made with experimental measurements for the case of a clamped-clamped SMAHC beam to fully validate the thermomechanical model for static response.

Note that the effects of initial stresses, initial deflections, thermal moments due to a temperature gradient through the thickness, and bending-membrane coupling (non-symmetric composite laminates) are not included in the analysis, although solution with such conditions is quite tractable by the thermal post-buckling solution technique. Therefore, the thermal buckling cases presented are true bifurcation problems and, as such, the resulting post-buckling deflection could be positive or negative. In practice, the predicted buckling direction is typically predetermined by the sign of the initial guess. The sense of the buckling deflection in a particular experimental configuration is usually influenced by some combination of imperfections including initial stresses, initial deflections, and anomalies in boundary conditions. The positive sense will be taken in the purely numerical results to be presented and the sense will be chosen to match the experimental behavior when comparing with experimental measurement.

5.4.1 Simply-Supported Isotropic Beam

Consider a simply-supported aluminum beam with dimensions of 0.5588x0.0254x0.0023 m (18x1x0.090 inches) and subject to a uniform temperature increase. The material properties for the specimen are shown in Table 5.1.

Table 5.1 Material properties for aluminum specimens.

Young's Modulus	68.95 GPa	10 Msi
Shear Modulus	26.55 GPa	3.85 Msi
Poisson's Ratio	0.3	
Coeff. of Thermal Exp.	22.3 $\mu\epsilon/^\circ$F	12.4 $\mu\epsilon/^\circ$F

A classical solution for the critical temperature change to induce buckling can be easily derived based upon beam-column theory, as shown by Boley and Weiner [49] for example. For a uniform temperature distribution, the axial load is given by

$$P_T = AE\alpha\Delta T \qquad (5.34)$$

96

where A is the beam cross-sectional area, E is the Young's modulus, and α is the thermal expansion coefficient. Thermal buckling occurs when the axial load reaches the Euler buckling load, defined by the familiar expression

$$P_{cr} = \frac{\pi^2 E I}{L^2}$$ (5.35)

where A is the area moment of inertia, and L is the beam length. Thus, the critical temperature change is found to be

$$\Delta T_{cr} = \frac{\pi^2 I}{\alpha A L^2}$$ (5.36)

This gives a numerical value of 1.658°F for the predicted critical temperature change from beam-column analysis as compared to 1.643°F for the present finite element analysis with a 36x2-element mesh. The slight discrepancy is attributable to the fact that the classical analysis does not include transverse effects because it is a one-dimensional analysis.

5.4.2 Simply-Supported and Clamped Isotropic Plates

A classical solution for the critical temperature change to induce buckling for an simply-supported isotropic plate is also given by Boley and Weiner [49]. For a uniform temperature distribution, the in-plane thermal force is given by

$$N_T = \alpha E \int\limits_{-\frac{h}{2}}^{\frac{h}{2}} \Delta T \, dz = \alpha E h \Delta T$$ (5.37)

where h is the thickness of the plate. Thermal buckling occurs when the in-plane thermal load reaches the reaches a critical value, given by

$$N_{T_{cr}} = (1 - \nu)\left(1 + \frac{a^2}{b^2}\right)\frac{\pi^2 D}{a^2}$$ (5.38)

where ν is the Poisson's ratio, a and b are the panel length and width, and D is the flexural rigidity given by

$$D = \frac{E h^3}{12(1 - \nu^2)}$$ (5.39)

Thus, the critical temperature change is given by the following expression

$$\Delta T_{cr} = (1 - \nu)\left(1 + \frac{a^2}{b^2}\right)\frac{\pi^2 D}{a^2 \alpha E h}$$ (5.40)

As an example, consider a simply-supported aluminum plate with dimensions of 0.3556x0.254x0.001 m (14x10x0.040 inches) and the material properties given in Table 5.1. The classical solution for this case gives a numerical value of 1.233°F for the predicted

97
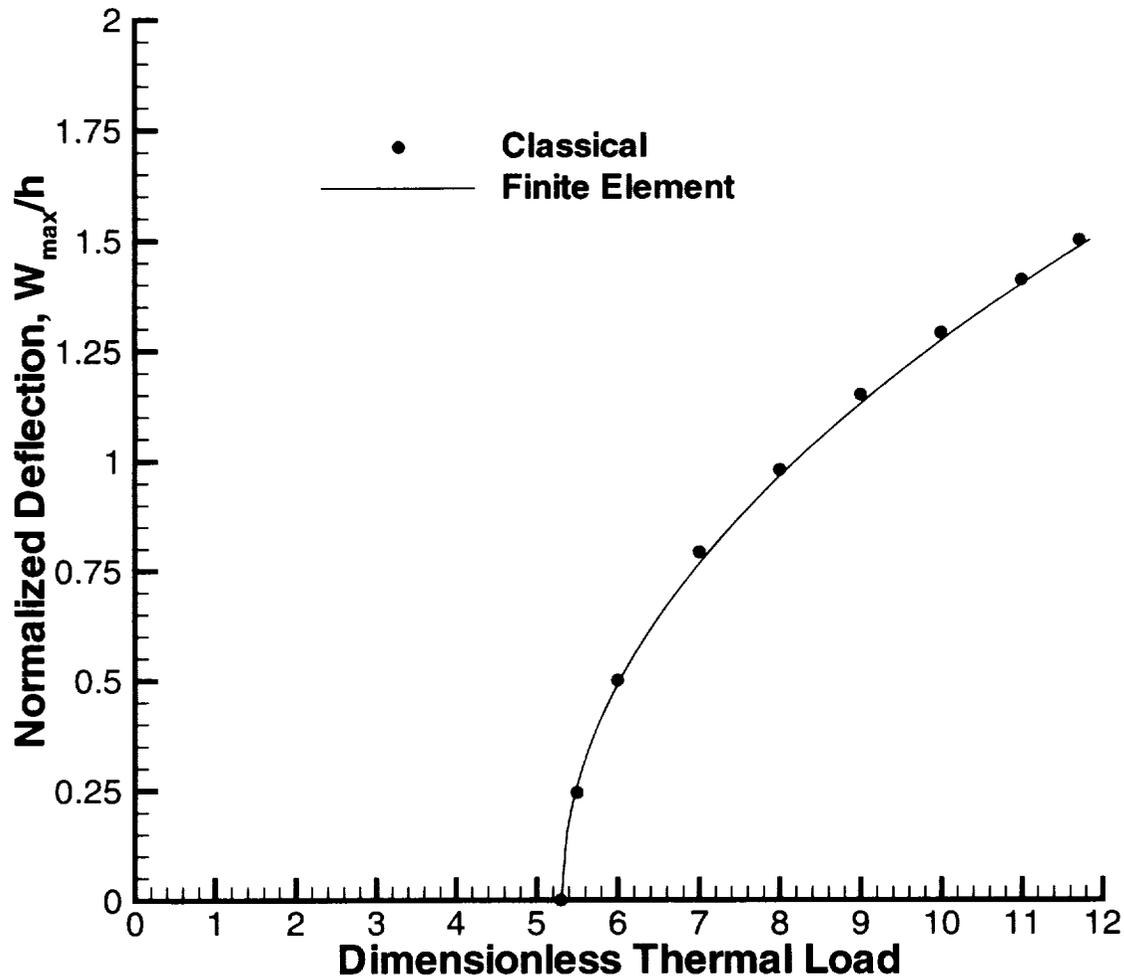
Figure 5.3 Normalized maximum deflection versus dimensionless thermal load for a clamped, 0.102x0.102x0.001 m (4x4x0.040 inch), aluminum plate with uniform thermal load.

critical temperature change, which is matched exactly by the present finite element analysis with a 14 x 10 element mesh.

A classical solution for the thermal post-buckling deflection of a clamped isotropic plate was developed by Paul [50]. He used a twenty-five term series approximation in a classical formulation with von Kármán deformation assumptions. One case he analyzed consisted of a clamped aluminum plate with dimensions of 0.102x0.102x0.001 m (4x4x0.040 inches) with material properties as given in Table 5.1, except with a slightly different thermal expansion coefficient $\alpha=22.5$ $\mu\epsilon/^\circ C$ (12.5 $\mu\epsilon/^\circ F$) and a uniform thermal load. A plot of the normalized center deflection versus dimensionless thermal load for this case is shown in Figure 5.3. It can be seen that the present finite element analysis is in excellent agreement with the classical

solution. The fine resolution $N_{\Delta T} = 100$ for the finite element results was used for presentation purposes only. Convergence on the solution at the final temperature was readily achieved with only one temperature step. In fact, the solution was much more expedient albeit not conducive to conveying information about the deflection behavior at intermediate temperatures. The dimensionless thermal load shown as the abscissa of the plot is given by Paul as

$$\text{Load} = 12(1 + \nu)\frac{\alpha \Delta T a^2}{\pi^2 h^2} \tag{5.41}$$

The range on the load from approximately 5.3 to 12 is equivalent to a ΔT from zero to 15.6°C (60°F).

5.4.3 Simply-Supported Composite Plate

Meyers and Hyer [51] employed a Rayleigh-Ritz method to developed a classical solution for the buckling temperature and the thermal post-buckling deflection of simply-supported, symmetrically-laminated composite plates. They analyzed plates with fixed and sliding simple supports. For example, Meyers and Hyer reported a buckling temperature of 20.8°C (69.4°F) for a graphite-epoxy plate with dimensions of 0.152x0.152x0.001 m (6x6x0.040 inches), quasi-isotropic lamination of (±45/0/90)$_s$, fixed simple supports, a uniform temperature distribution, and material properties as shown in Table 5.2. The corresponding solution from the present finite element analysis is 20.6°C (69.05°F) with a 6 x 6-element mesh.

Table 5.2 Material properties in principal material coordinates for a graphite-epoxy lamina.

Young's Modulus, E_1	155.1 GPa	22.5 Msi
Young's Modulus, E_2	8.07 GPa	1.17 Msi
Shear Modulus, G_{12}	4.55 GPa	0.66 Msi
Poisson's Ratio, ν_{12}	0.22	
Coeff. of Thermal Exp., α_1	-0.07 $\mu\epsilon/°C$	-0.04 $\mu\epsilon/°F$
Coeff. of Thermal Exp., α_2	30.1 $\mu\epsilon/°C$	16.7 $\mu\epsilon/°F$

Corresponding thermal post-buckling deflections predicted by the classical and finite element analyses are shown in Figure 5.4. In this case, normalized center deflection is plotted against normalized temperature change. Excellent agreement is achieved between the classical and finite element analyses. Again, a fine resolution $N_{\Delta T} = 100$ was used in the finite element analysis for presentation purposes, but more expedient calculation of the final thermal post-buckling deflection was achieved with only one temperature step.

Recall that both cases for which thermal post-buckling deflections were calculated are classified as bifurcation problems. The analogous negative deflection results could be attained by using a thermal buckling eigenvector of opposite sign in the formation of an initial trial vector. Note that this ambiguity is of no consequence to the thermal buckling solution as it is the relative magnitudes in the buckling eigenvector that are important.
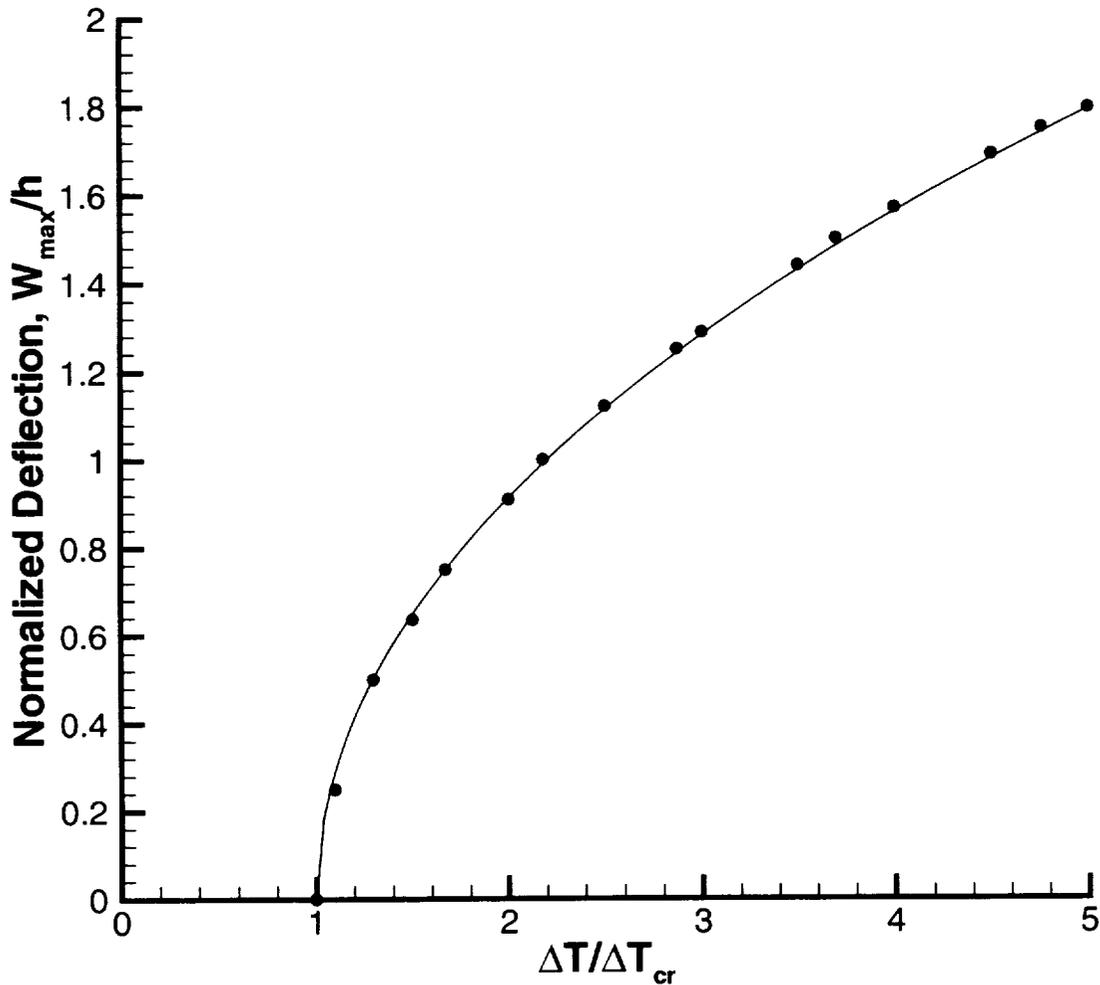
Figure 5.4 Normalized maximum deflection versus normalized ΔT for a simply-supported, 0.152x0.152x0.001 m (6x6x0.040 inches), $(\pm 45/0/90)_s$ graphite-epoxy laminate.

5.5 Experimental Validation

The thermal buckling and post-buckling solutions were validated against known solutions for conventional structures in the previous section. Attention will now turn to experimental measurement of the thermoelastic response of a SMAHC beam. The experimental results will be used to demonstrate some of the phenomena discussed earlier in this chapter and to validate the formulation and solution methods for the case of a SMAHC structure.

5.5.1 Clamped SMAHC Beam

One of the SMAHC beam specimens is shown mounted in an aluminum fixture designed to provide clamped boundary conditions for beam specimens with this geometry in Figure 5.5. The

beam has an unsupported length of 0.4572 m (18 in) within the mechanical grips. The fixture was also designed to provide electrical connection and mechanical restraint for the Nitinol ribbon leads protruding from the ends of the SMAHC beam specimens. The mechanical and electrical grips are indicated in the figure by the symbols "m" and "e", respectively. The electrical connections are isolated from the fixture by a layer of fibrous ceramic insulation. The beam is also thermally isolated from the fixture by a layer of this insulation on both sides. The beam is heated by DC electrical current controlled by a thermocouple measurement located approximately on the beam centerline and 0.0127 m (0.5 in) from the right mechanical grip, indicated in the figure by "tc". The thermal controller consists of a process controller (Omega model CN77353–PV), and a DC power supply (HP model 6652A). Thermocouples also monitor the temperature at each end of the fixture, indicated in Figure 5.5, and one measures the ambient air temperature.
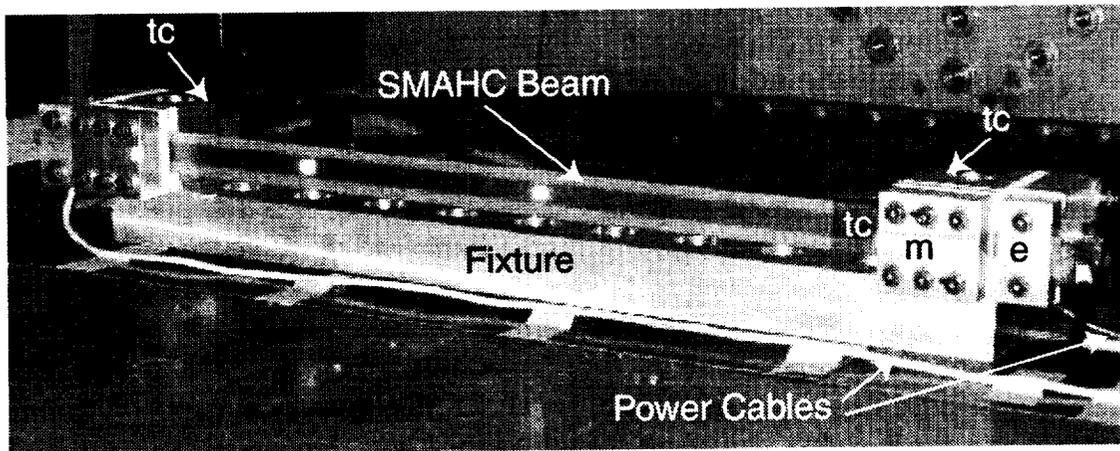
Figure 5.5 Front view of the SMAHC beam specimen mounted in clamping fixture used for static and dynamic testing.

A rear view of the experimental configuration is shown in Figure 5.6, which shows the installation of a laser displacement transducer. The laser displacement transducer (Aromat model LM100) was attached to a three-axis optical positioning traverse, and the assembly was mounted in the vicinity of the beam mid-span. The beam mechanical grips and the ribbon mechanical/electrical grips were torqued to 13.56 N•m (120 in•lbf). The three-axis traverse was used to position the laser impingement position at the beam mid-span and to adjust the laser transducer/beam surface distance to produce zero offset. Changes in beam and fixture temperatures during the gripping process and prior to starting the thermal controller were insignificant. The beam was heated from ambient temperature to 121.1°C (250°F) over a duration of 5 minutes and 11 seconds, then allowed to cool naturally to ambient temperature again. The overall duration of the test was 13 minutes and 26 seconds. Measurements of the ambient air, right/left fixture end, and beam temperatures and the laser transducer output were recorded at approximately 2.5 second intervals.

The beam was modeled with a 36x2 mesh of the 24 degree-of-freedom rectangular plate elements described in Chapter 4. This test constituted thermal cycle number four (4) on the
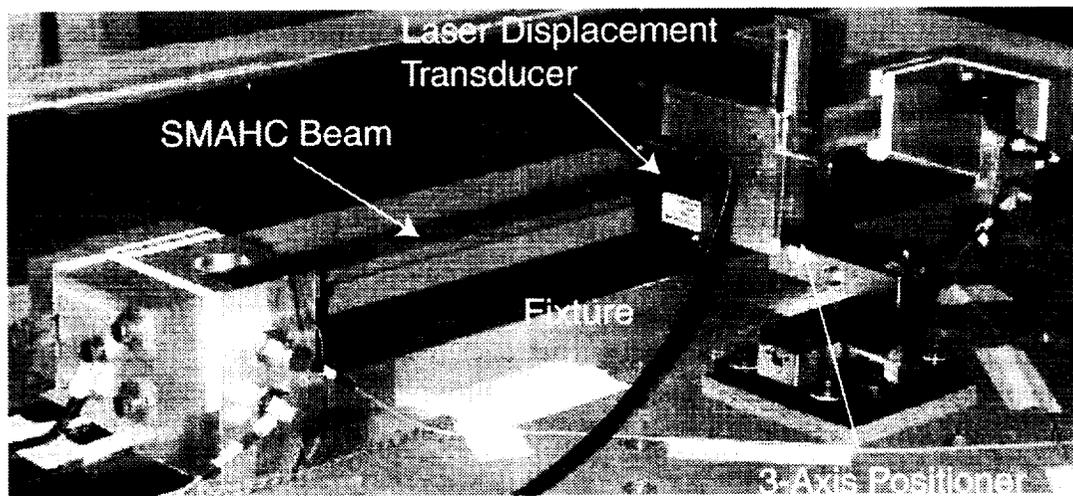
Figure 5.6 Experimental configuration for measurement of
the static thermoelastic response of a SMAHC beam specimen.

Nitinol ribbon in this particular beam specimen. Element properties were constructed from the appropriate measured material properties described in Chapter 3 and given in Tables 3.5 and 3.8. Although the beam ends are held firmly within the mechanical grips, the boundary conditions are not well approximated by perfectly clamped conditions. It will be shown in the Experimental Validation section of Chapter 6 that it was necessary to alter the clamped boundary conditions with torsional springs, with a spring rate of 1.98 N•m/rad (17.5 in•lbf/rad), applied to the longitudinal-slope degrees of freedom to match the fundamental natural frequency. It will be assumed that the boundary conditions for the thermal post-buckling solution are essentially the same as that for the dynamic analysis. In previous experiments, the temperature distribution generated under these conditions was measured with an infrared thermal imaging camera. It was found that the temperature distribution was remarkably uniform along the unsupported length of the beam. Therefore, the thermal load was modeled as a uniform temperature distribution.

A comparison between the measured and predicted thermal post-buckling deflection (normalized to the beam thickness) at the beam mid-span is shown in Figure 5.7. Note that the measured deflection does exhibit the first part of the complex thermoelasitic behavior described earlier in this chapter; buckling at a temperature below A_s, achieving a maximum deflection where the Nitinol recovery stress starts to dominate, and returns to a flat configuration for the remainder of the test. The reason that a second instance of buckling is not exhibited is that the volume fraction of Nitinol is high enough in this case to drive the predicted second buckling temperature well beyond the glass-transition temperature for the matrix material.

The predicted post-buckling behavior is in excellent qualitative agreement with the experimental measurement. The main differences between the predicted and measured responses are the slope of the curve from initial buckling to the maximum deflection point, the magnitude of the maximum deflection, and the temperature at which the post-buckling deflection is returned to zero. These discrepancies are attributable to the fact that these systems are extremely sensitive to a multitude of factors including initial deflection, initial stress, boundary conditions, etc. For example, initial deflection in the physical beam is the reason for the more gradual growth of
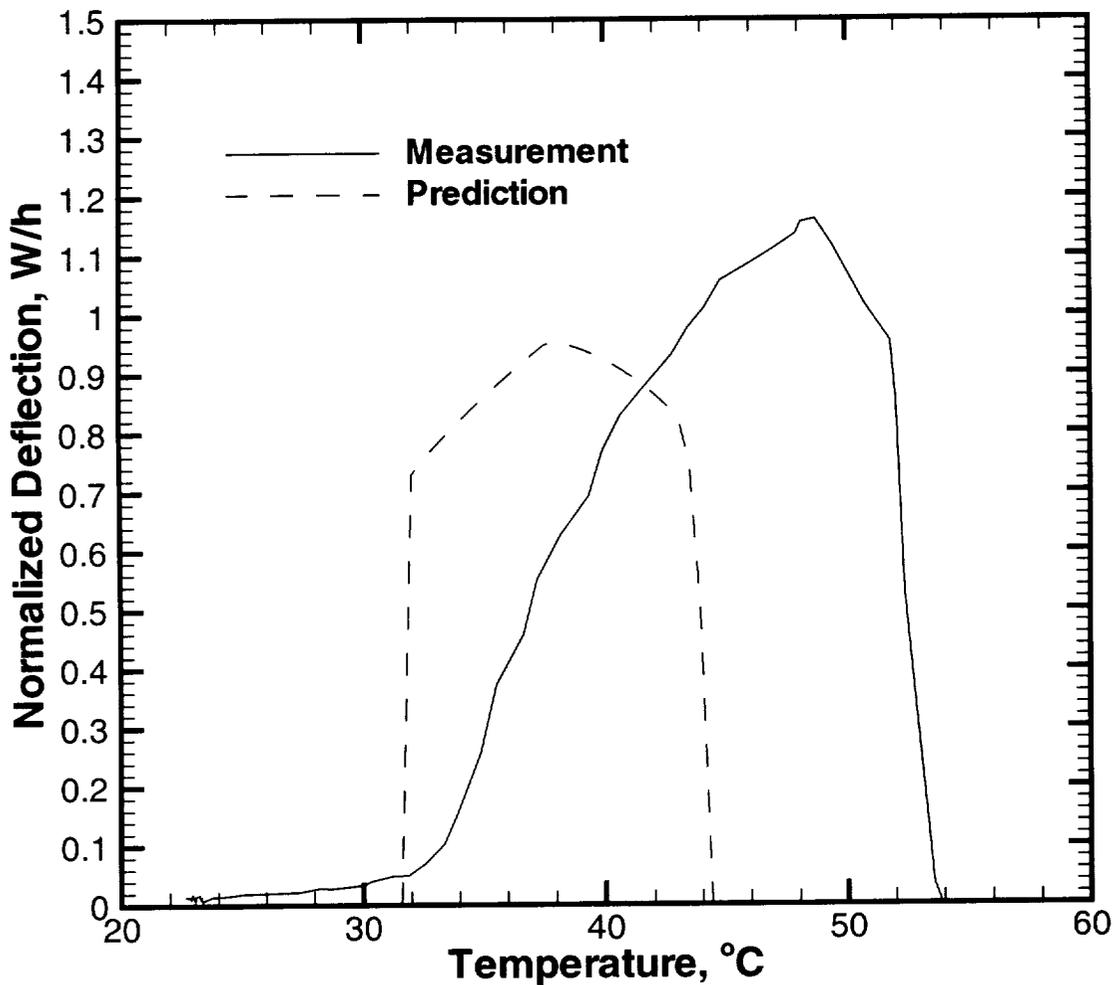
Figure 5.7 Measured and predicted thermal post-buckling deflection
(normalized to the beam thickness) at the mid-span of the SMAHC beam.

thermal deflection in the experimental results. The discrepancies in peak deflection and deflection elimination temperature are attributable to boundary conditions.

Note that the in-plane boundary conditions are modeled as immovable. Recall that in the physical system the beam continues through the mechanical grips and the Nitinol leads are terminated beyond that in the electrical grips. Only the ribbon/matrix interface supports the recovery force within the mechanical grip area. The main restraint for the Nitinol is the mechanical termination at the electrical grips. Thus, the compliance of the entire support structure, from one electrical grip to the other, needs to be considered. It was found that the layer of electrical insulation between the electrical and mechanical grips was the cause for the discrepancies. A compression test was performed on the insulating material and the modulus

was found to be less than 137.9 MPa (20 ksi). While the exact stiffness of the boundary would be difficult to quantify, there is no doubt that strain in the insulation is partially relieving the recovery stress and causing a diminished stiffening effect in the physical system. Changes in the model to reflect the compliant in-plane boundaries would move the predicted buckling temperature, peak deflection, and deflection elimination temperature to better agreement with experimental measurement.

In this chapter, the static stability of a structure described by the governing equations developed in the previous chapter was analyzed and solution procedures were developed to predict the thermal buckling and post-buckling behavior of SMAHC structures. The formulation and procedures were validated against known solutions prior to attempting correlation with experiment. Experimental results from a SMAHC beam specimen confirm complex thermoelastic behavior that was predicted by the model. Excellent agreement was achieved between prediction and experimental measurement and reasons for existing discrepancies were discussed. A similar approach will be taken in the next chapter, where the dynamic response performance of a SMAHC beam will be demonstrated and compared with numerical prediction.

Chapter 6
Dynamic Response

The analytical techniques and computational methods used to solve the equations governing the dynamic response of SMA hybrid composite panel-type structures subjected to mechanical and thermal loads are treated in this chapter. The thermal load is assumed to be steady-state and uniform through the thickness of the structure, i.e., $T = T(x, y)$. Mechanical loads are assumed to consist of surface pressure, concentrated forces, and inertial (base acceleration) loads. Continuous and discrete frequency domain analyses are presented. Validation of the analyses with known solutions for fundamental cases and with experimental results for several cases including a SMA hybrid composite beam are presented.

6.1 Equations of Motion

The equations of motion for the system described above were derived in Chapter 4, equation (4.108), and can be rewritten in the compact form

$$[M]\{\ddot{A}\} + [\bar{K}]\{A\} = \{P(t)\} + \{F(t)\} - [M]\{\ddot{U}_g\} \tag{6.1}$$

where $[\bar{K}]$ is the stiffness matrix for the flat or buckled/deflected structure. For a flat (unbuckled) structure

$$
\begin{aligned}
[\bar{K}] &= [K] - [K_{\Delta T}] + [N1] & \text{unbuckled} \\
[\bar{K}] &= [K_{tan}] = [K] - [K_{\Delta T}] + [N1] + [N2] & \text{buckled}
\end{aligned}
\tag{6.2}
$$

Note that the only nonzero entries in $[N1]$ for the unbuckled case are due to $[N1_b]$ resulting from the in-plane displacements, see equation (5.16), and the stiffness matrix for the thermally buckled structure is precisely the converged tangent stiffness matrix from the thermal post-buckling solution. For a thermally buckled/deflected structure

$$[\bar{K}] = ([K] - [K_{N_{\Delta T}}] + [N1] + [N2]) \tag{6.3}$$

where the nonlinear stiffness matrices $[N1]$ and $[N2]$ are evaluated using the thermally buckled/deflected displacements $\{A\}_s$. Although it is not necessary, the three dynamic load vectors will be considered separately for clarity in the dynamic response solution and because practical experimental configurations dictate separate loading cases.
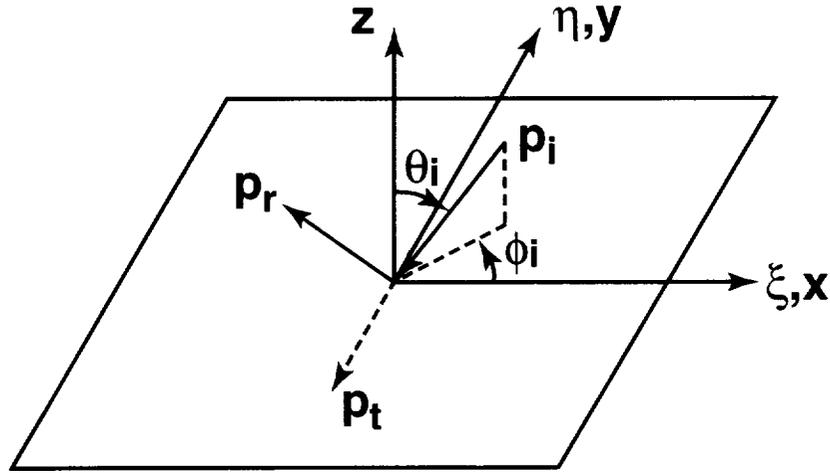
Figure 6.1 Schematic of acoustically excited panel.

6.1.1 Acoustic Excitation

Recall the form for the surface pressure excitation load vector from equation (4.56)

$$\{P(t)\} = \left\{ \begin{array}{c} P_b(t) \\ 0 \end{array} \right\}$$

(6.4)

The bending components for the system are assembled from the element contributions given in equations (4.55), which can be rewritten as

$$\{p_b(t)\} = \int_{A_e} p(\xi, \eta, t)\{L_w(\xi, \eta)\} \; dA_e$$

(6.5)

where $p(\xi, \eta, t)$ is the spatial and temporal description of the pressure, $\{L_w(\xi, \eta)\}$ is the vector of out-of-plane interpolation functions, (ξ, η) are the coordinates in the plane of the structure, and A_e is the area of the element.

In this study, it is assumed that the surface pressure is generated by acoustic excitation. Then the pressure loading on the structure consists of the incident pressure, the reflected pressure, and the transmitted pressure as shown schematically in Figure 6.1:

$$p(\xi, \eta, t) = p_i(\xi, \eta, t) + p_r(\xi, \eta, t) - p_t(\xi, \eta, t)$$

(6.6)

The pressure loading may also be written as the sum of the *blocked* pressure and the *radiated* pressure, as suggested by Roussos [52]. The blocked pressure is the pressure on the incident side when the structure is considered rigid, i.e., $p_b(\xi, \eta, t) = 2\,p_i(\xi, \eta, t)$, and the radiated pressure is that due to structure motion only. The acoustic radiation problem can be solved subsequent to the forced response solution by assuming that the radiated pressure is negligible compared to the blocked pressure. This assumption results in inaccurate predictions only at frequencies near the panel fundamental resonance. Thus, the load vector $\{P_b(t)\}$ is formed using the blocked pressure $(p(\xi, \eta, t) = p_b(\xi, \eta, t) = 2p_i(\xi, \eta, t))$ and the transmitted pressure (pressure radiated to the free field) can be determined from the resulting structural motion, without the need for a fully coupled analysis.

106

Furthermore, it is assumed in this study that the acoustic pressure excitation consists of obliquely incident plane waves of arbitrary temporal variation. Then, the general form for the acoustic pressure along the direction of propagation given by a Cartesian coordinate s has the form

$$p_i(\xi, \eta, t) = p(t - s/c)$$
$$= p(t - \hat{n} \cdot \vec{r}/c)$$

(6.7)

where $\hat{n}$ is a unit normal aligned with the direction of propagation in the coordinate system designated by $\vec{r}$. So, the incident pressure (i.e., $z = 0$) can be described by

$$p_i(\xi, \eta, t) = p(t - \xi \sin \theta_i \cos \phi_i/c - \eta \sin \theta_i \sin \phi_i/c)$$

(6.8)

where θ_i and ϕ_i are the polar and azimuthal angles of incidence, respectively.

The incident pressure is modeled by nodal pressures because of the spatial discretization of the finite element approach. Then, the blocked pressure element load vector in equation (6.5) becomes

$$\{p_b(t)\} = \int_{A_e} 2\{L_w(\xi, \eta)\} p(t - \xi \sin \theta_i \cos \phi_i/c - \eta \sin \theta_i \sin \phi_i/c) \, dA_e$$

(6.9)

A more simple form for non-normal blocked acoustic pressure loading will be developed in the discrete spectral response section. In the case of normal acoustic pressure excitation, equation 6.9 simplifies to the following

$$\{p_b(t)\} = \int_{A_e} 2\{L_w(\xi, \eta)\} p(t) \, dA_e$$
$$= \{\gamma_b\} p(t)$$

(6.10)

So, the acoustic load vector for the entire system is assembled from element contributions given in either of the latter two equations. The system load vector for the normal acoustic excitation case takes a simple form

$$\{P_b(t)\} = \{\Gamma\} p(t)$$

(6.11)

6.1.2 Concentrated Force Excitation

The concentrated force load vector from equation (4.56) has an analogous form as follows

$$\{F(t)\} = \left\{ \begin{array}{c} F_b(t) \\ 0 \end{array} \right\}$$

(6.12)

The out-of-plane displacement (bending) components for the system are assembled from the element contributions given in equations (4.55), which can be rewritten as

$$\{f_b(t)\} = \sum_{i=1}^{n_f} \int_{A_e} f_i'(t) \, \delta(\{\xi\} - \{\xi\}_i)\{L_w(\xi, \eta)\} \, dA_e$$

(6.13)

where $f_i'(t)$ is the temporal description of the concentrated force(s), $\delta(\{\xi\} - \{\xi\}_i)$ is a spatial Dirac delta function, and n_f is the number of forces within the element area. Note that the concentrated forces can be arbitrarily correlated.

It is assumed that the concentrated force(s) are applied at nodal locations in the model. Otherwise, the effect of the concentrated force would be distributed to nodes of the element containing the force, which is an undesirable effect. Evaluation of the element area integral in equation (6.13) simplifies the form for the element contributions to the concentrated force load vector:

$$\{f_b(t)\} = \sum_{i=1}^{n_f} f_i'(t)\{L_w(\xi_i, \eta_i)\}$$

$$= \sum_{i=1}^{n_f} \{\gamma_b\}_i f_i'(t)$$

(6.14)

Assembly of the element contributions in the system concentrated load vector simply positions each concentrated force at a location in the system load vector corresponding to the associated out-of-plane degree of freedom. Then, the resulting concentrated load vector for the entire system can be written as follows

$$\{F_b(t)\} = \{f'(t)\}$$

(6.15)

where the only nonzero components in $\{f'(t)\}$ correspond to forced nodal locations.

6.1.3 Inertial Excitation

The inertial loading can be expressed in an analogous load vector form from equation (4.56):

$$\{G(t)\} = \left\{\begin{array}{c} G_b(t) \\ 0 \end{array}\right\} = -\left[\begin{array}{cc} M_b & 0 \\ 0 & M_m \end{array}\right]\left\{\begin{array}{c} \ddot{U}_g(t) \\ 0 \end{array}\right\}$$

(6.16)

The out-of-plane displacement components for the system are assembled from the element contributions:

$$\{g_b(t)\} = -[m_b]\{\ddot{u}_g(t)\}$$

$$= -[m_b]\{1\}\ddot{u}_g(t)$$

$$= \{\gamma_b\}\ddot{u}_g(t)$$

(6.17)

where $\{1\}$ is a vector with unit entries and $\ddot{u}_g(t)$ is the temporal description of the spatially uniform base acceleration. So, the system inertial load vector can be written as follows

$$\{G_b(t)\} = \{\Gamma\}\ddot{u}_g(t)$$

(6.18)

Solutions to the system of equations given in equation (6.1) can be sought using physical or modal degrees of freedom. The modal approach has the advantage of vastly improved computational speed without significant loss in accuracy in many cases. The modal approach is also quite useful, particularly when comparing with experimental measurements, as powerful tools such as experimental modal analysis can be used for incremental validation of the analytical model. The modal approach will be used in this study and is discussed briefly here.

6.2 Eigen-solution and Modal Coordinates

Natural frequencies ω_r and mode shapes $\{\phi_r\}$ of the vibration about static equilibrium can be obtained from the dynamic eigenvalue problem

$$\omega_r^2 [M]\{\phi_r\} = [K]\{\phi_r\} \tag{6.19}$$

A set of uncoupled modal equations with reduced degrees of freedom can thus be obtained from equation (6.1) as

$$\lceil I \rfloor \{\ddot{q}(t)\} + \lceil 2\zeta_r\omega_r \rfloor \{\dot{q}(t)\} + \lceil \omega_r^2 \rfloor \{q(t)\} = \{f(t)\} \tag{6.20}$$

where $r = 1, 2, \ldots, N_q$, the delimiters $\lceil \rfloor$ indicate a diagonal matrix, and $\lceil I \rfloor$ is the identity matrix, and ζ_r is the modal critical damping ratio. The modal force vector $\{f(t)\}$ is given by one of the following expressions as the time dependent loads are considered separately

$$
\begin{aligned}
\{f(t)\} &= [\phi]^T \{p(t)\} && \text{acoustic pressure excitation} \\
&= [\phi]^T \{\Gamma\} p(t) && \text{normal acoustic pressure} \\
\{f(t)\} &= [\phi]^T \{f'(t)\} && \text{concentrated force excitation} \\
\{f(t)\} &= [\phi]^T \{\Gamma\} \ddot{u}_g(t) && \text{inertial/base excitation}
\end{aligned}
\tag{6.21}
$$

The physical degrees of freedom can be recovered from the truncated modal transformation:

$$\{A(t)\} = \sum_{r=1}^{N_q} \{\phi\}_r q_r(t) = [\phi]\{q(t)\} \qquad N_q \leq N_{dof} \tag{6.22}$$

where $[\phi]$ is the modal matrix, N_q is the number of modes retained, and N_{dof} is the total number of degrees of freedom.

The modal response, solution to the modal equations of motion (6.20), can be determined by time domain or frequency domain analysis. In either case, a continuous or discrete approach can be employed. In this study, dynamic analysis is done in the frequency domain through continuous and discrete techniques. The continuous frequency domain approach is included mainly for demonstrative and comparative purposes. The discrete frequency domain approach employed in this study is the main spectral solution tool because of the ability to handle complicated frequency distributions in a straightforward manner.

6.3 Continuous Spectral Analysis — Random Response

The time response of the modal coordinates can be obtained from the convolution (Duhamel's) integral

$$\{q(t)\} = \int_{t_0}^{t} \lceil h(t-\tau) \rfloor \{f(\tau)\}\, d\tau = \int_{0}^{t-t_0} \lceil h(\tau) \rfloor \{f(t-\tau)\}\, d\tau \tag{6.23}$$

where $\lceil h(t) \rceil$ is a diagonal matrix of impulse response functions and $\{f(t)\}$ is the modal force vector. The modal response correlation matrix $[C_{qq}(t_1, t_2)]$ can be formed from the following expected value

$$E[\{q(t_1)\}\{q(t_2)\}^T] = \int_0^{t_1-t_0} \int_0^{t_2-t_0} \lceil h(\tau_1) \rceil E[\{f(t_1 - \tau_1)\}\{f(t_2 - \tau_2)\}^T]\lceil h(\tau_2) \rceil \, d\tau_1 d\tau_2 \quad (6.24)$$

where the expected value in the integrand is the correlation matrix of the excitation $[C_{ff}(t_1 - \tau_1, t_2 - \tau_2)]$.

The correlation matrix for *stationary excitation* becomes a function of the time difference only and will be denoted as follows

$$E[\{f(t_1 - \tau_1)\}\{f(t_2 - \tau_2)\}^T] = [C_{ff}(t_2 - t_1 + \tau_1 - \tau_2)] \quad (6.25)$$

For a load with spectral density $S_{ff}(\omega)$ or $G_{ff}(f)$, the Wiener-Khinchine relations for stationary random processes gives

$$[C_{ff}(t_2 - t_1 + \tau_1 - \tau_2)] = \int_{-\infty}^{\infty} [S_{ff}(\omega)] e^{i\omega(t_2-t_1+\tau_1-\tau_2)} \, d\omega$$

$$= \int_0^{\infty} [G_{ff}(f)] e^{i2\pi f(t_2-t_1+\tau_1-\tau_2)} \, df \quad (6.26)$$

where $G_{ff}(f) = 4\pi S_{ff}(\omega)$ for $\omega = 2\pi f$ ($f \geq 0$). The modal response correlation matrix, equation (6.24), then becomes

$$[C_{qq}(t_1, t_2)] = \int_{-\infty}^{\infty} \int_0^{t_1-t_0} \lceil h(\tau_1) \rceil e^{i\omega\tau_1} d\tau_1 [S_{ff}(\omega)] e^{i\omega(t_2-t_1)} \int_0^{t_2-t_0} \lceil h(\tau_2) \rceil e^{-i\omega\tau_2} d\tau_2 \, d\omega$$

$$= \int_{-\infty}^{\infty} \lceil \mathcal{H}^*(\omega, t_1) \rceil [S_{ff}(\omega)] \lceil \mathcal{H}(\omega, t_2) \rceil e^{i\omega(t_2-t_1)} d\omega \quad (6.27)$$

where $\lceil \mathcal{H}(\omega, t) \rceil$ is a diagonal matrix of transient frequency response functions.

For *stationary response*, let $t_0 \rightarrow -\infty$ and $\mathcal{H}(\omega, t) \rightarrow H(\omega)$ so the modal displacement correlation matrix becomes

$$[C_{qq}(\tau)] = \int_{-\infty}^{\infty} \lceil H^*(\omega) \rceil [S_{ff}(\omega)] \lceil H(\omega) \rceil e^{i\omega\tau} d\omega \quad (6.28)$$

where $\tau = t_2 - t_1$ and

$$H_r(\omega) = \frac{1}{\omega_r^2 - \omega^2 + 2i\zeta_r\omega_r\omega} \quad (6.29)$$

110

is a stationary frequency response function. Assuming mean-square differentiability, Correlations of the modal velocity and acceleration responses can be determined by assuming mean-square differentiability:

$$[C_{\dot{q}\dot{q}}(\tau)] = \int_{-\infty}^{\infty} \omega^2 \lceil H^*(\omega) \rceil \left[S_{ff}(\omega) \right] \lceil H(\omega) \rceil e^{i\omega\tau} \, d\omega \qquad (6.30)$$

and

$$[C_{\ddot{q}\ddot{q}}(\tau)] = \int_{-\infty}^{\infty} \omega^4 \lceil H^*(\omega) \rceil \left[S_{ff}(\omega) \right] \lceil H(\omega) \rceil e^{i\omega\tau} \, d\omega \qquad (6.31)$$

where the relations $\frac{\partial}{\partial t_1} = -\frac{d}{d\tau}$ and $\frac{\partial}{\partial t_2} = \frac{d}{d\tau}$ have been employed. The three modal response correlation matrices can be written in the following concise form.

$$([C_{qq}(\tau)], [C_{\dot{q}\dot{q}}(\tau)], [C_{\ddot{q}\ddot{q}}(\tau)]) = \int_{-\infty}^{\infty} \omega^{(0,2,4)} \lceil H^*(\omega) \rceil \left[S_{ff}(\omega) \right] \lceil H(\omega) \rceil e^{i\omega\tau} \, d\omega \qquad (6.32)$$

Note that an arbitrary element (r,s) of the modal response correlation matrices has the following form

$$(E[q_r(t)q_s(t+\tau)], E[\dot{q}_r(t)\dot{q}_s(t+\tau)], E[\ddot{q}_r(t)\ddot{q}_s(t+\tau)]) = E[C_{q_r q_s}(\tau), C_{\dot{q}_r \dot{q}_s}(\tau), C_{\ddot{q}_r \ddot{q}_s}(\tau)]$$

$$= \int_{-\infty}^{\infty} \omega^{(0,2,4)} H_r^*(\omega) H_s(\omega) S_{ff}^{rs}(\omega) e^{i\omega\tau} d\omega$$

$$= \int_{-\infty}^{\infty} (2\pi f)^{(0,2,4)} H_r^*(f) H_s(f) G_{ff}^{rs}(f) e^{i2\pi f\tau} df$$

$$(6.33)$$

Recall the expression for the modal force vector $\{f(t)\}$ for each load type from equations (6.21). Then, the modal force vector correlation and spectral density matrices become

$$[C_{ff}(\tau)] = [\phi]^T [C_{pp}(\tau)][\phi] \qquad \Rightarrow \qquad [S_{ff}(\omega)] = [\phi]^T [S_{pp}(\omega)][\phi]$$

$$[C_{ff}(\tau)] = [\phi]^T [C_{f'f'}(\tau)][\phi] \qquad \Rightarrow \qquad [S_{ff}(\omega)] = [\phi]^T [S_{f'f'}(\omega)][\phi]$$

$$[C_{ff}(\tau)] = [\phi]^T \{\Gamma\} C_{\ddot{u}_g \ddot{u}_g}(\tau)\{\Gamma\}^T[\phi] \qquad \Rightarrow \qquad [S_{ff}(\omega)] = [\phi]^T \{\Gamma\} S_{\ddot{u}_g \ddot{u}_g}(\omega)\{\Gamma\}^T[\phi]$$

$$(6.34)$$

for acoustic pressure, concentrated force, and base acceleration excitation, respectively. For the case of normal acoustic pressure, the corresponding relations above reduce to

$$[C_{ff}(\tau)] = [\phi]^T \{\Gamma\} C_{pp}(\tau)\{\Gamma\}^T[\phi] \qquad \Rightarrow \qquad [S_{ff}(\omega)] = [\phi]^T \{\Gamma\} S_{pp}(\omega)\{\Gamma\}^T[\phi] \qquad (6.35)$$

The main simplification in these expressions is the presence of a single auto-correlation/power-spectral-density function rather than a covariance/spectral-density matrix describing the spatial variation of the acoustic load. Note that for the cases of normal acoustic, single concentrated

force, or base acceleration excitation, the spectral density function in the integrand of equation (6.33) is the same for all elements (r, s) of the modal response correlation matrices:

$$(E[q_r(t)q_s(t+\tau)], E[\dot{q}_r(t)\dot{q}_s(t+\tau)], E[\ddot{q}_r(t)\ddot{q}_s(t+\tau)]) = \int_{-\infty}^{\infty} \omega^{(0,2,4)} H_r^*(\omega) H_s(\omega) S_{**}(\omega) e^{i\omega\tau} d\omega$$

$$= \int_0^{\infty} (2\pi f)^{(0,2,4)} H_r^*(f) H_s(f) G_{**}(f) e^{i2\pi f\tau} df$$

(6.36)

Examples of the evaluation of these integrals for determination of the dynamic response quantities are given in Appendix F.

The responses in the physical coordinates can be recovered from the modal expansion, equation (6.22), i.e.,

$$[C_{AA}(\tau)] = [\phi][C_{qq}(\tau)][\phi]^T$$

(6.37)

Thus, the physical coordinate displacement, velocity, and acceleration correlation matrices become

$$([C_{AA}(\tau)], [C_{\dot{A}\dot{A}}(\tau)], [C_{\ddot{A}\ddot{A}}(\tau)]) = \int_{-\infty}^{\infty} \omega^{(0,2,4)} [\phi][H^*(\omega)][S_{ff}(\omega)][H(\omega)][\phi]^T e^{i\omega\tau} d\omega$$

(6.38)

6.4 Discrete Spectral Analysis

A discrete spectral analysis approach will now be formulated as an alternative to the continuous approach because continuous approaches are limited to rather simple loading cases, which are not very realistic for practical applications and not easily generated in an experimental situation. In practice, there is always a finite amount of data. Thus, one would employ a Finite Fourier Transform to a sampled time history as observed through a time window. Furthermore, for discretely sampled time data, a Discrete Fourier Transform (DFT) can be used to estimate the Finite Fourier Transforms, etc. A particularly efficient means of performing a DFT is known as the Fast Fourier Transform (FFT). Of greater importance is that most experimental data is processed via the FFT. A means of using experimentally measured data has obvious beneficial implications.

A discrete spectral analysis can be employed by assuming that the modal force vector, and thus the modal response, can be written as the sum of harmonic functions:

$$\{f(t)\} = \sum_{n=0}^{N_\omega-1} \{\hat{f}_n\} e^{i\omega_n t}$$

(6.39)

and

$$\{q(t)\} = \sum_{n=0}^{N_\omega-1} \{\hat{q}_n\} e^{i\omega_n t}$$

(6.40)

112

where N_ω is the number of discrete frequencies in the transformation and $\{\hat{f}_n\}$ and $\{\hat{q}_n\}$ are the complex spectral amplitude vectors, one for each frequency (see Doyle [53]). Recall the modal expansion for the physical coordinate response from equation (6.22):

$$
\begin{aligned}
\{A(t)\} &= \sum_{n=0}^{N_\omega-1} \{\hat{A}_n\} e^{i\omega_n t} \\
&= \sum_{n=0}^{N_\omega-1} [\phi]\{\hat{q}_n\} e^{i\omega_n t}
\end{aligned}
\tag{6.41}
$$

Substitution of equations (6.39) and (6.40) into the modal equations of motion, equation (6.20), gives

$$
\sum_{n=0}^{N_\omega-1} (-\omega_n^2 \lceil I \rfloor + i\omega_n \lceil 2\zeta_r\omega_r \rfloor + \lceil \omega_r^2 \rfloor)\{\hat{q}_n\} e^{i\omega_n t} = \sum_{n=0}^{N_\omega-1} \{\hat{f}_n\} e^{i\omega_n t}
\tag{6.42}
$$

This relation can be written for any one of the discrete frequencies ω_n as

$$
(\lceil -\omega_n^2 \rfloor + \lceil i2\zeta_r\omega_r\omega_n \rfloor + \lceil \omega_r^2 \rfloor)\{\hat{q}_n\} = \{\hat{f}_n\}
\tag{6.43}
$$

This relation is simply a set of uncoupled algebraic equations for the modal displacement spectral amplitudes. Thus, the modal displacement spectral amplitude vector becomes

$$
\{\hat{q}_n\} = \lceil H(\omega_n) \rfloor \{\hat{f}_n\}
\tag{6.44}
$$

where the $\lceil H(\omega_n) \rfloor$ is a diagonal matrix of frequency response functions given by

$$
H_r(\omega_n) = \frac{1}{\omega_r^2 - \omega_n^2 + i2\zeta_r\omega_r\omega_n}
\tag{6.45}
$$

Recall the expression for the incident acoustic pressure in equation (6.8). In this discrete spectral analysis, the incident pressure is written as a sum of harmonic components:

$$
\begin{aligned}
p_i(\xi, \eta, t) &= p(t - \xi \sin\theta_i \cos\phi_i - \eta \sin\theta_i \sin\phi_i) \\
&= \sum_{n=0}^{N_\omega-1} \hat{p}_n e^{i(\omega_n t - k_n \xi \sin\theta_i \cos\phi_i - k_n \eta \sin\theta_i \sin\phi_i)}
\end{aligned}
\tag{6.46}
$$

where $k_n = \omega_n/c$ is the acoustic wave number. Then, the blocked pressure element load vector from equation (6.9) becomes

$$
\begin{aligned}
\{p_b(t)\} &= \sum_{n=0}^{N_\omega-1} \int_{A_c} 2\hat{p}_n \{L_w(\xi, \eta)\} e^{i(\omega_n t - \xi\kappa_n - \eta\lambda_n)} \\
&= \sum_{n=0}^{N_\omega-1} \{\gamma_{bn}\} \hat{p}_n e^{i\omega_n t}
\end{aligned}
\tag{6.47}
$$

where $\kappa_n = k_n \sin\theta_i \cos\phi_i$ and $\lambda_n = k_n \sin\theta_i \sin\phi_i$ and $\{\gamma_{bn}\}$ contains the integrated spatial correlation information of the incident acoustic pressure. The assembled system load vector due to acoustic excitation would be written as

$$\{P_b(t)\} = \sum_{n=0}^{N_\omega-1} \{\Gamma_n\}\hat{p}_n e^{i\omega t} \tag{6.48}$$

The modal force vector is related to the mechanical excitation load vectors from the Galerkin weighted average of the modal system (modal system diagonalization), equation (6.21):

$$
\begin{aligned}
\{f(t)\} &= [\phi]^T\{p(t)\} &\Rightarrow&& \{\hat{f}_n\} &= [\phi]^T\{\Gamma_n\}\hat{p}_n \\
\{f(t)\} &= [\phi]^T\{f'(t)\} &\Rightarrow&& \{\hat{f}_n\} &= [\phi]^T\{\hat{f}'_n\} \\
\{f(t)\} &= [\phi]^T\{\Gamma\}\ddot{u}_g(t) &\Rightarrow&& \{\hat{f}_n\} &= [\phi]^T\{\Gamma\}\hat{u}_{gn}
\end{aligned}
\tag{6.49}
$$

where $\hat{p}_n$, $\hat{f}'_n$, and $\hat{u}_{gn}$ are the complex spectral amplitudes of the acoustic pressure, concentrated force, and base acceleration, respectively. Note that, in contrast to the acoustic pressure modal force spectral density matrix in the continuous spectral analysis, the expression for the modal force spectral amplitude due to acoustic pressure is valid for any angles of incidence.

If the excitation is deterministic, the dynamic response solution in terms of modal displacement, velocity, and acceleration time responses can be computed by an inverse FFT from equations (6.40) and (6.44):

$$\left(\{q(t)\},\{\dot{q}(t)\},\{\ddot{q}(t)\}\right) = \sum_{n=0}^{N_\omega-1} (i\omega_n)^{(0,1,2)}\lceil H(\omega)\rfloor\{\hat{f}_n\}e^{i\omega_n t} \tag{6.50}$$

where the modal force spectral amplitude has one of the forms given in equations (6.49). Then the responses in physical coordinates follow from equation (6.41):

$$\left(\{A(t)\},\{\dot{A}(t)\},\{\ddot{A}(t)\}\right) = \sum_{n=0}^{N_\omega-1} (i\omega_n)^{(0,1,2)}[\phi]\lceil H(\omega)\rfloor\{\hat{f}_n\}e^{i\omega_n t} \tag{6.51}$$

However, for stochastic excitation, a statistical approach must be used. Additionally, dynamic response cross-correlation quantities are of interest for the acoustic radiation discussion to follow in the next chapter. Therefore, the necessary relations for stochastic dynamic response will be developed next.

The modal displacement response correlation matrix can be formed from equation (6.40) as the following expected value

$$
\begin{aligned}
[C_{qq}(t_1,t_2)] &= E[\{q(t_1)\}\{q(t_2)\}^T] \\
&= \sum_{m=0}^{N_\omega-1}\sum_{n=0}^{N_\omega-1} E[\{\hat{q}_m^*\}\{\hat{q}_n\}^T]e^{i(\omega_n t_2 - \omega_m t_1)}
\end{aligned}
\tag{6.52}
$$

Substituting from equation (6.44) gives

$$[C_{qq}(t_1,t_2)] = \sum_{m=0}^{N_\omega-1}\sum_{n=0}^{N_\omega-1} \lceil H^*(\omega_m)\rfloor E[\{\hat{f}_m^*\}\{\hat{f}_n\}^T]\lceil H(\omega_n)\rfloor e^{i(\omega_n t_2 - \omega_m t_1)} \tag{6.53}$$

where $E[\{\hat{f}_m^*\}\{\hat{f}_n\}^T]$ is a generalized spectral matrix. Note that if the excitation is deterministic, the ensemble average indicated by the expected value in equation (6.53) is not necessary. If the excitation is stochastic, the necessary ensemble averages can be performed ahead of time.

For a stationary process, the expected value of the excitation complex spectral amplitudes takes a special form [54]

$$E[\{\hat{f}_m^*\}\{\hat{f}_n\}^T] = E[\{\hat{f}_m^*\}\{\hat{f}_n\}^T]\delta_{mn} \tag{6.54}$$

where δ_{mn} is the Kronecker delta. Then, the stationary modal displacement correlation matrix results

$$[C_{qq}(\tau)] = \sum_{n=0}^{N_\omega-1} E[\{\hat{q}_n^*\}\{\hat{q}_n\}^T]e^{i\omega_n\tau} \tag{6.55}$$

where $\tau = t_2 - t_1$. The stationary modal velocity and acceleration correlation matrices follow from the relations $\frac{\partial}{\partial t_1} = -\frac{d}{d\tau}$ and $\frac{\partial}{\partial t_2} = \frac{d}{d\tau}$ as

$$[C_{\dot{q}\dot{q}}(\tau)] = \sum_{n=0}^{N_2-1} \omega_n^2 E[\{\hat{q}_n^*\}\{\hat{q}_n\}^T]e^{i\omega_n\tau}$$

$$[C_{\ddot{q}\ddot{q}}(\tau)] = \sum_{n=0}^{N_2-1} \omega_n^4 E[\{\hat{q}_n^*\}\{\hat{q}_n\}^T]e^{i\omega_n\tau} \tag{6.56}$$

The full expressions can be written in the following concise form for convenience

$$([C_{qq}(\tau)], [C_{\dot{q}\dot{q}}(\tau)], [C_{\ddot{q}\ddot{q}}(\tau)]) = \sum_{n=0}^{N_\omega-1} \omega_n^{(0,2,4)} \lceil H^*(\omega_n) \rfloor E[\{\hat{f}_n^*\}\{\hat{f}_n\}^T]\lceil H(\omega_n)\rfloor e^{i\omega_n\tau}$$

$$= \sum_{n=0}^{N_\omega-1} \omega_n^{(0,2,4)} \lceil H^*(\omega_n)\rfloor [G_{ff}(\omega_n)]\lceil H(\omega_n)\rfloor e^{i\omega_n\tau} \tag{6.57}$$

where appropriate quantities from equations (6.49) are employed to evaluate the single-sided, stationary modal force spectral matrix $[G_{ff}(\omega_n)]$ for circular frequency ω_n:

$$[G_{ff}(\omega_n)] = [\phi]^T\{\Gamma_n^*\}\hat{p}_n^*\hat{p}_n\{\Gamma_n\}^T[\phi] \qquad \text{acoustic pressure}$$

$$[G_{ff}(\omega_n)] = [\phi]^T\{\hat{f}_n'^*\}\{\hat{f}_n'\}^T[\phi] \qquad \text{concentrated forces} \tag{6.58}$$

$$[G_{ff}(\omega_n)] = [\phi]^T\{\Gamma_n\}\hat{u}_{gn}^*\hat{u}_{gn}\{\Gamma_n\}^T[\phi] \qquad \text{base acceleration}$$

Again, the responses in physical coordinates are obtained from the modal expansion

$$([C_{AA}(\tau)], [C_{\dot{A}\dot{A}}(\tau)], [C_{\ddot{A}\ddot{A}}(\tau)]) = \sum_{n=0}^{N_\omega-1} \omega_n^{(0,2,4)}[\phi]\lceil H^*(\omega_n)\rfloor [G_{ff}(\omega_n)]\lceil H(\omega_n)\rfloor [\phi]^T e^{i\omega_n\tau} \tag{6.59}$$

These expressions for the modal and physical coordinate response correlation matrices are the discrete analogs to those given in equations (6.32) and (6.38). The modal/physical response

mean-square values (variances) are determined from the diagonal elements of the corresponding correlation matrices in the above equations with $\tau = 0$.

In general, the full expressions in equation (6.57)/(6.59) must be used for calculation of the modal/physical responses. However, significant computational savings can be realized by recognizing a simplification for an excitation class. Note that for the cases of a single concentrated force or multiple contemporaneous forces of the same amplitude, the expression for the single-sided, stationary spectral matrix can be simplified:

$$[G_{ff}(\omega_n)] = [\phi]^T\{\Gamma\}\hat{f}_n^{l*}\hat{f}_n^l\{\Gamma\}^T[\phi] \tag{6.60}$$

So, the general form for the spectral matrix for acoustic pressure, single or multiple equivalent concentrated forces, or base acceleration can be written as

$$[G_{ff}(\omega_n)] = [\phi]^T\{\Gamma_n^*\}G_{**}^n\{\Gamma_n\}^T[\phi] \tag{6.61}$$

Substituting into equation (6.59) for the physical coordinate correlation matrices results in

$$([C_{AA}(\tau)], [C_{AA}(\tau)], [C_{AA}(\tau)]) = \sum_{n=0}^{N_\omega-1} \omega_n^{(0,2,4)}[\phi]\lceil H^*(\omega_n)\rfloor[\phi]^T\{\Gamma_n^*\}G_{**}^n$$

$$\{\Gamma_n\}^T[\phi]\lceil H(\omega_n)\rfloor[\phi]^T e^{i\omega_n\tau}$$

$$= \sum_{n=0}^{N_\omega-1} \omega_n^{(0,2,4)}\{\mathbf{H}_\mathbf{A}^*(\omega_n)\}\{\mathbf{H}_\mathbf{A}(\omega_n)\}^T e^{i\omega_n\tau} \tag{6.62}$$

where

$$\{\mathbf{H}_\mathbf{A}^*(\omega_n)\} = [\phi]\lceil H^*(\omega_n)\rfloor[\phi]^T\{\Gamma_n^*\}g_*^n/\sqrt{2} \tag{6.63}$$

is the conjugated physical frequency response vector to the excitation amplitude determined by

$$g_*^n = \sqrt{2G_{**}^n} \tag{6.64}$$

at any discrete frequency ω_n.

It is clear that calculation of these physical response correlation matrices has been reduced to calculation of a frequency response vector. Mean-square ($\tau = 0$) physical responses are determined from

$$\{\sigma_q^2\} = \sum_{n=0}^{N_\omega-1} \omega_n^{(0,2,4)}|\{\mathbf{H}_\mathbf{A}(\omega_n)\}|^2 \tag{6.65}$$

Any excitation that can be put into the form given in equation (6.61) can take advantage of this efficient means of response calculation. Examples of excitations not satisfying this requirement include temporally random planar acoustic waves with *random incidence*, turbulent boundary layer loading, multiple non-contemporaneous concentrated forces, etc.

In the previous sections, forms for the time-dependent load vectors in equation (6.1) were derived and a modal approach for continuous and discrete frequency domain analysis of the vibration response of panel-type structures subjected to those loads was developed. The formulation and implementation will now be validated through comparison with classical solutions and experimental measurements in the next two sections.
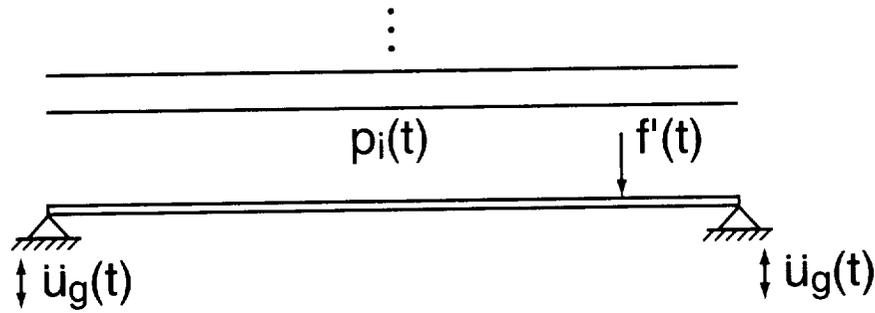
Figure 6.2 Schematic of simply-supported beam subject to planar acoustic, concentrated force, and base acceleration excitation.

Table 6.1 Material properties for aluminum specimens.

Young's Modulus	68.95 GPa	10 Msi
Shear Modulus	26.55 GPa	3.85 Msi
Poisson's Ratio	0.3	
Mass Density	2.767e+3 kg/m^3	2.588e-4 lbf s^2/in^4
Coeff. of Thermal Exp.	22.3 $\mu\epsilon$/°C	12.4 $\mu\epsilon$/°F

6.5 Analytical Validation

In this section, comparisons will be made with classical analysis for the cases of a simply-supported aluminum beam and a simply-supported aluminum panel to benchmark the analysis. All three dynamic, mechanical loads are considered; acoustic pressure, inertial, and concentrated force. Both the continuous and discrete frequency domain approaches are employed.

6.5.1 Simply-Supported Aluminum Beam

Consider a simply-supported aluminum beam shown schematically in Figure 6.2 with dimensions of 0.4572x0.0254x0.0023 m (18x1x0.090 inches). The material properties for the specimen are given in Table 6.1. It is assumed that the various loads are mutually exclusive, and results will be presented as such. Results for continuous and discrete spectral analysis from the present formulation will be presented. A classical solution for the random response of this structure subjected to each of the loads was derived for comparison.

The natural frequencies from the classical solution are governed by the equation

$$2\pi f_n = \omega_n = (n\pi)^2 \sqrt{\frac{EI}{ma^4}}$$

(6.66)

where m is the mass per unit length and a is the length of the beam. The beam was modeled by a finite element mesh of 36x2 elements. A comparison of the natural frequencies as predicted by the classical analysis and the finite element analysis are shown in Table 6.2. Excellent agreement between the two solutions is apparent.

The three excitation types are each modeled by white noise with spectral amplitudes which give consistent loading. For example, a 1g RMS loading over a 10–500 Hz bandwidth is

Table 6.2 Comparison of aluminum 0.4572x0.0254x0.0023 m (18x1x0.090 inch) simply-supported beam modal frequencies as predicted by classical and finite element analyses.

Mode Number	Classical, Hz	FEM, Hz
1	24.76	24.76
2	99.04	99.11
3	222.84	223.20
4	396.15	397.20

Table 6.3 Comparison of mid–span RMS responses for an aluminum 0.4572x0.0254x0.0023 m (18x1x0.090 inch) simply-supported beam as predicted by classical and finite element analyses.

Analysis	RMS Displ. (in)		RMS Vel. (in/s)		RMS Accel.	
	m	in	m/s	in/s	m/s^2	in/s^2
Base Acceleration						
Classical	7.26e-4	0.0286	0.1138	4.482	—	—
FE Continuous	7.21e-4	0.0284	0.1135	4.469	—	—
FE Discrete	7.21e-4	0.0284	0.1135	4.469	26.52	1044
Acoustic Pressure						
Classical	7.26e-4	0.0286	0.1138	4.482	—	—
FE Continuous	7.21e-4	0.0284	0.1135	4.469	—	—
FE Discrete	7.21e-4	0.0284	0.1135	4.469	26.52	1044
Concentrated Force						
Classical	5.74e-4	0.0226	0.1068	4.205	—	—
FE Continuous	5.69e-4	0.0224	0.1063	4.184	—	—
FE Discrete	5.69e-4	0.0224	0.1063	4.184	83.64	3293

considered to be a representative inertial loading. This overall load corresponds to a spectral level of 0.1966 $(m/s^2)^2$/Hz (304.704 $(in/s^2)^2$/Hz). One can arrive at an equivalent surface pressure excitation by equating the product of the acceleration level and mass of the beam, which results in a load of 0.721 N (0.162 lbf), with the product of the unknown surface pressure level and the surface area of the beam. The resulting equivalent acoustic pressure excitation has an overall value of 62.1 Pa (0.009 psi) RMS or a spectral level of 7.859 Pa^2/Hz (1.65307e-7 $(psi)^2$/Hz) over a 10–500 Hz bandwidth. Similarly, a concentrated force of 0.721 N (0.162 lbf) RMS or a spectral level of 1.0596e-3 N^2/Hz (5.35595e-5 lbf^2/Hz) over 10–500 Hz gives a consistent load when applied to the beam at mid-span. To make things more interesting, however, the concentrated force was applied at node 71 of 111 nodes with coordinates of (15, 0.5) inches. Comparisons of the classical and finite element predictions of the RMS mid-span responses are shown in Table 6.3. A value of 0.02 was used in all cases for the modal critical damping ratio to desensitize the solutions to frequency resolution. The classical and FE continuous spectral analysis predictions

were obtained using the assumption of white noise excitation with a summation over the first four modes. FE discrete spectral analysis predictions were obtained with a 10–500 Hz band-limited white noise model, a 0.5 Hz frequency resolution, and summation over the first four modes. The classical and finite element solutions are in excellent agreement in all cases.

6.5.2 Simply-Supported Aluminum Panel

Consider a simply-supported aluminum panel shown schematically in Figure 6.3 with dimensions of 0.3556x0.254x0.001 m (14x10x0.040 inches). The material properties for the specimen are the same as those given in Table 6.1 for the beam case. Again, it is assumed that the various loads are mutually exclusive. A classical solution for the random response of this structure subjected to each of the loads was derived for comparison.
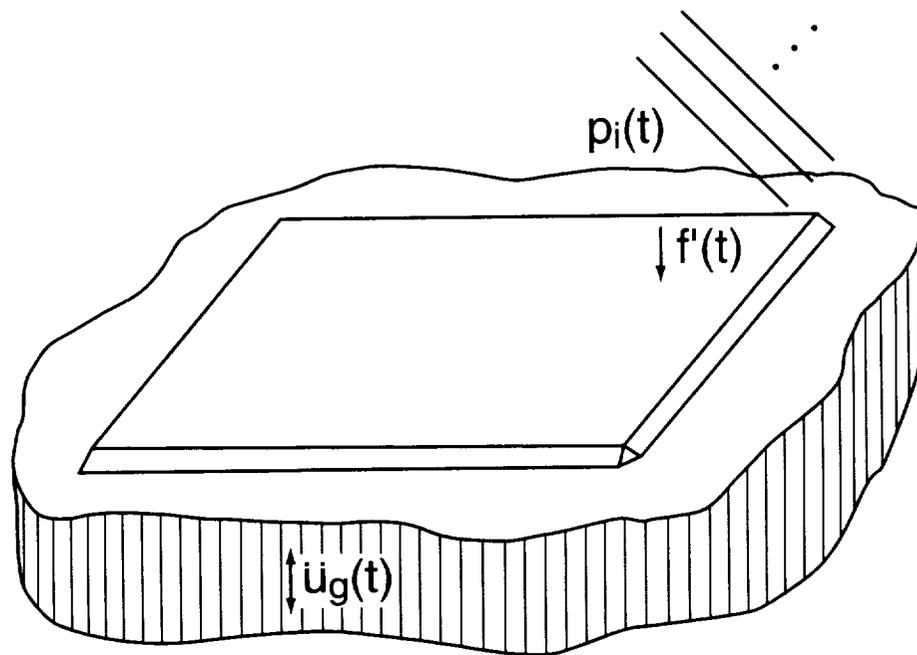
Figure 6.3 Schematic of simply-supported panel subjected to planar acoustic, concentrated force, and base acceleration excitation.

The natural frequencies from the classical solution are governed by the equation

$$2\pi f_{mn} = \omega_n = \pi^2 \sqrt{\frac{D}{\rho}} \left[\left(\frac{m}{a}\right)^2 + \left(\frac{n}{b}\right)^2 \right]$$
(6.67)

where ρ is the mass per unit area, a and b are the panel length and width, and D is the flexural rigidity given by

$$D = \frac{Eh^3}{12(1 - \nu^2)}$$
(6.68)

119

Table 6.4 Comparison of aluminum 0.3556x0.254x0.001 m (14x10x0.040 inch) simply-supported panel modal frequencies as predicted by classical and finite element analyses.

Mode Number	x-index	y-index	Classical, Hz	FEM, Hz
1	1	1	56.4	56.4
2	2	1	113.7	113.7
3	1	2	168.6	168.6
4	3	1	209.0	209.0
5	2	2	225.8	225.8
6	3	2	321.1	321.2
7	4	1	342.5	342.6
8	1	3	355.4	355.6
9	2	3	412.7	412.8
10	4	2	454.6	454.8

The panel was modeled by a finite element mesh of 14x10 elements. A comparison of the natural frequencies as predicted by the classical analysis and the finite element analysis are shown in Table 6.4. Negligible discrepancy exists between the two solutions.

The inertial excitation level used in the previous example will also be used in this case, i.e., 1g RMS or 0.1966 $(m/s^2)^2$/Hz (304.704 $(in/s^2)^2$/Hz) over a 10–500 Hz bandwidth. The overall load of this inertial excitation is 2.49 N (0.56 lbf). The equivalent surface pressure excitation for this case is 27.58 Pa (0.004 psi) RMS or a spectral level of 1.5524 Pa^2/Hz (3.265327e-8 $(psi)^2$/Hz) over a 10–500 Hz bandwidth. Finally, a concentrated force of 2.49 N (0.56 lbf) RMS or a spectral level of 12.66e-3 N^2/Hz (6.4000409e–4 lbf^2/Hz) over 10–500 Hz is applied at node 116 of 165 nodes with coordinates of x=0.254, y=0.178 m (x=10, y=7 inches). Comparisons of the classical and finite element predictions of RMS center-point responses are shown in Table 6.5. A value of 0.02 was used in all cases for the modal critical damping ratio. The classical and FE continuous spectral analysis predictions were obtained using the assumption of band-unlimited white noise with a summation over the first ten modes. FE discrete spectral analysis predictions were obtained with a 10–500 Hz band-limited white noise model, a 0.5 Hz frequency resolution, and summation over the first ten modes. It is clear that excellent comparisons are achieved in all cases.

Comparisons of the displacement power spectral densities PSDs at the coordinates x=0.102, y= 0.076 m (x=4, y=3 inches) predicted by the classical and finite element analyses for the three load cases above are presented in Figures 6.4–6.6. In all cases, the classical and finite element PSDs are indistinguishable. Note the presence of the non-symmetric modes in the concentrated force response case. PSDs for a random acoustic pressure case with angles of incidence (θ_i=60°, φ_i=45°) are shown in Figure 6.7. This case further demonstrates the excitation of the non-symmetric modes and will be useful for reference in Chapter 7.

Table 6.5 Comparison of center-point RMS responses for an aluminum 0.3556x0.254x0.001 m (14x10x0.040 inch) simply-supported panel as predicted by classical and finite element analyses.

Analysis	RMS Displ.		RMS Vel.		RMS Accel.	
	m	in	m/s	in/s	m/s^2	in/s^s
Base Acceleration						
Classical	2.692e-3	0.0106	0.098	3.845	—	—
FE Continuous	2.692e-3	0.0106	0.098	3.845	—	—
FE Discrete	2.692e-3	0.0106	0.098	3.844	49.96	1967
Acoustic Pressure						
Classical	2.692e-3	0.0106	0.098	3.845	—	—
FE Continuous	2.692e-3	0.0106	0.098	3.845	—	—
FE Discrete	2.692e-3	0.0106	0.098	3.844	49.96	1967
Concentrated Force						
Classical	4.216e-4	0.0166	0.157	6.167	—	—
FE Continuous	4.216e-4	0.0166	0.157	6.167	—	—
FE Discrete	4.216e-4	0.0166	0.157	6.167	92.63	3647
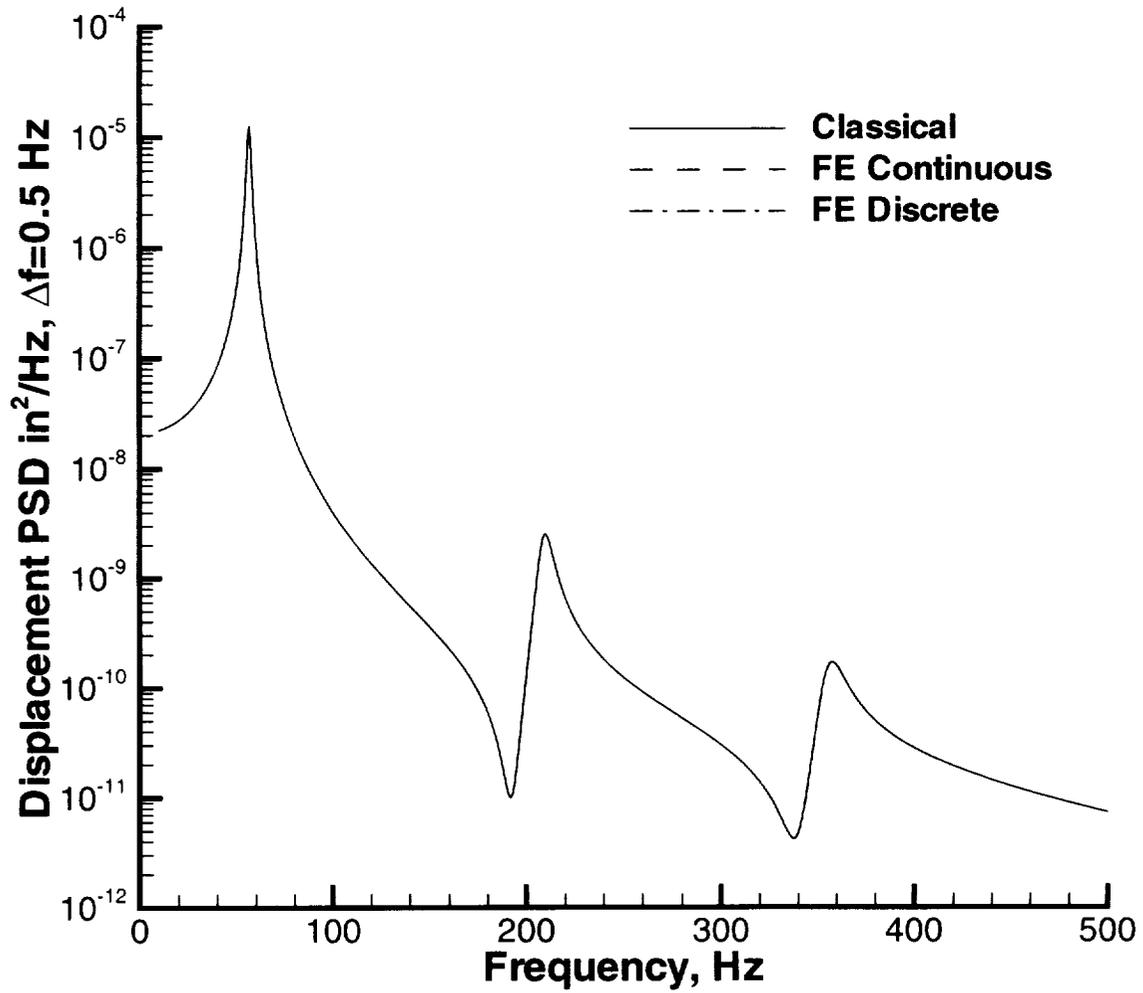
Figure 6.4 Classical and finite element displacement response PSDs at x=0.102, y= 0.076 m (x=4, y=3 inches) versus frequency for inertial loading case.
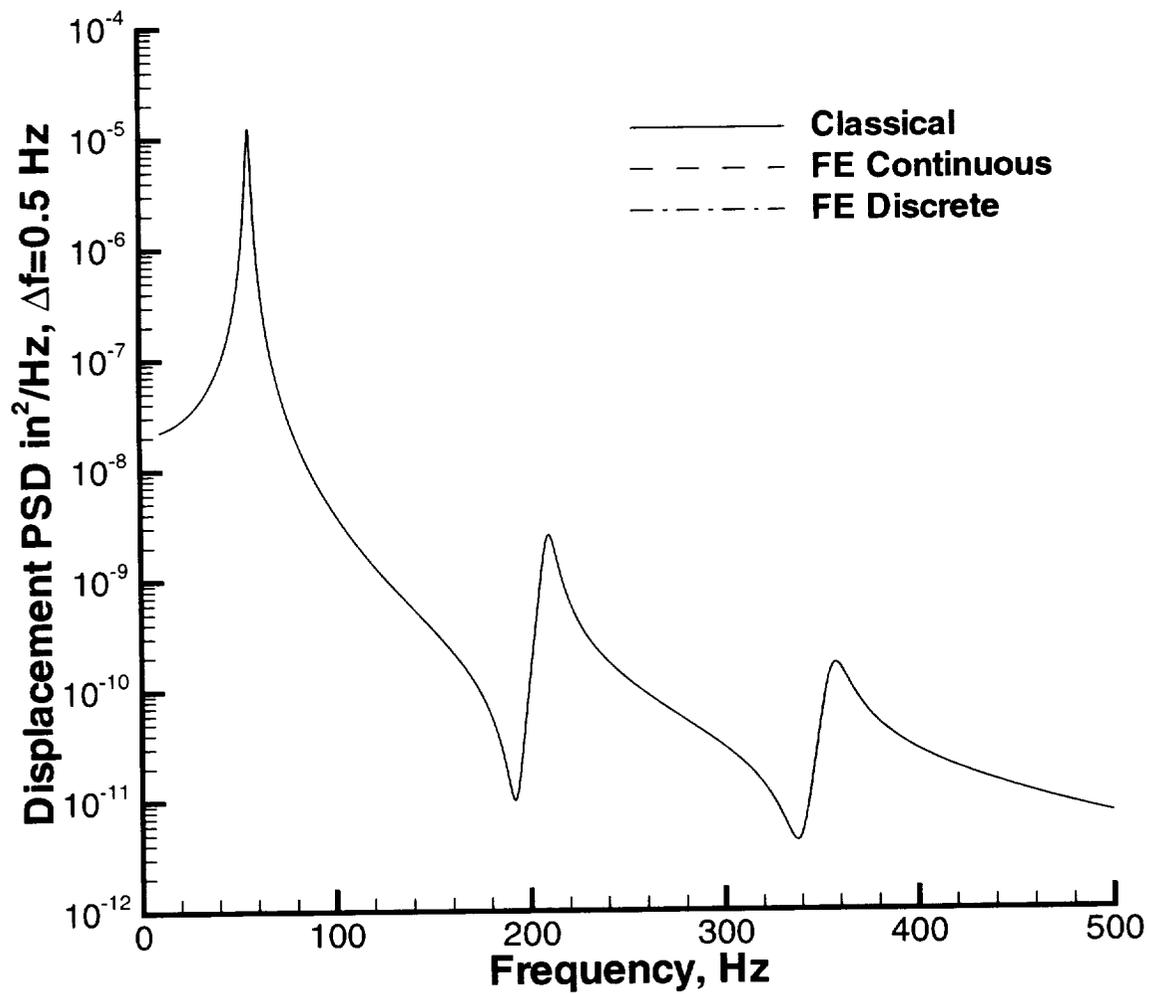
Figure 6.5 Classical and finite element displacement response PSDs at x=0.102, y= 0.076 m (x=4, y=3 inches) versus frequency for normal acoustic pressure loading case.
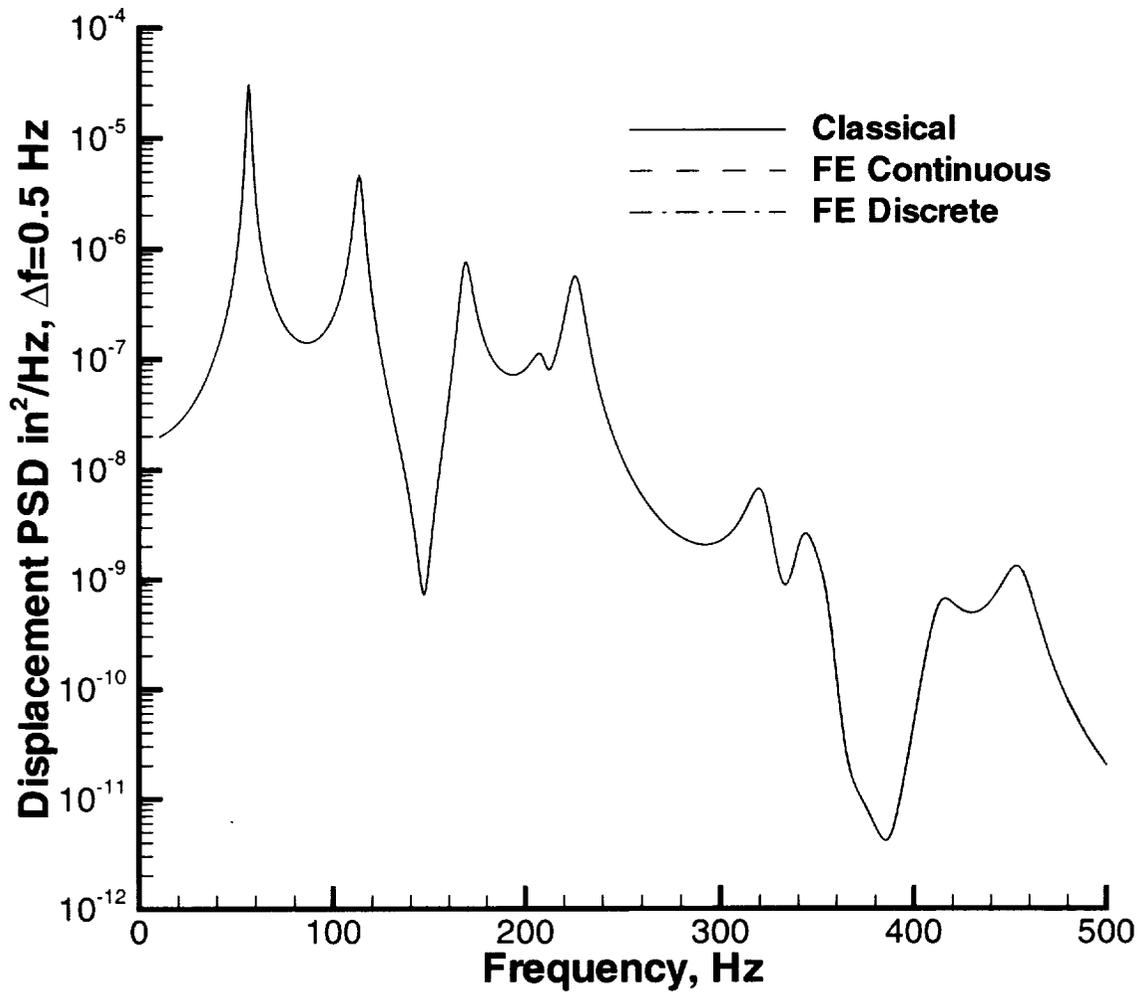
Figure 6.6 Classical and finite element displacement response PSDs at x=0.102, y= 0.076 m (x=4, y=3 inches) versus frequency for concentrated force loading case.
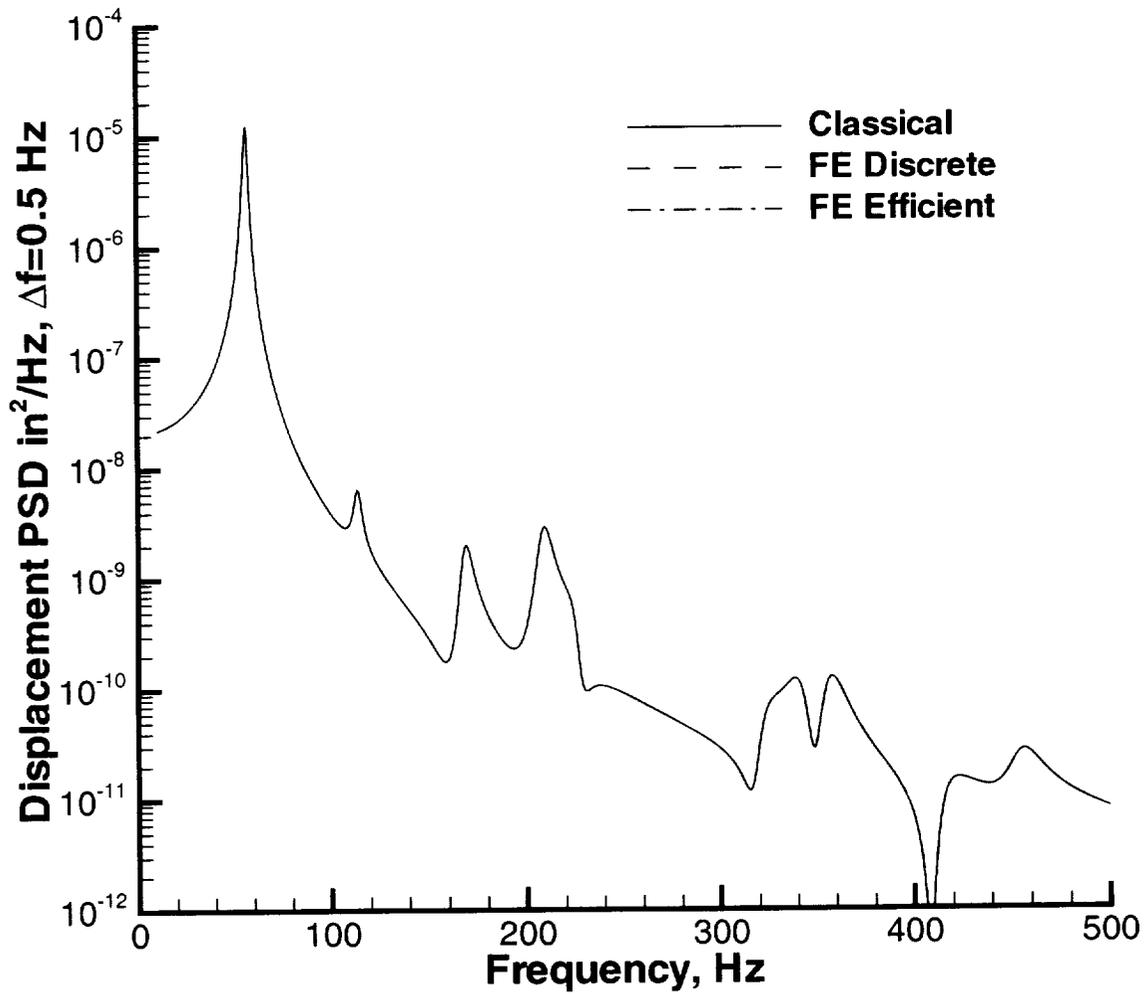
Figure 6.7 Classical and finite element displacement response PSDs at x=0.102, y= 0.076 m (x=4, y=3 inches) versus frequency for θ_i=60°, ϕ_i=45° acoustic pressure loading case.

It is physically intuitive as to which mechanical loads will excite the non-symmetric modes. However, some observations about the numerical modeling of such loads is worth mentioning here. In the discussion that follows, attention is limited to the vector and matrix components associated with the out-of-plane degrees of freedom only as all other components of the flexural eigenvectors are zero.

In general, a non-symmetric mode will not be excited by any excitation for which the corresponding mode shape is orthogonal with respect to the excitation spectral density matrix:

$$\{o\}_i^T [G(\omega)]\{o\}_i = 0 \qquad (6.69)$$

Normal acoustic pressure and inertial loading are special cases of this situation as they result in a real, uniform (full with all entries identical) excitation spectral density matrix. Obviously, the product of any antisymmetric modal vector transpose and a uniform matrix is the null vector transpose. The resulting modal force spectral density matrix is sparse with nonzero entries only at indices corresponding to the symmetric modes.

A concentrated force excitation is modeled by a null spectral density matrix with the exception of a single nonzero entry located by the index of the degree of freedom at the point of force application. The product of any modal vector with this matrix is nonzero except for the case when the nonzero matrix index corresponds to a zero in the modal vector. Hence, all modes are excited except those for which the point of force application falls on a nodal line. In this case, the modal force spectral density matrix is real and full, only the modes with nodal lines containing the point of force application are omitted.

Obliquely incident acoustic pressure excitation gives a complex, full but non-uniform spectral density matrix. The product of any modal vector with this matrix is nonzero except for cases when the angles of incidence direct the propagating pressure along an axis of the structure. In this special case, portions of the excitation spectral density matrix are uniform and these portions have indices corresponding to the antisymmetric nature of even-odd modes (e.g., $\theta_i=60°$, $\phi_i=0°$ does not excite the *,2 modes). So, with the exception of the modes excluded due to the latter situation, the modal force spectral density matrix is complex and full. One final note should be made regarding the extent to which the antisymmetric modes are excited. Modes occurring at lower frequencies are excited more weakly by excitations of this type because the wavelength of the propagating pressure may be long relative to the extent of the structure. This causes the incident pressure to appear to be close to uniform. This is exemplified in the case presented in Figure 6.7, where the pressure wavelengths range from 34.29 to 0.686 m (112.5 to 2.25 feet) at 10 Hz and 500 Hz, respectively. In this case, all antisymmetric modes are excited weakly as is evident in the figure.

The finite element analysis has been shown to produce very accurate results in comparison with classical analysis for all three loading types for simply-supported beam and panel structures. Now, attention will be turned to experimental configurations for validation of the analytical tool with experimental measurement.

6.6 Experimental Validation

Comparisons will be made with experimental measurements for the cases of a clamped-clamped aluminum beam and a clamped-clamped glass-epoxy beam to assess model and analysis

tool accuracy incrementally, prior to making comparisons with measurements from a clamped-clamped SMAHC beam. Results will be shown for the SMAHC beam at several temperatures indicative of various states in the beam thermomechanical response. Finally, comparisons will be made for the case of a fully-clamped aluminum panel as an introduction to the next chapter.

All of the experimental beam vibration results presented in this study result from base acceleration (inertial) excitation. A picture of the overall apparatus is shown in Figure 6.8. The shaker system consists of a large electromechanical shaker configured horizontally and attached to a magnesium slip table, which oscillates in a horizontal plane during operation. The specimen is mounted in the fixture with a vertical orientation to the width-direction in order to avoid complications due to gravity. The excitation acceleration is measured by accelerometers (PCB model T352M92) placed at each end of the specimen fixture. The normal velocity and acceleration responses of the beam are measured with a laser Doppler velocimeter (Ometron, VPI) and accelerometers (Endevco model 2250A-10). It is obvious that the beam response transducers measure the absolute motion of the beam specimens (including the base motion). Most structural dynamic prediction tools, in fact all of those used in this study, are formulated to provide relative motion response for such configurations. Therefore, it is imperative that experimental procedures allow for the removal of the base motion contributions. The importance is not so much for comparison of response amplitude as the base motion is typically much less than that of the flexible structure, but for comparison of frequency response or response spectra.
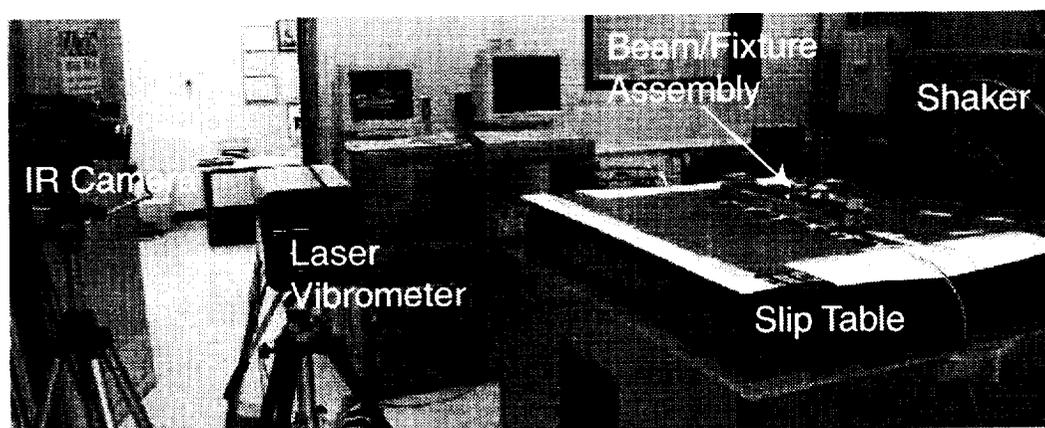
Figure 6.8 Overall configuration for base acceleration tests on beam specimens.

To allow the most flexibility in the procedure of base motion removal, a redundant accelerometer was attached to each end of the support fixture and connected to signal conditioning with hardware integration. The redundant reference accelerometer signals were integrated once to result in velocity measurements for subtraction from the laser vibrometer output. Subsequently, the base motion can be removed from the acceleration or velocity responses in either the time domain, by simple subtraction, or in the frequency domain as follows. This discussion will focus on the accelerometer measurements, but it equally valid for any response quantity. The relative acceleration can be written as

$$a = a_s - a_f \tag{6.70}$$

where the specimen and fixture accelerations have been denoted by a_s and a_f . For stationary stochastic response, the covariance can be obtained from the following expectation

$$E[a(t)a(t-\tau)] = E\left[\left(a_s(t) - a_f(t)\right)\left(a_s(t-\tau) - a_f(t-\tau)\right)\right] \tag{6.71}$$

This can be written in the frequency domain as

$$O_{aa}(\omega) = O_{a_s a_s}(\omega) - O_{a_s a_f}(\omega) - O_{a_f a_s}(\omega) + O_{a_f a_f}(\omega) \tag{6.72}$$

where the o are power and cross spectral density functions. Thus, it is clear that frequency domain measurements (i.e., spectral matrix) can be post-processed to obtain the relative motion spectra. In this study, the time data was collected and post-processed to remove the base motion and generate relative response spectra.

6.6.1 Clamped Aluminum Beam

A picture of the apparatus for the clamped-clamped aluminum beam configuration is shown in Figure 6.9. The fixture is the same as that described in Chapter 5, but the electrical connection blocks and electrical/thermal insulation layers have been removed. The overall beam dimensions are 0.5588x0.0254x0.0023 m (22x1x0.09 inches) with an unsupported length of 0.4572 m (18 inches). The overall beam mass was measured to be 89.79e-3 kg (0.198 lbf). The elastic properties of the material were also measured and are given in Table 6.6.
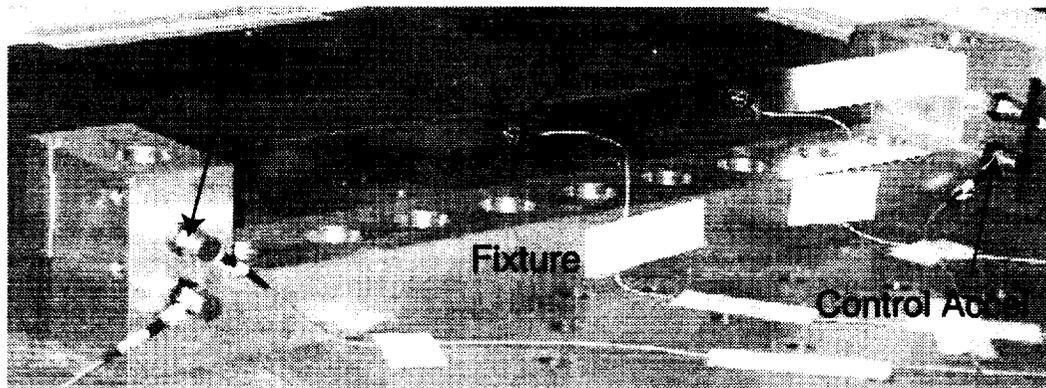
Figure 6.9 Aluminum beam specimen mounted in base acceleration test configuration.

The beam was excited by random base acceleration over a 20–400 Hz bandwidth with a RMS value of 0.25 g. The beam response was measured by the laser vibrometer and two accelerometers at locations 0.10 m (4 inches) and 0.25 m (10 inches) from right grip, indicated by position numbers 1 and 2 in Figure 6.9. Time records with an overall length of 200 seconds were collected with a sampling rate of 1024 Hz to allow 50–frame averages with a bandwidth of 0–400 Hz and a frequency resolution of 0.25 Hz. The time data were post-processed to construct relative response quantities, frequency response functions between the beam response transducers and the fixture transducers, and power spectral densities (PSDs) of the acceleration input and relative beam responses.

Table 6.6 Material properties for aluminum beam specimen in dynamic response test.

Young's Modulus	74.47 GPa	10.8 Msi
Shear Modulus	27.99 GPa	4.06 Msi
Poisson's Ratio	0.33	
Density	2.767e+3 kg/m^3	2.588e-4 lbf•s/in^4

Mode Number	Modal Critical Damping Ratio
1	0.0025
2	0.001
3	0.00086

The beam was modeled with a 36x2 mesh of the 24 degree-of-freedom rectangular plate elements described in Chapter 4. Modal damping estimates from measured frequency response functions, see Table 6.6, were used in the predictions. The beam grips were torqued to 13.56 N•m (120 in•lbf), which gave a measured fundamental frequency of 55.5 Hz. The fundamental frequency with perfectly clamped boundaries was predicted to be 58.4 Hz. The boundary conditions were modeled as clamped with the exception of torsional springs, with a spring rate of 113 N•m/rad (1000 in•lbf/rad) applied to the longitudinal-slope degrees of freedom to match the fundamental frequency. Only two symmetric modes were expected in the excitation bandwidth, but a total of 10 modes was used in the predictions to account for the residual effects of the higher order modes. A uniform modal critical damping ratio of 0.1% was used for modes 4–10. The influence of the accelerometers was modeled as lumped masses (~0.4e-3 kg, 2.283e-6 lbf•s^2/in^4) at appropriate nodes. The input acceleration PSDs, as measured by one of the control accelerometers, was taken as input for the predictions.

Comparisons of predicted and measured displacement PSDs for measurement locations 1 and 2 are shown in Figures 6.10 and 6.11. Note that the "measured" displacement PSDs were generated by integrating the acceleration responses in the frequency domain. It can be seen that excellent agreement is achieved, except in overall RMS response level. The discrepancy in RMS level is due to the fact that the damping is so light in this case that the frequency resolution of 0.25 Hz is insufficient to adequately capture the peak values in the FRFs or spectra. Of course, the spectral analysis conserves the total response energy by spill-over into adjacent frequency bins. This spill-over results in slightly broader response peaks with lower amplitude. Curve fitting techniques for estimation of modal parameters misinterpret this as higher damping values. The main culprit in this case is the damping value at the fundamental frequency, where the response peak is extremely sharp. A damping value of approximately 0.1% would probably be more representative of the actual damping value in the first mode because it is consistent with that at mode 3. With this change in damping, the displacement response RMS values at the two measurement locations are 1.24e-4 m and 2.54e-4 m, respectively, in nearly perfect agreement with measurement.
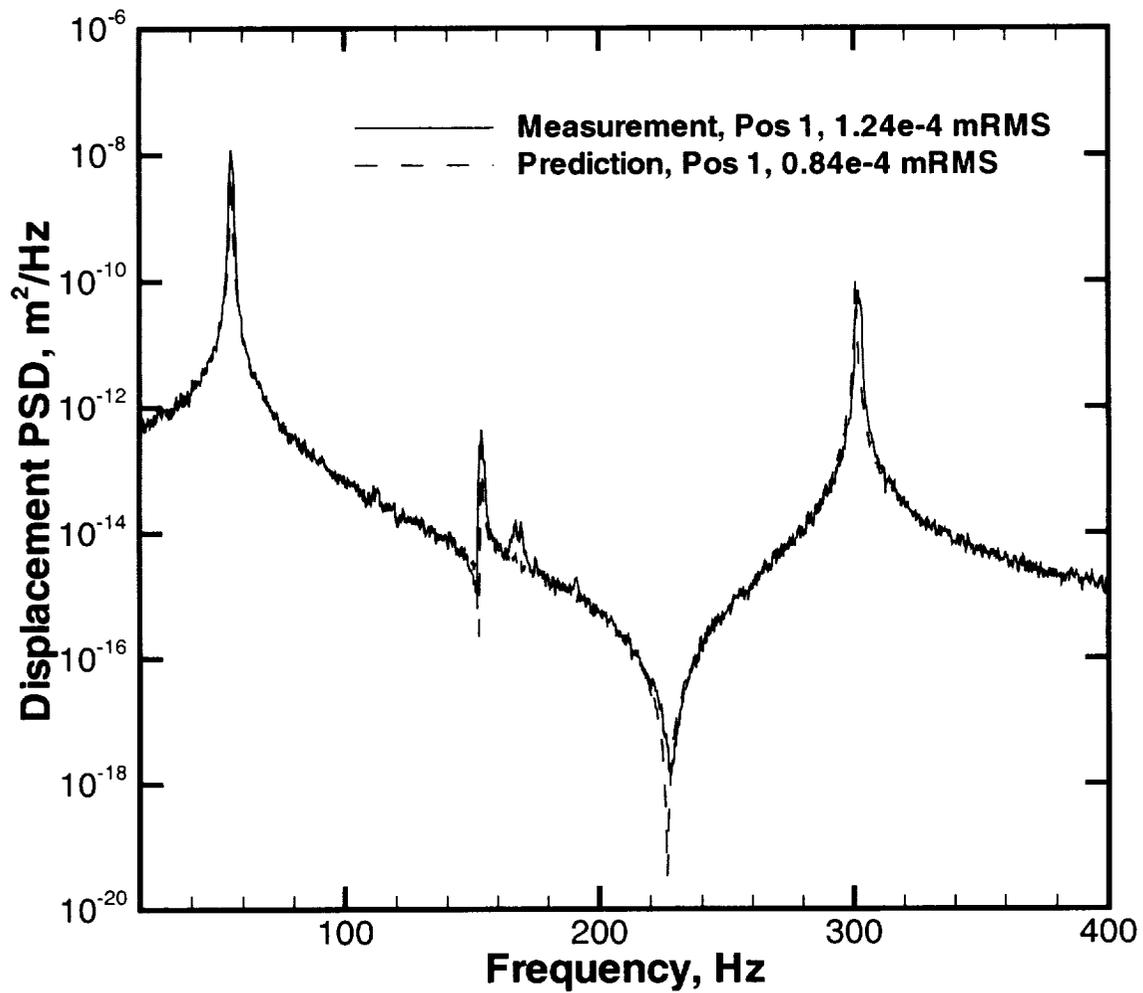
Figure 6.10 Measured and predicted displacement PSD
comparison for position 1 on the aluminum beam (Δf=0.25 Hz).
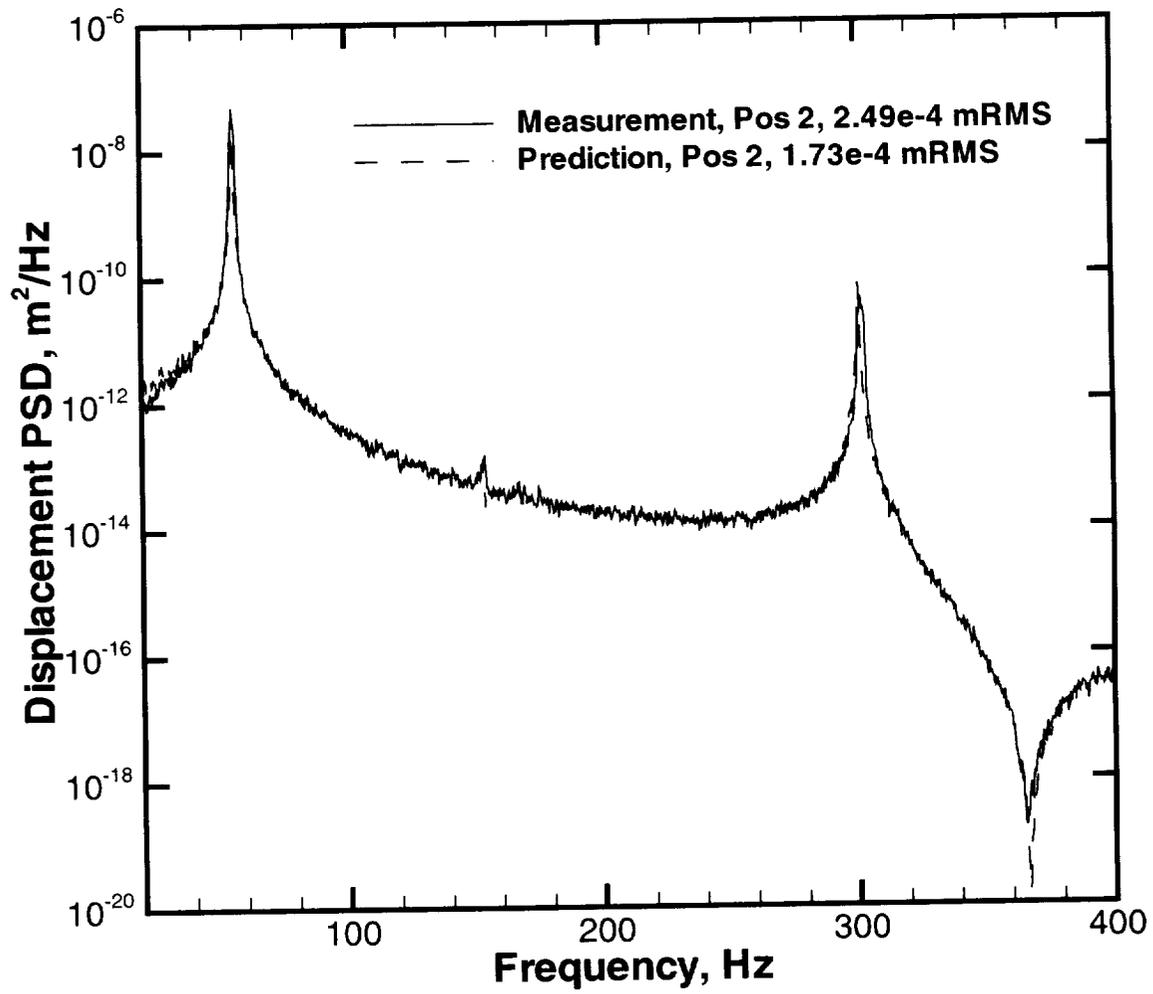
Figure 6.11 Measured and predicted displacement PSD comparison for position 2 on the aluminum beam (Δf=0.25 Hz).

Table 6.7 Material properties for glass–epoxy beam specimen in dynamic response test.

E_1	49.30 GPa	7.15 Msi
E_2	20.00 GPa	2.90 Msi
G_{12}	9.65 GPa	1.40 Msi
ν_{12}	0.29	0.29
ρ	2.031e+3 kg/m^3	0.19e-3 lbf•s/in^4

Mode Number	Modal Critical Damping Ratio
1	0.0055
2	0.005
3	0.0048
4	0.005

6.6.2 Clamped Glass-Epoxy Beam

The performance of the FE analysis will now be tested against a baseline composite beam. A glass-epoxy beam with dimensions of 0.5588x0.0254x0.0018 m (22x1x0.072 inches) with an unsupported length of 0.4572 m (18 inches) was tested in the same experimental configuration as that for the aluminum beam. The overall beam mass was measured to be 53.9e-3 kg (0.119 lbf). The elastic properties of the material system were described in Chapter 3. The material properties at ambient temperature were used to generate the predicted responses. Those properties are reiterated in Table 6.7 for convenience.

The beam excitation and data acquisition configuration was the same as that for the aluminum beam with the exception of the excitation bandwidth, which was changed to 10–400 Hz because of the lower fundamental frequency in this case. The overall excitation level of 0.25 gRMS was maintained. The measurement locations will again be referred to as positions 1 and 2. Time data were collected and post-processed to construct relative response quantities, frequency response functions between the beam response transducers and the fixture transducers, and power spectral densities (PSDs) of the acceleration input and relative beam responses.

An analogous FE model was also developed for this case. Modal damping values were estimated from the measured frequency response functions, see Table 6.7, and used in the predictions. In this case, a torque of 13.56 N•m (120 in•lbf) on the beam grips resulted in a measured fundamental frequency of 33.5 Hz. The fundamental frequency with perfectly clamped boundaries was predicted to be 35 Hz. Torsional springs with a rate of 19.21 N•m/rad (170 in•lbf/rad) were applied to match the fundamental frequency. Again, the input acceleration PSDs, as measured by one of the control accelerometers, were taken as input for the predictions.

Predicted and measured displacement PSDs for measurement locations 1 and 2 are shown in Figures 6.12 and 6.13. Again, excellent agreement is achieved, including the RMS response levels. There is a slight over-prediction of the second symmetric modal frequency, but the comparison is within experimental uncertainty.
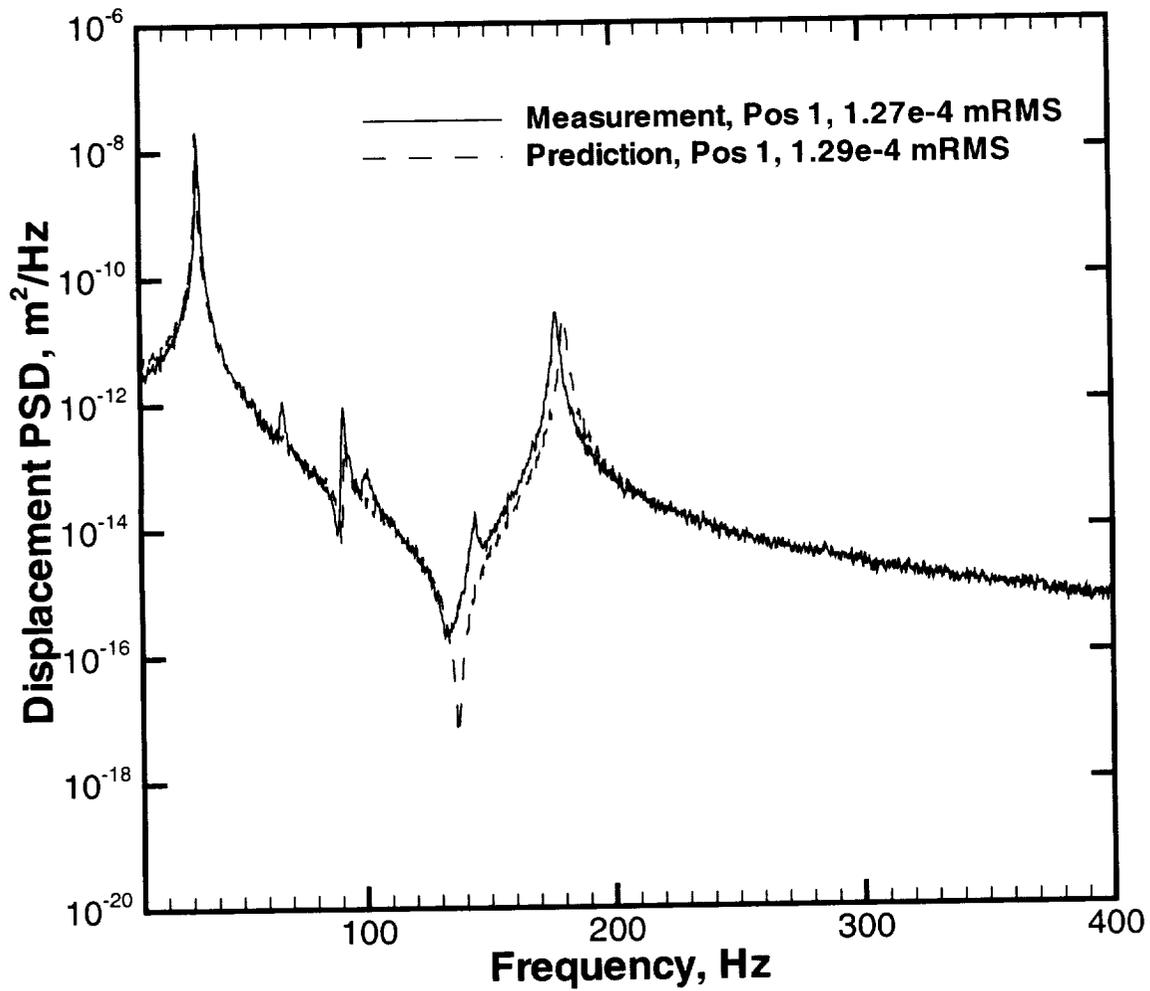
Figure 6.12 Measured and predicted displacement PSD comparison for position 1 on the glass-epoxy beam (Δf=0.25 Hz).
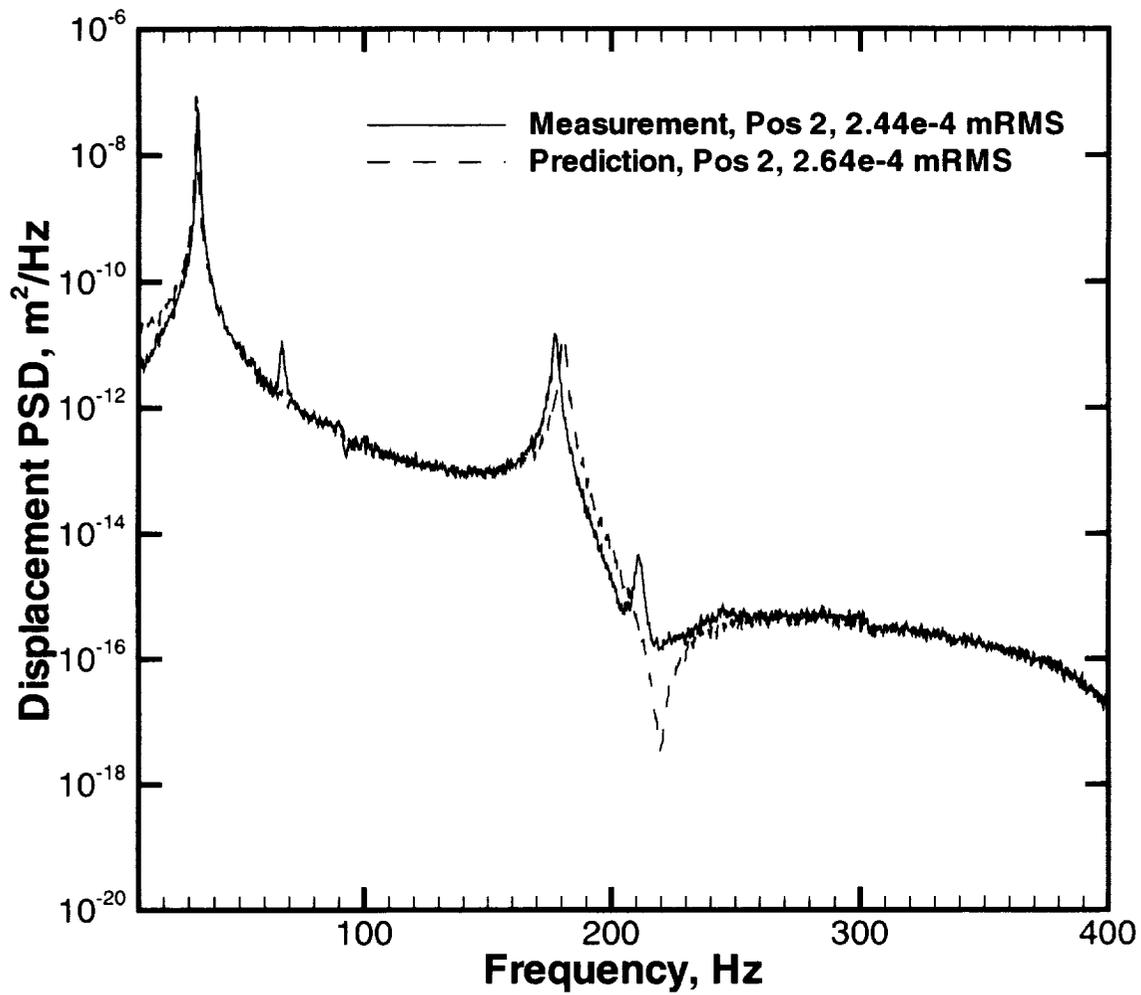
Figure 6.13 Measured and predicted displacement PSD comparison
for position 2 on the glass-epoxy beam (Δf=0.25 Hz).
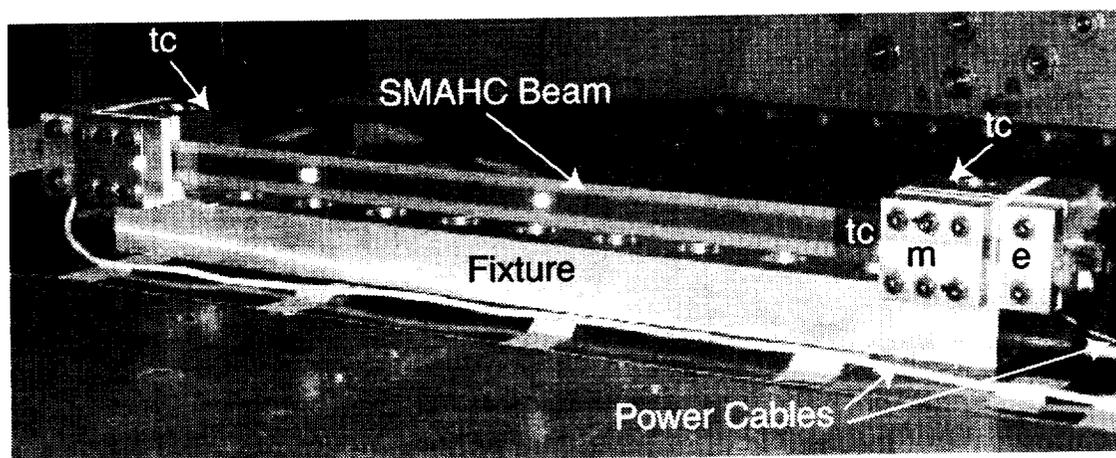
Figure 6.14 Front view of the SMAHC beam specimen
mounted in clamping fixture for dynamic testing.

The dynamic analysis has been validated by comparison with the measured response of conventional structures. Attention will now turn to demonstration of the dynamic response performance of a SMAHC beam specimen and validation of the formulation by comparison of the measured and predicted responses.

6.6.3 Clamped SMAHC Beam

The SMAHC beam specimen mounted in the support fixture and configured for base acceleration testing is shown in Figure 6.14. The configuration is essentially the same as that described in the Experimental Validation section of Chapter 5. The beam is supported by the mechanical grips indicated in the figure by "m". The grips designated as "e" are electrical connections for the Nitinol leads, but also provide mechanical restraint. The electrical connections are isolated from the fixture by a layer of fibrous ceramic insulation. The beam is also thermally isolated from the fixture by a layer of this insulation on both sides. The beam is heated by DC electrical current controlled by a thermocouple measurement located approximately on the beam centerline and 0.0127 m (0.5 in) from the right mechanical grip, indicated in the figure by "tc". The thermal controller consists of a process controller (Omega model CN77353–PV), and a DC power supply (HP model 6652A). Thermocouples also monitor the temperature at each end of the fixture, indicated in Figure 6.14, and one measures the ambient air temperature.

A rear view of the beam/fixture assembly is given in Figure 6.15, which shows additional detail on the dynamic experimental setup. The placement of the control thermocouple is more apparent in this view as is the presence of the electrical/thermal insulation. The base acceleration excitation was controlled with the average of the two control accelerometers. The "integrated accelerometers" were utilized in the calculation of relative velocity response from the laser vibrometer data, as described previously. The positions of the two response accelerometers are consistent with the descriptions of the previous tests and are again designated by position numbers 1 and 2.

The beam was excited by random base acceleration over a 10–400 Hz bandwidth with a RMS value of 0.25 g. Time records with an overall length of 200 seconds were collected with

135
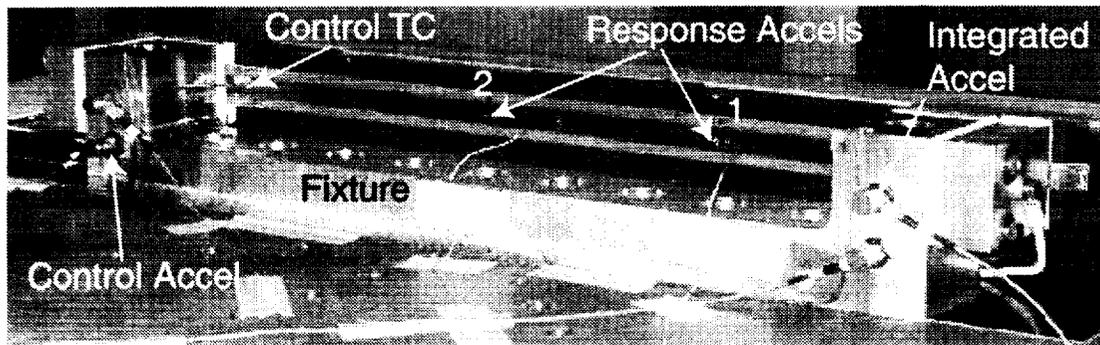
Figure 6.15 Rear view of the SMAHC beam specimen
mounted in clamping fixture for dynamic testing.

a sampling rate of 1024 Hz to allow 50–frame averages with a bandwidth of 0–400 Hz and a frequency resolution of 0.25 Hz. The time data were post-processed to construct relative response quantities, frequency response functions between the beam response transducers and the fixture transducers, and power spectral densities (PSDs) of the acceleration input and relative beam responses. Dynamic data were collected at ambient and at elevated temperatures from 32.22°C (90°F) to 121.11°C (250°F) in 5.56°C (10°F) increments. The beam mechanical and ribbon electrical grips were torqued to 13.56 N•m (120 in•lbf) just prior to dynamic excitation to minimize effects of changing environmental conditions. The fixture temperature increased by approximately 2.22°C (4°F) during the course of data collection, which was in almost direct proportion to the increase in ambient air temperature.

First, some general observations will be made concerning the experimental behavior and results. Because of the material system characteristics and test configuration, the beam exhibited a thermal post-buckling deflection over range of temperatures, as described in detail in Chapter 5. The beam exhibited some interesting dynamic behavior (such as intermittent snap-through) within this temperature range, particularly at the point of loss of stability in the flat configuration and then at the point of regaining stability in the flat configuration, as expected. No attempt will be made to predict the dynamic behavior within this range, although it is possible with the present analysis for the portions where the dynamic response is geometrically linear about a nonlinear static deflection. Although the beam was returned to a flat configuration at approximately 54.44°C (130°F), the presented results will focus on higher temperatures. The forced vibration amplitude was visually noticeable in the inactive state (ambient temperature), but was virtually undetectable at temperatures above 71.11°C (160°F). No evidence of delamination or other flaws were detected subsequent to testing, despite the large thermal post-buckling deflection and rather high temperature developed during the tests.

Other observations can be made from a summary of RMS displacement responses and modal parameter estimates shown as a function of temperature in Table 6.8. Temperatures for which the beam was buckled are excluded from the table. The RMS displacements correspond to location 2 and were calculated in the frequency domain from the corresponding accelerometer PSDs. It can be seen that, although a majority of the stiffening effect was achieved at approximately 93.33°C (200°F), performance remains good far beyond that temperature with a maximum

136

Table 6.8 Summary of RMS measured displacements at position 2
on the SMAHC beam and modal parameters versus temperature.

Temp., °C	RMS Displ., m	f_1, Hz	ζ_1, %	f_3, Hz	ζ_3, %
23	0.322e-3	26.4	0.89	160.3	0.95
—	—	—	—	—	—
60	0.15e-3	83.1	0.10	279.3	0.45
65.56	0.11e-3	94.4	0.13	309.4	
71.11	0.05e-3	107.0	0.50	342.7	0.16
76.67	0.063e-3	118.3	0.19	372.5	0.28
82.22	0.068e-3	126.7	0.15	—	—
87.78	0.063e-3	130.9	0.14	—	—
93.33	0.062e-3	134.0	0.14	—	—
98.89	0.066e-3	136.0	0.11	—	—
104.4	0.067e-3	137.6	0.11	—	—
110.0	0.073e-3	139.2	0.10	—	—
115.6	0.072e-3	138.7	0.10	—	—
121.1	0.067e-3	140.0	0.09	—	—

increase in the fundamental frequency of 430% at 121.11°C (250°F). The variation of the modal frequencies with temperature is more easily seen in Figure 6.16. There, it can be seen that the fundamental frequency starts to reach an asymptotic value at approximately 93.33°C (200°F) and mode three escapes the excitation bandwidth at temperatures above 82.22°C (180°F). Note the peculiar changes in the mode-1 damping near 71.11°C (160°F). This effect is reflected in the measured displacement response RMS values and can be seen in Figure 6.17, which shows the measured displacement response PSD at ambient and three elevated temperatures. The four PSDs correspond to the filled symbols in Figure 6.16. It can be seen that the maximum attenuation in the RMS displacement response is achieved at 71.11°C (160°F), where there is maximum peak response reduction due to higher damping, although the stiffening effect continues to increase at higher temperatures. One possible explanation is that there may be an optimal state near 71.11°C (160°F) where there is adequate austenite and dynamic stress and low enough temperature to allow enhanced damping by stress induced martensitic (SIM) transformation hysteresis. At higher temperatures, the dynamic stresses are insufficient to drive the SIM transformation as it becomes increasingly difficult to induce.

Recall that the beam dimensions are 0.5588x0.0254x0.0019 m (22x1x0.078 in) with a lamination of $(45/0_{sma}/-45/90)_{2s}$. Five ribbon widths are embedded within each 0° layer. Each ribbon has a cross section of 2.29e-3x1.52e-4 m (0.09x0.006 inches). This configuration was modeled as a Nitinol volume fraction of 0.5538 in the 0° layers, for an overall volume fraction of 13.8%. The mass densities of the glass-epoxy and Nitinol ribbon (prestrained 4%) were
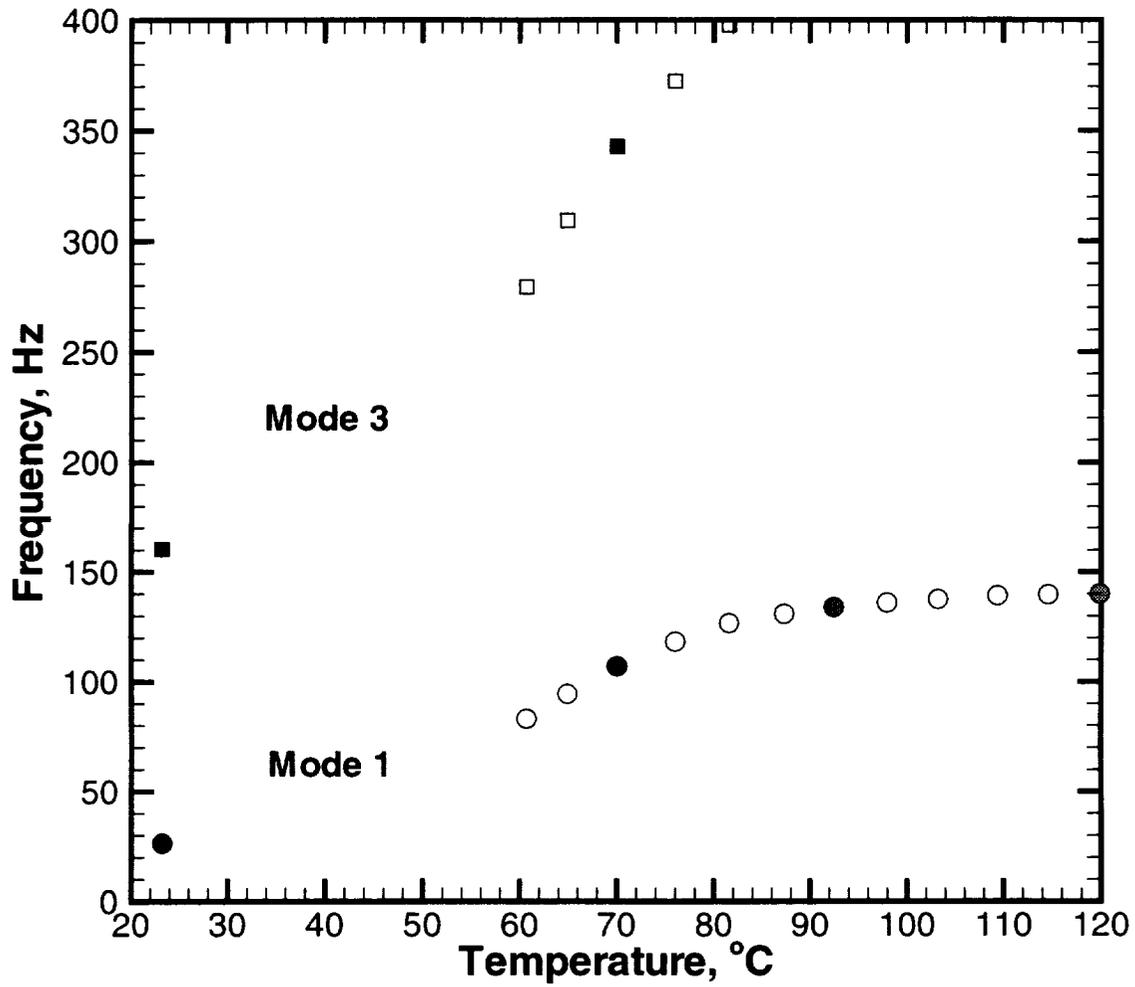
Figure 6.16 Measured mode 1 and mode 3 natural
frequencies of the SMAHC beam versus temperature.
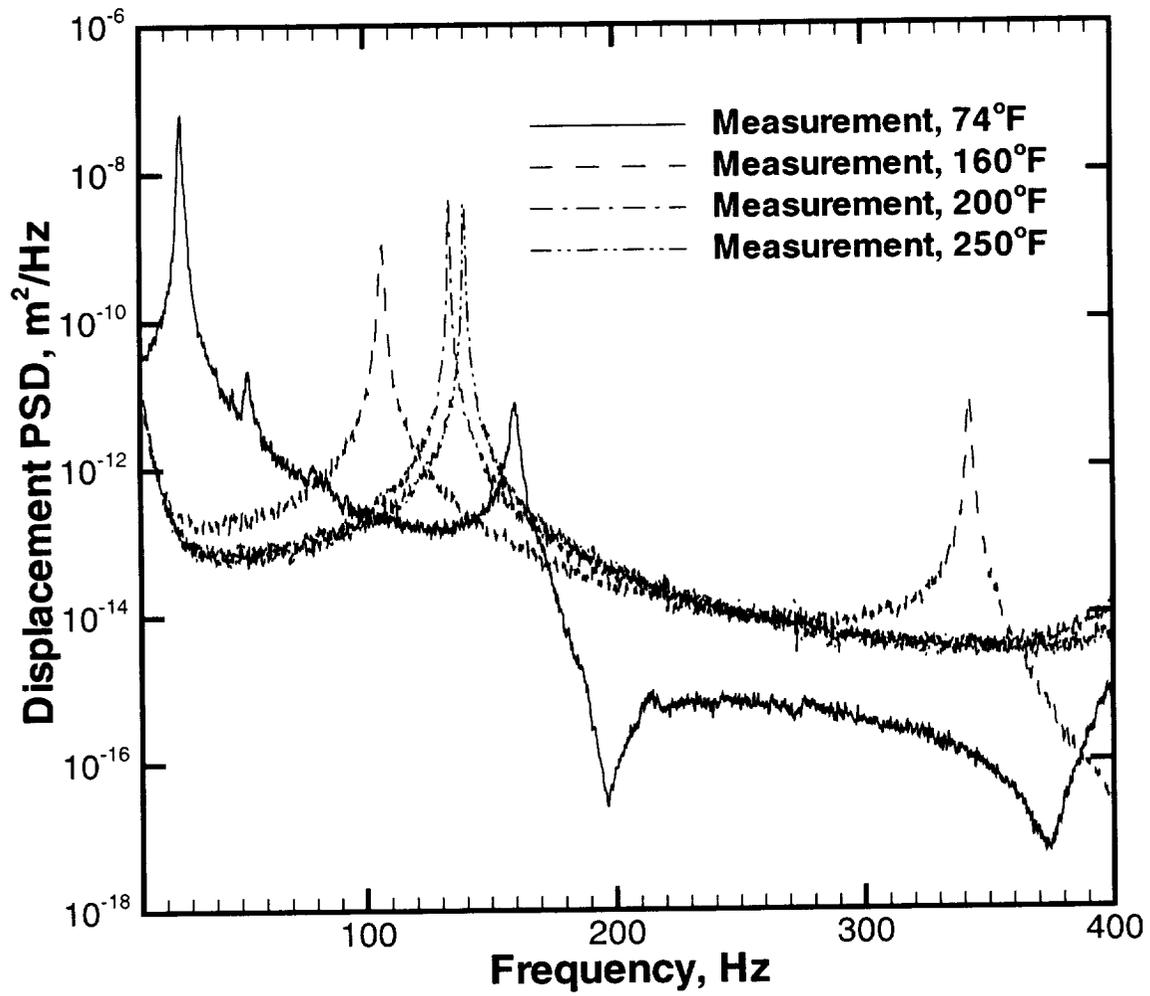
Figure 6.17 Measured displacement PSDs for position 2 on the SMAHC beam at ambient and elevated temperatures (Δf=0.25 Hz).

found to be 0.19e-3 lbf•s²/in⁴ and 0.5349e-3 lbf•s²/in⁴. With the beam/ribbon dimensions, the trimmed ribbon length of 0.66 m (26 inches) and the measured mass densities, the calculated mass of the beam is 75.5e-3 kg (0.166 lbf). This is within 1% of the measured overall mass of the SMAHC beam, which was found to be 74.92e-3 kg (0.165 lbf). The thermomechanical properties of the constituent materials were described in Chapter 3 and are given in Tables 3.5 and 3.8. Recall that the composite cure cycle constitutes thermal cycle number one (1) on the Nitinol ribbon. This was the first test of the SMAHC beam specimen, which corresponds to thermal cycle number two (2). The appropriate recovery stress data from Table 3.8 were used in the model to predict the dynamic response.

The element properties for a 32x2-element-mesh model of this beam were evaluated as a function of temperature from these material properties. Modal damping estimates were taken from the experimental data in Table 6.8. A total of ten modes was used in the predictions in all cases to account for residual effects. The damping was assumed to be 0.1% on all antisymmetric modes and modes out of bandwidth. In this case, the torque of 13.56 N•m (120 in•lbf) on the beam grips resulted in a measured fundamental frequency of 26.4 Hz at ambient temperature. The fundamental frequency with perfectly clamped boundaries was predicted to be 37.6 Hz. The boundary conditions in this test are not as close to clamped conditions as in the previous tests because of the insertion of the thermal insulating material between the beam and grip surfaces. Torsional springs with a rate of 1.98 N•m/rad (17.5 in•lbf/rad) were applied to match the fundamental frequency. The influence of the accelerometers was modeled as lumped masses (-0.4e-3 kg, 2.283e-6 lbf•s²/in⁴) at appropriate nodes. Again, the input acceleration PSDs, as measured by one of the control accelerometers, was taken as input for the predictions.

Measured and predicted displacement PSDs for measurement location 2 on the SMAHC beam at four temperatures are shown in Figures 6.18–6.21.   The figures show results for ambient temperature, 71.11°C (160°F), 93.33°C (200°F) and 121.1°C (250°F), respectively, and are representative of the comparisons at all temperatures. The correlation at ambient temperature is excellent with less than 9% difference between measured (3.23 mRMS, 0.0127 inRMS) and predicted (2.96 mRMS, 0.0116 inRMS) RMS response level. The comparisons at elevated temperature show some discrepancy, but are in excellent qualitative agreement. The predicted responses consistently show slightly higher modal frequencies and lower RMS levels than the corresponding experimental measurements. This trend is due to an over-prediction of the recovery force stiffening effect and is attributable to boundary condition modeling issues described in the Experimental Validation section of Chapter 5.

Recall from that discussion that the in-plane boundaries of the physical system are somewhat compliant due to the layer of insulation between the mechanical and electrical grips. The boundary compliance partially relieved the recovery stress and resulted in a reduced stiffening effect. This effect was captured in the model by applying axial springs with a spring rate of 1.97e+6 N/m (11,250 lbf/in) to the in-plane degrees of freedom at the mechanical grips. The effect of fixture expansion with temperature was also modeled by applying appropriate enforced displacements at the beam ends. New predicted responses were made with these changes. The measured and predicted displacement PSDs for measurement location 2 on the SMAHC beam are shown in Figures 6.22–6.25. Excellent agreement is achieved between the predicted and measured responses at all temperatures.
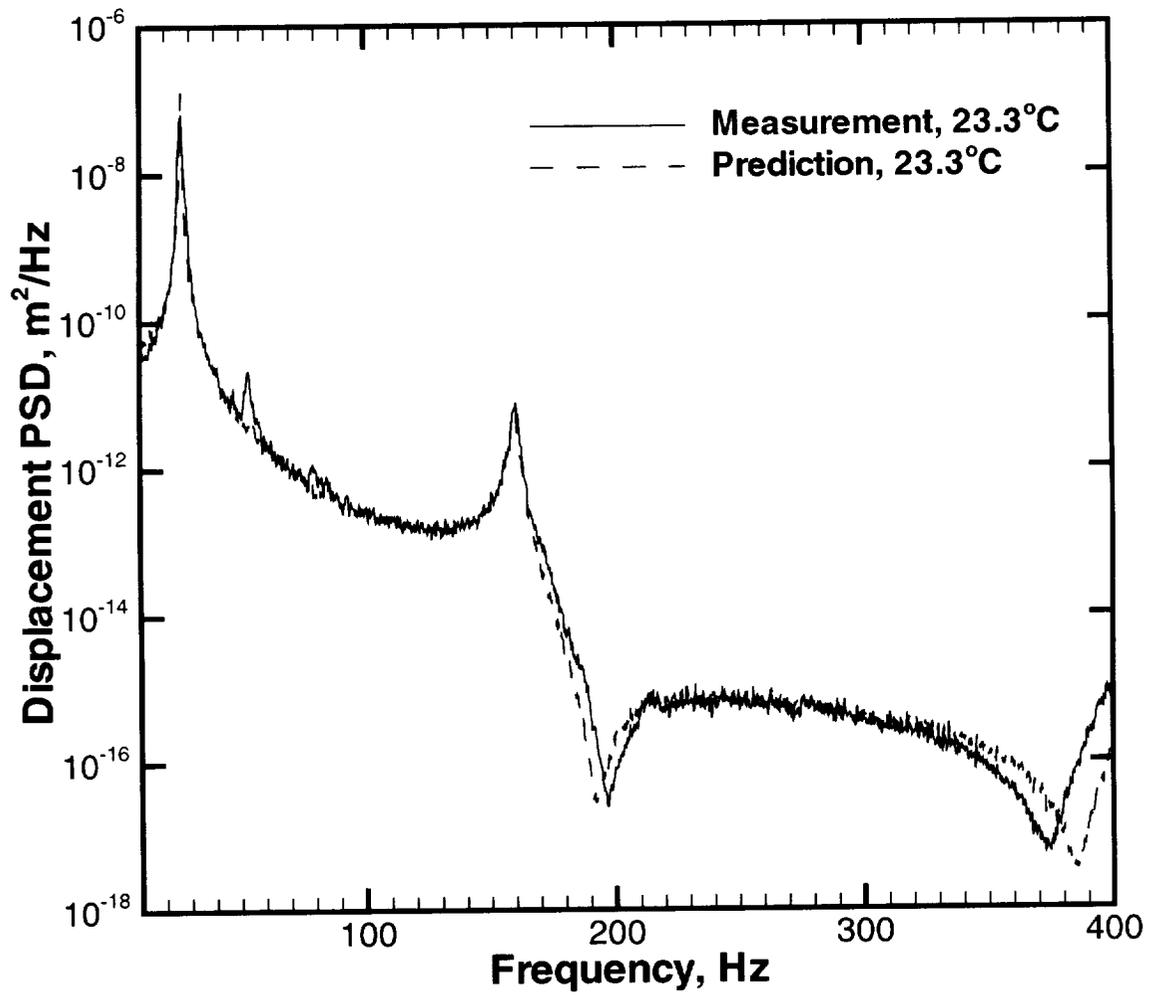
Figure 6.18 Measured and predicted displacement PSD comparison for position 2 on the SMAHC beam at ambient temperature (Δf=0.25 Hz).
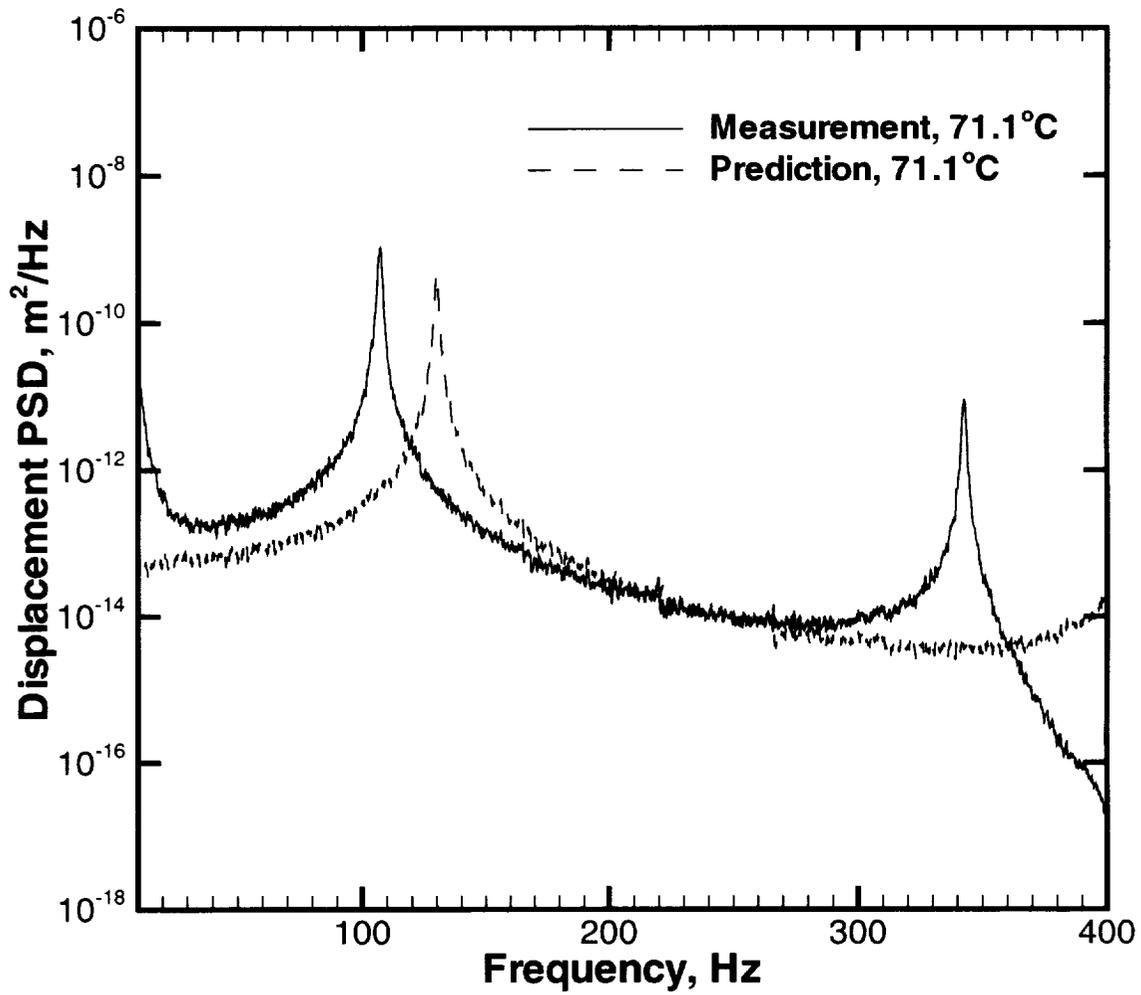
Figure 6.19 Measured and predicted displacement PSD comparison
for position 2 on the SMAHC beam at 71.1°C (160°F, Δf=0.25 Hz).
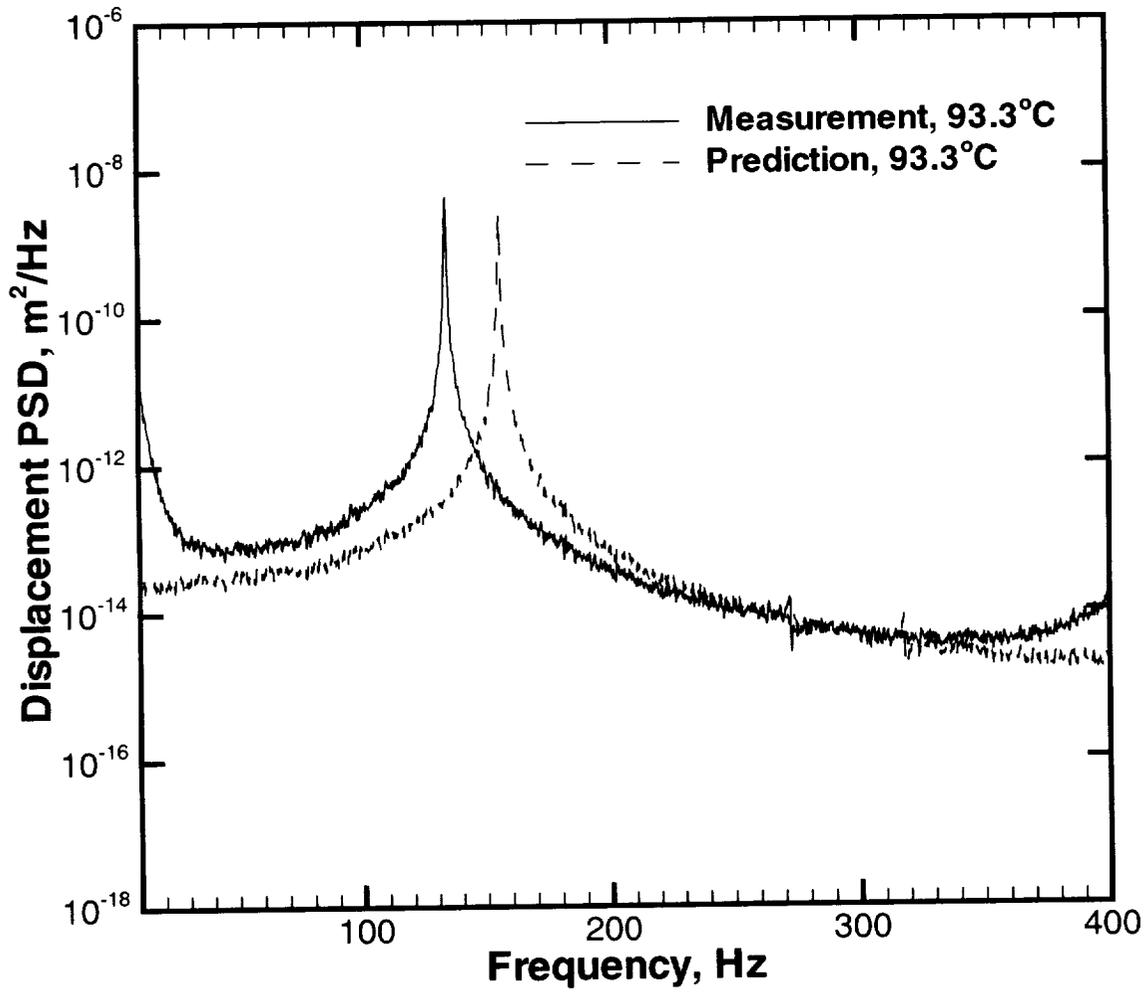
Figure 6.20 Measured and predicted displacement PSD comparison for position 2 on the SMAHC beam at 93.3°C (200°F, Δf=0.25 Hz).
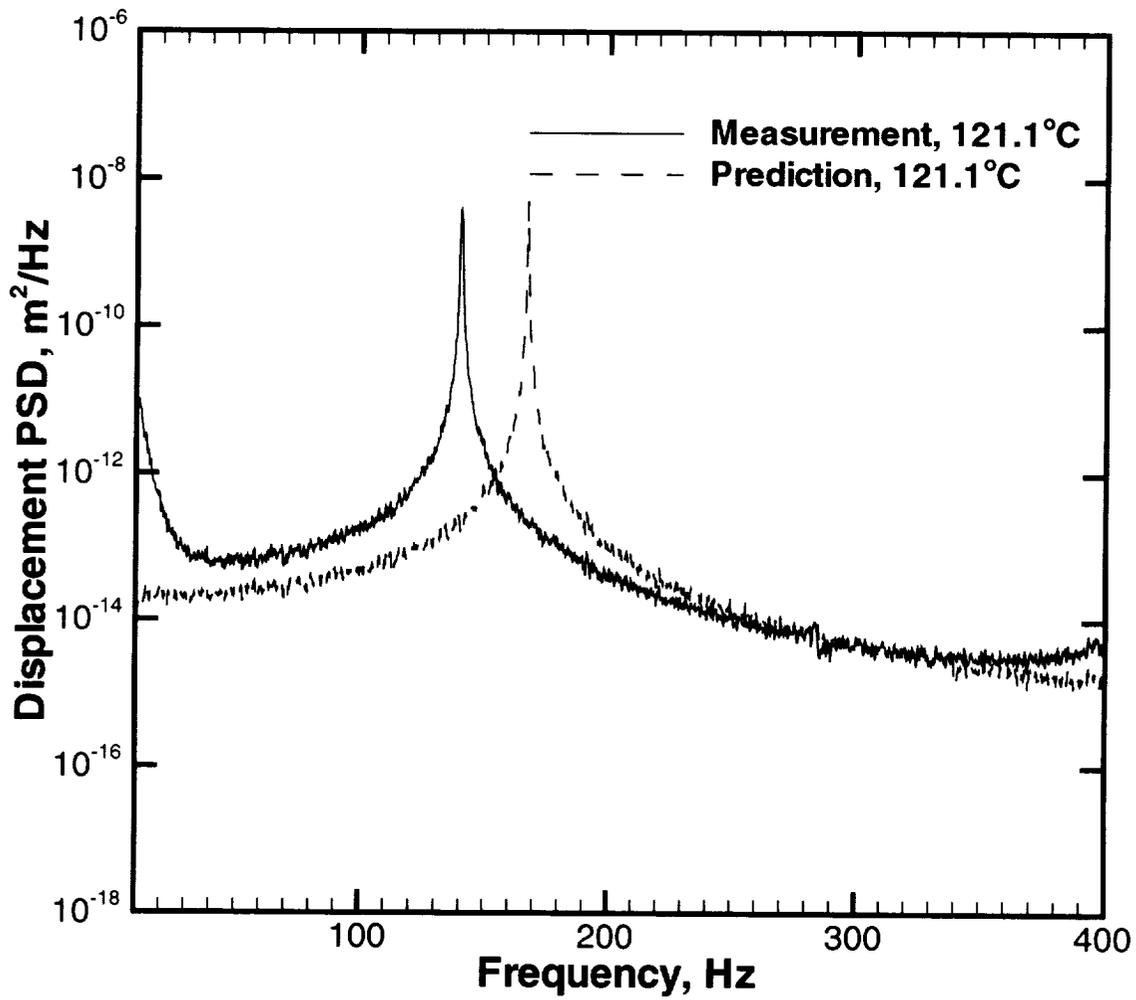
Figure 6.21 Measured and predicted displacement PSD comparison for position 2 on the SMAHC beam at 121.1°C (250°F, Δf=0.25 Hz).
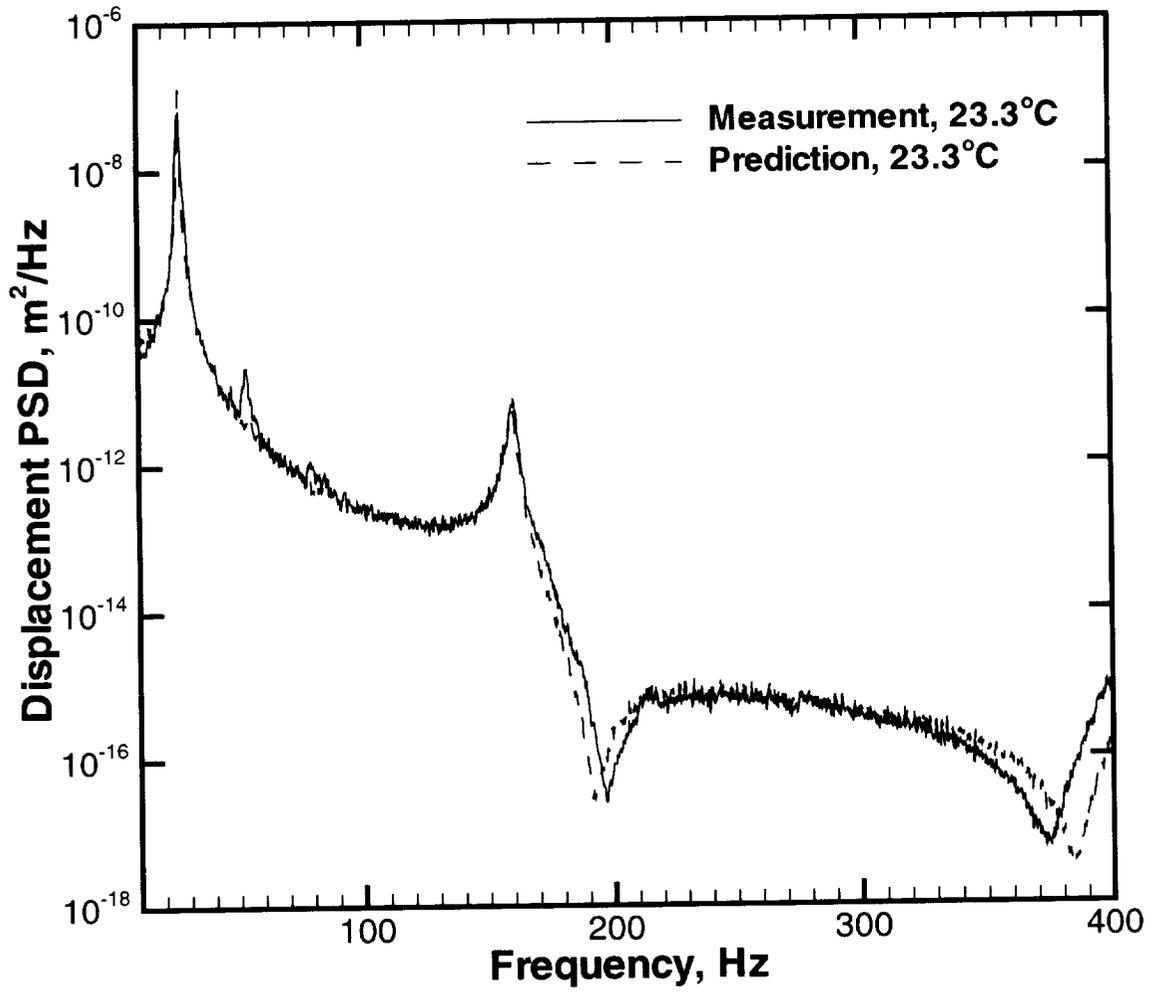
Figure 6.22 Measured and predicted displacement PSD comparison for the SMAHC beam at ambient temperature with boundary effects (Δf=0.25 Hz).
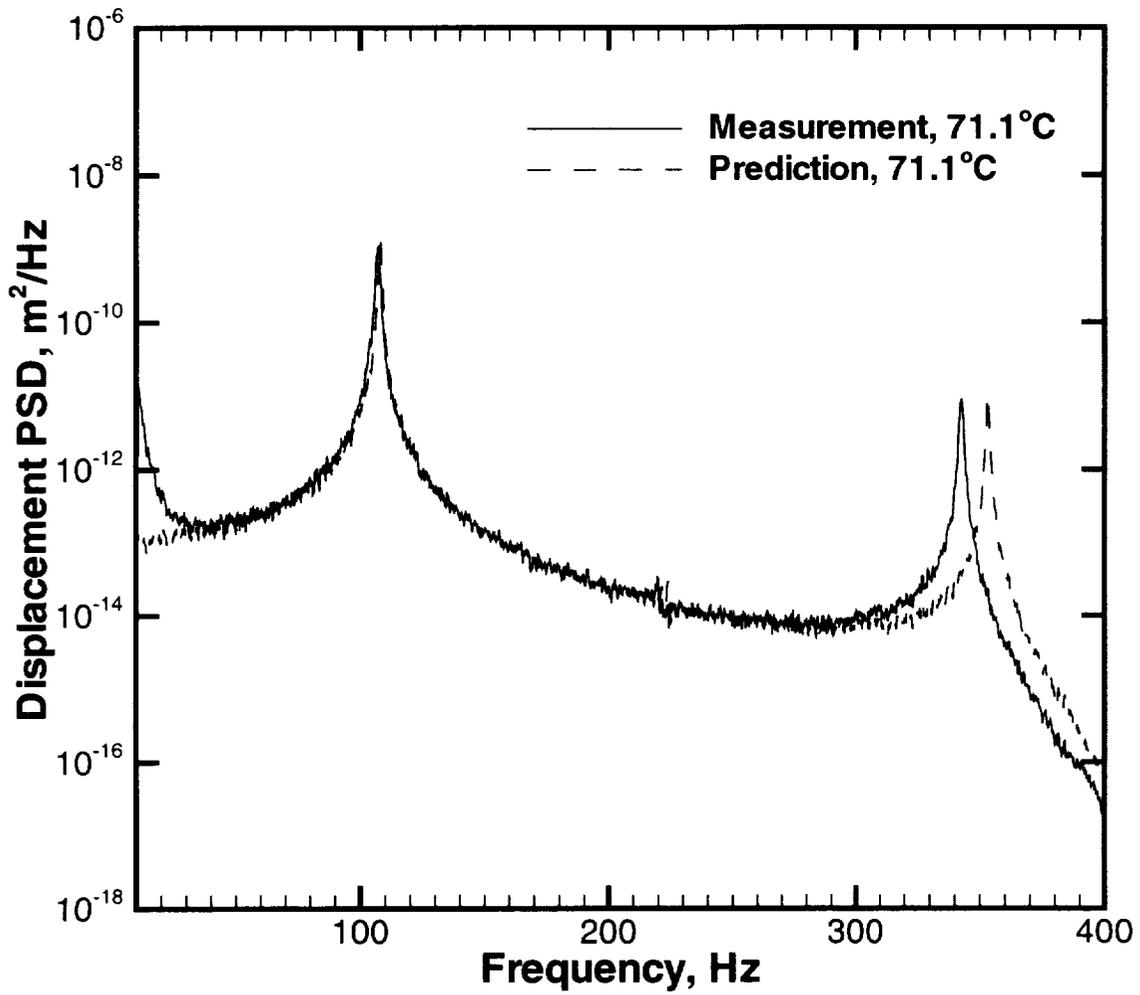
Figure 6.23 Measured and predicted displacement PSD comparison for the SMAHC beam at 71.1°C with boundary effects (160°F, Δf=0.25 Hz).
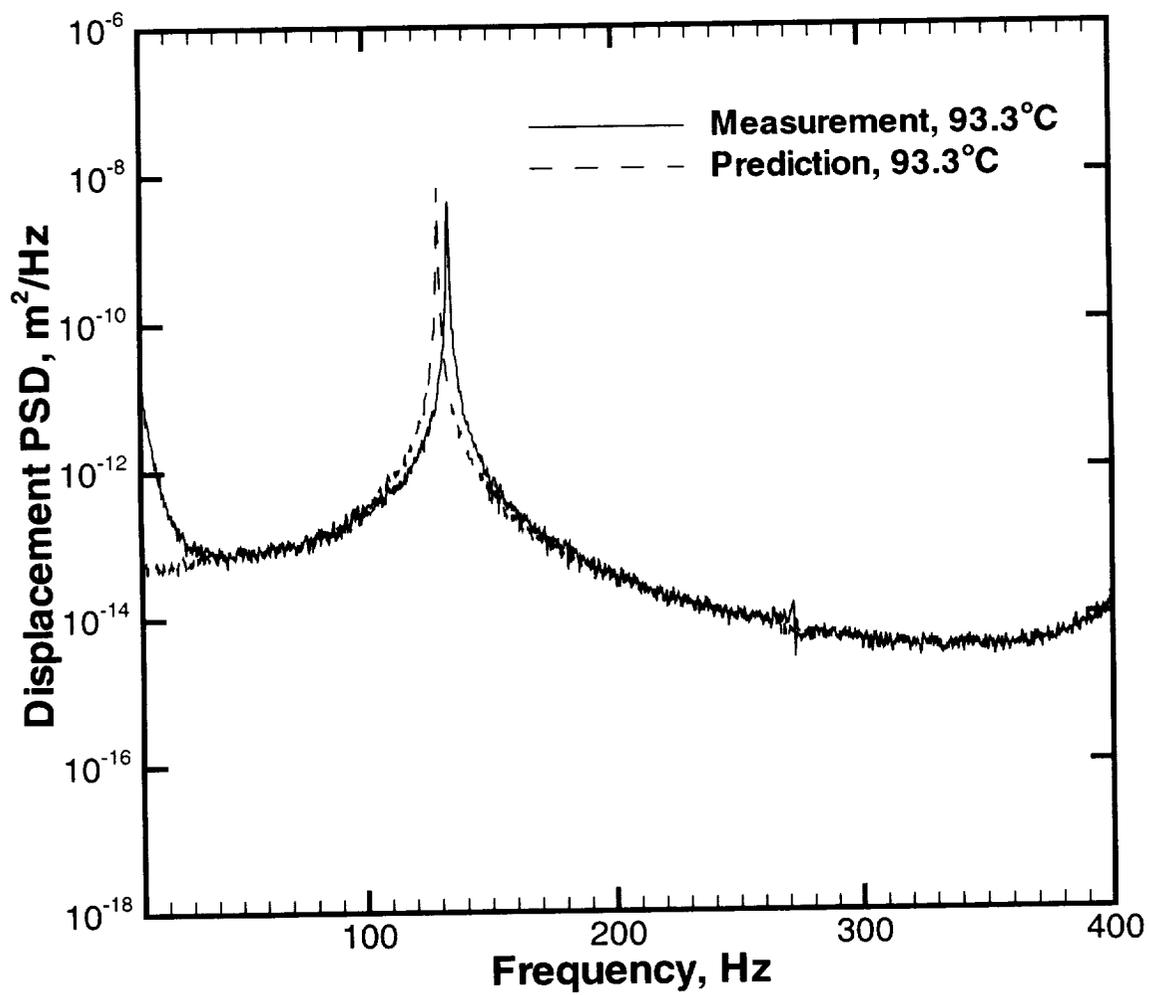
Figure 6.24 Measured and predicted displacement PSD comparison for the SMAHC beam at 93.3°C with boundary effects (200°F, Δf=0.25 Hz).
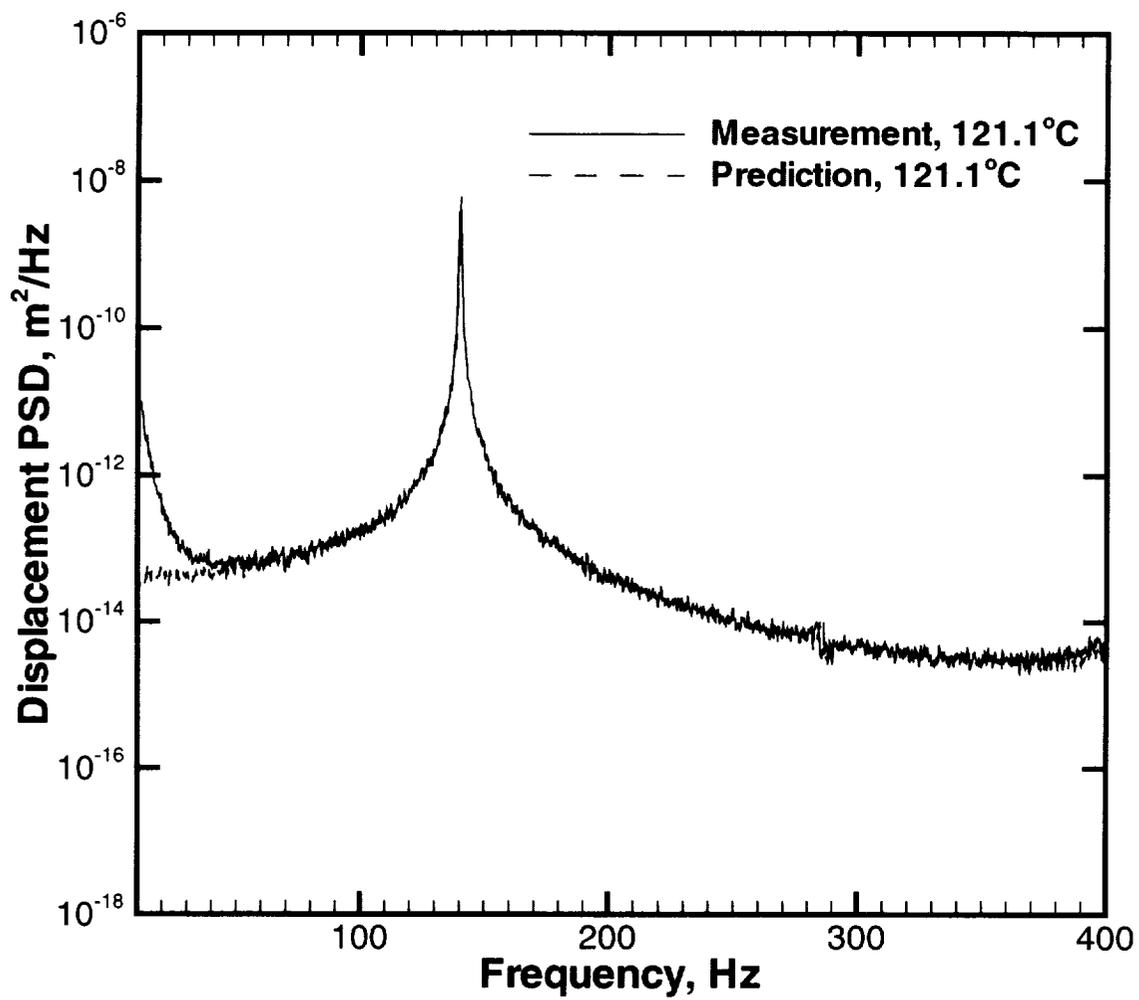
Figure 6.25 Measured and predicted displacement PSD comparison for the SMAHC beam at 121.1°C with boundary effects (250°F, Δf=0.25 Hz).
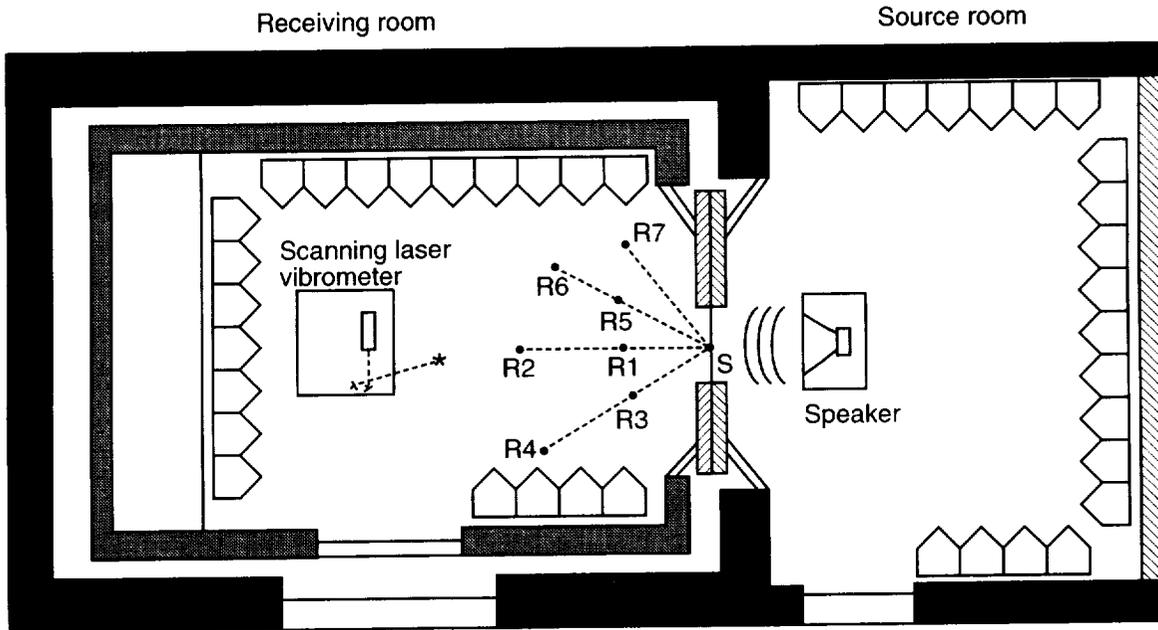
Figure 6.26 Transmission loss apparatus schematic.

The formulation and solution procedures have now been fully exercised and validated against a variety of experimental results, most importantly with the static and dynamic response of a SMAHC beam. Further work was done to validate the acoustic radiation model. Experimental validation was attempted for the case of a clamped aluminum panel. Dynamic responses of the panel due to acoustic excitation were measured during the acoustic radiation tests and validation of the dynamic response prediction capability for this case will be discussed in the next section.

6.6.4 Clamped Aluminum Panel

Experiments were conducted to measure the structural-acoustic response of an aluminum panel subject to broadband, normal acoustic excitation. The experiments were performed in the Transmission Loss Apparatus (TLA) at NASA Langley Research Center, shown schematically in Figure 6.26. The results of the experiments were reported by Turner and Rizzi [55], but are briefly reiterated here. Vibration results are reported in this chapter and acoustic radiation results are reported in the Experimental Validation section of Chapter 7.

The panel was installed in a picture-frame-type clamping fixture such that the unsupported dimensions were $0.305 \times 0.178 \times 1.02e{-}3$ m ($12 \times 7 \times 0.040$ inches). The entire assembly was mounted in the TLA partition baffle and subjected to normal-incidence, acoustic excitation provided by a speaker positioned approximately 0.914 m (36 inches) from the panel. The speaker was driven by a random signal, band-limited to a frequency range of 100–500 Hz. A centered 10×5 inch grid of 11 by 6 locations (total of 66 locations) was defined on the panel surface for vibration response measurements. Power spectra of the panel normal velocity at these locations were acquired with the laser vibrometer and a spectrum analyzer.

The incident acoustic pressure was measured at several locations in the plane of the panel, with the panel and clamping fixture removed from the baffle, under identical source conditions to that of the response measurements. These source measurements were collected to assess the

149

uniformity of the incident pressure across the panel and to provide input for the computational procedure. The overall sound pressure level in the plane of the panel at the opening center was approximately 109 dB (ref 20 μPa, 2.9E-9 psi).

A 12x7-element mesh of the 24 degree-of-freedom rectangular plate elements was used to model the structure. Torsional boundary springs of 15.82 N•m/rad (140 in•lbf/rad) were employed to match the fundamental measured frequency. The source pressure spectrum obtained in the plane of the panel at the center of the baffle hole, when the panel and fixture were removed, was doubled and used as the blocked pressure input to determine the predicted panel response and acoustic radiation. The predicted results were generated using the following material properties for aluminum: E=10 Msi, ν=0.33, and ρ=2.5756e-4 lbf s^2/in^4.

The power spectral density of the pressure incident upon the panel is shown in Figure 6.27. Comparisons of the predicted and measured panel normal velocity are shown in Figures 6.28 and 6.29 for two measurement locations; near the panel center and in the lower-right quadrant. The measurement location coordinates indicated in the figure are relative to the panel's lower left corner. The agreement is excellent with the exception of the appearance of additional peaks in the measured spectra. These peaks are attributable to the first and second non-symmetric modes of the panel. A number of factors could cause this type of phenomenon. The most likely culprit is the acoustic loading, but the source measurements indicated that the acoustic load was very nearly uniform and normal. Furthermore, it is expected that antisymmetric modes would be excited very weakly by acoustic pressure loading anomalies as previously discussed in the simply-supported aluminum panel section. It was later found that the panel was prestressed during fixturing, and it is believed that this is the reason for the significant antisymmetric modal response.
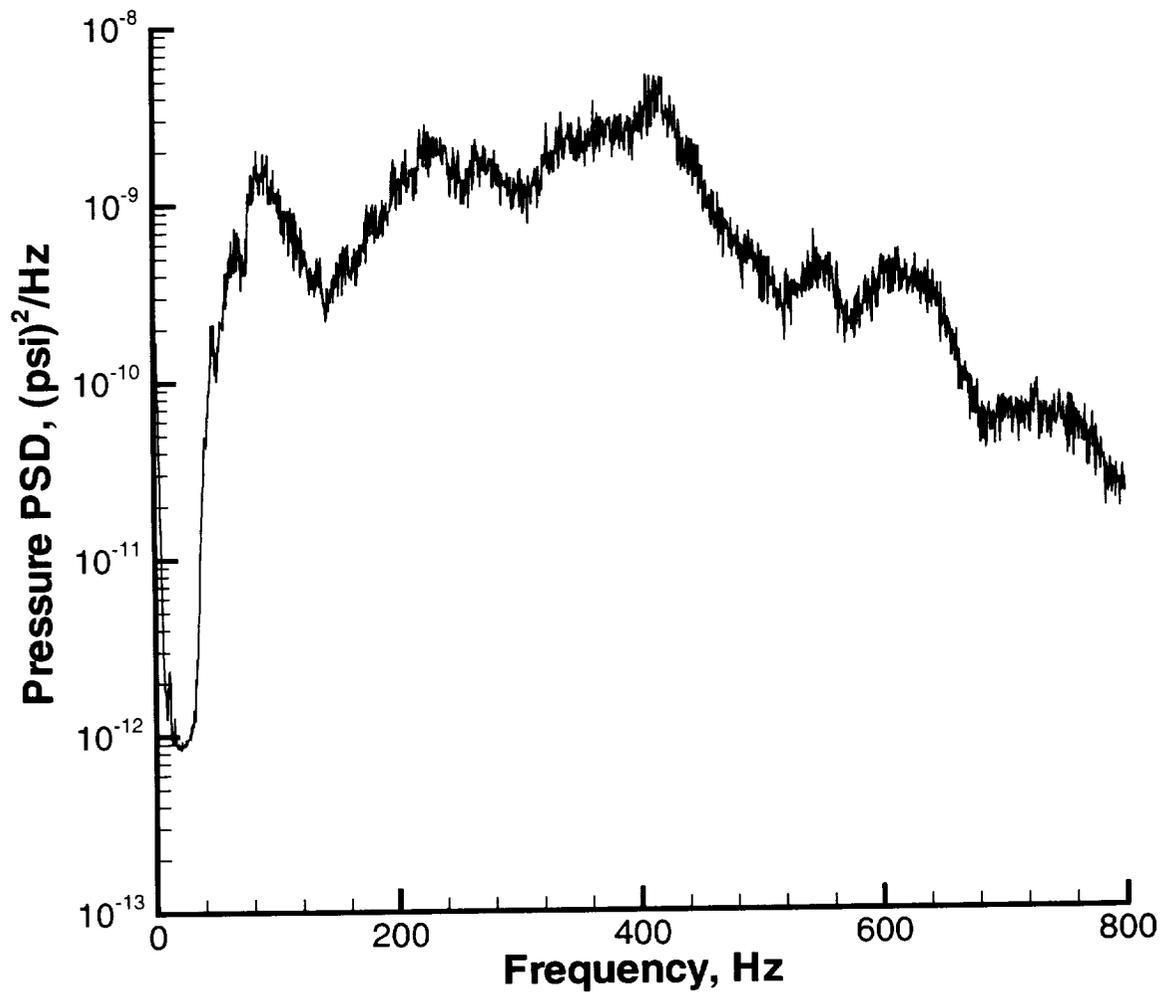
Figure 6.27 PSD of the acoustic excitation incident upon the panel (OASPL 109 dB, ref 20 μPa).
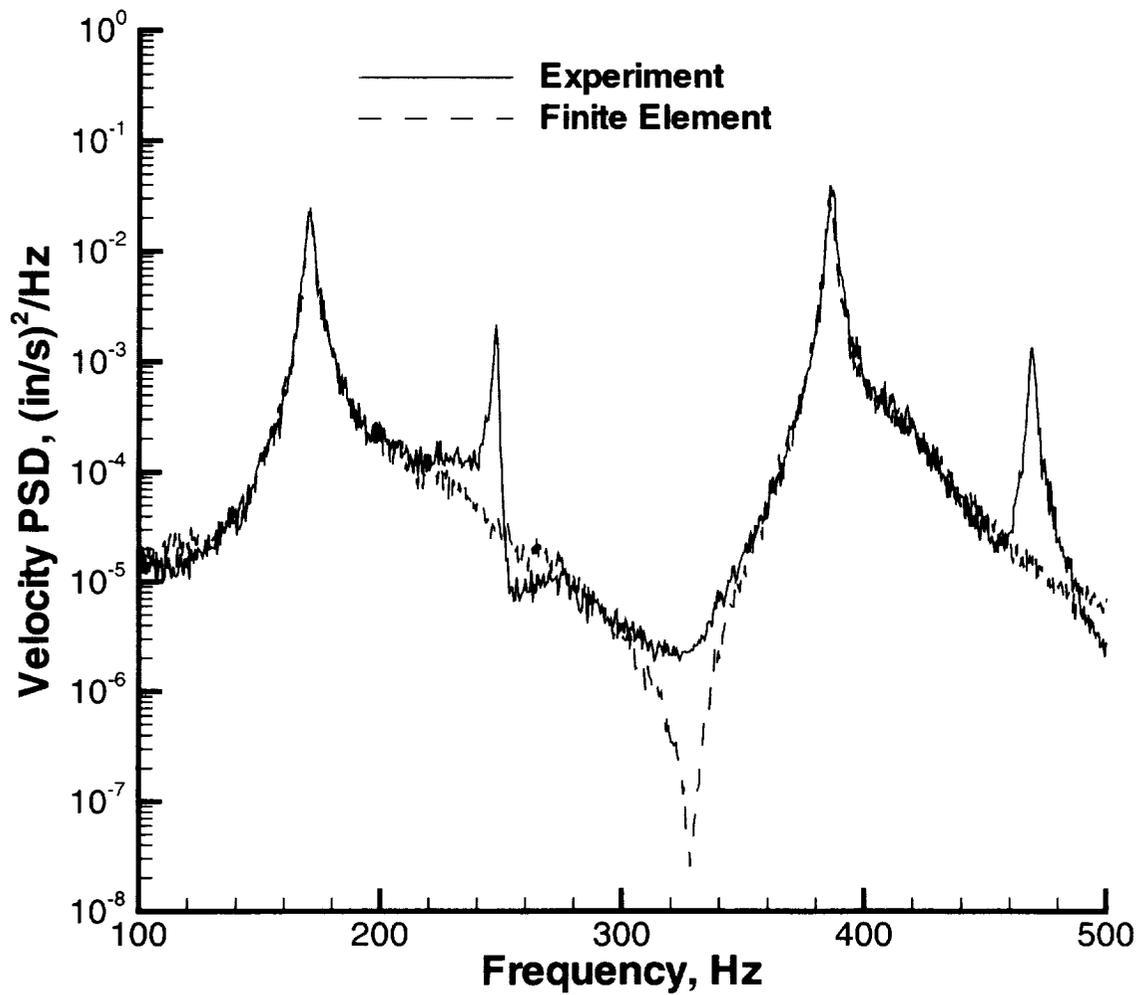
Figure 6.28 Comparison of predicted and measured panel normal velocity PSD at coordinates of x=0.152, y=0.102 m (x=6, y=4 inches) relative to panel lower left corner.
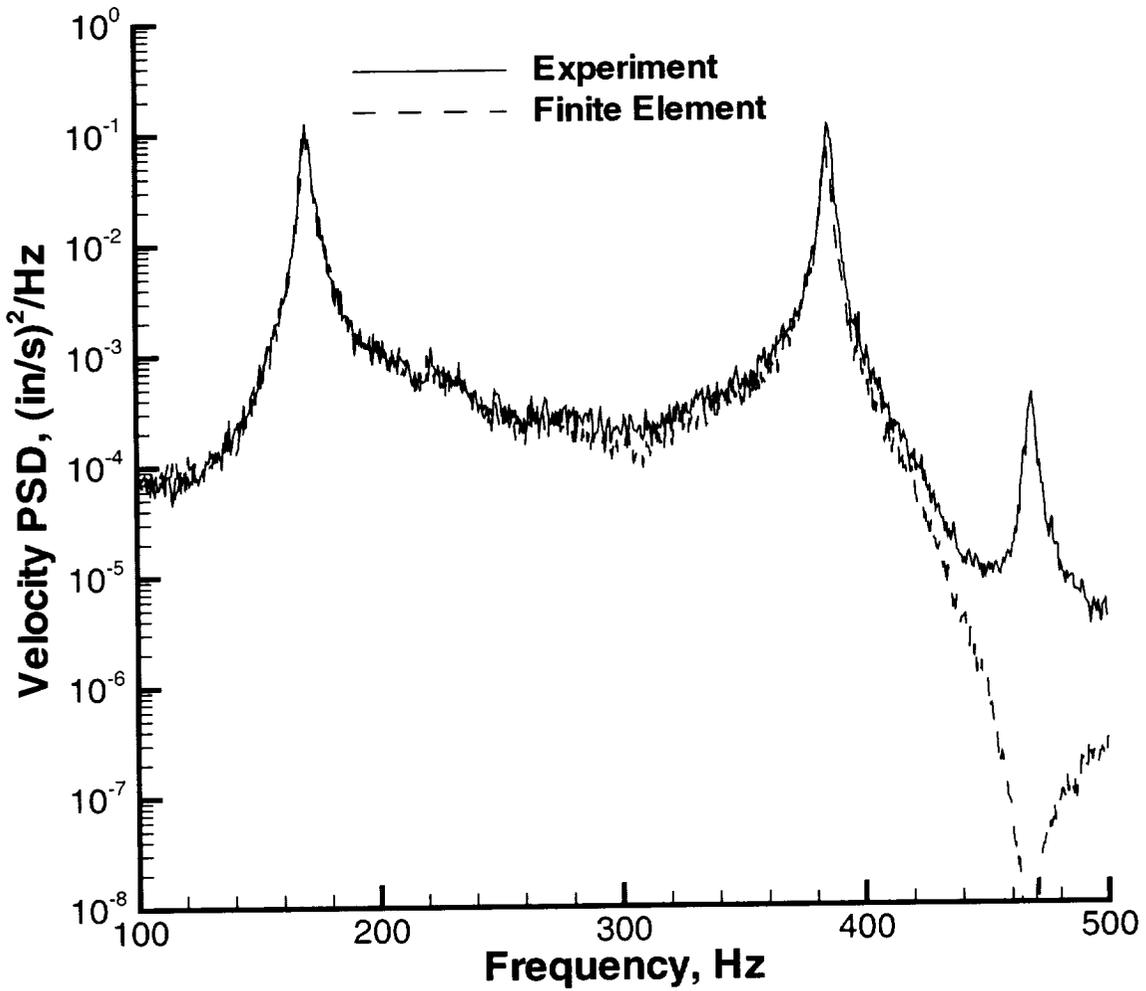
Figure 6.29 Comparison of predicted and measured panel normal velocity PSD at coordinates of x=0.229, y=0.051 m (x=9, y=2 inches) relative to panel lower left corner.

The dynamic load models and spectral analysis method used in this study was presented in this chapter. The formulation and procedures were validated against known solutions prior to attempting correlation with experiment. The analysis was incrementally validated with experimental measurements for the cases of inertially loaded beams including an aluminum beam, a glass-epoxy beam and a SMAHC beam. Experimental results from the SMAHC beam specimen show enormous control authority over the resonance frequencies and RMS response level. Excellent agreement was achieved between prediction and experimental measurement, and reasons for existing discrepancies were discussed. The chapter is concluded with comparisons of the measured and predicted responses of a fully-clamped aluminum panel in preparation for acoustic radiation analysis and validation, which will be presented in the next chapter.

Chapter 7
Acoustic Radiation

The equations derived in Chapter 4 governing the static and dynamic response of panel-type SMA hybrid composite structures subjected to thermal and mechanical loads are applicable to a variety of geometric configurations and arbitrary *natural* boundary conditions. However, acoustic radiation and transmission loss analyses are only practical for panel-type structures with constraints around the entire perimeter of the structure. Furthermore, it is assumed that the structure is supported in such a way that flanking paths for the propagation of acoustic energy are prohibited, i.e., acoustic energy can only be transmitted by the flexible structure. Thus, consider a rectangular composite panel supported in an infinite rigid baffle (infinitely stiff/massive wall) separating two semi-infinite acoustic media. This configuration is typically simulated in practice by a *transmission loss* facility, shown schematically in Figure 6.26. Acoustic radiation analysis will be limited to the cases of acoustic pressure or concentrated force excitation on the *source* side of the panel. The panel radiates acoustic pressures to the *receiving* acoustic field due to its dynamic response. The equations governing acoustic radiation responses under these conditions will be developed in this chapter using continuous and discrete frequency domain approaches.

Consider a panel supported in an infinite rigid baffle and radiating to a semi-infinite acoustic field, shown schematically in Figure 7.1. The acoustic pressure radiated by the panel to a point (x, y, z) in the acoustic field can be related to the dynamic response of the panel through the use of Rayleigh's integral [56]:

$$p_t(x, y, z, t) = \int_A \frac{\rho}{2\pi r} \ddot{w}\left(\xi, \eta, t - \frac{r}{c}\right) dA \tag{7.1}$$

where ρ is the fluid density, $\ddot{w}$ is the out-of-plane acceleration response of the panel, ξ and η are spatial coordinates in the plane of the panel, r is the distance from (ξ, η) on the plate to (x, y, z) in the acoustic field, c is the acoustic wave speed, $t - \frac{r}{c}$ is the retarded time between the two points, and A is the surface area of the panel. The subscript t indicates transmitted pressure to be consistent with the nomenclature in Chapter 6.
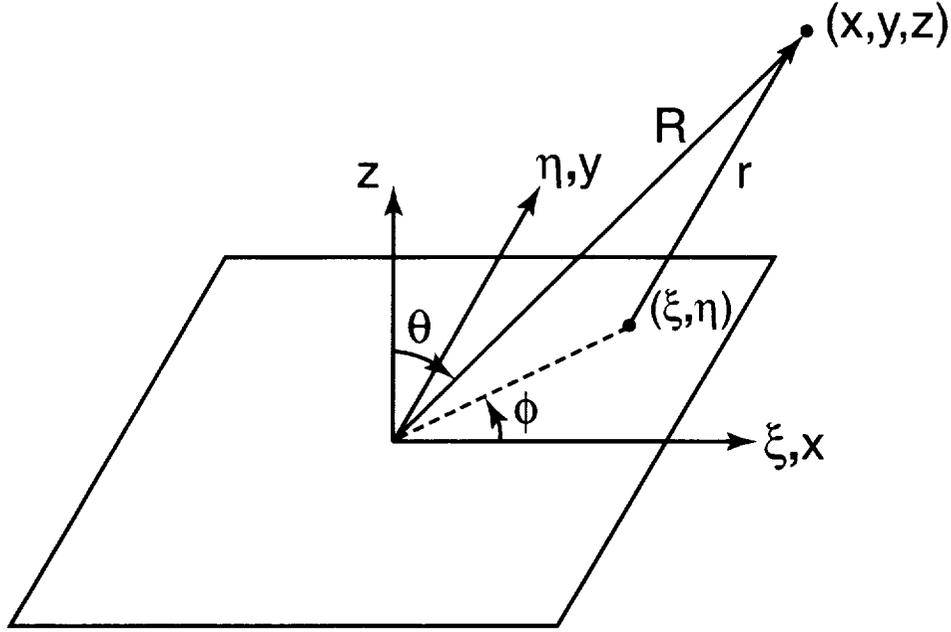
Figure 7.1 Schematic of a panel radiating to a semi-infinite acoustic field.

7.1 Continuous Spectral Analysis

The cross-correlation of the radiated pressure can be formed from the following expected value

$$C_{pp}(\vec{r}, t_1, \vec{r}', t_2) = E\left[p_t(x, y, z, t_1)p_t(x', y', z', t_2)\right]$$

$$= \left(\frac{\rho}{2\pi}\right)^2 \int\limits_A \int\limits_{A'} \frac{1}{r_1 r_2} E\left[\ddot{w}\left(\xi, \eta, t_1 - \frac{r_1}{c}\right)\ddot{w}\left(\xi', \eta', t_2 - \frac{r_2}{c}\right)\right] dA\, dA' \qquad (7.2)$$

where the expected value expression in the integrand is the cross-correlation function of the plate normal acceleration $C_{\ddot{w}\ddot{w}}(\xi, \eta, t_1 - \frac{r_1}{c}, \xi', \eta', t_2 - \frac{r_2}{c})$, r_1 is the distance from (ξ, η) on the structure to $\vec{r} = (x, y, z)$ in the acoustic field, and r_2 is the distance from (ξ', η') on the structure to $\vec{r}' = (x', y', z')$ in the acoustic field. For stationary response, the time lag can be defined as $\tau = t_2 - t_1$ so that $\frac{\partial^2}{\partial t_1^2}\frac{\partial^2}{\partial t_2^2} = \frac{\partial^4}{\partial \tau^4}$ and the assumption of mean-square differentiability allows equation (7.2) to be rewritten in the form

$$C_{pp}(x, y, z, x', y', z', \tau') = \left(\frac{\rho}{2\pi}\right)^2 \int\limits_A \int\limits_{A'} \frac{1}{r_1 r_2}\frac{\partial^4}{\partial \tau^4} C_{ww}(\xi, \eta, \xi', \eta', \tau')\, dA\, dA' \qquad (7.3)$$

where $\tau' = \tau + \frac{r_1 - r_2}{c}$. Because the plate normal deflection cross-correlation function is related to the cross spectral density function through the Wiener-Khinchine relation

$$C_{ww}(\xi, \eta, \xi', \eta', \tau') = \int\limits_{-\infty}^{\infty} S_{ww}(\xi, \eta, \xi', \eta', \omega)\, e^{i\omega\tau'} d\omega \qquad (7.4)$$

156

and the response is stationary, the following expression can be derived

$$\frac{\partial^4}{\partial \tau^4} C_{ww}(\xi, \eta, \xi', \eta', \tau') = \int_{-\infty}^{\infty} \omega^4 S_{ww}(\xi, \eta, \xi', \eta', \omega) e^{i\omega \tau'} d\omega \tag{7.5}$$

Substituting in equation (7.3) results in the following expression for the cross-correlation of the radiated pressure.

$$C_{pp}(x, y, z, x', y', z', \tau') = \left(\frac{\rho}{2\pi}\right)^2 \int_A \int_{A'} \frac{1}{r_1 r_2} \int_{-\infty}^{\infty} \omega^4 S_{ww}(\xi, \eta, \xi', \eta', \omega) e^{i\omega \tau'} d\omega \, dA \, dA' \tag{7.6}$$

Recall that the displacement field of the panel is known on the elemental level due to the finite element spatial discretization, shown in equation (4.5):

$$w_e(\xi, \eta) \approx \{L_w(\xi, \eta)\}^T \{a_b\} \tag{7.7}$$

where $\{L_w(\xi, \eta)\}$ is the vector of out-of-plane interpolation functions and $\{a_b\}$ is the out-of-plane displacement vector, both for element e. Then, the displacement cross-correlation function between portions of the plate belonging to elements i and j can be approximated by

$$C_{ww}^{ij}(\xi, \eta) \approx \{L_w(\xi, \eta)\}_i^T E\left[\{a_b\}_i \{a_b\}_j^T\right] \{L_w(\xi', \eta')\}_j \tag{7.8}$$

where $E[\{a_b\}_i \{a_b\}_j^T] = [C_{aa}^{ij}]$ is the physical displacement correlation matrix between elements i and j. Consequently, the panel area integrals in equation (7.6) can be replaced by a double sum over element area integrals to obtain

$$C_{pp} = \left(\frac{\rho}{2\pi}\right)^2 \sum_{i=1}^{N_e} \sum_{j=1}^{N_e} \int_{A_i} \int_{A'_j} \frac{1}{r_1 r_2} \{L_w(\xi, \eta)\}_i^T \int_{-\infty}^{\infty} \omega^4 [S_{aa}^{ij}(\omega)] e^{i\omega \tau'} d\omega \{L_w(\xi', \eta')\}_j \, dA_i \, dA'_j \tag{7.9}$$

where N_e is the number of elements. It follows that the mean square ($\tau = 0$) radiated pressure at the point (x, y, z) in the acoustic field has the form

$$\overline{p_f^2}(x, y, z) = \left(\frac{\rho}{2\pi}\right)^2 \sum_{i=1}^{N_e} \sum_{j=1}^{N_e} \int_{A_i} \int_{A'_j} \frac{1}{r_1 r'_1} \{L_w(\xi, \eta)\}_i^T \int_{-\infty}^{\infty} \omega^4 [S_{aa}^{ij}(\omega)] e^{i\omega \frac{r_1 - r'_1}{c}} d\omega$$

$$\{L_w(\xi', \eta')\}_j \, dA_i \, dA'_j \tag{7.10}$$

where

$$r_1 = \sqrt{(x - \xi)^2 + (y - \eta)^2 + z^2} \tag{7.11}$$

and

$$r'_1 = \sqrt{(x - \xi')^2 + (y - \eta')^2 + z^2} \tag{7.12}$$

are distances from the same point in the acoustic field to different points on the panel and $(r_1 - r'_1)/c$ is the zero-time-lag retarded time difference (the difference in the time it takes for an acoustic disturbance to travel from (ξ, η) to (x, y, z) versus (ξ', η') to (x, y, z)).

Note that the spectral density matrix of the physical displacement response in the integrand of the spectral integral in equation (7.10):

$$\int_{-\infty}^{\infty} \omega^{4}[S_{aa}^{ij}(\omega)] \epsilon^{i\omega\frac{r_1-r_1'}{c}} d\omega \tag{7.13}$$

is a subset of the system physical displacement spectral density matrix. The form for the system matrix is inferred from equation (6.38)

$$[S_{AA}(\omega)] = [\phi]\lceil H^{*}(\omega)\rfloor[S_{ff}(\omega)]\lceil H(\omega)\rfloor[\phi]^{T} \tag{7.14}$$

where $[\phi]$ is the modal matrix, $\lceil H(\omega)\rfloor$ is a diagonal matrix of stationary frequency response functions, and the modal force spectral density matrix is given by the appropriate form in equations (6.34). So, an arbitrary element (m, n) of the spectral integrand in equation (7.10) requires evaluation of an improper integral of the form

$$\int_{-\infty}^{\infty} \omega^{4} H_{m}^{*}(\omega)\ H_{n}(\omega)S_{**}^{mn}(\omega)\epsilon^{i\omega\frac{r_1-r_1'}{c}}\ d\omega \tag{7.15}$$

where the frequency response functions $H_{m}(\omega)$ are given by equation (6.29). Note that these integrals have the same form as those required for determining modal correlation functions of the structure's acceleration response for nonzero time lag $(\tau \neq 0)$, shown in equation (6.36). Refer to Appendix F for sample cases of the evaluation of these integrals.

The element area integrals in equation (7.10) can be evaluated via Gauss-Legendre numerical integration, which precludes the necessity for simplifications to the integrand. However, in the discussions to follow, it will be useful to introduce acoustic far-field assumptions. See Kinsler et al. [57] for a general description of these assumptions and Appendix D for details of this particular implementation. These assumptions entail making the approximations

$$\frac{1}{r_1} \approx \frac{1}{R} \qquad\qquad \frac{1}{r_1'} \approx \frac{1}{R} \tag{7.16}$$

and

$$\epsilon^{i\omega\left(\frac{r_1-r_1'}{c}\right)} \approx \epsilon^{i\omega\frac{(\xi'-\xi)K+(\eta'-\eta)\Lambda}{c}} \tag{7.17}$$

where R is the distance from the center of the panel to the point (x, y, z) in the acoustic field, $K = \sin\theta\cos\phi$, and $\Lambda = \sin\theta\sin\phi$ (see Figure 7.1).

Equation (7.10) can be rewritten for the acoustic far-field as

$$\overline{p_i^2}(R,\theta,\phi) = \left(\frac{\rho}{2\pi R}\right)^{2}\sum_{i=1}^{N_r}\sum_{j=1}^{N_r}\int_{A_i}\int_{A_j'}\{L_w(\xi,\eta)\}_i^{T}\int_{-\infty}^{\infty}\omega^{4}[S_{aa}^{ij}(\omega)]\epsilon^{i\omega\frac{(\xi'-\xi)K+(\eta'-\eta)\Lambda}{c}}d\omega$$
$$\{L_w(\xi',\eta')\}_j\ dA_i\ dA_j' \tag{7.18}$$

The out-of-plane interpolation functions $L_w(\xi,\eta)$ are defined in terms of element local coordinates in equation (4.4). Therefore, the complex exponential function in the integrand of equation

158

(7.18) must be separated into two components; one is constant for each element index pair (i,j), the other must be included in the integration over the element areas in local coordinates. The element area integrations can be performed numerically, via Gauss-Legendre numerical integration (see Appendix B), but significant improvements in computational efficiency can be realized by performing the integrations in closed form (see Appendix C). Other acoustic quantities, such as acoustic intensity and total radiated power, can be related to the mean square pressure $\overline{p_i^2}$ in equation (7.18), shown in Appendix E.

7.2 Discrete Spectral Analysis

Recall the relationship between the radiated acoustic pressure at a point (x,y,z) in the acoustic free-field and the dynamic response of the panel as described by Rayleigh's integral in equation (7.1). The physical degrees of freedom are known on an elemental basis from equation (4.5)

$$w_e(\xi,\eta,t) \approx \{L_w(\xi,\eta)\}^T\{a_b\} \tag{7.19}$$

where $\{L_w(\xi,\eta)\}$ is a vector of out-of-plane interpolation functions and $\{a_b\}$ is the vector of out-of-plane degrees of freedom. So, the area integral in the expression for the radiated acoustic pressure, equation (7.1), can be rewritten as the sum of element area integrals:

$$p_t(x,y,z,t) = \frac{\rho}{2\pi}\sum_{i=1}^{N_e}\int_{A_i}\frac{1}{r}\{L_w(\xi,\eta)\}_i^T\left\{\ddot{a}_b\left(t-\frac{r}{c}\right)\right\}_i dA_i \tag{7.20}$$

where N_e is the number of elements and A_i is the element area.

A discrete spectral analysis can be employed by writing the panel dynamic response and radiated acoustic pressure as a sum of harmonic functions given by

$$\left\{a_b\left(t-\frac{r}{c}\right)\right\} = \sum_{n=0}^{N_\omega-1}\{\hat{a}_{bn}\}e^{i\omega_n\left(t-\frac{r}{c}\right)} \tag{7.21}$$

and

$$p_t(x,y,z,t) = \sum_{n=0}^{N_\omega-1}\hat{p}_n(x,y,z)e^{i\omega_n t} \tag{7.22}$$

where N_ω is the number of discrete frequencies and $\{\hat{a}_{bn}\}$ and $\hat{p}_n$ are complex spectral amplitudes of the out-of-plane nodal displacement response and radiated acoustic pressure, respectively. Substitution of equations (7.21) and (7.22) in Rayleigh's integral, equation (7.20), results in

$$\sum_{n=0}^{N_\omega-1}\hat{p}_n(x,y,z)e^{i\omega_n t} = -\frac{\rho}{2\pi}\sum_{k=1}^{N_e}\int_{A_k}\frac{1}{r}\{L_w(\xi,\eta)\}_k^T\sum_{n=0}^{N_\omega-1}\omega_n^2\{\hat{a}_{bn}\}_k e^{i\omega_n\left(t-\frac{r}{c}\right)}dA_k \tag{7.23}$$

This expression can be written for any one of the discrete frequencies as

$$\hat{p}_n(x,y,z) = -\frac{\rho}{2\pi}\sum_{k=1}^{N_e}\int_{A_k}\frac{1}{r}\{L_w(\xi,\eta)\}_k^T\omega_n^2\{\hat{a}_{bn}\}_k e^{-i\omega_n\frac{r}{c}}dA_k \tag{7.24}$$

If the excitation is deterministic, the expression for the radiated pressure complex spectral amplitudes can be used in an inverse FFT, equation (7.22), to determine the radiated pressure time response:

$$p_t(x,y,z,t) = -\frac{\rho}{2\pi} \sum_{n=0}^{N_\omega-1} \sum_{k=1}^{N_e} \int_{A_e} \frac{1}{r} \{L_w(\xi,\eta)\}_k^T \omega_n^2 \{\hat{a}_{bn}\}_k e^{-i\omega_n \frac{r}{c}} dA_k e^{i\omega_n t} \qquad (7.25)$$

The vector $\{\hat{a}_{bn}\}_k$ is an element-k subset of the physical displacement spectral amplitude vector given by equations (6.41) and (6.59):

$$\{\hat{A}_{bn}\} = [\phi][H(\omega_n)]\{\hat{f}_n\} \qquad (7.26)$$

However, for stochastic excitation, a statistical approach must be used.

The cross-correlation function of the radiated acoustic pressure can be formulated from equation (7.22) through the following expectation

$$C_{pp}(x,y,z,t_1,x',y',z',t_2) = \sum_{n=0}^{N_\omega-1} \sum_{m=0}^{N_\omega-1} E[\hat{p}_m^* \hat{p}_n] e^{i(\omega_n t_2 - \omega_m t_1)} \qquad (7.27)$$

The cross-correlation function can be expressed in terms of the panel dynamic response by substituting from equation (7.24) as

$$C_{pp}(\vec{r},t_1,\vec{r}',t_2) = \left(\frac{\rho}{2\pi}\right)^2 \sum_{k=1}^{N_e} \sum_{l=1}^{N_e} \int_{A_k} \int_{A_l'} \frac{1}{r_1 r_2} \{L_w(\xi,\eta)\}_k^T \sum_{m=0}^{N_\omega-1} \sum_{n=0}^{N_\omega-1} \omega_m^2 \omega_n^2 E[\{\hat{a}_{bm}^*\}_k \{\hat{a}_{bn}\}_l^T]$$

$$e^{-i\omega_m(t_1-\frac{r_1}{c})} e^{i\omega_n(t_2-\frac{r_2}{c})} \{L_w(\xi',\eta')\}_l \, dA_k \, dA_l' \qquad (7.28)$$

where r_1 is the distance from (ξ,η) on the panel to $\vec{r} = (x,y,z)$ in the acoustic field and r_2 is the distance from (ξ',η') on the panel to $\vec{r}' = (x',y',z')$ in the acoustic field. The term $E[\{\hat{a}_{bm}^*\}_k \{\hat{a}_{bn}^*\}_l^T]$ contains the element k and l components of the generalized spectral matrix of the physical coordinate displacement response.

Recall that the expected value of the spectral amplitudes takes a special form for stationary response, so the generalized spectral matrix simplifies to

$$E[\{\hat{a}_{bm}^*\}_k \{\hat{a}_{bn}\}_l^T] = E[\{\hat{a}_{bm}^*\}_k \{\hat{a}_{bn}\}_l^T]\delta_{mn} \qquad (7.29)$$

where δ_{mn} is the Kronecker delta. Then, the stationary radiated pressure cross-correlation function results $C_{pp}(\vec{r}_1,t_1,\vec{r}_2,t_2) \to C_{pp}(\vec{r}_1,\vec{r}_2,\tau)$, which can be written as

$$C_{pp}(\vec{r}_1,\vec{r}_2,\tau) = \sum_{n=0}^{N_\omega-1} E[\hat{p}_m^* \hat{p}_n] e^{i\omega_n(\tau + \frac{r_1-r_2}{c})} \qquad (7.30)$$

where $\tau = t_2 - t_1$ is the time lag. This expression can be further simplified for zero time lag $(\tau = 0)$, which should not be confused with zero retarded time lag. Thus, the mean square

160

radiated acoustic pressure at a point (x, y, z) in the acoustic field becomes

$$\overline{p_t^2}(x, y, z) = \left(\frac{\rho}{2\pi}\right)^2 \sum_{k=1}^{N_e} \sum_{l=1}^{N_e} \int\int_{A_k \ A_l'} \frac{1}{r_1 r_1'} \{L_w(\xi, \eta)\}_k^T$$

$$\sum_{n=0}^{N_w-1} \omega_n^4 [G_{aa}^{kl}(\omega_n)] e^{i\omega_n \left(\frac{r_1 - r_1'}{c}\right)} \{L_w(\xi', \eta')\}_l \, dA_k dA_l' \tag{7.31}$$

where r_1 and r_1' are distances from the same point (x, y, z) in the acoustic field to different points on the panel, $(r_1 - r_1')/c$ is the retarded time difference, and $[G_{aa}^{kl}(\omega_n)]$ contains the element k and l entries of the single-sided, stationary, physical displacement spectral matrix $[G_{AA}(\omega_n)]$ inferred from equation (6.59):

$$[G_{AA}(\omega_n)] = [\phi] \lceil H^*(\omega_n) \rfloor [G_{ff}(\omega_n)] \lceil H(\omega_n) \rfloor [\phi]^T \tag{7.32}$$

Although the following discussion is analogous to that for acoustic radiation using the continuous spectral approach, a brief description will be reiterated here for convenience and because the resulting relations are slightly different for the discrete spectral analysis. The element area integrals can be evaluated via Gauss-Legendre numerical integration, which precludes the necessity for acoustic far-field approximations. However, in the discussions to follow, it will be useful to introduce acoustic far-field assumptions for acoustic intensity calculations. See Appendix D for a detailed discussion. These assumptions entail making the approximations

$$\frac{1}{r_1} \approx \frac{1}{R} \qquad\qquad \frac{1}{r_1'} \approx \frac{1}{R} \tag{7.33}$$

and

$$e^{i\omega\left(\frac{r_1 - r_1'}{c}\right)} \approx e^{i\omega\frac{(\xi' - \xi)\mathrm{K} + (\eta' - \eta)\Lambda}{c}} \tag{7.34}$$

where R is the distance from the panel center to the point (x, y, z) in the acoustic field, $\mathrm{K} = \sin\theta\cos\phi$, and $\Lambda = \sin\theta\sin\phi$, shown in Figure 7.1.

The mean square radiated acoustic pressure can be written for the acoustic far-field as

$$\overline{p_t^2}(R, \theta, \phi) = \left(\frac{\rho}{2\pi R}\right)^2 \sum_{k=1}^{N_e} \sum_{l=1}^{N_e} \int\int_{A_k \ A_l'} \{L_w(\xi, \eta)\}_k^T$$

$$\sum_{n=0}^{N_w-1} \omega_n^4 [G_{aa}^{kl}(\omega_n)] e^{i\omega_n \frac{(\xi' - \xi)\mathrm{K} + (\eta' - \eta)\Lambda}{c}} \{L_w(\xi', \eta')\}_l \, dA_k \, dA_l' \tag{7.35}$$

Note that the interpolation functions $L_w(\xi, \eta)$ are usually known in terms of element local coordinates. Therefore, the complex exponential function in the integrand of equation (7.35) must be separated into two components: one is constant for each element index pair (k, l); the other must be included in the integration over the element areas in local coordinates. The element area integrations can be performed numerically, via Gauss-Legendre numerical integration (see Appendix B), but significant improvements in computational efficiency can be realized by

performing the integrations in closed form (see Appendix C). Other acoustic quantities, such as the acoustic intensity and total radiated power, can be related to the mean square pressure in equation (7.35), shown in Appendix E.

In general, the expression in equation (7.35) must be used to calculate the far-field mean square acoustic pressure radiated by a panel. However, recall the simplifications presented, starting with equation (6.61), for the excitation class which includes acoustic pressure, single or multiple equivalent concentrated forces, and base acceleration. A general expression for the single-sided, physical displacement spectral matrix at discrete circular frequency ω_n is inferred from equation (6.62):

$$[G_{AA}(\omega_n)] = \{H_A^*(\omega_n)\}\{H_A(\omega_n)\}^T \tag{7.36}$$

Substituting into the expression for the far-field mean square pressure and changing the order of the summations results in

$$\overline{p_f^2}(R,\theta,\omega) = \left(\frac{\rho}{2\pi R}\right)^2 \sum_{n=0}^{N_\omega-1} \sum_{k=1}^{N_e} \int_{A_k} \{L_w(\xi,\eta)\}_k^T e^{-i\omega_n \frac{\xi K + \eta \Lambda}{r}} dA_k \, \omega_n^2 \{H_a^*(\omega_n)\}_k$$

$$\sum_{l=1}^{N_e} \omega_n^2 \{H_a(\omega_n)\}_l^T \int_{A_l} \{L_w(\xi',\eta')\}_l e^{i\omega_n \frac{\xi' K + \eta' \Lambda}{r}} dA_l' \tag{7.37}$$

$$= \left(\frac{\rho}{2\pi R}\right)^2 \sum_{n=0}^{N_\omega-1} \hat{p}_n^* \hat{p}_n$$

where

$$\hat{p}_n = \sum_{l=1}^{N_e} \omega_n^2 \{H_a(\omega_n)\}_l^T \{\varphi(\omega_n)\} \tag{7.38}$$

and $\{\varphi(\omega_n)\}$ contains the integrated shape functions with the complex exponential. It is obvious that the double element sum has been rendered a single element sum for excitations of this type. Enormous computational savings result from this simplification. Additional savings can be achieved by forming $\{\varphi(\omega_n)\}$ from the closed form integrations in Appendix C.

7.3 Analytical Validation

In the previous sections, forms for the far-field mean square pressure radiated by a flexible panel-type structure supported in an infinite baffle and driven by acoustic pressure or concentrated force excitation were developed from Rayleigh's integral using continuous and discrete spectral analysis methods. The formulation will now be validated through comparison with fundamental cases and experiment in the following two sections.

7.3.1 Simply-Supported Aluminum Panel

Comparisons will be made with the classical formulation developed by Roussos [52] for the case of a simply-supported aluminum panel. Consider a simply-supported aluminum panel with

162

Table 7.1 Material properties for aluminum panel specimen.

Young's Modulus	68.95 GPa	10 Msi
Shear Modulus	26.55 GPa	3.85 Msi
Poisson's Ratio	0.3	
Mass Density	2.767e+3 kg/m^3	2.588e-4 lbf s^2/in^4
Coeff. of Thermal Exp.	22.3 $\mu\epsilon$/°C	12.4 $\mu\epsilon$/°F

dimensions of 0.3556x0.254x0.001 m (14×10×0.040 inches). The material properties for the specimen are shown in Table 7.1.

As a first example, let the excitation be characterized by normally-incident, planar acoustic waves. The acoustic excitation had a spectral level of 1.52 Pa^2/Hz (3.2e-8 (psi)^2/Hz) over a bandwidth of 10–1000 Hz with a spectral resolution of 0.5 Hz. The panel was modeled by a finite element mesh of 14x10 elements. Thirty modes were used in both the classical and finite element models with a uniform modal critical damping ratio of 0.02.

A comparison of the tangential versus normal radiated acoustic intensity predicted by the classical and finite element methods is shown in Figure 7.2. The plot is for a radial distance of 3.05 m (120 inches), polar angles of θ=[0,π/2] with a π/18 increment, and an azimuthal angle of $\wp$=0. The same plot, but only considering the single frequency component at 800 Hz, is shown in Figure 7.3. It can be seen that the broadband frequency content tends to make the acoustic radiation directivity more diffuse as expected. The classical and finite element analyses show excellent agreement in both cases.

The transmission loss versus frequency for this case is shown in Figure 7.4. The usual behavior of a dip at the fundamental frequency separating the stiffness-controlled region from the resonance-controlled region can be easily seen. The upper end in frequency is approaching the mass-controlled region of the transmission loss. The classical and finite element analyses show excellent agreement. The transmission loss curves are indistinguishable up to approximately 800 Hz.

Now consider planar acoustic excitation with the following angles of incidence (θ_i=60°, ϕ_i=45°). The excitation has a spectral level of 1.52 Pa^2/Hz (3.2e-8 (psi)^2/Hz) over a 10–1000 Hz bandwidth with a spectral resolution of 0.5 Hz. The plot in Figure 7.5 presents the tangential versus normal component of the radiated acoustic intensity at a radial distance of 3.05 m (120 inches), polar angles of θ=[0,π/2] with a π/18 increment, and an azimuthal angle of $\wp$=0. The same plot for the single frequency component at 800 Hz is shown in Figure 7.6. These results further demonstrate the good agreement between the classical and finite element analyses. The transmission loss versus frequency for this case is shown in Figure 7.7. The antisymmetric modal resonances pointed out in Figure 6.7 are seen as tiny dips in the transmission loss curve.

The acoustic radiation analysis using the FE method for structural response has been shown to produce very accurate results in comparison with classical analysis. The analysis will now be correlated with experimental measurement.
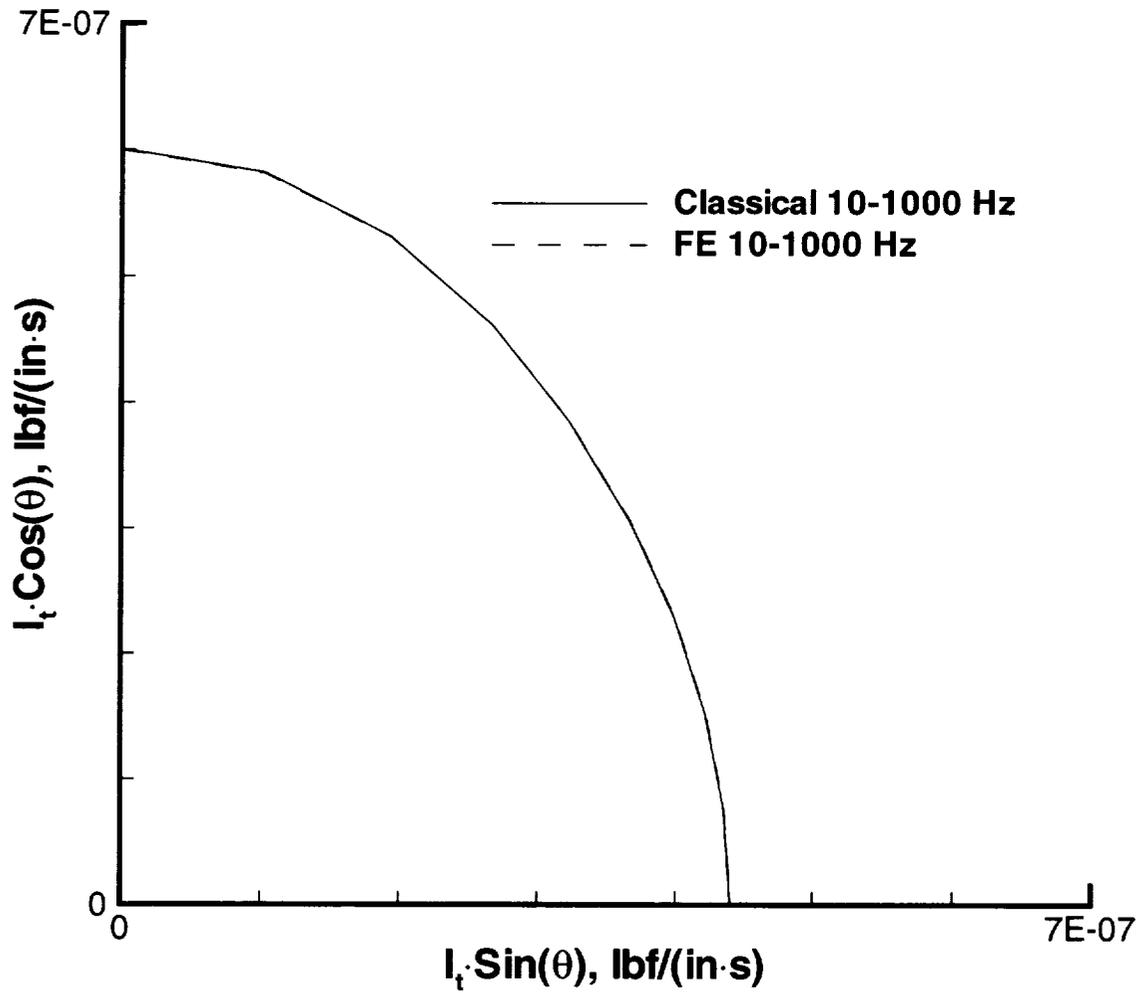
Figure 7.2 Normal versus tangential radiated acoustic intensity R=3.05 m (120 inches), $\theta=[0,2\pi]$, $\phi=0$ for normal acoustic incidence, 10–1000 Hz.
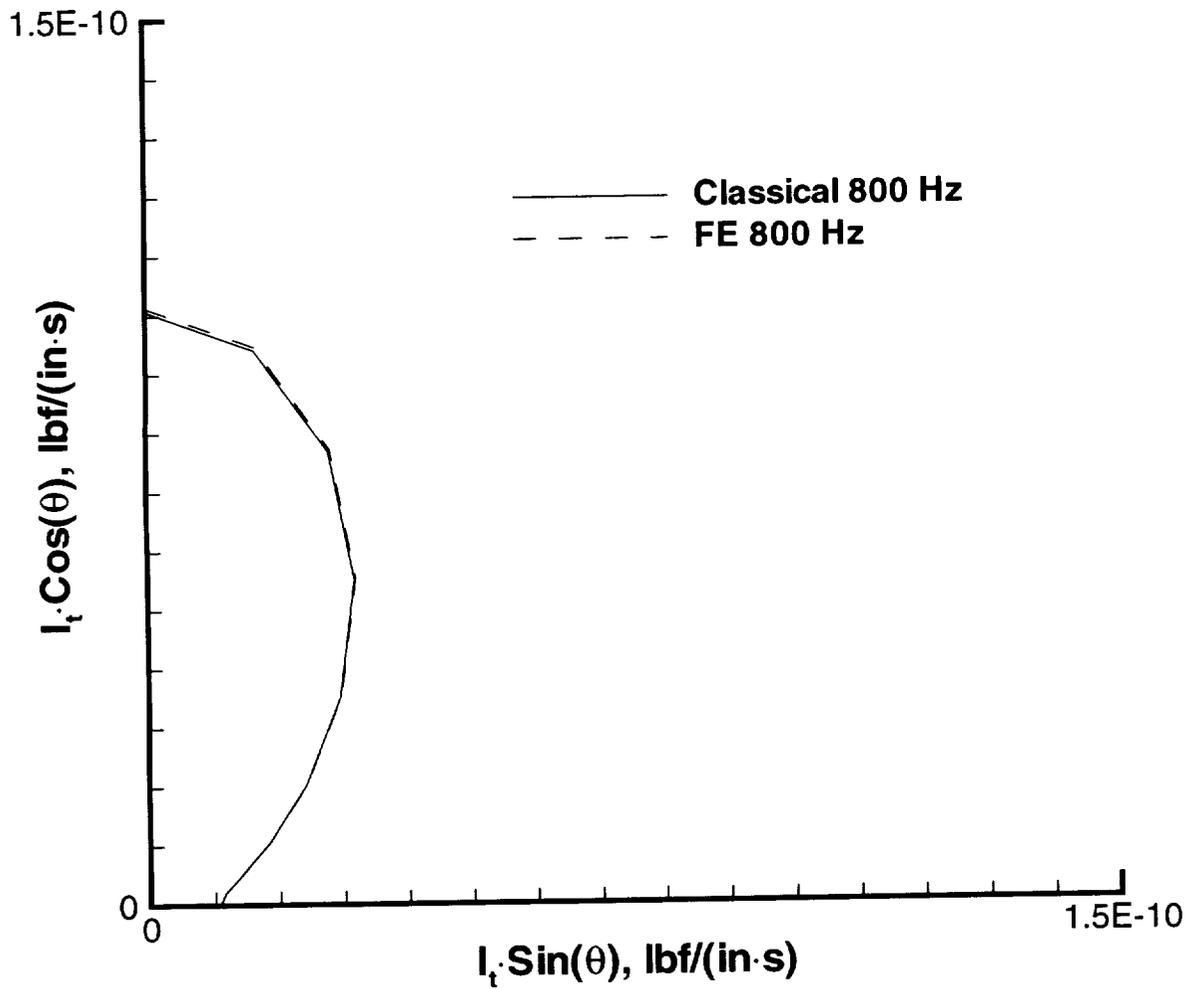
Figure 7.3 Normal versus tangential radiated acoustic intensity R=3.05 m
(120 inches), $\theta=[0,2\pi]$, $\phi=0$ for normal acoustic incidence, 800 Hz.
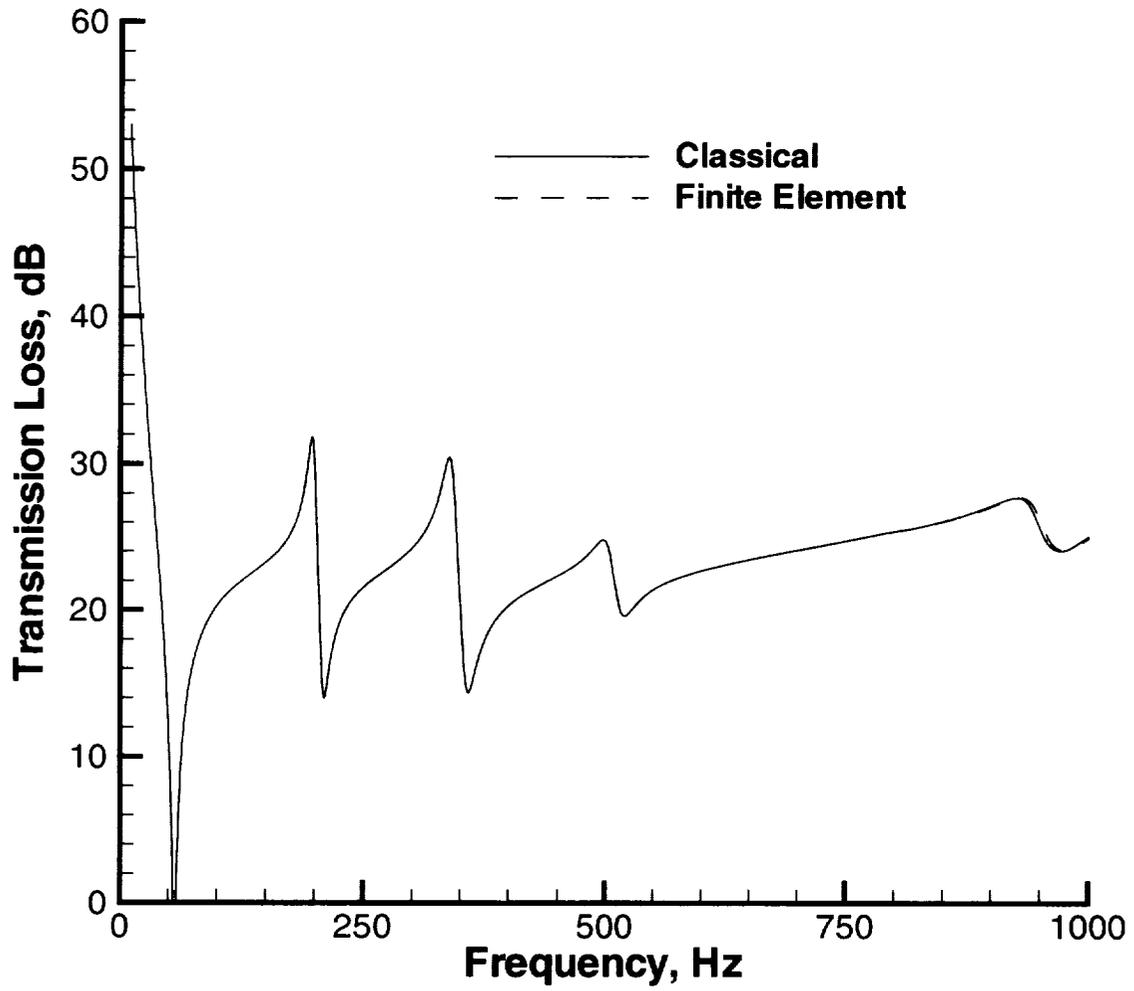
Figure 7.4 Transmission loss versus frequency for normal acoustic incidence, 10–1000 Hz.
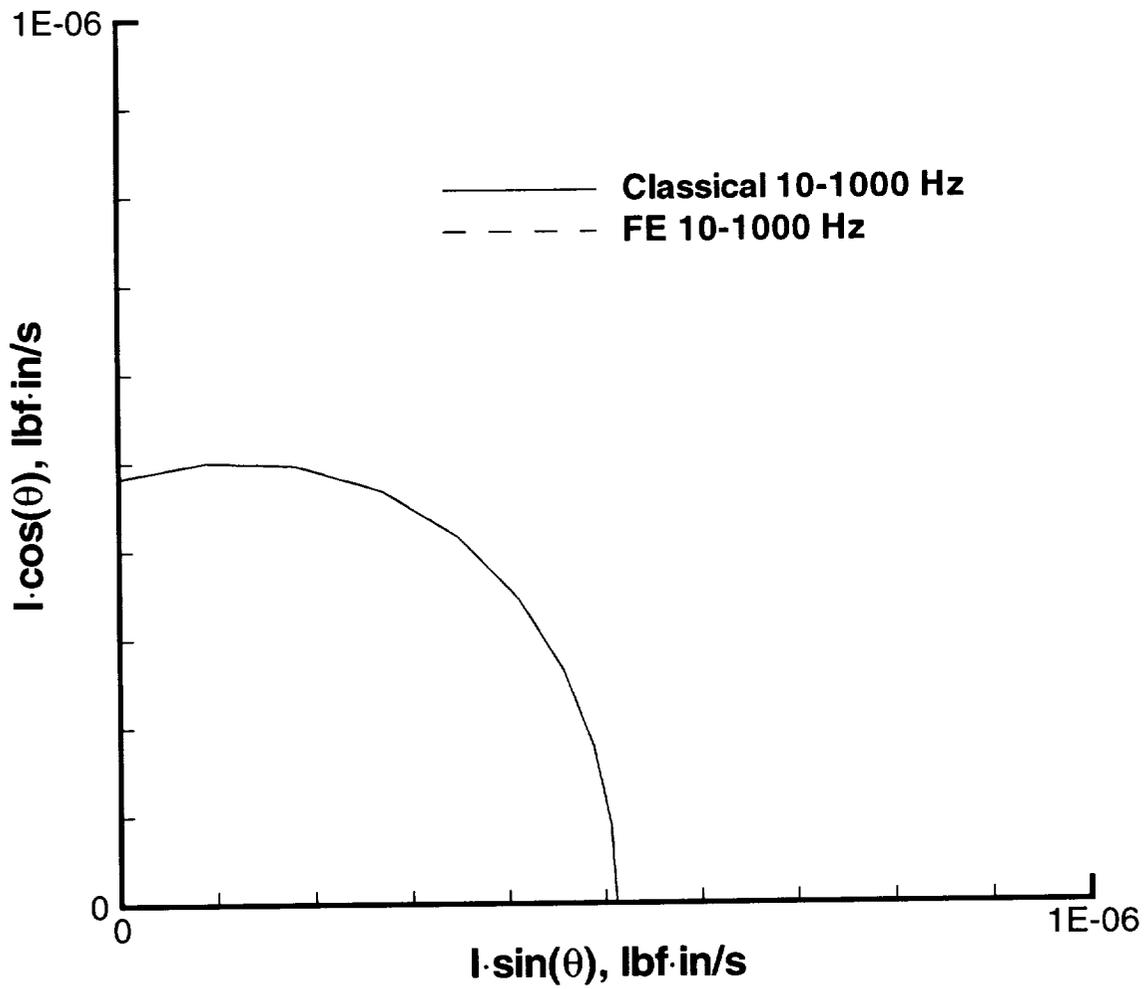
Figure 7.5 Normal versus tangential radiated acoustic intensity R=3.05 m (120 inches), $\theta=[0,2\pi]$, $\phi=0$ for θ_i=60, φ_i=45 acoustic incidence, 10–1000 Hz.
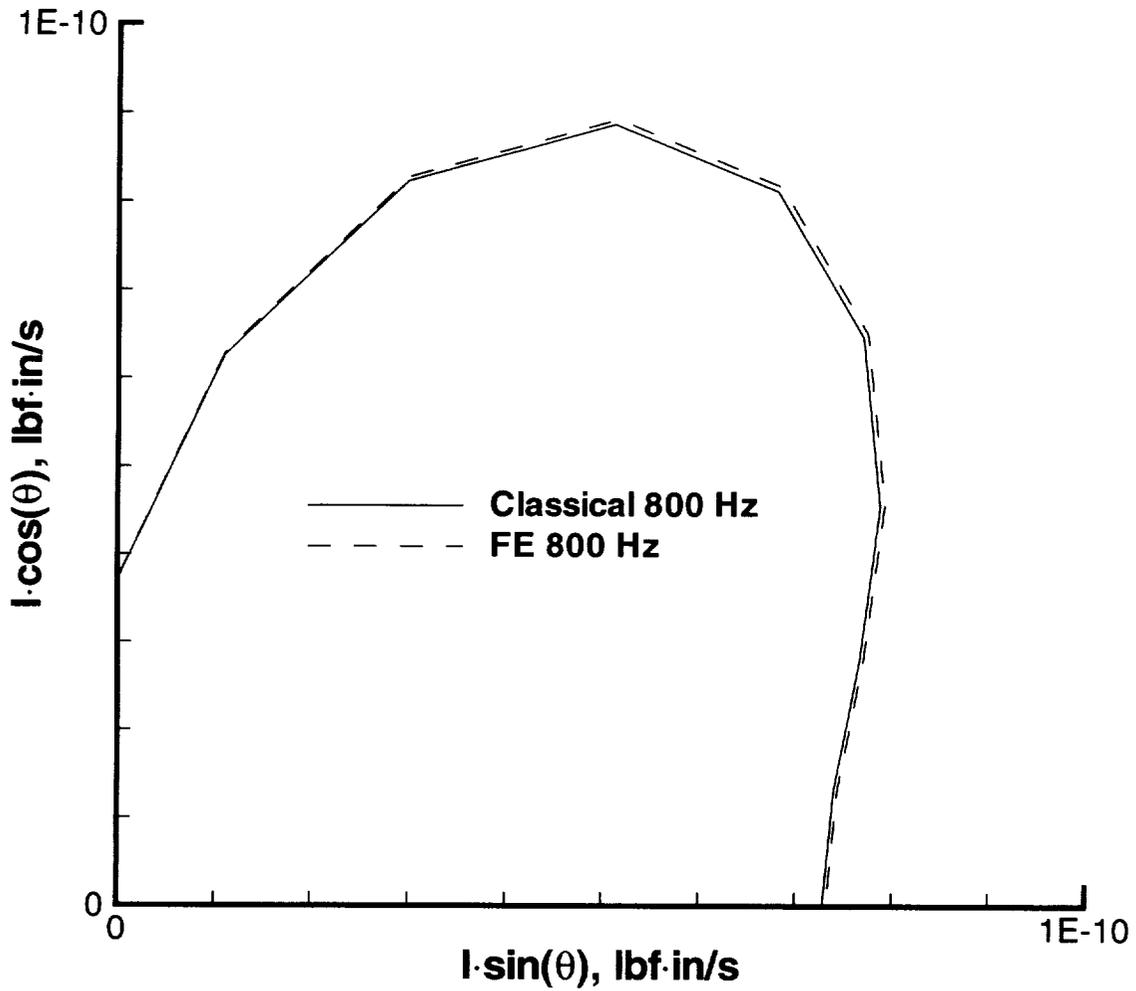
Figure 7.6 Normal versus tangential radiated acoustic intensity R=3.05 m (120 inches), θ=[0,2π], ω=0 for θ_i=60, ϕ_i=45 acoustic incidence, 800 Hz.
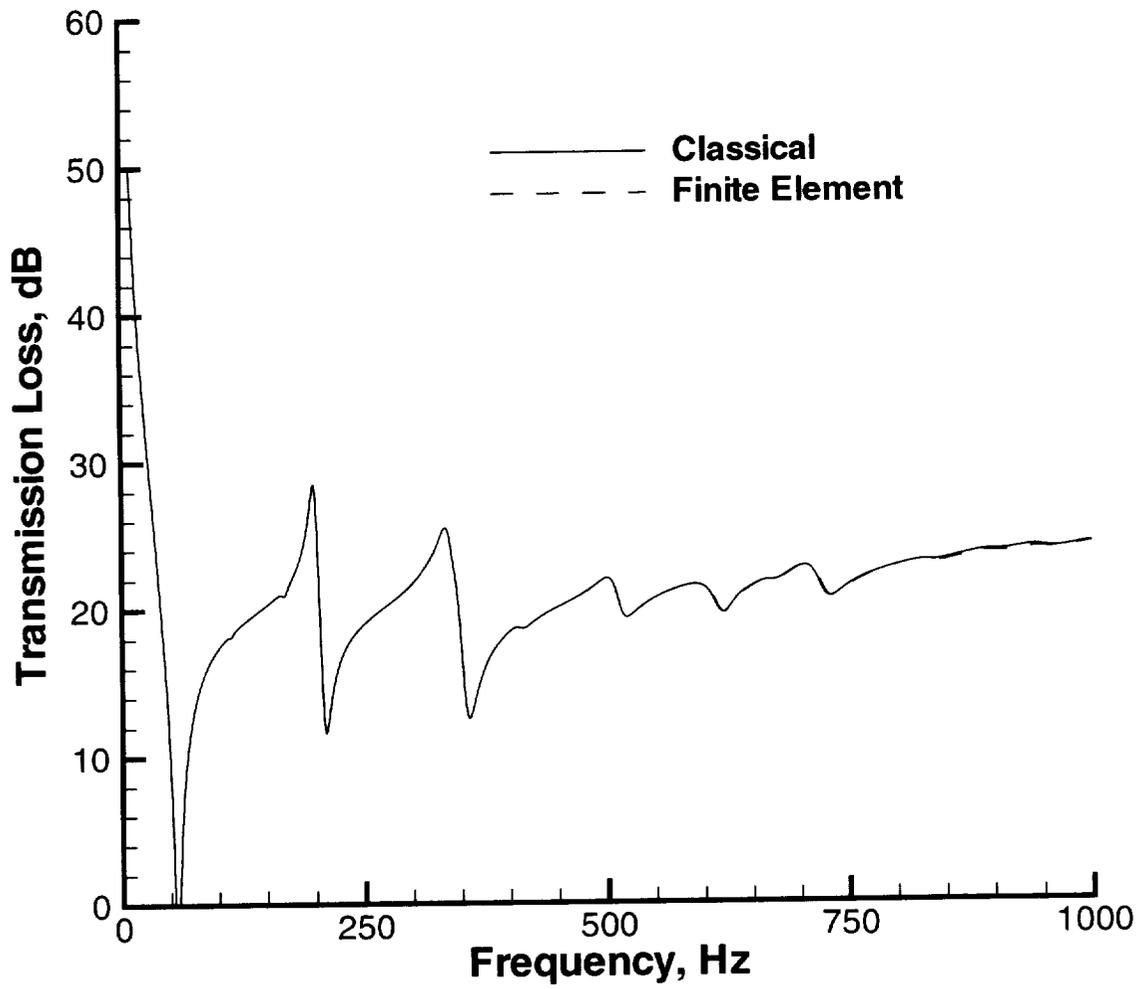
Figure 7.7 Transmission loss versus frequency for θ_i=60, ϕ_i=45 acoustic incidence, 10–1000 Hz.

Table 7.2: Receiving microphone array measurement locations, shown schematically in Figure 6.26.

Mic Position	Radial Distance (m)	Angle (deg)	Mic Position	Radial Distance (m)	Angle (deg)
R1	0.6096	0	R5	0.6096	-30
R2	1.2192	0	R6	1.2192	-30
R3	0.6096	30	R7	0.9144	-45
R4	1.2192	30			

7.4 Experimental Validation

The experimental case considered in this section consists of a clamped aluminum panel subjected to normally incident, random acoustic excitation. Comparisons will be made between predicted and measured radiated acoustic pressures in a transmission loss configuration.

7.4.1 Clamped Aluminum Panel

Experiments were conducted to measure the structural-acoustic response of an aluminum panel subject to broadband, normal acoustic excitation. The experiments were performed in the Transmission Loss Apparatus (TLA) at NASA Langley Research Center, shown schematically in Figure 6.26. The experimental apparatus is described in some detail in the validation section of Chapter 6 and in Turner and Rizzi [55]. Comparisons of the predicted and measured panel normal velocity are shown in the previous chapter. Acoustic radiation results will be presented here.

The transmitted acoustic pressure was measured using a single vertical microphone array consisting of three 1.27×10^{-2} m (half-inch) microphones; one at the height of the panel center, one 0.3048 m (12 inches) above the center mic, and one 0.3048 m (12 inches) below the center mic. Transmitted acoustic pressure autospectra were collected at 21 locations by positioning the three-microphone array in each of seven measurement locations, defined in Table 7.2 and shown schematically in Figure 6.26.

The power spectral density of the pressure incident upon the panel is shown in Figure 6.27. Comparisons of the predicted and measured transmitted pressure are shown in Figures 7.8 and 7.9 for two measurement locations; radially perpendicular to the panel center and at an oblique angle. The agreement is very good, particularly near the panel resonances. Theoretically, the pressure at the top and bottom microphones of the array should be the same, due to symmetry. However, the measured spectra showed an increase in the levels between the peaks with decreasing distance to the hard floor in the receiving room. Thus, some of the discrepancies are attributable to receiving room reflections. Also note that the non-symmetric modes, shown in the previous panel response data in Chapter 6, do not radiate, as expected.
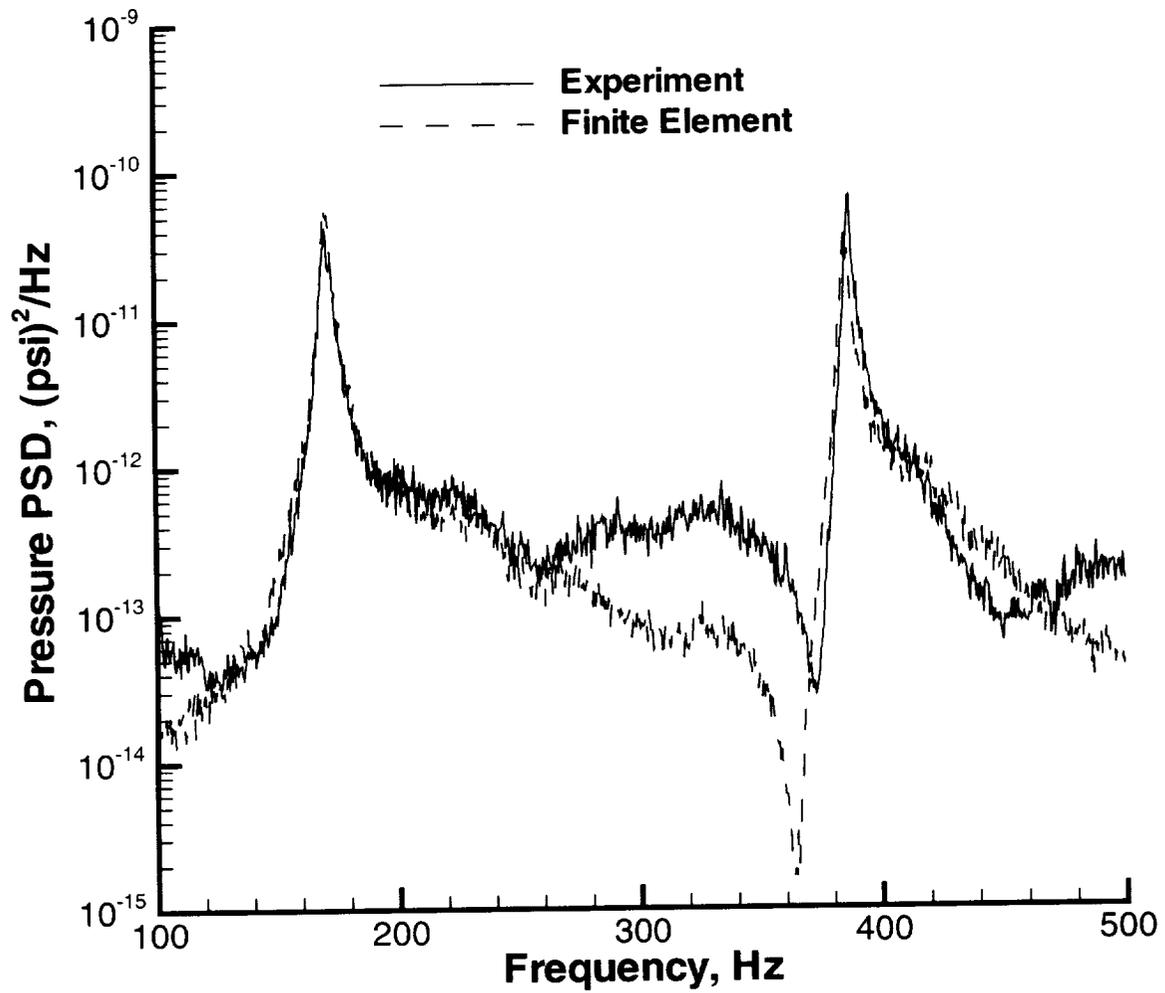
Figure 7.8 Comparison of the predicted and measured transmitted pressure PSD at the center microphone of array location R1 (see Table 7.2 and Figure 6.26).
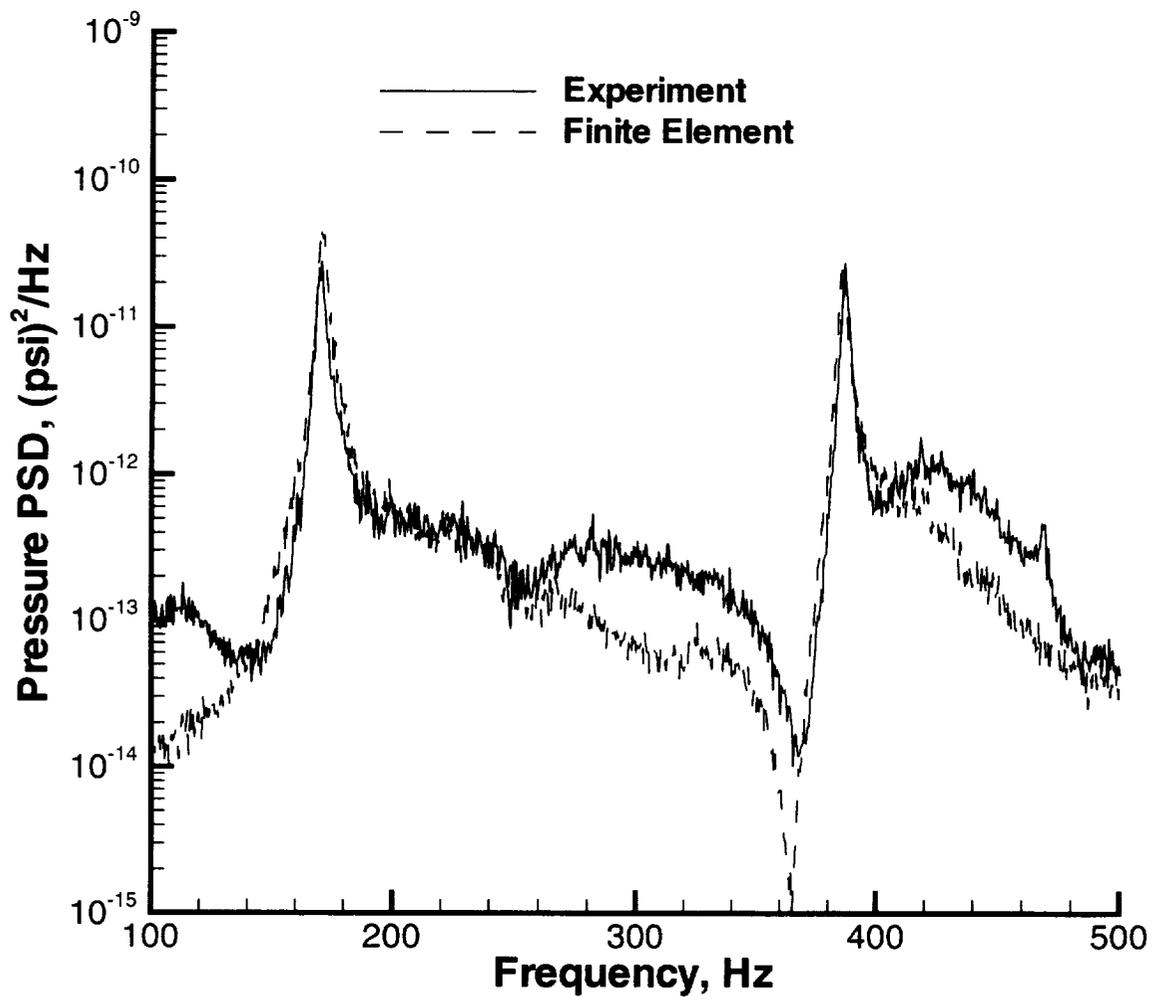
Figure 7.9 Comparison of the predicted and measured transmitted pressure PSD at bottom microphone of array location R3 (see Table 7.2 and Figure 6.26).

Chapter 8
Applications and Demonstrations

The tools developed and validated in the previous chapters will now be employed to demonstrate the static and dynamic thermomechanical behavior of SMAHC structures and compare performance gains achieved by embedded SMA actuators to conventional response abatement treatments. Results will be presented for SMAHC beam and panel structures. Early work performed in this study [16] showed that changes in SMA volume fraction have more effect on structural control authority than prestrain level. More recent work has corroborated this statement and shown that the SMA volume fraction is more easily varied/controlled in fabrication than the prestrain level. Finally, it is known that the thermomechanical fatigue performance of Nitinol actuators degrades substantially at prestrains greater than 5%. The results shown in this chapter will focus on conservative prestrain levels of 4% for the beam specimens and 5% for the panel specimens. For simplicity, a glass-epoxy matrix material system with constant material properties will be used in all cases. Mechanical property data for Nitinol from Cross et al. [28] will also be used. The material properties shown in Table 8.1 were used to generate the results shown in this chapter. Note that these predictions, using material properties for Nitinol from Cross et al. [28], are conservative relative to the properties measured from the Nitinol material used previously in this study, i.e., stable recovery stress for Nitinol used in this study at 4% prestrain is approximately 413 MPa (59.9 ksi) as compared to 310 MPa (45 ksi) for the corresponding case in Cross et al. [28].

Recall Figure 2.3 characterizing the recovery stress for Nitinol from Cross et al. [28]. The reverse transformation (austenitic) characteristic temperatures, under free recovery conditions, for the material represented in this plot are $A_s \approx 35°C$ (95°F) and $A_f \approx 50°C$ (120°F). Note from Figure 2.3 that A_f is increased by mechanical constraint and increasing prestrain, while A_s is not significantly affected by either. Furthermore, the "knee" in the recovery stress curve becomes less distinct with increasing prestrain. These are well-known phenomena and are attributable to stress increasingly inhibiting the formation of austenite and completion of the reverse transformation. These insights will be useful in later discussions.

8.1 General Observations

The physical behavior of SMA actuators embedded in a composite matrix is somewhat non-intuitive and is easily misinterpreted, so some general comments are deemed appropriate here. References will be made to Figures 8.1a–8.1d, which show the non-deformed/reference (gray-shade) and deformed (mesh) in-plane geometries of 0.457x0.025x0.001 m (18x1x0.040

Table 8.1 Material properties for glass-epoxy and Nitinol.

Glass/Epoxy		Nitinol	
E_1	53.78 GPa (7.8 Msi)	A_s	32.22°C (90°F)
E_2	17.93 GPa (2.6 Msi)	A_f	62.78°C (145°F)
G_{12}	8.62 GPa (1.25 Msi)	σ_r	from Figure 2.3
ν_{12}	0.25	E	from Figure 2.4
ρ	2031.8 kg/m^3	ν	0.3
	(0.19×10^{-3} lb s^2/in^4)		
α_1	5.4×10^{-6} /°C (3.5×10^{-6} /°F)	ρ	6450 kg/m^3 (0.6067×10^{-3} lbf s^2/in.^{4})
α_2	30.6×10^{-6} /°C (11.4×10^{-6} /°F)	α_{1a}	6.61×10^{-6} /°C (3.67×10^{-6} /°F), T<A_s
			from equation 2.4, T≥A_s
		α_{2a}	6.61×10^{-6} /°C (3.67×10^{-6} /°F), T<A_s
			11.0×10^{-6} /°C (6.11×10^{-6} /°F), T>A_f
			interpolation, A_s≤T≤A_f

in.) conventional and SMAHC beams with a lamination of (45/0/-45/90)$_s$ and cantilevered or clamped-clamped boundary conditions. Consider the case of a cantilevered, conventional beam (no SMA). As the beam is heated, with uniform temperature, it will expand everywhere except at the boundary and will be stress-free at locations away from the boundary, shown in Figure 8.1a. The thermal force that is generated is thereby relieved by in-plane deformation. If the other end is constrained, the thermal force in the axial direction cannot be relieved and a compressive in-plane load is generated. This load will increase with temperature until a critical value is reached, at which point the beam will buckle. Note that the thermal load in the transverse direction is balanced by reaction forces at the boundary and relieved by in-plane deformation in the transverse direction at locations away from the boundary (see Figure 8.1b). These physical phenomena can also be interpreted from the expression for the resultant internal force given by equation (2.38). As the cantilevered beam is heated, the thermal force $N_{\Delta T r}$ is balanced by the force due to in-plane deformation $N_{m r}$ such that the resultant force N_r is zero. Conversely, a nonzero resultant force exists for the clamped-clamped case because of an imbalance between $N_{\Delta T r}$ and $N_{m r}$. The imbalance is maintained after buckling by contributions from $N_{\theta r}$.

An analogous, but inverse, situation exists for a SMAHC consisting of glass-epoxy with uniformly distributed SMA in all layers (volume fraction of 30% and initial strain of 4%). The thermal force in this case has a sense opposite of that expected because the effective CTE is contractile rather than expansive. A cantilever beam of this type would contract everywhere except at the boundary and will be stress free at locations away from the boundary, exemplified in Figure 8.1c. The axial thermal force is again relieved by in-plane deformation (i.e., $N_{\Delta T r} = N_{m r}$). Imposing a constraint at the other end prevents the axial in-plane deformation and a substantial tensile in-plane force results. Note that the thermal forces (tensile) in the transverse direction are again balanced by reactions at the boundary and transverse in-plane
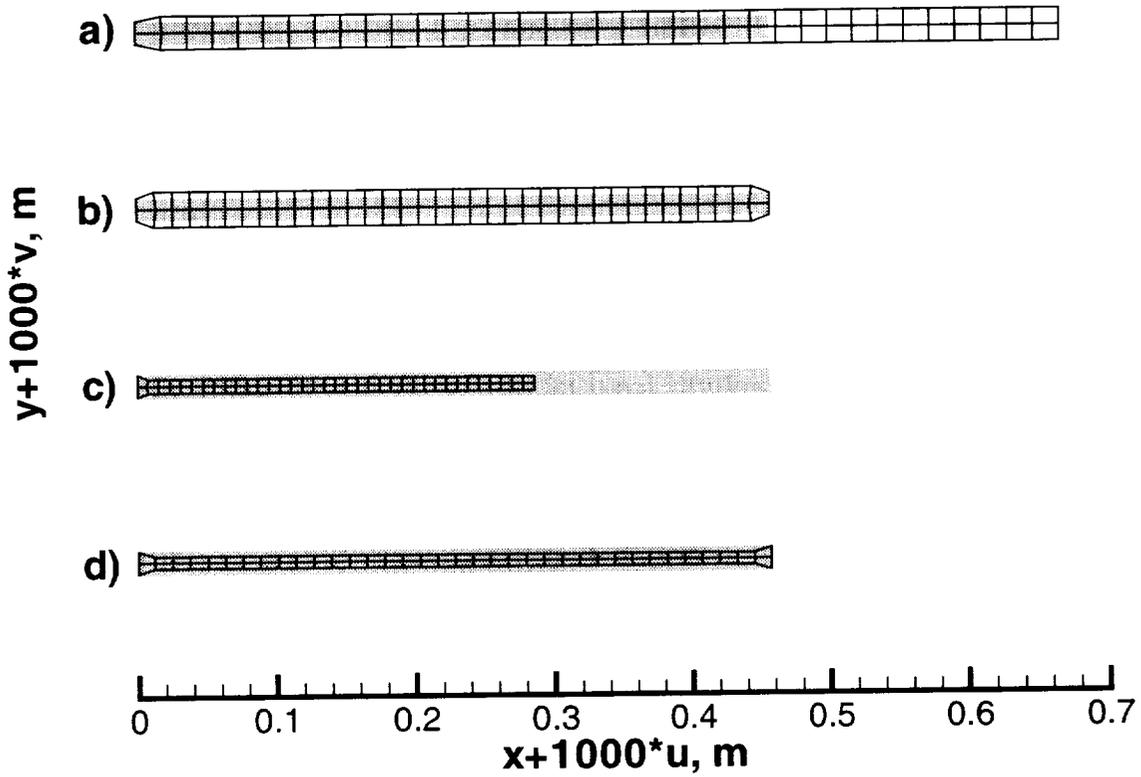
Figure 8.1 Non-deformed/reference (gray-shade) and deformed (mesh) in-plane geometries for 0.457x0.025x0.001 m (18x1x0.040 in.) cantilevered and clamped-clamped glass-epoxy and SMAHC beams. Displacements calculated at 65.56 °C (150 °F) and magnified 1000 times.

deformation at locations away from the boundary, shown in Figure 8.1d. Development of the tensile thermal force in the presence of mechanical constraints is the desirable attribute that is being explored for adaptive stiffening of composite structures by embedded SMA actuators.

It is noted that in the previous discussions the arguments regarding SMAHC beams with free boundaries are, strictly speaking, only qualitatively correct because the SMA material properties used, Figure 2.3, result from constrained recovery measurements. However, the in-plane displacements associated with the tensile recovery forces are small relative to the prestrain imparted to the SMA actuators, so the predictions should be reasonably accurate for such cases. Also note that a stiffening effect does result in this particular case of a SMA hybrid cantilever because the modulus of the SMA is superior to that of the matrix material at temperatures where the SMA is in the austenitic state. Additional insights will now be gleaned from a series of examples.

8.2 Thermal Buckling and Post-buckling

Consider a glass-epoxy beam of 0.457x0.025x0.001 m (18x1x0.040 in.) dimensions with a lamination of $(45/0/-45/90)_s$ and clamped boundaries at both ends. The critical temperature change for this structure with a uniform temperature distribution is $1.68°C$ $(3.03°F)$. The normalized maximum post-buckling deflection versus temperature change from ambient for the conventional beam ($v_a=0\%$) is shown in Figure 8.2 in comparison with SMAHC beams. The SMAHC beam responses correspond to the case of a 30% uniformly distributed volume fraction of SMA with an initial strain of 4%. The symbols v_a and A_s indicate SMA volume fraction, prestrain level, and austenite start temperature, respectively.

It can be seen that two buckling temperatures exist for the SMAHC beam with $A_s=32.22°C$ $(90°F)$; the first occurs at a temperature very near that for the conventional beam and the second at a much higher temperature. This phenomenon is attributable to the fact that A_s, for this particular alloy, is greater than the ambient temperature of $21.11°C$ $(70°F)$ and can be explained as follows. At temperatures less than A_s, the SMA is not activated and behaves like a conventional linear thermoelastic material. So the SMAHC beam buckles at a critical temperature below A_s. The SMA becomes activated at A_s and the recovery stress rapidly increases with temperature, which overcomes the compressive thermal stress and returns the beam to a flat configuration. At higher temperatures, the rate of increase of the recovery stress with temperature diminishes and may be surpassed by the rate of increase in matrix compressive thermal stress. Further increases in temperature will cause net-compressive stress development, eventually leading to a second incidence of thermal buckling.

In contrast, the $A_s=15.56°C$ $(60°F)$ case in Figure 8.2 exhibits only a single thermal buckling event at high temperature. This case was produced using the same SMA properties as before by shifting the temperature scale associated with those properties $-16.67°C$ $(-30°F)$. This can easily be achieved in practice by increasing the Nickel content of the alloy as little as 0.125 weight % (see Buehler and Wang [58]). Note that the buckling temperature is slightly higher in this case relative to the $A_s=32.22°C$ $(90°F)$ case. This result is due to the fact that the shift in the SMA property temperature scale for the $A_s=15.56°C$ $(60°F)$ case produces a slightly higher recovery force at the imposed temperature, which can be seen by referring to Figure 2.3.
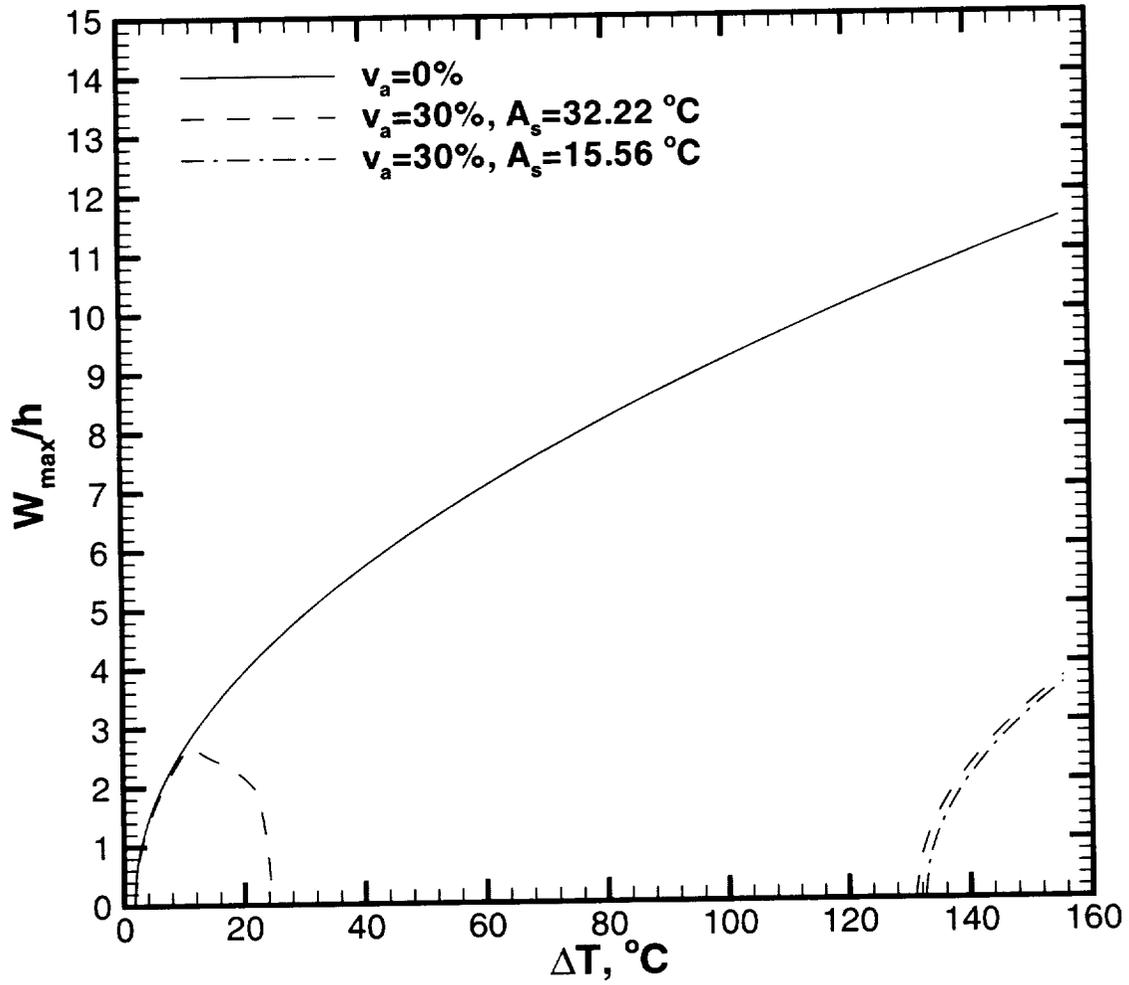
Figure 8.2 Normalized mid-span post-buckling deflection versus temperature change for conventional and SMAHC 0.457x0.025x0.001 m (18x1x0.040 in.) clamped beams.

Recall that the former effect, near-ambient buckling of a structure then complete arrestment of the thermal post-buckling deflection by SMA recovery stress, was demonstrated experimentally and correlated with prediction in Chapter 5 for the case of a clamped-clamped SMAHC beam. Proof of this behavior has a numerical basis also, which will be explained subsequently. There have been differing theories about the elimination of the thermal post-buckling deflection, which results in two buckling temperatures for A_s greater than ambient. The formulation by Turner, Zhong, and Mei [16], based upon the RSM of the SMA constitutive behavior, corroborates the results presented here. A different result was reported in Mei, Zhong, and Turner [59] where an incremental approach with many temperature increments was deemed necessary to account for the SMA material nonlinearity in arriving at the final temperature. That formulation is also based upon the RSM, but does not exhibit the complete elimination of thermal post-buckling deflection for cases with A_s greater than ambient. The difference between the two methods was attributed to a mismatch of recovery stress and out-of-plane deflection terms in a thermal post-buckling solution with multiple temperature increments based upon the formulation given in Turner, Zhong, and Mei [16]. The ECTEM of the SMA constitutive behavior, presented in this work, shows that the use of small temperature increments is not necessary because the model inherently takes the material nonlinearity into account. Furthermore, any mismatch in terms associated with multiple temperature increments in the thermal post-buckling solution can be avoided by using a single temperature increment. The results of this approach are shown in Figure 8.3 in comparison to the corresponding multi-step solution from Figure 8.2. The number of temperature steps used in each post-buckling solution is indicated in the figure by $N_{\Delta T}$. Each discrete symbol represents a separate solution achieved by initiating a post-buckling solution at the first buckling temperature with a single temperature increment. These results show that the present solution is insensitive to the number of temperature increments and complete elimination of thermal post-buckling deflection for cases with A_s greater than ambient and a flat, stress free initial configuration is a general theoretically valid result. The ability to use a single temperature increment can result in a huge computational savings also, particularly for high temperatures relative to the buckling temperature.

Recall that the SMAHC beams considered thus far employed a uniformly distributed SMA volume fraction of 30%. It is intuitive that performance gains could be achieved by strategically placing the SMA actuators. One example of this technique is shown in Figure 8.3, where the thermal post-buckling deflection is shown for a SMAHC beam with the same $(45/0/-45/90)_s$ lamination but SMA actuators in the 0° layers only. A 50% volume fraction in the two 0° layers results in an overall volume fraction of 12.5%. This overall volume fraction is less than half that of the beam with uniformly distributed actuators, but the performance is slightly improved. Note that this approach is more practical from a fabrication point of view as well, particularly for automated fabrication where one could imagine replacing strategic spools of prepreg with SMA ribbon in a continuous consolidation fabrication operation.

The effect of changing the SMA volume fraction within the 0° layers is shown in the thermal post-buckling results in Figure 8.4. It can be seen that a volume fraction of 2.5% is insufficient to eliminate thermal post-buckling, but its effect in reducing the deflection is clearly observed. Thermal post-buckling can be eliminated for a range of temperatures with as little as 7.5% SMA and the case of 12.5% SMA exhibits deflection elimination for a broad range of temperatures.
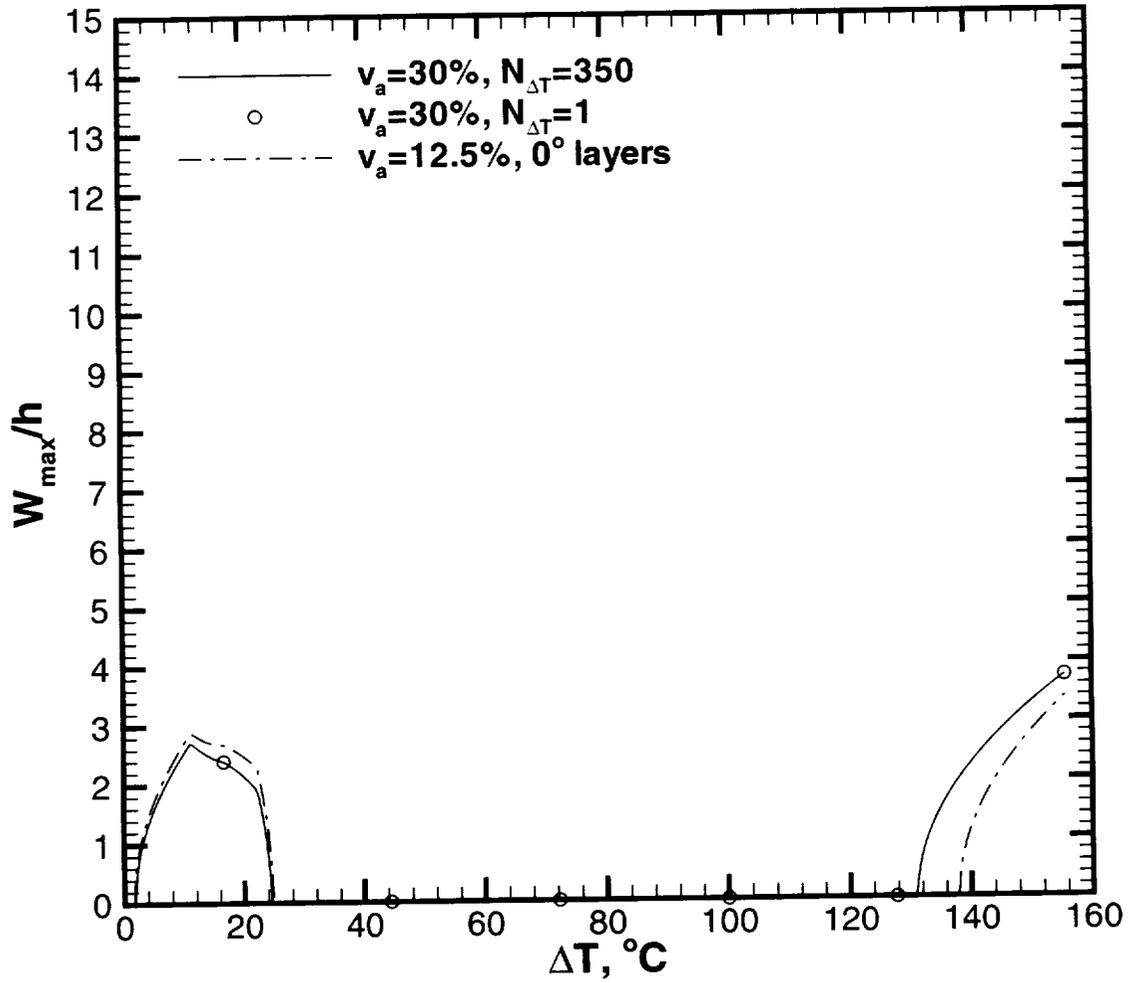
Figure 8.3 Normalized mid-span post-buckling deflection versus temperature change for SMAHC 0.457x0.025x0.001 m (18x1x0.040 in.) clamped beams with SMA in all/0° layers.
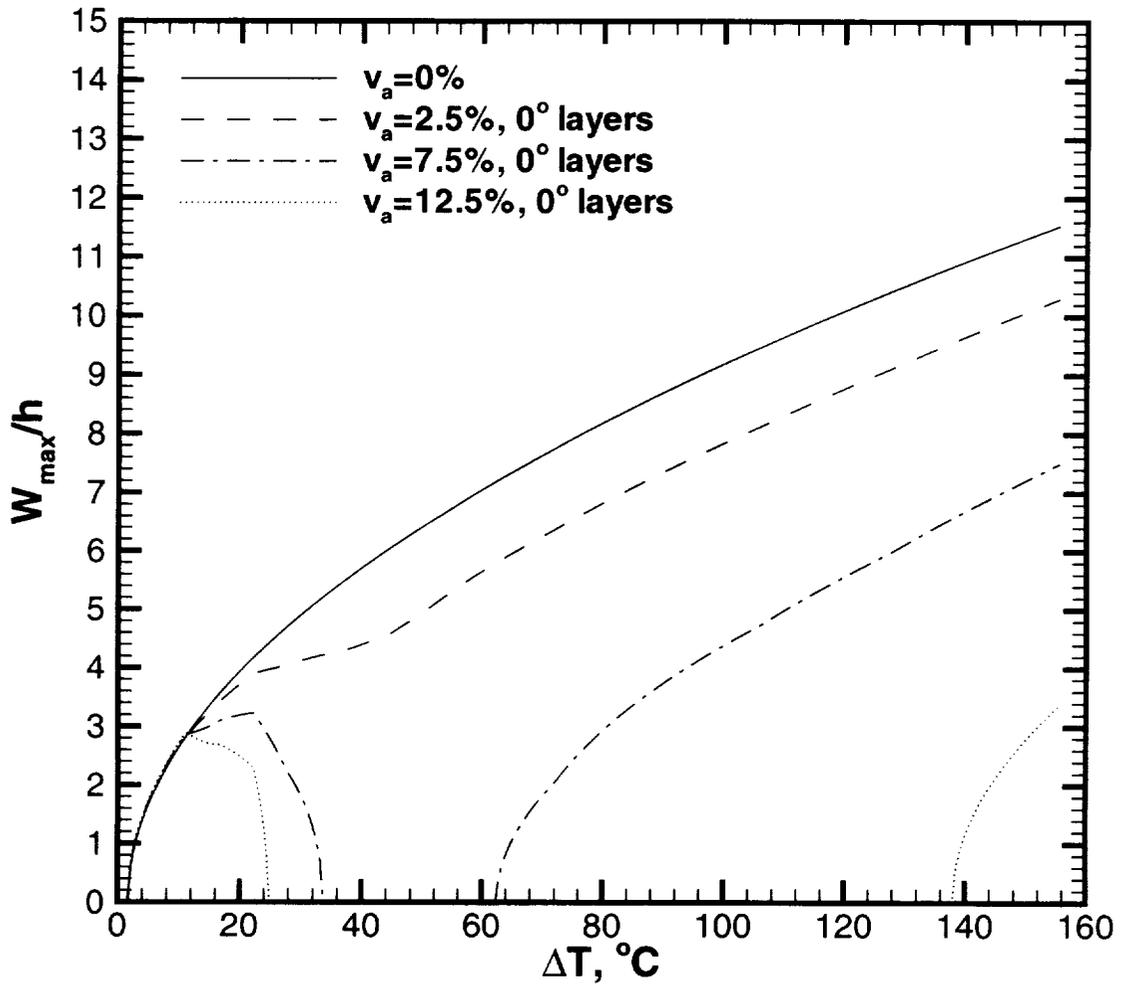
Figure 8.4 Normalized mid-span post-buckling deflection versus temperature change for composite 0.457x0.025x0.001 m (18x1x0.040 in.) clamped beams with various SMA volume fractions.

Similar behavior is exhibited by panel-type specimens as demonstrated in Figure 8.5. This figure shows the normalized center deflection as a function of temperature change for a glass-epoxy panel with dimensions of 0.36x0.25x0.001 m (14x10x0.045 in.), (45/0/-45/90/0/90/-45/0/45) lamination, a varying SMA volume fraction, and clamped boundary conditions. As in the latter beam specimen case, the SMA in the panel specimens is assumed to reside in the 90° and outer 0° layers only. Although it is not shown, it is noted that slight performance gain is achieved under these conditions relative to a corresponding laminate with SMA in all layers such that the overall SMA volume fraction is the same (see Turner [60]). This material system, i.e., with SMA in only a few layers, is consistent with the thought of automated fabrication made in the penultimate paragraph. Also note that the middle 0°-layer is necessary to separate the two 90° layers containing a substantial SMA volume fraction, thereby avoiding consolidation problems during cure. The results in Figure 8.5 show that a volume fraction of 4% is insufficient to eliminate thermal post-buckling in this case, but its effect in reducing the deflection is clearly observed. As little as 13% SMA will eliminate thermal post-buckling over a small range of temperatures; higher concentrations of SMA (e.g., 22%) can greatly extend the temperature range. The importance of these effects is more clear when considering the dynamic response of these structures.

8.3 Dynamic Response

Dynamic response and subsequent sonic fatigue and acoustic transmission analyses will focus on panel specimens with dimensions of 0.36x0.25x0.001 m (14x10x0.045 in.) and clamped boundary conditions. The dynamic response is assumed to be forced by a normally-incident, random acoustic pressure with an overall sound pressure level (OASPL) of 120 dB (ref 20μPa) and a bandwidth of 10–400 Hz. A uniform modal critical damping ratio of 1% was used in the dynamic response calculations. The maximum displacement response power spectral density (PSD) of the SMAHC panel is shown in comparison to that of the baseline panel in Figure 8.6. It is clear that the embedded SMA has little effect at ambient temperature. At 82°C (180°F,ΔT=61°C), however, substantial benefit from the SMA recovery stress is evident in shifting the fundamental frequency, shifting other modes out of bandwidth, and reducing peak responses. Thus, performance can be enhanced by shifting resonance out of the excitation bandwidth and by response reduction within the excitation bandwidth.

The thermal post-buckling observations have strong implications for the panels' dynamic response. An example is shown in Figure 8.7, where the maximum displacement PSD of the SMAHC panel (v_a=22%) is shown at ambient and two elevated temperatures. At 82°C (180°F, ΔT=61°C), substantial benefit of the embedded SMA is evident, while further heating to 121°C (250°F, ΔT=100°C) greatly diminishes the performance (RMS W_{max}=0.0927e-3 m) because continued thermal expansion has partially overcome the beneficial effects of the recovery stress. This particular material system, glass-epoxy matrix with 22% Nitinol volume fraction at 5% prestrain, achieves its "optimal" dynamic response at approximately 82°C (180°F), which corresponds to the "knee" in the recovery stress curve (see Figure 2.3). This result also holds for analogous SMAHC panels (v_a=22%) with embedded Nitinol having 3% and 4% prestrain, which exhibit "optimal" dynamic performance at their respective "knee" temperatures of 54°C
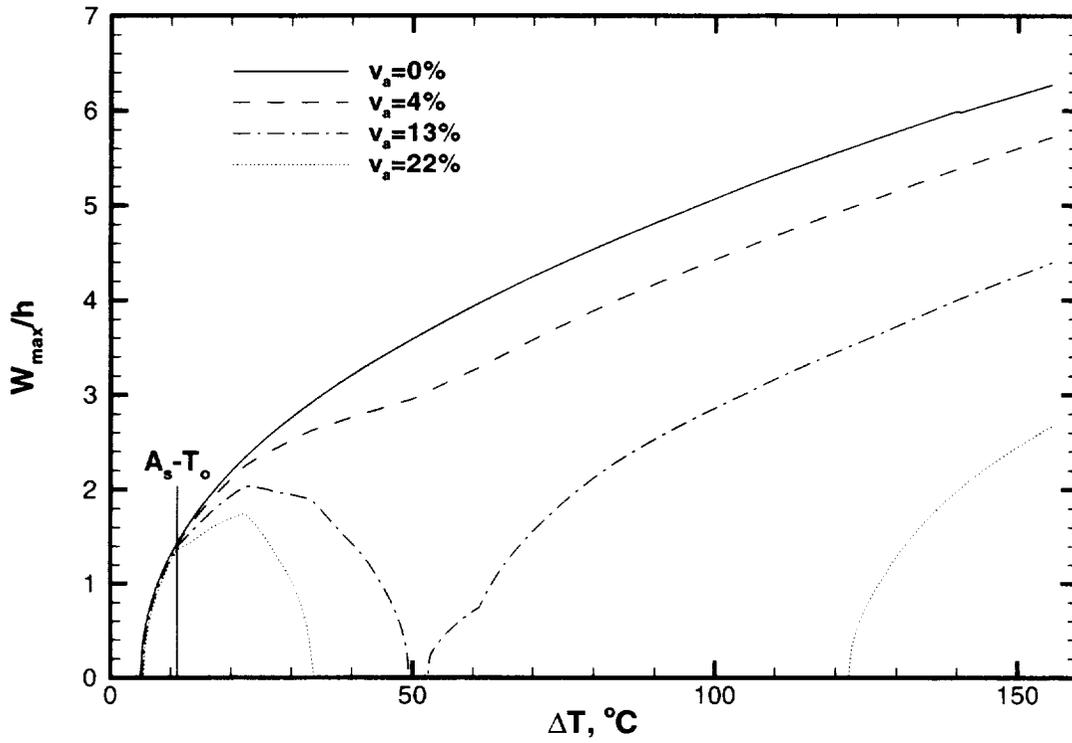
Figure 8.5 Post-buckling deflection of clamped 0.36x0.25x0.001
m (14x10x0.045 in.) SMAHC laminates versus ΔT and v_a.
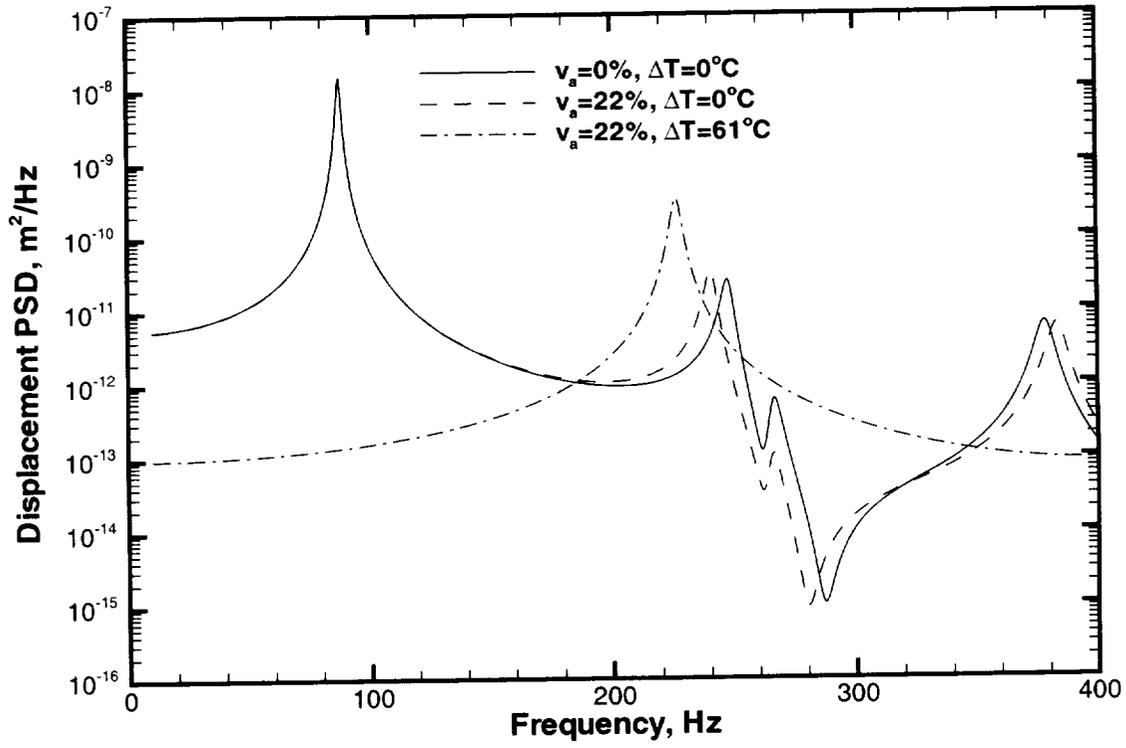
Figure 8.6 W_{max} PSD for 0.36x0.25x0.001 m (14x10x0.045 in.)
baseline and SMAHC laminates with clamped boundary conditions.
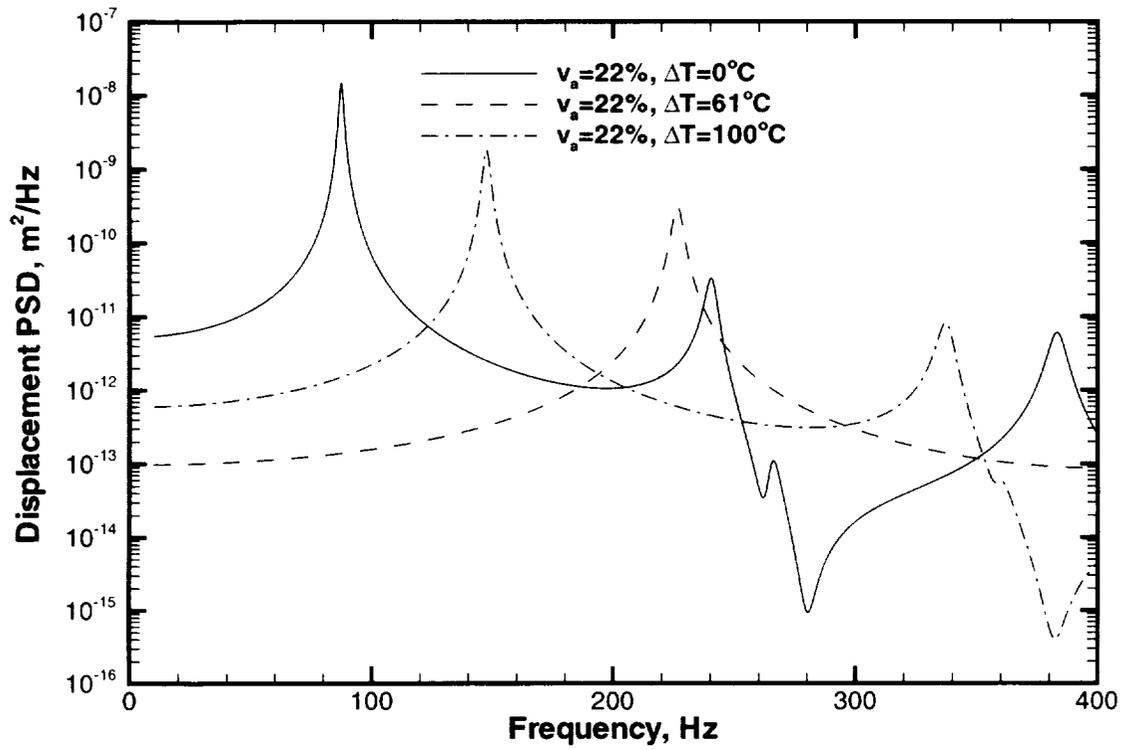
Figure 8.7 W_{max} PSD for a clamped 0.36x0.25x0.001 m
(14x10x0.045 in.) SMAHC laminate at three temperatures.

(130°F) and 66°C (150°F). The optimal temperature for dynamic performance will be designated by A_o and is governed by the same thermoelastic balance as that described in the thermal post-buckling discussion. In general, with a different material system or at higher prestrain levels (in the absence of a distinct "knee"), A_o must be determined numerically or by comparing the slope of the recovery stress curve with that of the matrix thermal stress versus temperature.

Selection of an alloy composition and processing combination that will place A_o near the application temperature is obviously recommended for dynamic control applications. An alternate approach to achieve similar performance would entail increasing the SMA volume fraction and/or prestrain, which will result in a less efficient and/or durable design. Requirements previously cited for desirable static and dynamic performance imply potential for a delicate balance between avoiding thermal buckling by imposing A_s to be less than ambient temperature and "optimizing" dynamic performance by specifying A_o to be near the application temperature. Thermal buckling can also be avoided by boundary expansion, a common approach for aerospace structures, so A_s can be neglected in such cases and A_o should be used to guide efficient design.

8.4 Sonic Fatigue and Acoustic Transmission

The performance of the SMAHC laminate will now be compared with conventional approaches including increased stiffness through additional composite layers and a constrained layer damping (CLD) treatment. The conventional approaches were analyzed at ambient temperature to simulate the conditions of boundary expansion, i.e., no thermal buckling. No attempt was made to account for changes in matrix properties with temperature. A variety of dynamic response performance characteristics are compiled in Table 8.2 for convenience of comparison. The SMAHC panel achieves a 77% RMS displacement response reduction, relative to the baseline 9–layer glass-epoxy panel, with a 48% mass increase. A conventional composite laminate of 13 layers (45/0/-45/90/45/0/90/0/45/90/-45/0/45) exhibits a similar mass increase (44%), but only achieves a 61% RMS displacement reduction. A RMS displacement response of 0.0474e-3 m (nearly equivalent to that of the SMAHC panel) can be achieved with a 16–layer $(45/0/-45/90)_{2s}$ conventional laminate, but at the expense of a 78% mass increase. A typical CLD treatment was modeled as a 19.16 N/m^2 (0.2 lbf/ft^2) weight addition and a uniform modal critical damping ratio of 6%, which are considered to be representative values. This treatment also happens to result in a mass increase (42%) similar to that of the SMAHC, but the RMS displacement response reduction of 63% is again inferior to the SMAHC. Additional insights are more clear from comparisons of the displacement response spectra, as discussed subsequently.

A comparison of the respective maximum displacement response PSDs is shown in Figure 8.8. As anticipated, the means by which the three systems achieve dynamic response reduction is quite different. The SMAHC achieves a much more weight-efficient stiffening effect relative to that of adding layers, while the CLD treatment achieves reduction primarily by damping enhancement. The weight-efficient stiffening effect of the embedded SMA is advantageous for combination with other passive treatments, which are typically more effective at higher frequencies. SMAHCs are also attractive for combination with control approaches involving piezoelectric actuators, which typically exhibit actuation authority roll-off below 200 Hz. Such combined active-passive approaches could achieve enormous dynamic response reductions by

Table 8.2: Results from clamped 0.36x0.25x0.001 m (14x10x0.045 in.) baseline, SMAHC, and panels with conventional response abatement treatments.

Case	Added Mass	f_1, Hz	RMS W_{max}, m	TL, dB	Max RMS $\mu\epsilon$ @ 120dB	Life @ 150 dB
Baseline	0%	87.48	0.2062e-3	17.9	42.0	63.7e+3
SMAHC @ 82°C	48%	226.4	0.0476e-3	14.3	12.0	205e+6
13-Layer	44%	128.3	0.0805e-3	19.1	23.3	2.84e+6
16-Layer	78%	158.6	0.0474e-3	20.2	16.8	23.4e+6
Baseline-CLD	42%	73.4	0.0768e-3	27.4	15.6	37.8e+6

using the embedded SMA to shift resonance frequencies and provide peak response control by stiffness enhancement, while the active approach would provide enhanced damping at resonances still within the excitation bandwidth.

The dynamic response results have direct implication for sonic fatigue life prediction. Consider an analogous acoustic pressure loading condition with an OASPL of 150 dB (ref 20μPa). It is clear that linear dynamic response analysis is no longer valid, but its use at high response levels is still common practice in the aerospace industry for sonic fatigue design. This condition is more representative of a sonic fatigue environment and will produce more realistic life predictions, while it is understood that conservative estimates will be obtained. A representative strain-life (S-N) relationship for glass-epoxy laminates was modeled by $\epsilon = 7385\epsilon^{-6}(N)^{-0.1551}$ and the maximum RMS normal strain was taken as the failure criterion. In all cases, the maximum strain was the transverse normal strain at the mid-span of the long boundary. Under these conditions, the baseline panel has an expected life of 63.7k cycles. The corresponding life predictions for the SMAHC, 13–layer conventional, and CLD panels are 205M, 2.84M, and 37.8M cycles, respectively. These estimates are in direct relation with the corresponding peak displacements in Figure 8.8. It is intuitive that measures to further attenuate the SMAHC peak response would result in excellent sonic fatigue performance. The previously mentioned active-passive system, for example, might be a particularly attractive solution.

A plot of the transmission loss (TL) versus frequency for the SMAHC panel at two temperatures is shown in comparison to the baseline panel in Figure 8.9. The main effect of the embedded SMA in its most effective state at 82°C (180°F) is a vast increase in the stiffness-controlled portion of the TL. This improvement is diminished at higher temperatures (e.g., 121°C) for the same reasons as stated above for the dynamic response. Although the stiffness-controlled TL for the SMAHC panel shows dramatic improvement, the TL over the 400 Hz bandwidth is actually diminished because the mass-law effect has been moved to higher frequencies. The TL for the SMAHC panel at 82°C (180°F) is shown in comparison to that for the two conventional approaches in Figure 8.10. It can be seen that the SMAHC panel is superior over a 200 Hz bandwidth, but not as effective at mid-range (resonance-controlled) frequencies due to the shift in mass-law effects. Combination of the SMAHC with other passive and/or active approaches is again an attractive alternative for this frequency range. At high frequencies (mass controlled) the three approaches will produce nearly equivalent TL.
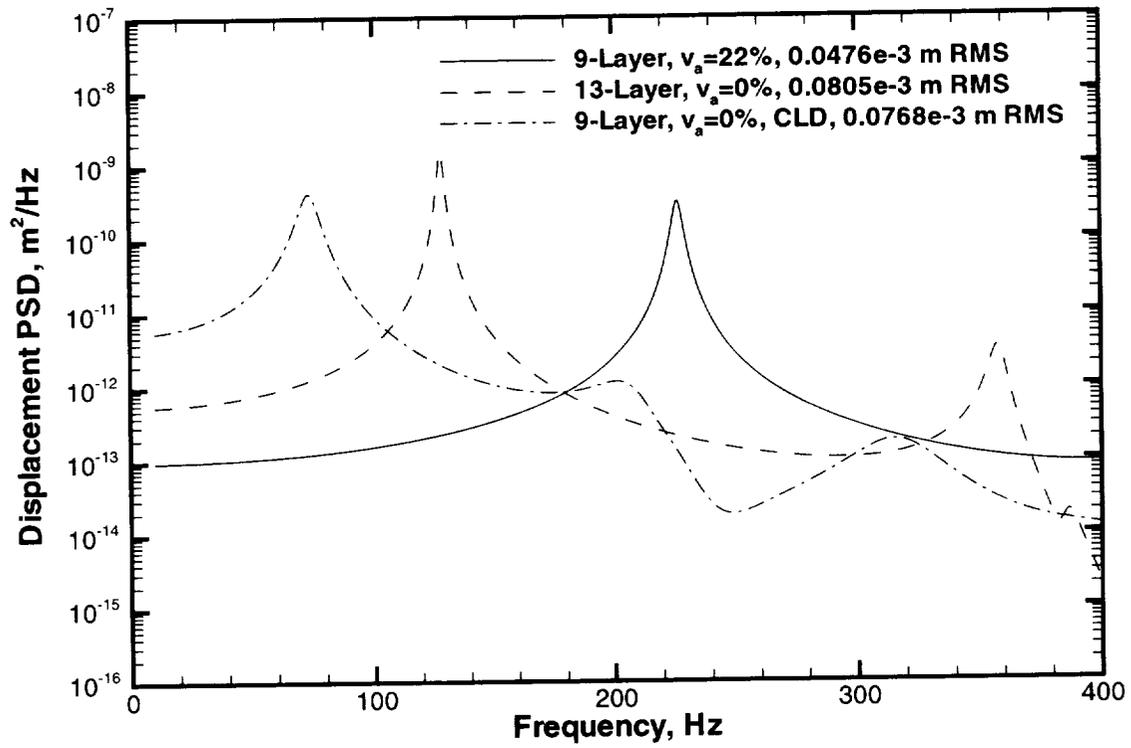
Figure 8.8 W_{max} PSD comparison of two SMAHCs with conventional treatments.
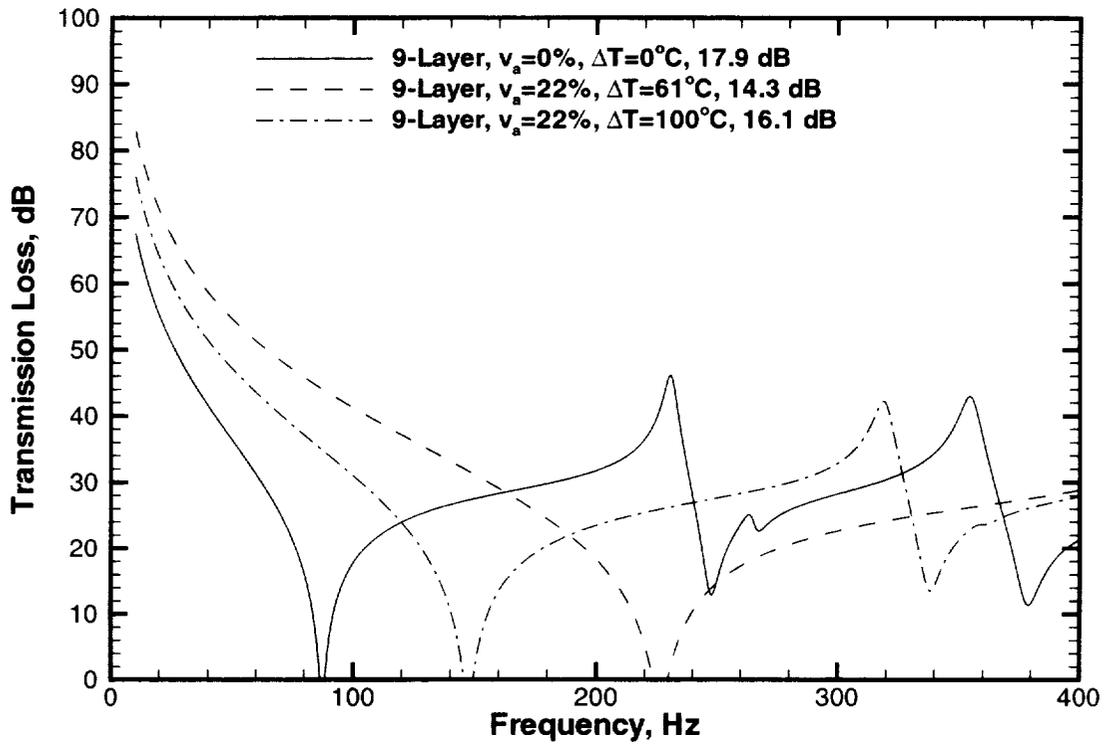
Figure 8.9 TL versus frequency for the baseline and SMAHC laminates.
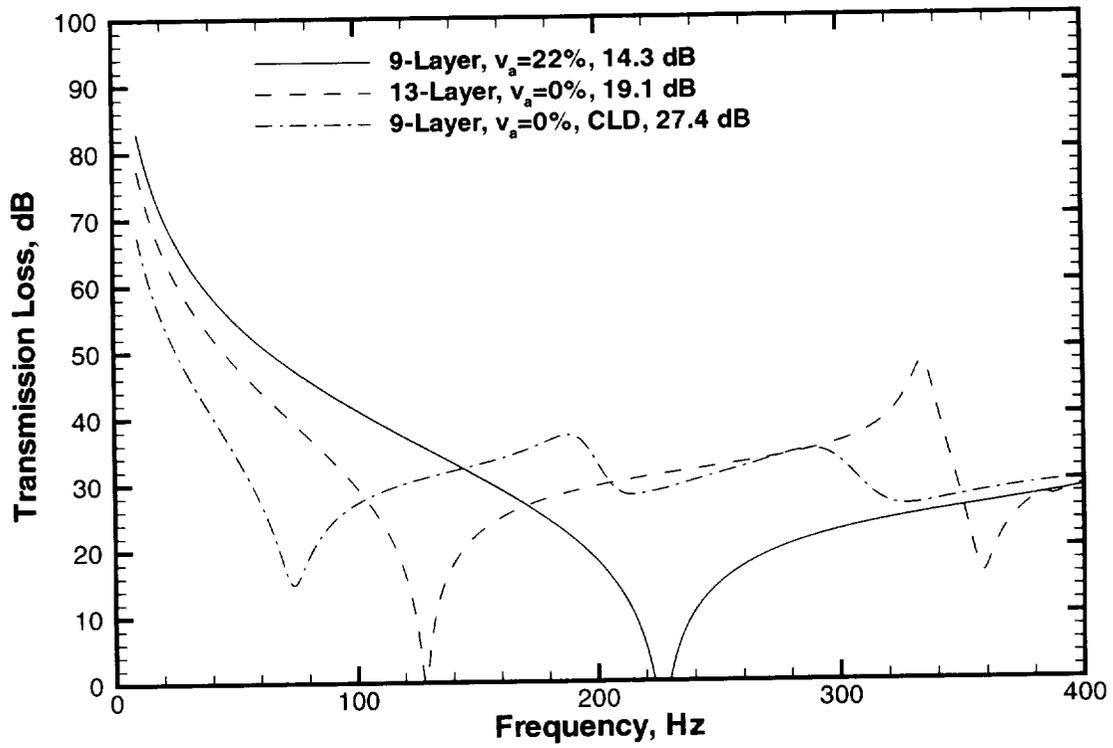
Figure 8.10 TL comparison of two SMAHCs with conventional treatments.

Chapter 9
Summary and Concluding Remarks

The main objectives of this work were to develop a themomechanical model for predicting the behavior of composite structures with embedded shape memory alloy (SMA) actuators and to validate that model with experimental measurements. Other objectives were to develop SMA actuator processing/characterization and SMA hybrid composite (SMAHC) fabrication techniques for manufacturing structures with predictable and repeatable behavior. Finally, the experimental results from the SMAHC specimens developed in this work were intended to demonstrate the control authority of SMA actuators and demonstrate some of the complex behavior of SMAHC structures.

A fairly extensive review of SMAs and their thermomechanical behavior was given in Chapter 2 to introduce the topic and the demands on a constitutive model. A constitutive model was then developed by a mechanics-of-materials approach to describe the behavior of a composite lamina with an embedded SMA constituent. The thermoelastic model captures the material nonlinearity of the SMA thermal strain/stress with temperature and is valid for constrained, restrained, or free recovery behavior with appropriate measurements of fundamental engineering properties. The constitutive model is also capable of modeling matrix material nonlinearity and is in a form that is amenable to implementation in a commercial analysis environment. Classical lamination theory was used to derive the resultant force and moment relations from the SMAHC constitutive relations and von Kármán strain-displacement relations.

Fabrication and material system characterization processes for SMAHC specimens were described in Chapter 3. The particular SMAHC material system used in this study consists of a glass-epoxy, unidirectional, prepreg, tape with embedded Nitinol ribbon. Several practical solutions for achieving repeatable results and overcoming practical fabrication issues were demonstrated.

Extensive testing of the glass-epoxy and Nitinol materials was conducted to quantify the behavior of a structure fabricated from the SMAHC material system. The mechanical properties of the glass-epoxy in principal material directions (E_1, E_2 and G_{12}, α_1, α_2) were determined as a function of temperature from unidirectional and angle-ply tensile specimens. Isothermal (modulus) and isolength (recovery force) tests were performed on Nitinol ribbon samples in two conditions to determine the material properties as a function of temperature and thermal cycle. Thermomechanical properties from the two conditions showed similar trends, but some quantitative differences were evident. These differences were attributable mainly to aging effects and stressed the importance of testing the actuator material in a condition that closely matches the

intended application as the actuator properties are very sensitive to condition and are a dominant effect in the SMAHC performance.

In Chapter 4, the resultant force and moment relations were used along with the nodal degrees of freedom and interpolation functions associated with a rectangular 24 degree-of-freedom plate element to form a potential energy functional. The extended Hamilton's principle was used to derive the equations governing the response of a SMAHC plate-type structure to steady-state thermal and dynamic mechanical loads. The governing equations were then separated into static and dynamic components.

In Chapter 5, the equations governing static stability were derived within the framework of the present formulation and used to develop a thermal buckling solution approach. The iterative method was shown to produce valid solutions for an arbitrary material system with nonlinear matrix material properties in addition to the nonlinearities associated with the SMA. A thermal post-buckling solution method was also developed to predict the thermally deflected shape subsequent to a thermal buckling event. An iterative Newton-Raphson approach was used to account for geometric nonlinearities associated with large thermal deflections. The thermal buckling and post-buckling solutions were validated against known solutions for conventional structures to benchmark the formulation and implementation.

A SMAHC beam specimen was tested to determine its thermoelastic response in a clamped-clamped configuration with a thermal load generated by resistive heating. The out-of-plane deflection was measured as a function of temperature at the beam mid-span by a laser displacement transducer. The predicted thermoelastic response was in excellent agreement with the experimental measurement. Existing discrepancies were attributable to the effects of initial deflection and mechanical boundary compliance in the physical system.

Continuous and discrete frequency domain methods were applied in Chapter 6 to the dynamic equations of motion to predict geometrically linear dynamic responses of SMAHC plate-type structures to various mechanical loads. The same approach was used in Chapter 7 with a Rayleigh integral method to develop expressions for the radiated acoustic pressure resulting from the dynamic motion of the structure. These solutions/implementations were validated against classical solutions to benchmark the analyses. Further validation was performed with experiment for conventional structures to assess the capability of the analyses to capture the behavior of a physical system.

A SMAHC beam specimen was tested in a clamped-clamped configuration with a uniform thermal load generated by resistive heating and band-limited random inertial excitation. Dynamic response data was collected at ambient and at elevated temperatures from 32.22°C (90°F) to 121.11°C (250°F) in 5.56°C (10°F) increments. The fundamental frequency of the beam was shifted 430% at 121.11°C (250°F), relative to the ambient temperature resonance. The maximum RMS displacement response attenuation of 84% was achieved at a temperature of 71.11°C (160°F) rather than at the maximum temperature. This was apparently caused by enhanced damping due to stress induced martensitic transformation hysteresis. Nonetheless, similar attenuations of around 80% were achieved at higher temperatures.

The predicted dynamic responses were in good agreement with experimental measurement with the exception of a slightly over-predicted stiffening effect at elevated temperatures. This

discrepancy was again attributable to the fact that the mechanical boundaries were modeled as perfectly rigid, when in fact the presence of thermal/electrical insulation in the gripping apparatus resulted in significant boundary compliance. This effect was incorporated into the model, and excellent agreement between prediction and measurement was achieved at all temperatures.

The model and analysis tools developed and validated in this work were then used in Chapter 8 to demonstrate a variety of thermomechanical response phenomena associated with SMAHC structures and to compare the performance of a SMAHC panel-type specimen with conventional dynamic response abatement techniques. Two buckling temperatures can exist for SMAHC structures with a SMA constituent having an austenite start temperature A_s greater than ambient. This effect results from the SMA recovery stress "pulling" the structure flat after initially buckling at a temperature less than A_s and buckling again when continued thermal expansion overcomes the recovery stress. The low-temperature buckling phenomenon can be avoided by selecting a SMA with A_s less than ambient, thereby suppressing buckling altogether for a large range of temperatures above ambient. This effect was later supported by experimental observations described in Chapters 5 and 6.

Substantial improvements in performance can be realized by selectively placing the embedded SMA in strategic locations such that the SMA volume fraction can be used more effectively, which is also driven by fabrication considerations. Relatively modest changes in the volume fraction in such cases can result in enormous changes in the performance. SMAHC structures exhibit an "optimal" operating temperature (A_o) for dynamic response performance. A_o is a function of the matrix material and SMA composition, volume fraction, and prestrain level. For many cases A_o corresponds to the "knee" temperature in the recovery stress curve. In general, A_o must be determined numerically or by comparing the slope of the recovery stress curve with that of the matrix thermal stress versus temperature. The implied conflict in choosing an alloy for aerospace structures with $A_s < T_o$ to avoid thermal buckling and $A_o \approx T$ to "optimize" dynamic response can be resolved by taking the conventional approach of allowing boundary expansion to prevent buckling and using $A_o \approx T$ to guide structural design.

The performance of a SMAHC panel was compared to that of a baseline panel and two conventional approaches including additional conventional composite layers and a constrained layer damping (CLD) treatment. The three response abatement approaches had similar added mass relative to the baseline panel, but the SMAHC panel exhibited superior dynamic response and sonic fatigue behavior. The SMAHC panel also exhibited superior transmission loss (TL) characteristics in the low-frequency, stiffness-controlled region. The weight-efficient stiffening effect of the embedded SMA makes it ideal for low-frequency, noise transmission abatement and for combination with other passive or active approaches, which are typically more effective at higher frequencies. These combined approaches have significant implications for dynamic response/sonic fatigue also.

The major conclusions from the preceding discussions can be summarized as follows:

1) A practical constitutive model has been developed that accurately captures the mechanics of a SMAHC material system.

2) Reliable SMAHC specimen fabrication procedures were developed and SMAHC beam specimens were fabricated.

3) Experimental measurements from the SMAHC beam specimens demonstrated enormous

control over thermal buckling, post-buckling, and vibration responses.

4) Predicted static and dynamic responses using the model developed in this study were in excellent agreement with the experimental measurements.

5) A SMAHC structure can exhibit two buckling temperatures. This phenomenon was supported by experimental measurements.

6) SMAHC structures can exhibit an optimal operating temperature for dynamic response performance.

7) SMAHC panel structures exhibit superior dynamic response characteristics to the conventional approaches considered.

8) SMAHC structures are ideal for low-frequency TL and for combination with other treatments for dynamic response and noise transmission abatement.

In conclusion, this study takes an engineering approach at considering embedded SMA actuators as a means of achieving quasi–static control of composite structures through adaptive stiffening in response to environmental (temperature) effects. The model was validated against experimental measurement for static and dynamic responses. It is believed that implementation of this model in a commercial FE code will lead to a very useful and practical analysis/design tool. It is hoped that this study will provide useful information for the research and engineering community in regard to fabrication, characterization, and modeling of SMAHC structures.

References

1. Buehler, W. J. and Wiley, R. C.: "TiNi-Ductile Intermetallic Compound," *Transactions of the American Society of Metals*, 55, 1962, pp. 269–276.

2. Wayman, C. M. and Shimizu, K.: "The Shape Memory ("Marmem") Effect in Alloys," *Metal Science Journal*, 6, 1972, pp. 175–183.

3. Wayman, C. M.: "Some Applications of Shape-Memory Alloys," *Journal of Metals*, June, 1980, pp. 129–137.

4. Otsuka, K. and Shimizu, K.: "Pseudoelasticity and Shape Memory Effects in Alloys," *International Metals Reviews*, 31(3), 1986, pp. 93–114.

5. Rogers, C. A. and Robertshaw, H. H.: "Shape Memory Alloy Reinforced Composites," *Engineering Science Preprints 25*, Society of Engineering Science, Inc., ESP25.8027, June 1988.

6. Rogers, C. A.: "Active Vibration and Structural Acoustic Control of Shape Memory Alloy Hybrid Composites: Experimental Results," *J. of the Acoustical Society of America*, 88(6), 1990, pp. 2803–2811.

7. Baz, A., Iman, K., and McCoy, J.: "Active Vibration Control of Flexible Beams Using Shape Memory Actuators," *Journal of Sound and Vibration*, 140(3), 1990, pp. 437–456.

8. Srinivasan, A. V., Cutts, D. G., and Schetky, L. M.: "Thermal and Mechanical Consideration in Using Shape Memory Alloys to Control Vibrations in Flexible Structures," *Metallurgical Transactions A*, Vol. 22A, 1991, pp. 623–627.

9. Chaudhry, Z. and Rogers, C. A.: "Bending and Shape Control of Beams Using SMA Actuators," *Journal of Intelligent Systems and Structures*, Vol. 2, 1991, pp. 581–602.

10. Baz, A. and Tampe, L.,: "Active Control of Buckling of Flexible Beams," *Proceedings of the 8th Biennial Conference on Failure Prevention and Reliability*, Montreal, Canada, September 17–21, 1989, pp. 211–218.

11. Maclean, B. J., Patterson, G. J., and Misra, M. S.: "Modeling of a Shape Memory Integrated Actuator for Vibration Control of Large Space Structures," *Journal of Intelligent Materials Systems and Structures*, Vol. 2, 1991, pp. 72–94.

12. Maclean, B. J., Patterson, G. J., and Misra, M. S.: "Structural Modification of Simply-Supported Laminated Plates Using Embedded Shape Memory Alloy Fibers," *Computers and Structures*, 38(5/6), 1991, pp. 569–580.

13. Liang, C., Rogers, C. A., and Fuller, C. R.: "Acoustic Transmission and Radiation Analysis of Adaptive Shape Memory Alloy Reinforced Laminated Plates," *Journal of Sound and Vibration*, 145(1), 1991, pp. 23–41.

14. Venkatesh, A., Hilborn, J., Bidaux, J. E., and Gotthardt, R.: "Active Vibration Control of Flexible Linkage Mechanisms Using Shape Memory Alloy Fiber-Reinforced Composites," *Proceedings of the 1st European Conference on Smart Structures and Materials*, Glasgow, UK, May 12–14, 1992, pp. 185–188.

15. Zhong, Z. W., Chen, R. R., Mei, C., and Pates, C. S. III: "Buckling and Postbuckling of Shape Memory Alloy Fiber-Reinforced Composite Plates," *Symposium on Buckling and Postbuckling of Composite Structures*, ASME AD-Vol. 41/PVP-Vol. 293, 1994, pp. 115–132.

16. Turner, T. L., Zhong, Z. W., and Mei, C.: "Finite Element Analysis of the Random Response Suppression of Composite Panels at Elevated Temperatures Using Shape Memory Alloy Fibers," AIAA-94–1324–CP, *Proc. of the 35th AIAA/ASME/ASCE/AHS/ASC Structures, Structural Dynamics and Materials Conf.*, Hilton Head, SC, April 18–21, 1994, pp. 136–146.

17. Ro, J. and Baz, A.: "Nitinol-Reinforced Plates: Part I. Thermal Characteristics," *Composites Engineering*, 5(1), 1995, pp. 61–75.

18. Ro, J. and Baz, A.: "Nitinol-Reinforced Plates: Part II. Static and Buckling Characteristics," *Composites Engineering*, 5(1), 1995, pp. 77–90.

19. Ro, J. and Baz, A.: "Nitinol-Reinforced Plates: Part III. Dynamic Characteristics," *Composites Engineering*, 5(1), 1995, pp. 91–106.

20. Birman, V.: "Stability of Functionally Graded Shape Memory Alloy Sandwich Panels," *Smart Materials and Structures*, 6, 1997, pp. 278–286.

21. Barker, D. K.: "Active Dynamic Response Tuning of Adaptive Composites Utilizing Embedded Nitinol Actuators," Ph.D. Dissertation, Virginia Polytechnic Institute and State University, Blacksburg, Virginia, July 1989.

22. Anders, W. S., Rogers, C. A., and Fuller, C. R.: "Vibration and Low Frequency Acoustic Analysis of Piecewise-Activated Adaptive Composite Panels," *Journal of Composite Materials*, Vol. 26, 1992, pp. 103–120.

23. Buehler, W. J. and Wiley, R. C.: "Nickel-Base Alloys," U. S. Patent 3,174,851, March 23, 1965.

24. Tanaka, K. and Nagaki, S.: "A Thermomechanical Description of Materials with Internal Variables in the Process of Phase Transformation," *Ingenieur-Archiv*, 51, 1982, pp. 287–299.

25. Liang, C. and Rogers, C. A.: "One-Dimensional Thermomechanical Constitutive Relations for Shape Memory Materials," *Journal of Intelligent Material Systems and Structures*, Vol. 1, April, 1990, pp. 207–235.

26. Brinson, L. C.: "One-Dimensional Constitutive Behavior of Shape Memory Alloys: Thermomechanical Derivation with Non-Constant Material Functions," *Journal of Intelligent Material Systems and Structures*, 4(2), 1993, pp. 229–242.

27. Boyd, J. G. and Lagoudas, D. C.: "A Thermodynamical Constitutive Model for Shape Memory Materials – Part I: The Monolithic Shape Memory Alloy," *Int. J. of Plasticity*, 12(7), 1996, pp. 805–842.

28. Cross, W. B., Kariotis, A. H., and Stimler, F. J.: "Nitinol Characterization Study," NASA CR-1433, 1969.

29. Jackson, C. M., Wagner, H. J., and Wasilewski, R. J.: "55–Nitinol The Alloy with a Memory: Its Physical Metallurgy, Properties, and Applications," NASA SP-5110, 1972.

30. Dye, T. E.: "An Experimental Investigation of the Behavior of Nitinol," M.S. Thesis, Virginia Polytechnic Institute and State University, Blacksburg, Virginia, August 1990.

31. Perkins, J. (Editor): *Shape Memory Effects in Alloys*, Plenum Press, New York, NY, 1975.

32. Duerig, T. W., Melton, K. N., Stockel, D., and Wayman, C. M. (Editors): *Engineering Aspects of Shape Memory Alloys*, Butterworth-Heinemann Ltd., Boston, MA, 1990.

33. Funakubo, H. (Editor) (Translated by J. B. Kennedy): *Shape Memory Alloys*, Gordon and Breach Science Publishers, New York, NY, 1987.

34. Otsuka, K. and Wayman, C. M. (Editors): *Shape Memory Materials*, Cambridge University Press, Cambridge, CB2 2RU, UK, 1998.

35. Birman, V.: "Review of Mechanics of Shape Memory Alloy Structures," *Applied Mechanics Reviews*, 50(11), 1997, pp. 629–645.

36. Boyd, J. G. and Lagoudas, D. C.: "A Thermodynamical Constitutive Model for Shape Memory Materials – Part II: The SMA Composite Material," *Int. J. of Plasticity*, 12(7), 1996, pp. 843–873.

37. Birman, V.: "Micromechanics of Composites with Shape Memory Alloy Fibers in Uniform Thermal Fields," *AIAA Journal*, 34(9), 1996, pp. 1905–1912.

38. Goldstein, D., Kabacoff, L., and Tydings, J.: "Stress Effects on Nitinol Phase Transformations," *Journal of Metals*, 39(3), March 1987, pp. 19–26.

39. Jones, R. M.: *Mechanics of Composite Materials*, 2nd Edition, Hemisphere Publishing Corporation, New York, NY, 1999.

40. Shames, I. H.; and Dym, C. L.: *Energy and Finite Element Methods in Structural Mechanics*, Hemisphere Publishing Corporation, New York, NY, 1985.

41. *Materials Handbook*, E Edition, Fiberite, Inc., Tempe, AZ, 1995.

42. Arvidson, J. M., Goyack, M., Morgan, P., and Blount, K.: "Evaluation of Glass Composite Material in a Temperature Range of 75°F to 300°F," Lockheed Aeronautical Systems Company, Denver, CO, 18 May 2000.

43. Draper, J. L.: "Thermomechanical Characterization Report for NiTi Shape Memory Alloy Ribbon," SOW 4271–LASC-96 Rev 02, Materials Research and Engineering, Inc., Boulder, CO, 19 January 1997.

44. Yang, T. Y.: *Finite Element Structural Analysis*, Prentice-Hall, Inc., Englewood Cliffs, New Jersey, 1986.

45. Meirovitch, L.: *Analytical Methods in Vibrations*, Macmillan Publishing Co., Inc., New York, New York, U.S.A., 1967.

46. Whitney, J. M.: *Structural Analysis of Laminated Anisotropic Plates*, Technomic Publishing Company, Inc., Lancaster, Pennsylvania, 1987.

47. Brush, D. O. and Almroth, B. O.: *Buckling of Bars, Plates, and Shells*, McGraw-Hill, Inc., New York, NY, 1975.

48. Bergan, P. C. and Clough, R. W.: "Convergence Criteria for Iterative Processes," *AIAA Journal*, 10(8), August, 1972, pp. 1107–1108.

49. Boley, B. A. and Weiner, J. H.: *Theory of Thermal Stresses*, Robert E. Kreiger Publishing Company, Inc., Malabar, FL, 1960.

50. Paul, D. B.: "Large Deflections of Clamped Rectangular Plates with Arbitrary Temperature Distributions," AFWAL-TR-81–3003, Wright-Patterson Air Force Base, February 1982.

51. Meyers, C. A. and Hyer, M. W.: "Thermal Buckling and Postbuckling of Symmetrically Laminated Composite Plates," *Journal of Thermal Stresses*, Vol. 14, 1991, pp. 519–540.

52. Roussos, L. A.: "Noise Transmission Loss of a Rectangular Plate in an Infinite Baffle," NASA TP-2398, March, 1985.

53. Doyle, J. F.: *Static and Dynamic Analysis of Structures*, Kluwer Academic Publishers, Dordrecht, The Netherlands, 1991.

54. Nigam, N. C.: *Introduction to Random Vibrations*, The MIT Press, Cambridge, Massachusetts, 1983.

55. Turner, T. L. and Rizzi, S. A.: "Prediction and Measurement of the Vibration and Acoustic Radiation of Panels Subjected to Acoustic Loading," *Proceedings of the 1995 International Congress on Noise Control Engineering*, Newport Beach, CA, July 10–12, 1995, pp. 315–318.

56. Pierce, A. D.: *Acoustics: An Introduction to its Physical Principles and Applications*, Acoustical Society of America, Woodbury, NY, 1989.

57. Kinsler, L. E., Frey, A. R., Coppens, A. B., and Sanders, J. V.: *Fundamentals of Acoustics*, 3rd Edition, John Wiley and Sons, Inc., New York, NY, 1982.

58. Buehler, W. J. and Wang, F. E.: "A Summary of Recent Research on the Nitinol Alloys and Their Potential Application in Ocean Engineering," *Journal of Applied Physics*, Vol. 34, 1963, pp. 1475–1477.

59. Mei, C., Zhong, Z. W., and Turner, T. L.: "Control of Sonic Fatigue for High Speed Flight Vehicles Using Shape Memory Alloys," *Proceedings of SPIE's 6th International Symposium on Smart Structures and Materials*, San Diego, CA, March 1–6, 1998.

60. Turner, T. L.: "A New Thermoelastic Model for Analysis of Shape Memory Alloy Hybrid Composites," *Journal of Intelligent Material Systems and Structures*, In Press.

61. Churchill, R. V.; Brown, J. W.: *Complex Variables and Applications*, 4th Edition, McGraw-Hill, Inc., New York, NY, 1984.

62. Hildebrand, F. B.: *Advanced Calculus for Engineers*, 2nd Edition, Prentice-Hall, Inc., Englewood Cliffs, NJ, 1976.

Appendix A
RSM Hybrid Lamina Constitutive Relations

The constitutive relations developed in this appendix are referred to as the recovery stress model (RSM) as described in Chapter 2. A mechanics-of-materials approach is used to derive the thermoelastic constitutive relations governing a SMAHC lamina, based upon observation of the recovery stress phenomenon.

A representative volume element of a SMA fiber-reinforced hybrid composite lamina is shown in Figure A.1. The element is taken to be in the plane of the plate. The composite matrix, for example graphite-epoxy, has the principal material directions 1 and 2, and the SMA fiber is embedded in the 1-direction.
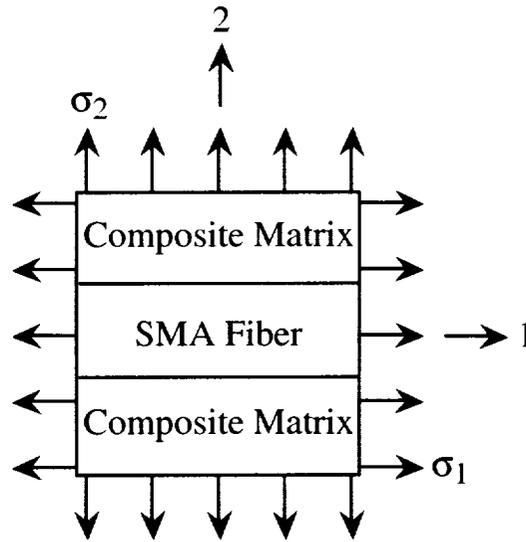
Figure A.1 Representative volume element for SMA fiber-reinforced hybrid composite lamina.

In order to derive the constitutive relation for the 1-direction, it is assumed that a stress σ_1 acts alone on the element $(\sigma_2 = 0)$ and that the SMA fiber and composite matrix are strained by the same amount, ϵ_1 (i.e., plane sections remain plane). The 1-direction stress-strain relation of the SMA fiber can be described as

$$\sigma_{1a} = E_a \epsilon_1 + \sigma_r \quad , \quad T \geq A_s \tag{A.1}$$

or

$$\sigma_{1a} = E_a(\epsilon_1 - \alpha_a \Delta T) \quad , \quad T < A_s \tag{A.2}$$

where A_s is the austenite start temperature and α_a is the thermal expansion coefficient. The Young's modulus E_a and the recovery stress σ_r are temperature dependent. The recovery stress σ_r is also dependent on the initial strain ϵ_r. Description of the recovery stress and modulus behavior

200

for Nitinol is discussed in Chapters 2 and 3. Similarly, the one–dimensional stress–strain relation in the 1–direction for the composite matrix can be expressed as

$$\sigma_{1m} = E_{1m}(\epsilon_1 - \alpha_{1m}\Delta T) \tag{A.3}$$

The resultant force in the 1-direction $(\sigma_2 = 0)$ is distributed over the SMA fiber and composite matrix and can be written as

$$\sigma_1 A_1 = \sigma_{1a} A_a + \sigma_{1m} A_m \tag{A.4}$$

where (σ_1, A_1), (σ_{1a}, A_a), and (σ_{1m}, A_{1m}) are the (stress, cross-sectional area) of the entire element, SMA fiber, and composite matrix, respectively. Thus, the average stress σ_1 is

$$\sigma_1 = \sigma_{1a} v_a + \sigma_{1m} v_m \tag{A.5}$$

where $v_a = A_a/A_1$ and $v_m = A_m/A_1$ are the volume fractions of SMA and composite matrix, respectively. When $T > A_s$, the SMA effect is activated and the one-dimensional stress-strain relation in the 1-direction becomes

$$\sigma_1 = (E_a \epsilon_1 + \sigma_r) v_a + E_{1m}(\epsilon_1 - \alpha_{1m}\Delta T) v_m$$
$$= E_1 \epsilon_1 + \sigma_r v_a - E_{1m}\alpha_{1m} v_m \Delta T \tag{A.6}$$

where

$$E_1 = E_{1m} v_m + E_a v_a \tag{A.7}$$

When $T < A_s$, the SMA effect is not activated and the stress σ_1 is

$$\sigma_1 = E_1 \epsilon_1 - (E_a \alpha_a v_a + E_{1m}\alpha_{1m} v_m)\Delta T$$
$$= E_1(\epsilon_1 - \alpha_1 \Delta T) \tag{A.8}$$

where

$$\alpha_1 = \frac{(E_{1m}\alpha_{1m} v_m + E_a \alpha_a v_a)}{(E_{1m} v_m + E_a v_a)} \tag{A.9}$$

A similar constitutive relation may be derived for the 2–direction by assuming that the applied stress σ_2 acts upon both the fiber and the matrix $(\sigma_1 = 0)$. Thus, the one-dimensional stress-strain relations in the 2–direction for the SMA fiber and the composite matrix become

$$\sigma_{2s} = \sigma_2 = E_a(\epsilon_{2a} - \alpha_a \Delta T) \tag{A.10}$$

and

$$\sigma_{2m} = \sigma_2 = E_{2m}(\epsilon_{2m} - \alpha_{2m}\Delta T) \tag{A.11}$$

respectively. The recovery stress does not appear in equation (A.10), since the SMA fiber initial strain ϵ_r and recovery stress σ_r are considered to be a 1–direction effect only.

The total elongation is due to strain in the composite matrix and the SMA fiber and may be written in the form

$$A_1 \epsilon_2 = A_m \epsilon_{2m} + A_a \epsilon_{2a} \tag{A.12}$$

201

Thus, the total strain becomes

$$\epsilon_2 = \epsilon_{2m} v_m + \epsilon_{2a} v_a \tag{A.13}$$

Since $\sigma_2 = E_2(\epsilon_2 - \alpha_2 \Delta T)$, equations (A.10) and (A.11) may be substituted into equation (A.13) to give

$$\begin{aligned}
\epsilon_2 &= \frac{\sigma_2}{E_2} + \alpha_2 \Delta T \\
&= \frac{\sigma_2 v_a}{E_a} + \frac{\sigma_2 v_m}{E_{2m}} + (\alpha_a v_a + \alpha_{2m} v_m)\Delta T
\end{aligned} \tag{A.14}$$

Therefore, the modulus and thermal expansion coefficient in the 2–direction become

$$E_2 = \frac{E_{2m} E_a}{(E_{2m} v_a + E_a v_m)} \tag{A.15}$$

and

$$\alpha_2 = \alpha_{2m} v_m + \alpha_a v_a \tag{A.16}$$

Expressions for the hybrid composite Poisson's ratios and shear moduli follow from similar derivations.

The constitutive relations for a thin composite lamina with embedded SMA fibers can be derived using a similar engineering approach to give

$$\begin{aligned}
\begin{Bmatrix} \sigma_1 \\ \sigma_2 \\ \tau_{12} \end{Bmatrix} &= \begin{bmatrix} Q_{11}^* & Q_{12}^* & 0 \\ Q_{12}^* & Q_{22}^* & 0 \\ 0 & 0 & Q_{66}^* \end{bmatrix} \begin{Bmatrix} \epsilon_1 \\ \epsilon_2 \\ \gamma_{12} \end{Bmatrix} + \begin{Bmatrix} \sigma_r \\ 0 \\ 0 \end{Bmatrix} v_a - [Q]_m \begin{Bmatrix} \alpha_1 \\ \alpha_2 \\ 0 \end{Bmatrix}_m v_m \Delta T \\
&= [Q^*] \begin{Bmatrix} \epsilon_1 \\ \epsilon_2 \\ \gamma_{12} \end{Bmatrix} + \begin{Bmatrix} \sigma_r \\ 0 \\ 0 \end{Bmatrix} v_a - \left([Q] \begin{Bmatrix} \alpha_1 \\ \alpha_2 \\ 0 \end{Bmatrix} v \right)_m \Delta T \quad , \quad T \geq A_s
\end{aligned} \tag{A.17}$$

and

$$\begin{Bmatrix} \sigma_1 \\ \sigma_2 \\ \tau_{12} \end{Bmatrix} = [Q^*] \left(\begin{Bmatrix} \epsilon_1 \\ \epsilon_2 \\ \gamma_{12} \end{Bmatrix} - \begin{Bmatrix} \alpha_1 \\ \alpha_2 \\ 0 \end{Bmatrix} \Delta T \right) \quad , \quad T < A_s \tag{A.18}$$

where $[Q]_m$ and $[Q^*]$ are the reduced stiffness matrices of the composite matrix and the SMA hybrid composite lamina, respectively. The $[Q^*]$ matrix is temperature dependent and is evaluated using the previously derived relations as

$$(E_1, \nu_{12}) = (E_{1m}, \nu_{12m})v_m + (E_a, \nu_a)v_a \tag{A.19}$$

and

$$(E_2, G_{12}) = \frac{(E_{2m} E_a, G_{12m} G_a)}{[(E_{2m}, G_{12m})v_a + (E_a, G_a)v_m]} \tag{A.20}$$

where the ν's are Poisson's ratios and the G's are the shear moduli. The thermal expansion coefficients α_1 and α_2 are derived in equations (A.9) and (A.16).

Appendix B
Gauss-Legendre Numerical Integration

B.1 Element Matrices

The element area integrals necessary for evaluation of the element matrices in equations (4.55) can be performed numerically using Gauss-Legendre quadrature. The four-node, rectangular, 24–dof plate element used in this study has interpolation functions given by equations (4.3) and (4.4) for the in-plane and out-of-plane degrees of freedom, respectively. Consider the element bending mass matrix for example, i.e.,

$$[m_b] = \int_A \rho h \{H_w(x,y)\} \{H_w(x,y)\}^T \, dA$$

$$= \int_0^b \int_0^a \rho h \{H_w(x,y)\} \{H_w(x,y)\}^T \, dx dy \tag{B.1}$$

where (x,y) are the element coordinates and a and b are the element length and width, respectively.

The element area integrations in equation (B.1) are in a form that is easily adapted to Gauss-Legendre numerical integration. The coordinates can be transformed to non-dimensional element-centered coordinates (ξ, η) with the variable transformation

$$x : [0, a] \quad \xi = 2\frac{x}{a} - 1 : [-1, 1] \quad d\xi = \frac{a}{2} \, dx$$

$$y : [0, b] \quad \eta = 2\frac{y}{b} - 1 : [-1, 1] \quad d\eta = \frac{b}{2} \, dy \tag{B.2}$$

Thus, the expression in equation (B.1) can be rewritten as

$$[m_b] = \int_{-1}^{1} \int_{-1}^{1} \rho h \{\dot{H}_w(\xi,\eta)\} \{\dot{H}_w(\xi,\eta)\}^T \, |J(\xi,\eta)| \, d\xi d\eta \tag{B.3}$$

where $|J(\xi,\eta)|$ is the determinant of the Jacobian matrix of the transformation:

$$|J(\xi,\eta)| = \begin{vmatrix} \frac{\partial x}{\partial \xi} & \frac{\partial x}{\partial \eta} \\ \frac{\partial y}{\partial \xi} & \frac{\partial y}{\partial \eta} \end{vmatrix} = \begin{vmatrix} \frac{2}{a} & 0 \\ 0 & \frac{2}{b} \end{vmatrix} = \frac{4}{ab} \tag{B.4}$$

The element displacement functions are now written in terms of the non-dimensional coordinates (ξ, η) as

$$w(x,y) = \sum_{i=1}^{4} \left[G_i(\xi)G_i(\eta)w_i + \frac{a}{2}H_i(\xi)G_i(\eta)\left(\frac{\partial w}{\partial x}\right)_i \right. $$
$$\left. + \frac{b}{2}G_i(\xi)H_i(\eta)\left(\frac{\partial w}{\partial y}\right)_i + \frac{ab}{4}H_i(\xi)H_i(\eta)\left(\frac{\partial^2 w}{\partial x \partial y}\right)_i \right] \tag{B.5}$$
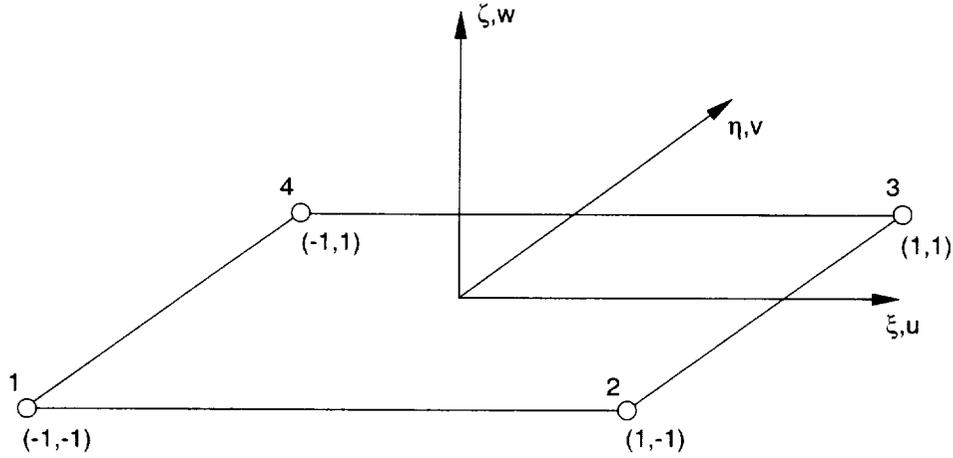
Figure B.1 Schematic of plate element in centroidal non-dimensional coordinates.

where

$$G_i(\xi) = \frac{1}{4}(-\xi_i\xi^3 + 3\xi_i\xi + 2)$$

$$H_i(\xi) = \frac{1}{4}(\xi^3 + \xi_i\xi^2 - \xi - \xi_i)$$

(B.6)

and (ξ_i, η_i) are the coordinates of node i. A schematic of an element in the non-dimensional coordinates is shown in Figure B.1

The integral over the element are in equation (B.3) is now in a form that is easily evaluated numerically. Gauss-Legendre integration entails evaluating the integrand at a number of equally spaced (Gauss) points within the region of integration and summing the product of these contributions with corresponding weights. Exact evaluation is possible for polynomial-type functions when the order of the function is less than or equal to one less than twice the number of Gauss points, i.e., $(2N_g - 1 \geq p)$ where N_g is the number of Gauss points and p is the order of the polynomial. Employing this method, the integral in equation (B.3) can be rewritten as

$$[m_b] = \sum_{i=1}^{N_g}\sum_{j=1}^{N_g} W_i W_j \rho h \left\{ \dot{H}_w(\xi_i, \eta_j) \right\} \left\{ \dot{H}_w(\xi_i, \eta_j) \right\}^T |J(\xi_i, \eta_j)|$$

(B.7)

where W_* are the weights at the Gauss points denoted by ξ_i and η_j.

B.2 Mean Square Radiated Acoustic Pressure

A similar approach can be used to evaluate the element area integrals for acoustic radiation calculations in Chapter 7. Recall the form for the mean square radiated pressure from the

continuous spectral analysis approach in equation (7.18). In this case, the element physical coordinates are denoted by (ξ, η) and the non-dimensional element-centered coordinates will be denoted by (μ, ν). Equation (7.18) can be written in terms of the element physical coordinates as follows

$$\overline{p^2}(R, \theta, \phi) = \left(\frac{\rho}{2\pi R}\right)^2 \sum_{i=1}^{N_r} \sum_{j=1}^{N_r} \int_0^b \int_0^a \int_0^b \int_0^a \{H_w(\xi, \eta)\}_i^T \int_{-\infty}^{\infty} \omega^4 [S_{aa}^{ij}(\omega)] e^{i\omega \frac{(\xi'-\xi)K+(\eta'-\eta)\Lambda}{c}} d\omega$$

$$\{H_w(\xi', \eta')\}_j \, d\xi \, d\eta \, d\xi' \, d\eta' \tag{B.8}$$

Applying the variable transformation given in equation (B.2) yields

$$\overline{p^2}(R, \theta, \phi) = \left(\frac{\rho}{2\pi R}\right)^2 \sum_{i=1}^{N_r} \sum_{j=1}^{N_r} \int_{-1}^1 \int_{-1}^1 \int_{-1}^1 \int_{-1}^1 \{H_w(\mu, \nu)\}_i^T \int_{-\infty}^{\infty} \omega^4 [S_{aa}^{ij}(\omega)] e^{i\omega \frac{(\mu'-\mu)K+(\nu'-\nu)\Lambda}{c}} d\omega$$

$$\{H_w(\mu', \nu')\}_j \, |J(\mu, \nu)||J(\mu', \nu')| \, d\mu \, d\nu \, d\mu' \, d\nu' \tag{B.9}$$

where the $|J|$ are determinants of the Jacobian of the transformation as before. Now, applying Gauss-Legendre numerical integration gives the final expression for the mean square pressure at a point (i.e., for a given set of observer direction angles θ and ϕ) in the acoustic far-field:

$$\overline{p^2}(R, \theta, \phi) = \left(\frac{\rho}{2\pi R}\right)^2 \sum_{i=1}^{N_r} \sum_{j=1}^{N_r} \sum_{k=1}^{N_g} \sum_{l=1}^{N_g} \sum_{m=1}^{N_g} \sum_{n=1}^{N_g} W_k W_l W_m W_n \{H_w(\mu_k, \nu_l)\}_i^T$$

$$\int_{-\infty}^{\infty} \omega^4 [S_{aa}^{ij}(\omega)] e^{i\omega \frac{(\mu_m - \mu_k)K + (\nu_n - \nu_l)\Lambda}{c}} d\omega \, \{H_w(\mu_m, \nu_n)\}_j \, |J(\mu_k, \nu_l)||J(\mu_m, \nu_n)| \tag{B.10}$$

The same procedure can be applied to the expression for the mean square radiated pressure from the discrete spectral approach, equation (7.35), which yields

$$\overline{p_t^2}(R, \theta, \phi) = \left(\frac{\rho}{2\pi R}\right)^2 \sum_{i=1}^{N_r} \sum_{j=1}^{N_r} \sum_{k=1}^{N_g} \sum_{l=1}^{N_g} \sum_{m=1}^{N_g} \sum_{n=1}^{N_g} W_k W_l W_m W_n \{H_w(\mu_k, \nu_l)\}_i^T$$

$$\sum_{r=0}^{N_w - 1} \omega_r^4 E[\{\hat{a}_{br}^*\}_i \{\hat{a}_{br}\}_j^T] e^{i\omega_r \frac{(\mu_m - \mu_k)K + (\nu_n - \nu_l)\Lambda}{c}} \{H_w(\mu_m, \nu_n)\}_j \, |J(\mu_k, \nu_l)||J(\mu_m, \nu_n)| \tag{B.11}$$

It is apparent that numerical integration for the computation of the radiated pressure can be computationally intensive due to the multiply-nested loops. Clever computer coding and/or compilation optimizers can diminish this problem, but another approach would be to evaluate the necessary element area integrals in closed form. This can save significant computational effort and a discussion of this approach is given in Appendix C.

B.3 Radiated Acoustic Power

Determination of the radiated acoustic power requires integration of the normal acoustic intensity over a hemispherical surface, given by equation (E.6). This integral must be evaluated numerically. Gauss-Legendre numerical integration can be employed through selection of a suitable change of variables. The following change of variables results in the desired integral limits:

$$\theta : [0, \pi/2] \qquad u = \frac{4}{\pi}\left(\theta - \frac{\pi}{4}\right) : [-1, 1] \qquad d\theta = \frac{\pi}{4} du$$

$$\phi : [0, 2\pi] \qquad v = \frac{1}{\pi}(\phi - \pi) : [-1, 1] \qquad d\phi = \pi \, dv$$

(B.12)

Then the radiated acoustic power becomes

$$\Pi = \int_{-1}^{1} \int_{-1}^{1} I(r, u, v) \, r^2 \sin\left(\frac{\pi}{4}u + \frac{\pi}{4}\right) |J(u, v)| \, du \, dv$$

(B.13)

where the determinant of the Jacobian matrix is as follows

$$|J(u, v)| = \begin{vmatrix} \frac{\partial\theta}{\partial u} & \frac{\partial\theta}{\partial v} \\ \frac{\partial\phi}{\partial u} & \frac{\partial\phi}{\partial v} \end{vmatrix} = \begin{vmatrix} \frac{\pi}{4} & 0 \\ 0 & \pi \end{vmatrix} = \frac{\pi^2}{4}$$

(B.14)

as is easily seen in making the substitution for $d\theta$ and $d\phi$ in equation (B.13) from the transformation. Applying Gauss-Legendre integration results in the following expression for the total acoustic power radiated by the panel

$$\Pi = \sum_{r=1}^{N_g} \sum_{s=1}^{N_y} I(r, u_r, v_s) \, r^2 \sin\left(\frac{\pi}{4}u_r + \frac{\pi}{4}\right) |J(u_r, v_s)|$$

(B.15)

where the acoustic intensity I is related to the mean square radiated acoustic pressure by equation (E.4) and the mean square pressure is given in equation (B.10) or (B.11).

Appendix C
Closed Form Evaluation of Element Area Integrals

Recall the expressions for the far-field mean square radiated acoustic pressure, given in equations (7.18) or (7.35):

$$\overline{p_f^2}(R,\theta,\phi) = \left(\frac{\rho}{2\pi R}\right)^2 \sum_{i=1}^{N_c}\sum_{j=1}^{N_c} \int\int_{A_i \ A'_j} \{H_w(\xi,\eta)\}_i^T \int_{-\infty}^{\infty} \omega^4 [S_{aa}^{ij}(\omega)]\epsilon^{i\omega\frac{(\xi'-\xi)K+(\eta'-\eta)\Lambda}{c}} d\omega$$

$$\{H_w(\xi',\eta')\}_j \ dA_i \ dA'_j \quad \text{(C.1)}$$

or

$$\overline{p_f^2}(R,\theta,\phi) = \left(\frac{\rho}{2\pi R}\right)^2 \sum_{i=1}^{N_c}\sum_{j=1}^{N_c} \int\int_{A_i \ A'_j} \{H_w(\xi,\eta)\}_i^T$$

$$\sum_{n=0}^{N_\omega-1} \omega_n^4 E[\{\hat{a}_{bn}^*\}_i\{\hat{a}_{bn}\}_j^T]\epsilon^{i\omega_n\frac{(\xi'-\xi)K+(\eta'-\eta)\Lambda}{c}} \{H_w(\xi',\eta')\}_j \ dA_i \ dA'_j$$

$$\text{(C.2)}$$

The form for the out-of-plane interpolation functions $\{H_w(\xi,\eta)\}$ for the 24 degree-of-freedom rectangular plate element are given in equation (4.4). As stated previously in the respective acoustic radiation sections, the complex exponential function in the integrand of the above equations must be separated into two components. One is constant for each element index pair (i,j) and the other must be included in the integration over the element areas in local coordinates.

Consider the expression for the mean-square pressure in the discrete frequency domain formulation for example. Splitting the complex exponential into element-constant and element-variable components and changing the order of the summations gives

$$\overline{p_f^2}(R,\theta,\phi) = \left(\frac{\rho}{2\pi R}\right)^2 \sum_{n=0}^{N_\omega-1} \omega_n^4 \sum_{i=1}^{N_c}\sum_{j=1}^{N_c} \epsilon^{i\omega_n\frac{(\xi'_j-\xi_i)K+(\eta'_j-\eta_i)\Lambda}{c}}$$

$$\int_{A_i} \{H_w(u,v)\}_i^T \epsilon^{-i\omega_n\frac{uK+v\Lambda}{c}} dA_i \quad \text{(C.3)}$$

$$E[\{\hat{a}_{bn}^*\}_i\{\hat{a}_{bn}\}_j^T] \int_{A'_j} \{H_w(u',v')\}_j \epsilon^{i\omega_n\frac{u'K+v'\Lambda}{c}} dA'_j$$

where (u,v) are element local coordinates. There are four cases which must be considered in evaluation of these area integrals; $(K \neq 0, \Lambda \neq 0)$, $(K \neq 0, \Lambda = 0)$, $(K = 0, \Lambda \neq 0)$ and $(K = 0, \Lambda = 0)$. Integration of each of the 16 out-of-plane interpolation functions with the complex exponential, for each of the four cases involving the argument of the exponential

function, was performed. The resulting functions are denoted as follows

$$I_1(\omega_n, \mathrm{K}, \Lambda) = \int_0^a \int_0^b M_1(u, v) e^{i\omega_n \frac{u\mathrm{K}+v\Lambda}{c}} \, du\,dv$$

$$\vdots$$

$$I_{16}(\omega_n, \mathrm{K}, \Lambda) = \int_0^a \int_0^b M_{16}(u, v) e^{i\omega_n \frac{u\mathrm{K}+v\Lambda}{c}} \, du\,dv$$

$$I_1(\omega_n, \mathrm{K}) = \int_0^a \int_0^b M_1(u, v) e^{i\omega_n \frac{u\mathrm{K}}{c}} \, du\,dv$$

$$\vdots$$

$$I_{16}(\omega_n, \mathrm{K}) = \int_0^a \int_0^b M_{16}(u, v) e^{i\omega_n \frac{u\mathrm{K}}{c}} \, du\,dv$$

$$I_1(\omega_n, \Lambda) = \int_0^a \int_0^b M_1(u, v) e^{i\omega_n \frac{v\Lambda}{c}} \, du\,dv \qquad\qquad (C.4)$$

$$\vdots$$

$$I_{16}(\omega_n, \Lambda) = \int_0^a \int_0^b M_{16}(u, v) e^{i\omega_n \frac{v\Lambda}{c}} \, du\,dv$$

$$I_1 = \int_0^a \int_0^b M_1(u, v) \, du\,dv$$

$$\vdots$$

$$I_{16} = \int_0^a \int_0^b M_{16}(u, v) \, du\,dv$$

where a and b are the element length and width, respectively. The expressions resulting from integration of the shape functions along with the various exponentials follow. Note that wave number is used in these expressions $k = \omega/c$.
$(\mathrm{K} \neq 0, \Lambda \neq 0)$

$$I_1(k, \mathrm{K}, \Lambda) = -[\left(-12i + 12i e^{ibk\Lambda} + 6bk\Lambda + 6bk\Lambda e^{ibk\Lambda} + b^3 k^3 \Lambda^3\right)$$
$$\left(-12i + 12i e^{iakK} + 6ak\mathrm{K} + 6ak\mathrm{K}e^{iakK} + a^3 k^3 \mathrm{K}^3\right)]/(a^3 b^3 \mathrm{K}^4 \Lambda^4 k^8) \qquad (C.5)$$

208

$$I_2(k, \mathrm{K}, \Lambda) = \left[\left(-12i + 12ie^{ibk\Lambda} + 6bk\Lambda + 6bk\Lambda e^{ibk\Lambda} + b^3k^3\Lambda^3\right)\right.$$
$$\left.\left(-12i + 12ie^{iak\mathrm{K}} + 6ak\mathrm{K} + 6ak\mathrm{K}e^{iak\mathrm{K}} + a^3k^3\mathrm{K}^3e^{iak\mathrm{K}}\right)\right]/\left(a^3b^3\mathrm{K}^4\Lambda^4k^8\right)$$

(C.6)

$$I_3(k, \mathrm{K}, \Lambda) = -\left[\left(-12i + 12ie^{ibk\Lambda} + 6bk\Lambda + 6bk\Lambda e^{ibk\Lambda} + b^3k^3\Lambda^3e^{ibk\Lambda}\right)\right.$$
$$\left.\left(-12i + 12ie^{iak\mathrm{K}} + 6ak\mathrm{K} + 6ak\mathrm{K}e^{iak\mathrm{K}} + a^3k^3\mathrm{K}^3e^{iak\mathrm{K}}\right)\right]/\left(a^3b^3\mathrm{K}^4\Lambda^4k^8\right)$$

(C.7)

$$I_4(k, \mathrm{K}, \Lambda) = \left[\left(-12i + 12ie^{ibk\Lambda} + 6bk\Lambda + 6bk\Lambda e^{ibk\Lambda} + b^3k^3\Lambda^3e^{ibk\Lambda}\right)\right.$$
$$\left.\left(-12i + 12ie^{iak\mathrm{K}} + 6ak\mathrm{K} + 6ak\mathrm{K}e^{iak\mathrm{K}} + a^3k^3\mathrm{K}^3\right)\right]/\left(a^3b^3\mathrm{K}^4\Lambda^4k^8\right)$$

(C.8)

$$I_5(k, \mathrm{K}, \Lambda) = -\left[\left(-12i + 12ie^{ibk\Lambda} + 6bk\Lambda + 6bk\Lambda e^{ibk\Lambda} + b^3k^3\Lambda^3\right)\right.$$
$$\left.\left(-6i + 6ie^{iak\mathrm{K}} + 4ak\mathrm{K} + 2ak\mathrm{K}e^{iak\mathrm{K}} + ia^2k^2\mathrm{K}^2\right)\right]/\left(a^2b^3\mathrm{K}^4\Lambda^4k^8\right)$$

(C.9)

$$I_6(k, \mathrm{K}, \Lambda) = \left[\left(12 - 12e^{ibk\Lambda} + 6ibk\Lambda + 6ibk\Lambda e^{ibk\Lambda} + ib^3k^3\Lambda^3\right)\right.$$
$$\left.\left(6 - 6e^{iak\mathrm{K}} + 2iak\mathrm{K} + 4iak\mathrm{K}e^{iak\mathrm{K}} + a^2k^2\mathrm{K}^2e^{iak\mathrm{K}}\right)\right]/\left(a^2b^3\mathrm{K}^4\Lambda^4k^8\right)$$

(C.10)

$$I_7(k, \mathrm{K}, \Lambda) = \left[\left(-12 + 12e^{ibk\Lambda} - 6ibk\Lambda - 6ibk\Lambda e^{ibk\Lambda} - ib^3k^3\Lambda^3e^{ibk\Lambda}\right)\right.$$
$$\left.\left(6 - 6e^{iak\mathrm{K}} + 2iak\mathrm{K} + 4iak\mathrm{K}e^{iak\mathrm{K}} + a^2k^2\mathrm{K}^2e^{iak\mathrm{K}}\right)\right]/\left(a^2b^3\mathrm{K}^4\Lambda^4k^8\right)$$

(C.11)

$$I_8(k, \mathrm{K}, \Lambda) = \left[\left(-12i + 12ie^{ibk\Lambda} + 6bk\Lambda + 6bk\Lambda e^{ibk\Lambda} + b^3k^3\Lambda^3e^{ibk\Lambda}\right)\right.$$
$$\left.\left(-6i + 6ie^{iak\mathrm{K}} + 4ak\mathrm{K} + 2ak\mathrm{K}e^{iak\mathrm{K}} + ia^2k^2\mathrm{K}^2\right)\right]/\left(a^2b^3\mathrm{K}^4\Lambda^4k^8\right)$$

(C.12)

$$I_9(k, \mathrm{K}, \Lambda) = -\left[\left(-6i + 6ie^{ibk\Lambda} + 4bk\Lambda + 2bk\Lambda e^{ibk\Lambda} + ib^2k^2\Lambda^2\right)\right.$$
$$\left.\left(-12i + 12ie^{iak\mathrm{K}} + 6ak\mathrm{K} + 6ak\mathrm{K}e^{iak\mathrm{K}} + a^3k^3\mathrm{K}^3\right)\right]/\left(a^3b^2\mathrm{K}^4\Lambda^4k^8\right)$$

(C.13)

$$I_{10}(k, \mathrm{K}, \Lambda) = \left[\left(-6i + 6ie^{ibk\Lambda} + 4bk\Lambda + 2bk\Lambda e^{ibk\Lambda} + ib^2k^2\Lambda^2\right)\right.$$
$$\left.\left(-12i + 12ie^{iak\mathrm{K}} + 6ak\mathrm{K} + 6ak\mathrm{K}e^{iak\mathrm{K}} + a^3k^3\mathrm{K}^3e^{iak\mathrm{K}}\right)\right]/\left(a^3b^2\mathrm{K}^4\Lambda^4k^8\right)$$

(C.14)

$$I_{11}(k, \mathrm{K}, \Lambda) = \left[\left(6 - 6e^{ibk\Lambda} + 2ibk\Lambda + 4ibk\Lambda e^{ibk\Lambda} + b^2k^2\Lambda^2e^{ibk\Lambda}\right)\right.$$
$$\left.\left(-12 + 12e^{iak\mathrm{K}} - 6iak\mathrm{K} - 6iak\mathrm{K}e^{iak\mathrm{K}} - ia^3k^3\mathrm{K}^3e^{iak\mathrm{K}}\right)\right]/\left(a^3b^2\mathrm{K}^4\Lambda^4k^8\right)$$

(C.15)

$$I_{12}(k, \mathrm{K}, \Lambda) = \left[\left(6 - 6e^{ibk\Lambda} + 2ibk\Lambda + 4ibk\Lambda e^{ibk\Lambda} + b^2k^2\Lambda^2e^{ibk\Lambda}\right)\right.$$
$$\left.\left(12 - 12e^{iak\mathrm{K}} + 6iak\mathrm{K} + 6iak\mathrm{K}e^{iak\mathrm{K}} + ia^3k^3\mathrm{K}^3\right)\right]/\left(a^3b^2\mathrm{K}^4\Lambda^4k^8\right)$$

(C.16)

$$I_{13}(k, \mathrm{K}, \Lambda) = -\left[\left(-6i + 6ie^{ibk\Lambda} + 4bk\Lambda + 2bk\Lambda e^{ibk\Lambda} + ib^2k^2\Lambda^2\right)\right.$$
$$\left.\left(-6i + 6ie^{iak\mathrm{K}} + 4ak\mathrm{K} + 2ak\mathrm{K}e^{iak\mathrm{K}} + ia^2k^2\mathrm{K}^2\right)\right]/\left(a^2b^2\mathrm{K}^4\Lambda^4k^8\right)$$

(C.17)

$$I_{14}(k, \mathrm{K}, \Lambda) = \left[\left(6 - 6\epsilon^{ibk\Lambda} + 4ibk\Lambda + 2ibk\Lambda\epsilon^{ibk\Lambda} - b^2k^2\Lambda^2\right)\right.$$
$$\left.\left(6 - 6\epsilon^{iak\mathrm{K}} + 2iak\mathrm{K} + 4iak\mathrm{K}\epsilon^{iak\mathrm{K}} + a^2k^2\mathrm{K}^2\epsilon^{iak\mathrm{K}}\right)\right]/\left(a^2b^2\mathrm{K}^4\Lambda^4k^8\right) \tag{C.18}$$

$$I_{15}(k, \mathrm{K}, \Lambda) = \left[\left(6 - 6\epsilon^{ibk\Lambda} + 2ibk\Lambda + 4ibk\Lambda\epsilon^{ibk\Lambda} + b^2k^2\Lambda^2\epsilon^{ibk\Lambda}\right)\right.$$
$$\left.\left(6 - 6\epsilon^{iak\mathrm{K}} + 2iak\mathrm{K} + 4iak\mathrm{K}\epsilon^{iak\mathrm{K}} + a^2k^2\mathrm{K}^2\epsilon^{iak\mathrm{K}}\right)\right]/\left(a^2b^2\mathrm{K}^4\Lambda^4k^8\right) \tag{C.19}$$

$$I_{16}(k, \mathrm{K}, \Lambda) = \left[\left(6 - 6\epsilon^{ibk\Lambda} + 2ibk\Lambda + 4ibk\Lambda\epsilon^{ibk\Lambda} + b^2k^2\Lambda^2\epsilon^{ibk\Lambda}\right)\right.$$
$$\left.\left(6 - 6\epsilon^{iak\mathrm{K}} + 4iak\mathrm{K} + 2iak\mathrm{K}\epsilon^{iak\mathrm{K}} - a^2k^2\mathrm{K}^2\right)\right]/\left(a^2b^2\mathrm{K}^4\Lambda^4k^8\right) \tag{C.20}$$

$(\mathrm{K} \neq 0, \Lambda = 0)$

$$I_1(k, \mathrm{K}) = b\left(12 - 12\epsilon^{iak\mathrm{K}} + 6iak\mathrm{K} + 6iak\mathrm{K}\epsilon^{iak\mathrm{K}} + ia^3k^3\mathrm{K}^3\right)/\left(2a^3k^4\mathrm{K}^4\right) \tag{C.21}$$

$$I_2(k, \mathrm{K}) = b\left(-12 + 12\epsilon^{iak\mathrm{K}} - 6iak\mathrm{K} - 6iak\mathrm{K}\epsilon^{iak\mathrm{K}} - ia^3k^3\mathrm{K}^3\epsilon^{iak\mathrm{K}}\right)/\left(2a^3k^4\mathrm{K}^4\right) \tag{C.22}$$

$$I_3(k, \mathrm{K}) = b\left(-12 + 12\epsilon^{iak\mathrm{K}} - 6iak\mathrm{K} - 6iak\mathrm{K}\epsilon^{iak\mathrm{K}} - ia^3k^3\mathrm{K}^3\epsilon^{iak\mathrm{K}}\right)/\left(2a^3k^4\mathrm{K}^4\right) \tag{C.23}$$

$$I_4(k, \mathrm{K}) = b\left(12 - 12\epsilon^{iak\mathrm{K}} + 6iak\mathrm{K} + 6iak\mathrm{K}\epsilon^{iak\mathrm{K}} + ia^3k^3\mathrm{K}^3\right)/\left(2a^3k^4\mathrm{K}^4\right) \tag{C.24}$$

$$I_5(k, \mathrm{K}) = b\left(6 - 6\epsilon^{iak\mathrm{K}} + 4iak\mathrm{K} + 2iak\mathrm{K}\epsilon^{iak\mathrm{K}} - a^2k^2\mathrm{K}^2\right)/\left(2a^2k^4\mathrm{K}^4\right) \tag{C.25}$$

$$I_6(k, \mathrm{K}) = b\left(6 - 6\epsilon^{iak\mathrm{K}} + 2iak\mathrm{K} + 4iak\mathrm{K}\epsilon^{iak\mathrm{K}} + a^2k^2\mathrm{K}^2\epsilon^{iak\mathrm{K}}\right)/\left(2a^2k^4\mathrm{K}^4\right) \tag{C.26}$$

$$I_7(k, \mathrm{K}) = b\left(6 - 6\epsilon^{iak\mathrm{K}} + 2iak\mathrm{K} + 4iak\mathrm{K}\epsilon^{iak\mathrm{K}} + a^2k^2\mathrm{K}^2\epsilon^{iak\mathrm{K}}\right)/\left(2a^2k^4\mathrm{K}^4\right) \tag{C.27}$$

$$I_8(k, \mathrm{K}) = b\left(6 - 6\epsilon^{iak\mathrm{K}} + 4iak\mathrm{K} + 2iak\mathrm{K}\epsilon^{iak\mathrm{K}} - a^2k^2\mathrm{K}^2\right)/\left(2a^2k^4\mathrm{K}^4\right) \tag{C.28}$$

$$I_9(k, \mathrm{K}) = b^2\left(12 - 12\epsilon^{iak\mathrm{K}} + 6iak\mathrm{K} + 6iak\mathrm{K}\epsilon^{iak\mathrm{K}} + ia^3k^3\mathrm{K}^3\right)/\left(12a^3k^4\mathrm{K}^4\right) \tag{C.29}$$

$$I_{10}(k, \mathrm{K}) = b^2\left(-12 + 12\epsilon^{iak\mathrm{K}} - 6iak\mathrm{K} - 6iak\mathrm{K}\epsilon^{iak\mathrm{K}} - ia^3k^3\mathrm{K}^3\epsilon^{iak\mathrm{K}}\right)/\left(12a^3k^4\mathrm{K}^4\right) \tag{C.30}$$

$$I_{11}(k, \mathrm{K}) = b^2\left(12 - 12\epsilon^{iak\mathrm{K}} + 6iak\mathrm{K} + 6iak\mathrm{K}\epsilon^{iak\mathrm{K}} + ia^3k^3\mathrm{K}^3\epsilon^{iak\mathrm{K}}\right)/\left(12a^3k^4\mathrm{K}^4\right) \tag{C.31}$$

$$I_{12}(k, \mathrm{K}) = b^2\left(-12 + 12\epsilon^{iak\mathrm{K}} - 6iak\mathrm{K} - 6iak\mathrm{K}\epsilon^{iak\mathrm{K}} - ia^3k^3\mathrm{K}^3\right)/\left(12a^3k^4\mathrm{K}^4\right) \tag{C.32}$$

$$I_{13}(k, \mathrm{K}) = b^2\left(6 - 6\epsilon^{iak\mathrm{K}} + 4iak\mathrm{K} + 2iak\mathrm{K}\epsilon^{iak\mathrm{K}} - a^2k^2\mathrm{K}^2\right)/\left(12a^2k^4\mathrm{K}^4\right) \tag{C.33}$$

$$I_{14}(k, \mathrm{K}) = b^2\left(6 - 6\epsilon^{iak\mathrm{K}} + 2iak\mathrm{K} + 4iak\mathrm{K}\epsilon^{iak\mathrm{K}} + a^2k^2\mathrm{K}^2\epsilon^{iak\mathrm{K}}\right)/\left(12a^2k^4\mathrm{K}^4\right) \tag{C.34}$$

$$I_{15}(k, \mathrm{K}) = b^2\left(-6 + 6\epsilon^{iak\mathrm{K}} - 2iak\mathrm{K} - 4iak\mathrm{K}\epsilon^{iak\mathrm{K}} - a^2k^2\mathrm{K}^2\epsilon^{iak\mathrm{K}}\right)/\left(12a^2k^4\mathrm{K}^4\right) \tag{C.35}$$

$$I_{16}(k, \mathrm{K}) = b^2\left(-6 + 6\epsilon^{iak\mathrm{K}} - 4iak\mathrm{K} - 2iak\mathrm{K}\epsilon^{iak\mathrm{K}} + a^2k^2\mathrm{K}^2\right)/\left(12a^2k^4\mathrm{K}^4\right) \tag{C.36}$$

$(K = 0, \Lambda \neq 0)$

$$I_1(k, \Lambda) = a\left(12 - 12\epsilon^{ibk\Lambda} + 6ibk\Lambda + 6ibk\Lambda\epsilon^{ibk\Lambda} + ib^3k^3\Lambda^3\right)/\left(2b^3k^4\Lambda^4\right) \tag{C.37}$$

$$I_2(k, \Lambda) = a\left(12 - 12\epsilon^{ibk\Lambda} + 6ibk\Lambda + 6ibk\Lambda\epsilon^{ibk\Lambda} + ib^3k^3\Lambda^3\right)/\left(2b^3k^4\Lambda^4\right) \tag{C.38}$$

$$I_3(k, \Lambda) = a\left(-12 + 12\epsilon^{ibk\Lambda} - 6ibk\Lambda - 6ibk\Lambda\epsilon^{ibk\Lambda} - ib^3k^3\Lambda^3\epsilon^{ibk\Lambda}\right)/\left(2b^3k^4\Lambda^4\right) \tag{C.39}$$

$$I_4(k, \Lambda) = a\left(-12 + 12\epsilon^{ibk\Lambda} - 6ibk\Lambda - 6ibk\Lambda\epsilon^{ibk\Lambda} - ib^3k^3\Lambda^3\epsilon^{ibk\Lambda}\right)/\left(2b^3k^4\Lambda^4\right) \tag{C.40}$$

$$I_5(k, \Lambda) = a^2\left(12 - 12\epsilon^{ibk\Lambda} + 6ibk\Lambda + 6ibk\Lambda\epsilon^{ibk\Lambda} + ib^3k^3\Lambda^3\right)/\left(12b^3k^4\Lambda^4\right) \tag{C.41}$$

$$I_6(k, \Lambda) = a^2\left(-12 + 12\epsilon^{ibk\Lambda} - 6ibk\Lambda - 6ibk\Lambda\epsilon^{ibk\Lambda} - ib^3k^3\Lambda^3\right)/\left(12b^3k^4\Lambda^4\right) \tag{C.42}$$

$$I_7(k, \Lambda) = a^2\left(12 - 12\epsilon^{ibk\Lambda} + 6ibk\Lambda + 6ibk\Lambda\epsilon^{ibk\Lambda} + ib^3k^3\Lambda^3\epsilon^{ibk\Lambda}\right)/\left(12b^3k^4\Lambda^4\right) \tag{C.43}$$

$$I_8(k, \Lambda) = a^2\left(-12 + 12\epsilon^{ibk\Lambda} - 6ibk\Lambda - 6ibk\Lambda\epsilon^{ibk\Lambda} - ib^3k^3\Lambda^3\epsilon^{ibk\Lambda}\right)/\left(12b^3k^4\Lambda^4\right) \tag{C.44}$$

$$I_9(k, \Lambda) = a\left(6 - 6\epsilon^{ibk\Lambda} + 4ibk\Lambda + 2ibk\Lambda\epsilon^{ibk\Lambda} - b^2k^2\Lambda^2\right)/\left(2b^2k^4\Lambda^4\right) \tag{C.45}$$

$$I_{10}(k, \Lambda) = a\left(6 - 6\epsilon^{ibk\Lambda} + 4ibk\Lambda + 2ibk\Lambda\epsilon^{ibk\Lambda} - b^2k^2\Lambda^2\right)/\left(2b^2k^4\Lambda^4\right) \tag{C.46}$$

$$I_{11}(k, \Lambda) = a\left(6 - 6\epsilon^{ibk\Lambda} + 2ibk\Lambda + 4ibk\Lambda\epsilon^{ibk\Lambda} + b^2k^2\Lambda^2\epsilon^{ibk\Lambda}\right)/\left(2b^2k^4\Lambda^4\right) \tag{C.47}$$

$$I_{12}(k, \Lambda) = a\left(6 - 6\epsilon^{ibk\Lambda} + 2ibk\Lambda + 4ibk\Lambda\epsilon^{ibk\Lambda} + b^2k^2\Lambda^2\epsilon^{ibk\Lambda}\right)/\left(2b^2k^4\Lambda^4\right) \tag{C.48}$$

$$I_{13}(k, \Lambda) = a^2\left(6 - 6\epsilon^{ibk\Lambda} + 4ibk\Lambda + 2ibk\Lambda\epsilon^{ibk\Lambda} - b^2k^2\Lambda^2\right)/\left(12b^2k^4\Lambda^4\right) \tag{C.49}$$

$$I_{14}(k, \Lambda) = a^2\left(-6 + 6\epsilon^{ibk\Lambda} - 4ibk\Lambda - 2ibk\Lambda\epsilon^{ibk\Lambda} + b^2k^2\Lambda^2\right)/\left(12b^2k^4\Lambda^4\right) \tag{C.50}$$

$$I_{15}(k, \Lambda) = a^2\left(-6 + 6\epsilon^{ibk\Lambda} - 2ibk\Lambda - 4ibk\Lambda\epsilon^{ibk\Lambda} - b^2k^2\Lambda^2\epsilon^{ibk\Lambda}\right)/\left(12b^2k^4\Lambda^4\right) \tag{C.51}$$

$$I_{16}(k, \Lambda) = a^2\left(6 - 6\epsilon^{ibk\Lambda} + 2ibk\Lambda + 4ibk\Lambda\epsilon^{ibk\Lambda} + b^2k^2\Lambda^2\epsilon^{ibk\Lambda}\right)/\left(12b^2k^4\Lambda^4\right) \tag{C.52}$$

$(K = 0, \Lambda = 0)$

$$I_1 \rightarrow I_4 = \frac{ab}{4} \tag{C.53}$$

$$I_5, I_8 = \frac{a^2b}{24} \qquad\qquad I_6, I_7 = -\frac{a^2b}{24} \tag{C.54}$$

$$I_9, I_{10} = \frac{ab^2}{24} \qquad\qquad I_{11}, I_{12} = -\frac{ab^2}{24} \tag{C.55}$$

$$I_{13}, I_{15} = \frac{a^2b^2}{144} \qquad\qquad I_{14}, I_{16} = -\frac{a^2b^2}{144} \tag{C.56}$$

These expressions were used as function calls to evaluate the vectors pre- and post-multiplying the element-ij displacement spectral matrix in equation (C.3).

Appendix D
Radiation Far-Field Approximations

Prediction of the radiated acoustic pressure to a free field from a vibrating surface requires evaluation of Rayleigh's integral, equation (7.1). The present work casts the radiated acoustic pressure response in three forms: continuous spectral analysis of stochastic response, given by equation (7.10); and discrete spectral analysis of deterministic and stochastic responses, given by equations (7.24) and (7.31). The existence of the radial distance dependence in the integrand requires the use of numerical integration or some simplifying assumptions. The integrand can be simplified extensively by considering only far-field observer locations in the acoustic free-field. Let the observation point (x, y, z) in the acoustic field be designated by its distance R from the panel center and two direction angles: the polar angle $\theta = [0, \pi/2]$, and the azimuthal angle $\phi = [0, 2\pi]$. Thus,

$$
\begin{aligned}
R &= \sqrt{x^2 + y^2 + z^2} \\
x &= R \sin\theta \cos\phi \\
y &= R \sin\theta \sin\phi \\
z &= R \cos\theta
\end{aligned}
\tag{D.1}
$$

and the distance from a point on the panel to the observation point

$$
r = \sqrt{(x - \xi)^2 + (y - \eta)^2 + z^2}
\tag{D.2}
$$

becomes

$$
r = R\sqrt{1 - \frac{2\sin\theta \cos\phi}{R}\xi + \left(\frac{\xi}{R}\right)^2 - \frac{2\sin\theta \sin\phi}{R}\eta + \left(\frac{\eta}{R}\right)^2}
\tag{D.3}
$$

The acoustic far-field approximation entails neglecting the terms in the expression for r that involve $1/R^2$ and letting

$$
\frac{1}{r} \approx \frac{1}{R}
\tag{D.4}
$$

The remaining terms in the expression for r may be expanded in a binomial series:

$$
r = R\left[1 - \frac{1}{2}\left(\frac{2\xi \sin\theta \cos\phi}{R} + \frac{2\eta \sin\theta \sin\phi}{R}\right) + O\left(\frac{1}{R^2}\right) + \cdots\right]
\tag{D.5}
$$

Retaining the first two terms in the expansion results in

$$
r \approx R\left(1 - \frac{\sin\theta \cos\phi}{R}\xi - \frac{\sin\theta \sin\phi}{R}\eta\right)
\tag{D.6}
$$

or

$$
r \approx R - K\xi - \Lambda\eta
\tag{D.7}
$$

where $K = \sin\theta\cos\phi$ and $\Lambda = \sin\theta\sin\phi$. Thus, the exponential term in the integrand of equation (7.24) can be simplified as follows.

$$e^{-i\omega_n \frac{r}{c}} \approx e^{-i\frac{\omega_n}{c}(R - K\xi - \Lambda\eta)} \tag{D.8}$$

Finally, the difference in radial distances encountered in equations (7.10) and (7.31) becomes

$$r_1 - r_1' \approx K(\xi' - \xi) + \Lambda(\eta' - \eta) \tag{D.9}$$

and the corresponding exponential term in the integrand takes the following form.

$$e^{i\omega_n\left(\frac{r_1 - r_1'}{c}\right)} \approx e^{i\frac{\omega_n}{c}[(\xi' - \xi)K + (\eta' - \eta)\Lambda]} \tag{D.10}$$

Appendix E
Acoustic Intensity, Power, and TL

The acoustic intensity at a point is equal to the time average of the product of the perturbed pressure and velocity. For a pressure and velocity that are random processes, this temporal average must be taken in the limit as the characteristic time $T \to \infty$:

$$I(x,y,z) = \langle p(x,y,z,t)\vec{u}(x,y,z,t)\rangle = \lim_{T\to\infty} \frac{1}{T} \int_0^T p(x,y,z,t)\vec{u}(x,y,z,t)\,dt \qquad (E.1)$$

where $\vec{u}(x,y,z,t)$ is the acoustic velocity vector. This temporal average may be replaced by an expected value:

$$\begin{aligned} I(x,y,z) &= \langle p(x,y,z,t)\vec{u}(x,y,z,t)\rangle \\ &= E[p(x,y,z,t)\vec{u}(x,y,z,t)] \end{aligned} \qquad (E.2)$$

by assuming that the processes are *ergodic in correlation*. In general, the relationship between the acoustic pressure and velocity is not known and must be determined concurrently. However, in the acoustic far-field, the radial velocity is dominant and the propagating acoustic waves appear planar. Consequently, the relationship between the acoustic pressure and velocity can be approximated by

$$\vec{u}(R,\theta,\phi,t) \approx u_r(R,\theta,\phi,t) = \frac{p(R,\theta,\phi,t)}{\rho c} \qquad (E.3)$$

where the spatial description has been changed to spherical coordinates for consistency with equations (7.18), (7.35), or (7.37). Thus, the far-field radiated acoustic intensity becomes

$$I_t(R,\theta,\phi) = \frac{1}{\rho c} E[p_t^2(R,\theta,\phi,t)] = \frac{\overline{p_t^2}}{\rho c} \qquad (E.4)$$

where the mean square acoustic pressure is given by one of the equations referenced above.

The acoustic power incident upon a surface is defined as the integral of the normal acoustic intensity over the surface:

$$\Pi_s = \int_S I(r,\theta,\phi) \cdot \hat{n}\, dS \qquad (E.5)$$

where $\hat{n}$ is the surface unit normal. Therefore, the total acoustic power radiated by the plate is calculated by integrating the acoustic intensity over a far-field hemisphere as follows.

$$\Pi_r = \int_{\phi=0}^{2\pi} \int_{\theta=0}^{\pi/2} I(r,\theta,\phi)\, R^2 \sin\theta\, d\theta\, d\phi \qquad (E.6)$$

where the radiated intensity has the form given in equation (E.4). Note that the R^2 in the integrand cancels with that in the expression for the far-field acoustic intensity, equations

(7.18)/(7.35)/(7.37) and (E.4). This integral must be evaluated numerically, which can be accomplished via Gauss-Legendre numerical integration (see Appendix B).

Recall that for the case of acoustic pressure excitation the incident acoustic pressure consists of obliquely incident plane waves. The incident acoustic intensity is then, from the above discussion,

$$I_i = \frac{\overline{p_i^2}}{\rho c} \tag{E.7}$$

and the incident acoustic power is simply the product of the normal acoustic intensity and the area of the plate

$$\Pi_i = \frac{\overline{p_i^2} a b \cos\theta_i}{\rho c} \tag{E.8}$$

Finally, the transmission loss (TL) is defined in units of dB by the logarithm of the ratio of incident acoustic power to radiated acoustic power

$$TL = 10 \log\left(\frac{\Pi_i}{\Pi_r}\right) \tag{E.9}$$

Appendix F
Continuous Spectral Examples

A continuous spectral analysis was one approach used in Chapter 6 to derive the expression for the dynamic response correlation matrices of a panel-type structure subjected to elevated and/or one of the following mechanical loads; acoustic pressure, concentrated forces, or base acceleration. A similar approach was used in Chapter 7 to derive an expression for the mean square radiated acoustic pressure due to the same structure, but limited to two of the three mechanical loads; acoustic pressure or concentrated forces. The dynamic response correlation matrices and mean square radiated pressure require evaluation of spectral integrals of the forms given in equations (6.36) and (7.15), respectively. It is clear that these equations have a very similar form and will be denoted by $I_{mn}^{(d,v,a)}(\tau)$ in the following generic expression

$$
I_{mn}^{(d,v,a)}(\tau) = \int_{-\infty}^{\infty} \omega^{(0,2,4)} H_m^*(\omega) H_n(\omega) S_{**}(\omega) e^{i\omega\tau}\, d\omega
$$

$$
= \int_{-\infty}^{\infty} \frac{\omega^{(0,2,4)} S_{**}(\omega)}{(\omega_m^2 - \omega^2 - i2\zeta_m\omega_m\omega)(\omega_n^2 - \omega^2 + i2\zeta_n\omega_n\omega)} e^{i\omega\tau}\, d\omega
$$

(F.1)

where the expressions for the frequency response functions $H_*(\omega)$ have been substituted from equation (6.29) and $S_{**}(\omega)$ is the power spectral density function of the excitation. The superscript (d, v, a) indicates that the multiplier of $\omega^{(0,2,4)}$ corresponds to displacement, velocity, and acceleration response, respectively.

Two sample cases for the evaluation of the integral in equation (F.1) are presented in this appendix including harmonic and band-unlimited white noise excitation. The case of harmonic excitation is obviously not stochastic, but is included as a simple comparative case.

F.1 Harmonic Excitation

Harmonic excitation can be described in either of the following forms

$$
S_{**}(\omega) = \begin{cases} S_0 & |\omega| = \omega_0 \\ 0 & \text{otherwise} \end{cases}, \qquad S_{**}(\omega) = S_0\, \delta(|\omega| - \omega_0)
$$

(F.2)

or

$$
C_{**}(\tau) = 2S_0 \, \cos\omega_0\tau
$$

(F.3)

where S_0 is a constant, $\delta(|\omega| - \omega_0)$ is a spectral Dirac delta function, $\tau = t_2 - t_1$, and the subscript $**$ indicates the excitation could be due to acoustic pressure, concentrated forces, or base acceleration. Substitution of $S_{**}(\omega)$ into equation (F.1) results in

$$
I_{mn}^{(d,v,a)}(\tau) = \int_{-\infty}^{\infty} \frac{\omega^{(0,2,4)}}{(\omega_m^2 - \omega^2 - i2\zeta_m\omega_m\omega)(\omega_n^2 - \omega^2 + i2\zeta_n\omega_n\omega)} S_0\delta(|\omega| - \omega_0) e^{i\omega\tau}\, d\omega
$$

(F.4)

This equation may be simplified by retaining only even terms, because the integral of odd terms over even limits vanishes, as

$$I_{mn}^{(d,v,a)}(\tau) = 2 \int_0^\infty \left(\frac{\omega^{(0,2,4)} \left[\left(\omega_m^2 - \omega^2\right)\left(\omega_n^2 - \omega^2\right) + 4\zeta_m\zeta_n\omega_m\omega_n\omega^2 \right] \cos \omega\tau}{\left[\left(\omega_m^2 - \omega^2\right)^2 + 4\zeta_m^2\omega_m^2\omega^2 \right]\left[\left(\omega_n^2 - \omega^2\right)^2 + 4\zeta_n^2\omega_n^2\omega^2 \right]} \right.$$
$$\left. + \frac{2\omega^{(1,3,5)} \left[\zeta_m\omega_m\left(\omega_n^2 - \omega^2\right) - \zeta_n\omega_n\left(\omega_m^2 - \omega^2\right) \right] \sin \omega\tau}{\left[\left(\omega_m^2 - \omega^2\right)^2 + 4\zeta_m^2\omega_m^2\omega^2 \right]\left[\left(\omega_n^2 - \omega^2\right)^2 + 4\zeta_n^2\omega_n^2\omega^2 \right]} \right) S_0\delta(\omega - \omega_0) \, d\omega$$

(F.5)

Enforcing the Dirac delta function results in

$$I_{mn}^{(d,v,a)}(\tau) = \frac{2S_0\omega_0^{(0,2,4)} \left[\left(\omega_m^2 - \omega_0^2\right)\left(\omega_n^2 - \omega_0^2\right) + 4\zeta_m\zeta_n\omega_m\omega_n\omega_0^2 \right]}{\left[\left(\omega_m^2 - \omega_0^2\right)^2 + 4\zeta_m^2\omega_m^2\omega_0^2 \right]\left[\left(\omega_n^2 - \omega_0^2\right)^2 + 4\zeta_n^2\omega_n^2\omega_0^2 \right]} \cos \omega_0\tau$$
$$+ \frac{4S_0\omega_0^{(1,3,5)} \left[\zeta_m\omega_m\left(\omega_n^2 - \omega_0^2\right) - \zeta_n\omega_n\left(\omega_m^2 - \omega_0^2\right) \right]}{\left[\left(\omega_m^2 - \omega_0^2\right)^2 + 4\zeta_m^2\omega_m^2\omega_0^2 \right]\left[\left(\omega_n^2 - \omega_0^2\right)^2 + 4\zeta_n^2\omega_n^2\omega_0^2 \right]} \sin \omega_0\tau$$

(F.6)

This expression can be used directly for calculation of the dynamic response correlation matrices given by equation (6.38). The mean square radiated pressure makes use of the acceleration response case, i.e., $I_{mn}^{(a)}(\tau)$, by making the substitution

$$\tau = \frac{(\xi' - \xi)K + (\eta' - \eta)\Lambda}{c}$$

(F.7)

and using the result in equation (7.18). Finally, the mean square dynamic responses can be obtained from the diagonal elements of the dynamic response correlation matrices for zero time difference ($\tau = 0$) which get input from the following simplified form for $I_{mn}^{(d,v,a)}(0)$

$$I_{mn}^{(d,v,a)}(0) = \frac{2S_0\omega_0^{(0,2,4)} \left[\left(\omega_m^2 - \omega_0^2\right)\left(\omega_n^2 - \omega_0^2\right) + 4\zeta_m\zeta_n\omega_m\omega_n\omega_0^2 \right]}{\left[\left(\omega_m^2 - \omega_0^2\right)^2 + 4\zeta_m^2\omega_m^2\omega_0^2 \right]\left[\left(\omega_n^2 - \omega_0^2\right)^2 + 4\zeta_n^2\omega_n^2\omega_0^2 \right]}$$

(F.8)

F.2 Band-Unlimited White Noise Excitation

Band-unlimited white noise excitation may be described by either of the two following forms:

$$S_{**}(\omega) = S_0$$

(F.9)

or

$$C_{**}(\tau) = 2\pi S_0\delta(\tau)$$

(F.10)

where S_0 is a constant for all frequencies and $\tau = t_2 - t_1$. Substitution of $S_{**}(\omega)$ into equation (F.1) results in

$$I_{mn}^{(d,v,a)}(\tau) = \int_{-\infty}^{\infty} \frac{\omega^{(0,2,4)} S_0}{(\omega_m^2 - \omega^2 - i2\zeta_m\omega_m\omega)(\omega_n^2 - \omega^2 + i2\zeta_n\omega_n\omega)} e^{i\omega\tau} \, d\omega$$

(F.11)

217
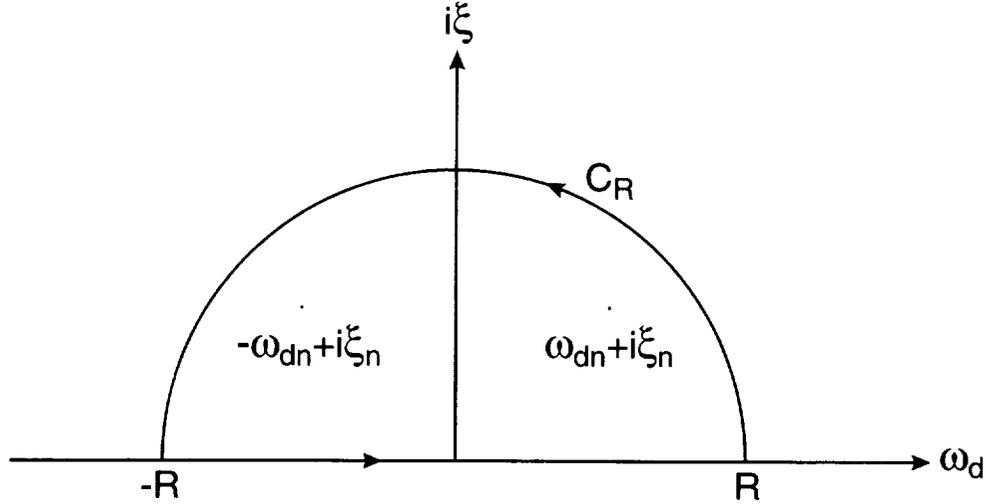
Figure F.1 Schematic of upper-half-plane contour for evaluation of dynamic response due to band-unlimited white noise excitation.

One way to evaluate the integral in equation F.11 is to employ the Cauchy residue theorem by integrating over a semicircular contour, in the limit as the radius of the contour becomes infinite, in the upper half plane (for $\tau > 0$) enclosing the poles of the integrand in the UHP. The case for $I_{mn}^{(a)}(\tau)$, i.e., acceleration response—ω^4 in the numerator, in equation (F.11) is unbounded. Therefore, attention is limited to $I_{mn}^{(d,v)}(\tau)$, the cases for $\omega^{(0,2)}$ in the numerator. A schematic of the contour of integration is shown in Figure F.1.

The integral around the closed contour can be written as

$$\oint_C f(\omega) e^{i\omega\tau} d\omega = \int_{-R}^{R} f(\omega) e^{i\omega\tau} d\omega + \int_{C_R} f(\omega) e^{i\omega\tau} d\omega \tag{F.12}$$

where the integrand in equation (F.11) has been denoted by $f(\omega)e^{i\omega\tau}$ and C_R denotes the circular portion of the contour. In the limit as $R \to \infty$, the first integral on the right-hand side takes the desired form, the Cauchy principal value, and the sum of the two integrals can be evaluated by employing the Cauchy residue theorem as

$$\lim_{R\to\infty} \int_{-R}^{R} f(\omega) e^{i\omega\tau} d\omega + \lim_{R\to\infty} \int_{C_R} f(\omega) e^{i\omega\tau} d\omega = 2\pi i \sum_{k=1}^{N_r} \mathrm{Res}\left[f(\omega)e^{i\omega\tau}; r_k\right] \tag{F.13}$$

where the expression on the right of the summation represents the residue of $f(\omega)e^{i\omega\tau}$ at the pole r_k and N_r is the number of poles of $f(\omega)$ enclosed within the contour (which becomes all

218

of those in the UHP as $R \to \infty$). Recall the expression for $f(\omega)$ shown in equation (F.11). This expression can be rewritten in terms of simple poles as follows

$$f(\omega) = \frac{\omega^{(0.2)} S_0}{(\omega_m^2 - \omega^2 - i2\zeta_m \omega_m \omega)(\omega_n^2 - \omega^2 + i2\zeta_n \omega_n \omega)}$$

$$= \frac{\omega^{(0.2)} S_0}{(\omega - \omega_1)(\omega - \omega_2)(\omega - \omega_3)(\omega - \omega_4)} \tag{F.14}$$

where

$$\begin{aligned} \omega_{1,2} &= -i\zeta_m \omega_m \pm \sqrt{-\zeta_m^2 \omega_m^2 + \omega_m^2} \\ &= \pm\omega_m\sqrt{1 - \zeta_m^2} - i\zeta_m\omega_m \\ &= \pm\omega_{dm} - i\xi_m \end{aligned} \quad \text{and} \quad \begin{aligned} \omega_{3,4} &= i\zeta_n\omega_n \pm \sqrt{-\zeta_n^2\omega_n^2 + \omega_n^2} \\ &= \pm\omega_n\sqrt{1 - \zeta_n^2} + i\zeta_n\omega_n \\ &= \pm\omega_{dn} + i\xi_n \end{aligned} \tag{F.15}$$

Because $f(\omega)$ can be written as

$$f(\omega) = \frac{\varphi_i(\omega)}{(\omega - \omega_i)} \qquad \text{for} \qquad i = 1 \to 4 \tag{F.16}$$

the residue of $f(\omega)$ at the pole ω_i is given by the coefficient of $1/(\omega - \omega_i)$ in the Laurent expansion (see Churchill and Brown [61]) given by

$$f(\omega) = \frac{\varphi_i(\omega)}{(\omega - \omega_i)} + \frac{\varphi_i'(\omega)}{1!} + \cdots \tag{F.17}$$

Thus, the integral on the closed contour becomes

$$\lim_{R \to \infty} \int_{-R}^{R} f(\omega)e^{i\omega\tau}d\omega + \lim_{R \to \infty} \int_{C_R} f(\omega)e^{i\omega\tau}d\omega = 2\pi i \Big[\lim_{\omega \to \omega_3} \left\{ (\omega - \omega_3)f(\omega)e^{i\omega\tau} \right\}$$
$$+ \lim_{\omega \to \omega_4} \left\{ (\omega - \omega_4)f(\omega)e^{i\omega\tau} \right\} \Big] \tag{F.18}$$

It can be shown that the integral on the circular portion of the contour is zero (see Hildebrand [62]) so the desired result has been achieved as

$$I_{mn}^{(d,v)}(\tau) = \int_{-\infty}^{\infty} f(\omega)e^{i\omega\tau}\,d\omega$$

$$= 2\pi i \Big[\lim_{\omega \to \omega_3} \left\{ (\omega - \omega_3)f(\omega)e^{i\omega\tau} \right\} + \lim_{\omega \to \omega_4} \left\{ (\omega - \omega_4)f(\omega)e^{i\omega\tau} \right\} \Big]$$

$$= 2\pi i \left[\frac{\omega_3^{(0.2)} S_0 e^{i\omega_3\tau}}{(\omega_3 - \omega_1)(\omega_3 - \omega_2)(\omega_3 - \omega_4)} + \frac{\omega_4^{(0.2)} S_0 e^{i\omega_4\tau}}{(\omega_4 - \omega_1)(\omega_4 - \omega_2)(\omega_4 - \omega_3)} \right] \tag{F.19}$$

The terms in this expression can the expanded into a sum of real and imaginary components and simplified to the following

$$I_{mn}^{(d)}(\tau) = \frac{4\pi(\xi_m + \xi_n)S_0 e^{-\xi_n\tau}\cos\omega_{dn}\tau}{\left[(\omega_{dm} - \omega_{dn})^2 + (\xi_m + \xi_n)^2\right]\left[(\omega_{dm} + \omega_{dn})^2 + (\xi_m + \xi_n)^2\right]}$$

$$- \frac{4\pi\left[\omega_{dn}^2 - \omega_{dm}^2 - (\xi_m + \xi_n)^2\right]S_0 e^{-\xi_n\tau}\sin\omega_{dn}\tau}{\left[(\omega_{dm} - \omega_{dn})^2 + (\xi_m + \xi_n)^2\right]\left[(\omega_{dm} + \omega_{dn})^2 + (\xi_m + \xi_n)^2\right]} \tag{F.20}$$

and

$$I_{mn}^{(v)}(\tau) = \frac{4\pi \left(\omega_{dn}^2 \xi_m + \omega_{dm}^2 \xi_n + \xi_n \xi_m^2 + \xi_n^2 \xi_m \right) S_0 e^{-\xi_n \tau} \cos \omega_{dn} \tau}{\left[(\omega_{dm} - \omega_{dn})^2 (\xi_m + \xi_n)^2 \right] \left[(\omega_{dm} + \omega_{dn})^2 (\xi_m + \xi_n)^2 \right]}$$
$$- \frac{4\pi \left[\omega_{dn}^4 - \omega_{dn}^2 \omega_{dm}^2 - \omega_{dn}^2 \xi_m^2 + 2\omega_{dn}^2 \xi_m \xi_n + \omega_{dm}^2 \xi_n^2 + \xi_n^2 (\xi_m + \xi_n)^2 \right] S_0 e^{-\xi_n \tau} \sin \omega_{dn} \tau}{\left[(\omega_{dm} - \omega_{dn})^2 (\xi_m + \xi_n)^2 \right] \left[(\omega_{dm} + \omega_{dn})^2 (\xi_m + \xi_n)^2 \right]}$$

(F.21)

These expressions can be used directly for calculation of the dynamic response correlation matrices given by equation (6.38). The mean square radiated pressure cannot be computed in this case as the acceleration response for band-unlimited white noise is unbounded, as stated previously. Finally, the mean square dynamic responses can be obtained from the diagonal elements of the dynamic response correlation matrices for zero time difference $(\tau = 0)$ which get input from the following simplified forms for $I_{mn}^{(d)}(0)$ and $I_{mn}^{(v)}(0)$

$$I_{mn}^{(d)}(0) = \frac{4\pi S_0 (\xi_m + \xi_n)}{\left[(\omega_{dn} - \omega_{dm})^2 + (\xi_m + \xi_n)^2 \right] \left[(\omega_{dn} + \omega_{dm})^2 + (\xi_m + \xi_n)^2 \right]}$$

(F.22)

and

$$I_{mn}^{(v)}(0) = \frac{4\pi S_0 \left[\xi_m \left(\omega_{dn}^2 + \xi_n^2 \right) + \xi_n \left(\omega_{dm}^2 + \xi_m^2 \right) \right]}{\left[(\omega_{dn} - \omega_{dm})^2 + (\xi_m + \xi_n)^2 \right] \left[(\omega_{dn} + \omega_{dm})^2 + (\xi_m + \xi_n)^2 \right]}$$

(F.23)

REPORT DOCUMENTATION PAGE

1. AGENCY USE ONLY (Leave blank)	2. REPORT DATE	3. REPORT TYPE AND DATES COVERED
	January 2001	Technical Memorandum

4. TITLE AND SUBTITLE
Thermomechanical Response of Shape Memory Alloy Hybrid Composites

5. FUNDING NUMBERS
WU 706-32-31-02

6. AUTHOR(S)
Travis L. Turner

7. PERFORMING ORGANIZATION NAME(S) AND ADDRESS(ES)

NASA Langley Research Center
Hampton, VA 23681-2199

8. PERFORMING ORGANIZATION REPORT NUMBER

L-18057

9. SPONSORING/MONITORING AGENCY NAME(S) AND ADDRESS(ES)

National Aeronautics and Space Administration
Washington, DC 20546-0001

10. SPONSORING/MONITORING AGENCY REPORT NUMBER

NASA/TM-2001-210656

11. SUPPLEMENTARY NOTES
The information presented in this report was offered as a thesis in partial fulfillment of the requirements for the Degree of Doctor of Philosophy in Engineering Mechanics, Virginia Polytechnic Institute and State University, Blacksburg, Virginia, November 2000.

12a. DISTRIBUTION/AVAILABILITY STATEMENT

Unclassified–Unlimited
Subject Category 71   Distribution: Standard
Availability: NASA CASI (301) 621-0390

12b. DISTRIBUTION CODE

13. ABSTRACT (Maximum 200 words)

This study examines the use of embedded shape memory alloy (SMA) actuators for adaptive control of the thermo-mechanical response of composite structures. A nonlinear thermomechanical model is presented for analyzing shape memory alloy hybrid composite (SMAHC) structures exposed to steady-state thermal and dynamic mechanical loads. Also presented are (1) fabrication procedures for SMAHC specimens, (2) characterization of the constituent materials for model quantification, (3) development of the test apparatus for conducting static and dynamic experiments on specimens with and without SMA, (4) discussion of the experimental results, and (5) validation of the analytical and numerical tools developed in the study. Excellent agreement is achieved between the predicted and measured SAMHC responses including thermal buckling, thermal post-buckling and dynamic response due to inertial loading. The validated model and thermomechanical analysis tools are used to demonstrate a variety of static and dynamic response behaviors including control of static (thermal buckling and post-buckling) and dynamic responses (vibration, sonic fatigue, and acoustic transmission), and SMAHC design considerations for these applications. SMAHCs are shown to have significant advantages over conventional response abatement approaches for vibration, sonic fatigue, and noise control.

14. SUBJECT TERMS
Nitinol; Embedded actuators; Hybrid composite fabrication; Nonlinear thermoelasticity; Geometric nonlinearity

15. NUMBER OF PAGES
239

16. PRICE CODE
A11

17. SECURITY CLASSIFICATION OF REPORT	18. SECURITY CLASSIFICATION OF THIS PAGE	19. SECURITY CLASSIFICATION OF ABSTRACT	20. LIMITATION OF ABSTRACT
Unclassified	Unclassified	Unclassified	UL